

**FLOW FIELD MEASUREMENTS IN A COUNTER-SWIRL
STABILIZED LIQUID COMBUSTOR**

A Thesis
Presented to
The Academic Faculty

by

Jonathan A. Colby

In Partial Fulfillment
of the Requirements for the Degree
Masters of Science in the
School of Aerospace Engineering

Georgia Institute of Technology
May, 2006

COPYRIGHT 2006 BY JONATHAN A. COLBY

**FLOW FIELD MEASUREMENTS IN A COUNTER-SWIRL
STABILIZED LIQUID COMBUSTOR**

Approved by:

Dr. Suresh Menon, Advisor
School of Aerospace Engineering
Georgia Institute of Technology

Dr. Jeff Jagoda
School of Aerospace Engineering
Georgia Institute of Technology

Dr. Jerry Seitzman
School of Aerospace Engineering
Georgia Institute of Technology

Date Approved: March 10, 2006

To the improvement of our World

ACKNOWLEDGEMENTS

The author gratefully acknowledges the support of GE Transportation, under the University Strategic Alliance (U.S.A.) project, contract number 200-10-14R53108. Hardware and technical support is also appreciated. The support of NASA/ARC is acknowledged as well; contract number NAG 2-1615.

Further acknowledgement is given to the faculty and staff of the Georgia Institute of Technology College of Aerospace Engineering, specifically Dr. Suresh Menon, Dr. Jeff Jagoda, and Dr. Jerry Seitzman. Thank you for your patience and diligence.

An additional thanks to the students and research engineers of the Aerospace Combustion Lab, both former and current, for all of your counsel and assistance in this research. Special acknowledgement is given to the efforts of Suraj Nair, Oleksandr Bibik, Zachary Snider, Ward Bradshaw, and Keith Becker.

Thank you Ella, for your support from the beginning; without your patience, this would not be possible. Thanks also to my mother, father, family and friends; to whom I am indebted.

TABLE OF CONTENTS

	Page
ACKNOWLEDGEMENTS	iv
LIST OF TABLES	vii
LIST OF FIGURES	viii
NOMENCLATURE	xiii
SUMMARY	xvi
 <u>CHAPTER</u>	
1 INTRODUCTION	1
Overview	1
Background	1
Motivation	2
Review	3
2 OBJECTIVES	9
3 EXPERIMENTATION	10
Hardware	12
Measurement Capabilities	15
Error Estimation	19
4 RESULTS	24
Operating Conditions	24
Non-Reacting Gas Phase	25
Reacting Gas Phase	47
Liquid Phase	79
Exhaust Gas Properties	98

5	CONCLUSIONS	105
6	RECOMMENDATIONS	107
	APPENDIX A: GAS PHASE COMPARISONS	109
	APPENDIX B: CONTOUR PLOT COMPARISONS	128
	REFERENCES	141

LIST OF TABLES

	Page
Table 3.1: Uncertainties in Operating Condition Measurements	20
Table 4.1: Non-Reacting Gas Phase Steady State Operating Conditions	24
Table 4.2: Reacting Flow Steady State Operating Conditions	25
Table 4.3: Legend	28

LIST OF FIGURES

	Page
Figure 3.1: Operation of the Counter-Swirl Stabilized Liquid Combustor	10
Figure 3.2: Experimental Geometry Downstream, Vertical Cross-Section	11
Figure 3.3: Experimental Counter-Swirl Burner, Vertical Cross-Section	11
Figure 3.4: Combustion Chamber Cross-Section	12
Figure 4.1: Non-Reacting Gas Phase Downstream Centerline, Case 1 and Case 2	27
Figure 4.2: Schematic of the Non-Reacting Gas Phase Swirling Flow Field	29
Figure 4.3: Z-Y plane ($Y/R_o = 0$), Case 1 Non-Reacting Axial Mean Velocity	30
Figure 4.4: Z-Y plane ($Y/R_o = 0$), Case 1 Non-Reacting Vertical Mean Velocity	31
Figure 4.5: Z-Y plane ($Y/R_o = 0$), Case 1 Non-Reacting Turbulent Kinetic Energy	34
Figure 4.6: Z-Y plane ($Y/R_o = 0$), Case 1 Non-Reacting Reynolds Shear Stress	35
Figure 4.7: Z-Y plane ($Z/R_o = 0$), Case 1 Non-Reacting Axial Mean Velocity	37
Figure 4.8: Z-Y plane ($Z/R_o = 0$), Case 1 Non-Reacting Vertical Mean Velocity	37
Figure 4.9: Z-Y plane ($Z/R_o = 0$), Case 1 Non-Reacting Turbulent Kinetic Energy	40
Figure 4.10: Z-Y plane ($Z/R_o = 0$), Case 1 Non-Reacting Reynolds Shear Stress and Axial Mean Velocity Vertical Gradient	40
Figure 4.11: Z-Y plane ($Z/R_o = 0$), Case 1 Non-Reacting Axial Mean Velocity and Vertical Gradient	41
Figure 4.12: Schematic of the Non-Reacting Gas Phase Diffusion Characteristics	41
Figure 4.13: Z-Y plane ($Y/R_o = 0$), Case 1 and Case 2 Non-Reacting Axial Mean Velocity	43
Figure 4.14: Z-Y plane ($Y/R_o = 0$), Case 1 and Case 2 Non-Reacting Vertical Mean Velocity	44
Figure 4.15: Z-Y plane ($Y/R_o = 0$), Case 1 and Case 2 Non-Reacting Turbulent Kinetic Energy	46

Figure 4.16: Z-Y plane ($Y/R_o = 0$), Case 1 and Case 2 Non-Reacting Reynolds Shear Stress	47
Figure 4.17: Gas Phase Axial Mean Velocity Downstream Centerline Case 1, Non-Reacting and Reacting	49
Figure 4.18: Gas Phase Axial RMS Velocity Downstream Centerline Case 1, Non-Reacting and Reacting	49
Figure 4.19: Z-Y plane ($Y/R_o = 0$), Case 1 Reacting Axial Mean Velocity	52
Figure 4.20: Z-Y plane ($Y/R_o = 0$), Case 1 Reacting Vertical Mean Velocity	53
Figure 4.21: Z-Y plane ($Y/R_o = 0$), Case 1 Reacting Turbulent Kinetic Energy	56
Figure 4.22: Z-Y plane ($Y/R_o = 0$), Case 1 Reacting Reynolds Shear Stress	57
Figure 4.23: Z-Y plane ($Z/R_o = 0$), Case 1 Reacting Axial Mean Velocity	59
Figure 4.24: Z-Y plane ($Z/R_o = 0$), Case 1 Reacting Vertical Mean Velocity	60
Figure 4.25: Z-Y plane ($Z/R_o = 0$), Case 1 Reacting Turbulent Kinetic Energy	62
Figure 4.26: Z-Y plane ($Z/R_o = 0$), Case 1 Reacting Reynolds Shear Stress and Axial Mean Velocity Vertical Gradient	63
Figure 4.27: Z-Y plane ($Z/R_o = 0$), Case 1 Reacting Axial Mean Velocity and Vertical Gradient	63
Figure 4.28: Schematic of the Reacting Gas Phase Diffusion Characteristics	64
Figure 4.29: Gas Phase Axial Mean Velocity Downstream Centerline Case 2, Non-Reacting and Reacting	66
Figure 4.30: Gas Phase Axial RMS Velocity Downstream Centerline Case 2, Non-Reacting and Reacting	67
Figure 4.31: Z-Y plane ($Y/R_o = 0$), Case 2 Reacting Axial Mean Velocity	70
Figure 4.32: Z-Y plane ($Y/R_o = 0$), Case 2 Reacting Vertical Mean Velocity	71
Figure 4.33: Z-Y plane ($Y/R_o = 0$), Case 2 Reacting Turbulent Kinetic Energy	73
Figure 4.34: Z-Y plane ($Y/R_o = 0$), Case 2 Reacting Reynolds Shear Stress	74
Figure 4.35: Z-Y plane ($Z/R_o = 0$), Case 2 Reacting Axial Mean Velocity	76
Figure 4.36: Z-Y plane ($Z/R_o = 0$), Case 2 Reacting Vertical Mean Velocity	76

Figure 4.37: Z-Y plane ($Z/R_0 = 0$), Case 2 Reacting Turbulent Kinetic Energy	78
Figure 4.38: Z-Y plane ($Z/R_0 = 0$), Case 2 Reacting Reynolds Shear Stress and Axial Mean Velocity Vertical Gradient	78
Figure 4.39: Z-Y plane ($Z/R_0 = 0$), Case 2 Reacting Axial Mean Velocity and Vertical Gradient	79
Figure 4.40: Z-Y Plane at $X/R_0 = 1.60$ ($Y/R_0 = 0$), Case 1 Reacting and Non-Reacting Droplet Distributions	83
Figure 4.41: Z-Y Plane at $X/R_0 = 1.60$ ($Y/R_0 = 0$), Case 1 Filtered and Unfiltered Non-Reacting Mass Mean Diameter and Sauter Mean Diameter	84
Figure 4.42: Z-Y Plane at $X/R_0 = 1.60$ ($Y/R_0 = 0$), Case 1 Filtered and Unfiltered Reacting Mass Mean Diameter and Sauter Mean Diameter	84
Figure 4.43: Z-Y Plane at $X/R_0 = 1.60$ ($Y/R_0 = 0$), Case 1 Filtered Reacting and Non-Reacting Mass Mean Diameter and Sauter Mean Diameter	88
Figure 4.44: Z-Y plane at $X/R_0 = 1.60$ ($Y/R_0 = 0$), Case 1, Filtered and Unfiltered, Reacting and Non-Reacting Droplet Axial, Vertical Mean Velocity, Turbulent Kinetic Energy	89
Figure 4.45: Z-X plane ($Y/R_0 = 0$), Case 1 Reacting Droplet Arithmetic Mean Diameter Contours	91
Figure 4.46: Z-X plane ($Y/R_0 = 0$), Case 1 Reacting Droplet Sauter Mean Diameter Contours	91
Figure 4.47: Z-X plane ($Y/R_0 = 0$), Case 1 Reacting Droplet Number Density Contours	92
Figure 4.48: Z-Y Plane at $X/R_0 = 1.60$ ($Y/R_0 = 0$), Case 2 Reacting Droplet Distributions	94
Figure 4.49: Z-Y Plane at $X/R_0 = 1.60$ ($Y/R_0 = 0$), Case2 Filtered Reacting Mass Mean Diameter and Sauter Mean Diameter	95
Figure 4.50: Z-X plane ($Y/R_0 = 0$), Case 2 Reacting Droplet Arithmetic Mean Diameter Contours	96
Figure 4.51: Z-X plane ($Y/R_0 = 0$), Case 2 Reacting Droplet Sauter Mean Diameter Contours	97
Figure 4.52: Z-X plane ($Y/R_0 = 0$), Case 2 Reacting Droplet Number Density Contours	97

Figure 4.53: Z-Y plane ($Y/R_o = 0$) Case 1 Exhaust Gas Temperature and Oxygen Content	101
Figure 4.54: Z-Y plane ($Y/R_o = 0$) Case 1 Exhaust Gas Corrected Emission Concentrations	101
Figure 4.55: Z-Y plane ($Y/R_o = 0$) Case 2 Exhaust Gas Temperature and Oxygen Content	104
Figure 4.56: Z-Y plane ($Y/R_o = 0$) Case 2 Exhaust Gas Corrected Emission Concentrations	104
Figure A.1: Z-Y plane ($Y/R_o = 0$), Case 1 Reacting and Non-Reacting Axial Mean Velocity	110
Figure A.2: Z-Y plane ($Y/R_o = 0$), Case 1 Reacting and Non-Reacting Vertical Mean Velocity	111
Figure A.3: Z-Y plane ($Y/R_o = 0$), Case 1 Reacting and Non-Reacting Turbulent Kinetic Energy	112
Figure A.4: Z-Y plane ($Y/R_o = 0$), Case 1 Reacting and Non-Reacting Reynolds Shear Stress	113
Figure A.5: Z-Y plane ($Z/R_o = 0$), Case 1 Reacting and Non-Reacting Axial Mean Velocity	114
Figure A.6: Z-Y plane ($Z/R_o = 0$), Case 1 Reacting and Non-Reacting Vertical Mean Velocity	114
Figure A.7: Z-Y plane ($Z/R_o = 0$), Case 1 Reacting and Non-Reacting Turbulent Kinetic Energy	115
Figure A.8: Z-Y plane ($Z/R_o = 0$), Case 1 Reacting and Non-Reacting Reynolds Shear Stress	115
Figure A.9: Z-Y plane ($Z/R_o = 0$), Case 1 Reacting and Non-Reacting Axial Mean Velocity Vertical Gradient	116
Figure A.10: Z-Y plane ($Y/R_o = 0$), Case 2 Reacting and Non-Reacting Axial Mean Velocity	117
Figure A.11: Z-Y plane ($Z/R_o = 0$), Case 2 Reacting and Non-Reacting Vertical Mean Velocity	118
Figure A.12: Z-Y plane ($Z/R_o = 0$), Case 2 Reacting and Non-Reacting Turbulent Kinetic Energy	119

Figure A.13: Z-Y plane ($Y/R_o = 0$), Case 2 Reacting and Non-Reacting Reynolds Shear Stress	120
Figure A.14: Z-Y plane at $X/R_o = 1.60$ ($Y/R_o = 0$), Case 1 Non-Reacting Droplet and Gas Phase Axial, Vertical Mean Velocity, Turbulent Kinetic Energy	121
Figure A.15: Z-Y plane ($Y/R_o = 0$), Case 1 Reacting Droplet and Gas Phase Axial Mean Velocity	122
Figure A.16: Z-Y plane ($Z/R_o = 0$), Case 1 Reacting Droplet and Gas Phase Vertical Mean Velocity	123
Figure A.17: Z-Y plane ($Z/R_o = 0$), Case 1 Reacting Droplet and Gas Phase Turbulent Kinetic Energy	124
Figure A.18: Z-Y plane ($Y/R_o = 0$), Case 2 Reacting Droplet and Gas Phase Axial Mean Velocity	125
Figure A.19: Z-Y plane ($Y/R_o = 0$), Case 2 Reacting Droplet and Gas Phase Vertical Mean Velocity	126
Figure A.20: Z-Y plane ($Y/R_o = 0$), Case 2 Reacting Droplet and Gas Phase Turbulent Kinetic Energy	127
Figure B.1: Z-X plane ($Y/R_o = 0$), Case 1 Axial Mean Velocity Comparison	129
Figure B.2: Z-X plane ($Y/R_o = 0$), Case 1 Vertical Mean Velocity Comparison	130
Figure B.3: Z-X plane ($Y/R_o = 0$), Case 1 Turbulent Kinetic Energy Comparison	131
Figure B.4: Z-X plane ($Y/R_o = 0$), Case 1 Reynolds Shear Stress Comparison	132
Figure B.5: X-Y plane ($Z/R_o = 0$), Case 1 Axial Mean Velocity Comparison	133
Figure B.6: X-Y plane ($Z/R_o = 0$), Case 1 Vertical Mean Velocity Comparison	134
Figure B.7: X-Y plane ($Z/R_o = 0$), Case 1 Turbulent Kinetic Energy Comparison	135
Figure B.8: X-Y plane ($Z/R_o = 0$), Case 1 Reynolds Shear Stress Comparison	136
Figure B.9: Z-X plane ($Y/R_o = 0$), Case 2 Axial Mean Velocity Comparison	137
Figure B.10: Z-X plane ($Y/R_o = 0$), Case 2 Vertical Mean Velocity Comparison	138
Figure B.11: Z-X plane ($Y/R_o = 0$), Case 2 Turbulent Kinetic Energy Comparison	139
Figure B.12: Z-X plane ($Y/R_o = 0$), Case 2 Reynolds Shear Stress Comparison	140

NOMENCLATURE

Roman Symbols

b	Beam Separation
D	Measured Droplet Diameter
D_{10}	Arithmetic Mean Diameter
D_{32}	Sauter Mean Diameter
D_o	Rated Fuel Nozzle Sauter Mean Diameter
FN	Flow Number
f	Transmitting Optics Focal Length
HHV	Net Heat of Combustion
k	2-D Turbulent Kinetic Energy
L_T	Thermal Load
l_m	Mixing Length
\dot{m}	Total Mass Flow Rate
N	Total Number of Samples per Data Point
n_{drop}	Refractive Index of any Scattering Droplet
n_{fuel}	Refractive Index of Liquid Jet-A
n_{gas}	Refractive Index of Ambient Gas Phase
P	Pressure
Q	Volumetric Flow Rate
R_o	Effective Fuel Nozzle Radius
Re_o	Inflow Reynolds Number
S	Swirl Number
T	Temperature

t	Time
t_{coinc}	Coincidence Window Time Interval
U	Axial Mean Velocity
U_0	Bulk Velocity
u	Axial Root-Mean-Square Velocity
u'	Axial Fluctuating Velocity
u^*	Velocity Scale Based on Turbulent Kinetic Energy
uv	Time Averaged 2-D Reynolds Shear Stress
$u'v'$	Instantaneous 2-D Reynolds Shear Stress
V	Vertical Mean Velocity
v	Vertical Root-Mean-Square Velocity
v'	Vertical Fluctuating Velocity
X	Combustion Chamber Downstream Coordinate
Y	Combustion Chamber Vertical Coordinate
Z	Combustion Chamber Horizontal Coordinate

Greek Symbols

α_0	Fuel Nozzle Rated Spray Angle
Δ	Change in
ε	Dissipation of Turbulent Kinetic Energy
ν_T	Turbulent Viscosity
ν_0	Kinematic Viscosity
Φ	Overall Equivalence Ratio

Abbreviations

CFD	Computational Fluid Dynamics
-----	------------------------------

cc	Cubic Centimeter
LBO	Lean Blow Out
LDV	Laser Doppler Velocimetry
PDA	Phase Doppler Anemometry
PDPA	Phase Doppler Particle Analyzer
PMT	Photo-Multiplier Tube
ppm	Parts per Million
RMS	Root-Mean-Square
SMD	Sauter Mean Diameter
TKE	Turbulent Kinetic Energy

Subscripts

AIR	Air Property Upstream of the Swirler
eq	Combustion Product Property at Chemical Equilibrium
FUEL	Fuel Property Upstream of the Nozzle
INJ	Fuel Property at the Nozzle Tip
LBO	Lean Blow Out
SW	Swirler

Other

$\langle \rangle$	Time Averaging
d/dx	Spatial Derivative in the X-Coordinate Direction
$\partial/\partial x$	Partial Derivative in the X-Coordinate Direction
d/dy	Spatial Derivative in the Y-Coordinate Direction
$\partial/\partial y$	Partial Derivative in the Y-Coordinate Direction
[]	Gas Concentration

SUMMARY

To adhere to the current requirements for NO_x and CO emissions in combustion systems, modern land and air based gas turbine engines often operate in the fuel lean regime. While operating near the lean blow out (LBO) limit does reduce some harmful emissions, combustor stability is sacrificed and extinction becomes a major concern. To fully understand the characteristics of lean operation, an experimental study was conducted to map the time averaged flow field in a typical aeroengine, counter-swirling, liquid fuel combustor. This study examined two steady-state operating conditions, both near the lean extinction limit for this burner. Using an LDV/PDPA system, 2-D mean and fluctuating velocities, as well as Reynolds stresses, were measured throughout the combustor. These measurements were taken for both non-reacting and reacting flow fields, enabling a direct analysis of the result of heat addition and increased load on a turbulent swirling flow field. To further understand the overall flow field, liquid droplet diameter measurements were taken to determine the fuel spray characteristics as a function of operating pressure and rated spray angle. Chemical composition at the combustor exit was also measured, with an emphasis on the concentrations of both CO and NO_x emissions. This large database of aerodynamic and droplet measurements will lead to an improved understanding of swirling, reacting flow fields and aid in the accurate prediction of lean blow-out events. With this understanding of the lean blow-out limit, increased fuel efficiency and decreased pollutant emissions can be achieved in aeroengine and gas turbine combustors.

CHAPTER 1

INTRODUCTION

Overview

This thesis presents an experimental description of the confined flow field downstream of a counter-swirl stabilized gas turbine engine burner. The main goals of this research were to improve understanding of lean combustion, with specific application to emission reductions in current thrust and power generation systems, and develop a large, benchmark set of aerodynamic and droplet data for numerical model validation. The non-reacting, or isothermal, gas phase flow and the reacting gas phase flow were characterized at two loading conditions, each determined by the pressure drop across the swirler hardware. The non-reacting results are presented first to establish the dynamics of the air flow without liquid fuel or combustion and to examine the influence of inlet air mass flow rate changes on the flow structure. Next, measurements of the reacting gas phase using two simplex atomizing nozzles, $\Phi \leq 0.5$ at both loading conditions, are presented to highlight the influence of lean combustion on the flow.

Following the description of the gas phase measurements, the droplet characteristics for both nozzles are examined. A number of factors, including atomization quality, spray angle, etc. are shown to influence the combustor performance and overall emission levels. The understanding of this behavior is significant for the future use of efficient lean operation, as flame stability is sacrificed for reduced combustion temperatures. To complete this research, exhaust gas temperature and emission levels are presented to quantify the combustion process upstream.

Background

Stringent emission level requirements on gas turbine engines generally require improved combustor design and/or a decrease in the specific fuel consumption [1]. In

modern land based turbines, the improvements in lean combustion technology include premixed-prevaporized fuel systems and dry-low NO_x technology to help limit emission levels. These systems operate over a small range of loading conditions for extended run times, generally with large pre-mixers. In aircraft engines, on the other hand, combustor modifications are not practical due to strict weight and size restrictions. In addition, while aeroengines do operate over a wide range of inlet conditions, a significant portion of the NO_x and CO emissions come during altitude cruise [1]. Thus, the effective implementation of stable, lean combustion in existing, swirl-stabilized gas turbine aeroengines, specifically at idle and cruise conditions, could reduce emission levels further without requiring major combustor redesign.

While lean combustion does reduce combustor temperatures and some harmful emissions, global flame extinction becomes a major concern. The result, lean blow out (LBO), is both costly and dangerous for gas turbine operation. For aircraft turbine engines, an extinction event at altitude means a sudden loss of thrust. A loss of thrust at altitude is very dangerous and must be avoided to ensure the safety of those on board. Further, localized extinction events imply the production of large quantities of unburned hydrocarbons, both inefficient and harmful. As such, the effective implementation of stable, lean combustion, necessary for improved combustor lifetime and reduced emission levels, requires the prevention of LBO events throughout operation.

Motivation

To ensure the safety and stability of lean operation in existing gas turbine technology, the dynamics of the two-phase flow, including primary and secondary atomization, evaporation, and mixing must be well understood. The results presented here provide insight into the influence of mass addition and heat release on the recirculating flow field downstream of a counter-swirl stabilized burner. Droplet and gas phase measurements in the lean reacting flow field enable a direct analysis of the liquid

spray's influence on the combustion performance, specifically the flow uniformity and the exhaust emission levels.

Given the large costs associated with testing full scale combustors, the design of valid numerical models is essential for the future of combustor design. Further, the accurate prediction of LBO and flame extinction events is essential for dynamic control of lean operation [2]. With these measurements, progress can be made in accurately predicting lean blow-out events numerically. They can also provide a deeper understanding of the flow dynamics associated with lean combustion. Together, these advances will allow future combustors to be designed with low emission characteristics and large stability limits, ideal for both land and air based turbine engines.

Review

This section presents a review of the experimental and numerical research conducted in the field of swirl-stabilized spray combustion. While this research has been extensive for the last three decades in industrial, government, and university laboratories, the rise in laser based diagnostics is of significant importance. These non-intrusive methods allow the measurement of flow velocities and droplet distributions in various combustor geometries, including the research presented here.

Early work in the field of swirl-stabilized spray combustion is thoroughly surveyed in the text Combustor Aerodynamics [3]. In this book, it is shown that at large enough degrees of swirl, “an adverse pressure gradient [results] so that ... the flow reverses direction and a central torroidal vortex is set up.” This firm establishment of a recirculation zone in swirling flows confirmed the value of swirl-type flame stabilization. The degree of swirl is characterized by the swirl number, S , the ratio of the axial flux of angular momentum to the axial flux of linear momentum, or thrust. Above a critical swirl number, $S \sim 0.6$, it was shown that the recirculation zone develops, and grows in length with increasing swirl [3]. Extensive experimental data highlight the key flow

features of co-axial swirl, or co-swirl, flows, including turbulence quantities and flame characteristics. Further work by Syred, Beer, and Gupta, confirmed that the position of the vortex core varied around the downstream centerline, or axis of symmetry [4,5]. The characteristics of this Precessing Vortex Core (PVC) were examined for various swirl and fuel injection conditions, and it was shown that the PVC was only maintained in premixed flames, with larger oscillation intensities and increased precessing frequencies compared to those of non-reacting PVCs.

Following this work, measurement techniques based on laser interference fringes began to dominate spray combustion research. Laser anemometer measurements by Chigier and Dvorak, [6] and dual beam velocimetry measurements by Owen, [7] are two of the earliest uses of such techniques. Both experiments confirmed the existence of a recirculation zone, or vortex break down bubble, in swirl flows, as well as the downstream decay of both turbulent kinetic energy and stress. Owen further confirmed the large scale motion of the vortex core. However, he obtained results for the co-swirl, non-reacting case only. Later, Owen et al. [8] evaluated the effects of inlet swirl on the structure of low swirl number, co-swirl stabilized diffusion flames, with emphasis on both time-mean and fluctuating behavior. In their work, the fuel spray was portrayed as a conical core of large droplets whose velocities are governed by nozzle characteristics. These large droplets are surrounded by clouds of small droplets that respond quickly to changes in relative air velocity. For swirl numbers below the critical value, $S \sim 0.6$, increasing swirl increased both flame length and total unburned hydrocarbons (UHC) along the combustor centerline. This was mainly due to the inability of the fuel droplets to penetrate into the co-axial swirling air stream. Gupta et al. [9] examined stability limits and emissions characteristics for high swirl flows with a multi-annular swirl burner. They concluded, "...high volumetric heat release rates can be achieved by matching the concentrations and directions of flow of reactants in such a way that regions

of high fuel concentration overlap regions of large shear stresses in the flow.” Further, the authors showed the absence of unsteady PVCs in their experimental system [9].

The characterization of droplet behavior and swirl dynamics improved significantly with the advent of phase doppler anemometry (PDA) measurements in swirl-stabilized spray flames. An early application by McDonell and Samuelsen [10] determined that the presence of the liquid phase reduced velocity fluctuations in a two-phase system, similar to results shown here. These results were also verified in extensive studies of swirl-stabilized flame structure and velocity/drop size measurements by Edwards et al. [11] and Bulzan [12], respectively. Combining results from schlieren/luminosity imaging, LDV, and PDA, Edwards found six regions of importance in a dual, co-rotating swirl, or co-swirl, stabilized flame: “the dense spray region; the rich, two-phased, fuel jet; the main air jet; the internal product recirculation zone; the external product recirculation zone; and the gaseous diffusion flame zone.” Edwards also observed that the droplet velocities exceeded those of the reacting gas phase, with droplets showing no recirculation in the near-injector region. Bulzan, however, concluded that all droplet velocities were less than that of the gas phase, with only 15 μm and smaller droplets showing any recirculation. Bulzan also asserted that the smallest droplets were affected most dramatically by the turbulent gas phase, seen in the increase in fluctuating droplet velocity components with decreasing droplet diameter. While these small droplets also show the largest number flux, the distribution of large droplets, containing most of the liquid mass, was shown to be of major importance in the combustion dynamics [12].

More recent work in the field of spray combustion has focused on the effects of droplet size distribution on, and the local droplet interactions in, the reacting flow field. In a study by Bossard and Peck [13], a co-annular spray combustor was designed to provide variable droplet size distributions based on the volume of liquid in a given size class, while maintaining a constant Sauter mean diameter (SMD):

$$D_{32} = \left(\frac{\sum D^3}{\sum D^2} \right) \quad (1.1)$$

To quantify these distributions, the relative span factor (span), a ratio of the volume in large or small droplets to the mean droplet volume, was calculated; an increase in the span corresponds to a broadening of the droplet distribution, and vice versa. From experimental measurements, a decrease in the span, or a narrowing of the droplet distribution, led to more complete combustion. As the span decreases, the droplet diameters become more uniform, providing more uniform evaporation and mixing. Conversely, an increase in the span led to a decrease in flame length and intensity [13]. The increased population of larger and smaller droplets associated with an increasing span also accounts for the droplet-size-segregating effects seen in the periphery of the flow field, which lead to the selective transport of smaller droplets radially outward. This selective transport changes mixing rates in the spray periphery, or flame, significantly, leading to reduced combustion efficiency and heat release.

An extensive theoretical review of trends and challenges in droplet dynamics and spray combustion by Chiu [14] dealt directly with the complex droplet interactions responsible for the presence of large scale liquid structures. He further introduced “hierarchal group combustion,” the ordered evolution of group combustion modes, “as the result of the spatial and temporal variations in the effective droplet separation, drop size, group combustion number, cluster structures and the state of the gaseous environment.” He noted the following areas of importance: the isolated droplet, the interacting droplet, a spray group combustion mode, large scale structure (LSS) formation, and collective spray phenomena, especially in highly turbulent sprays. The transition beyond a “critical group combustion number” was confirmed, at which point a sheath type, or external, combustion mode is established in the near-injector region, while isolated droplet/gas phase, or internal group, combustion dominates downstream. The review further concluded that “all practical spray flames exhibit LSS featured by non-

homogeneous clustering of droplets forming the regions of excess droplet population...,” which have a direct effect on the interphase exchange rates of all flow properties. The tendency of fuel ligaments in the near-injector region to accelerate the formation of LSS was established, as was the decay of these LSS downstream, mainly determined by the gas expansion rate and droplet inertia.

Most recently, an experimental study on the effect of co- vs. counter-swirl on the non-reacting flow field was conducted by Merkle et al. [15]. The clear decay of a central recirculation region, the localization of velocity fluctuations near the fuel nozzle, and the similar localization and decay of TKE and Reynolds shear stress all agree well with the non-reacting flow field presented below. From these results, Merkle concluded that there was, “considerable attenuation of the turbulent exchange of momentum perpendicular to the main flow direction for counter-rotating airflows.” This review did not, however, address the issues of droplet addition or combustion effects, both of which will be shown to influence the turbulent momentum exchange significantly.

While a thorough review of the progress in the computational modeling of spray combustion is beyond the scope of this thesis, it is worth noting particular work directly related to the geometry and results presented here. Numerical simulations run using a standard $k - \epsilon$ model by Datta [16] focused specifically on the effect of inlet swirl variations in swirl-stabilized spray combustion. This model showed an increase in the magnitude of the reverse flow velocity, i.e. recirculation strength, with counter-rotating swirls, as well as a dramatic increase in radial variation of tangential velocity. Large increases in turbulent kinetic energy were also shown for counter-rotation, with peaks in the regions of intense velocity gradients associated with the shear layer formed at the recirculation boundary. Highly relevant work by Hsiao and Mongia [17, 18, 19, 20] uses a similar $k - \epsilon$ model to predict the flow field in a burner identical to that used in this thesis, including the details of the swirl cup; both primary and secondary swirl as well as injection. However, these numerical studies were limited to non-reacting flows. LDV

measurements were also made in a similar geometry to the model for comparison. While the downstream geometry varies slightly from that in this proposal, the results of Hsiao and Mongia show very good agreement for the cold flow results presented below. The clear presence of the large recirculation region at similar axial locations and increased turbulent kinetic energy in the near-injector region match well with results shown here. Equally relevant research by Menon et al. [21, 22] has focused on the use of Large-Eddy Simulation (LES) methods for numerically simulating combustion, both premixed and non-premixed. Specific emphasis on the prediction of emissions near lean blow out (LBO) in industrial type swirl burners clearly shows a dramatic NO_x reduction and CO increase near $\Phi \sim 0.4$. Additional LES simulations of a geometrically identical combustor have yielded good agreement for the non-reacting flow field.

In summary, the field of spray combustion has seen dramatic improvements in understanding and technology, clarifying the complex droplet/gas phase interactions. Further understanding of the dynamics of swirl stabilization has solidified the use of swirl burners in aircraft and power gas turbine engines. It should be noted, however, that a significant portion of the research to date is for co-swirl and co-annular flow fields. More research should be dedicated to counter-swirl stabilization, especially in annular combustors, as suggested by Lefebvre [1]. Furthermore, little work has been conducted for swirl combustors near the LBO limit, with most coming from computational modeling. The need for reduced emission combustors in the future should warrant the push for research in the field of lean, low NO_x , spray combustion. With lean operation, a firm understanding of the flow dynamics is integral in providing increased combustion stability. This increased stability is necessary for the prevention of LBO, a critical requirement for gas turbine engines.

CHAPTER 2

OBJECTIVES

- Characterize the non-reacting gas phase flow field downstream of a single swirl stabilized burner, including the effects of increased inlet mass flow rates on vortex dynamics and mixing.
- Improve upon the current understanding of the effects of combustion, namely heat release, on the aerodynamics of an industrial type counter-swirler, with direct application to improved annular combustor performance.
- Identify important interactions between the liquid fuel droplets and gas phase in the near-injector region, focusing specifically on the effects of fuel pressure on the spray performance.
- Examine the changes in flow structure, droplet characteristics, and emissions near the lean blow out limit, with particular attention to the reduction of both CO and NO_x concentrations over a range of loading conditions.
- Describe key turbulent properties in the near-injector region, including effects of the liquid phase and heat release on the 2-D turbulent kinetic energy and Reynolds shear stress.
- Develop an extensive database for the validation of Large Eddy Simulation models of counter-swirling flow fields, with and without spray combustion.
- Contribute to the improved stability and implementation of lean operation at idle and cruise conditions for future aircraft engines.

CHAPTER 3

EXPERIMENTATION

All experimental measurements presented below were conducted at the Georgia Institute of Technology Aerospace Combustion Laboratory, on a single industrial type counter-rotating swirl burner mounted in a test combustion chamber. Preheated air enters the confined chamber through the swirler around a central fuel nozzle and fused silica walls allow optical access downstream of the swirl stabilizer. The trapezoidal cross-section of this combustor attempts to geometrically model part of the annular cross-section of most gas turbine engine combustors, especially those used to generate thrust for aircraft. The combustor is shown operating in Figure 3.1 below. The exhaust constriction has been removed to aid in visualization of the combustion chamber cross-section. A vertical cross-section of the combustor is shown schematically in Figure 3.2, and a detail view of the swirler geometry is included in Figure 3.3. The combustion chamber cross-section (Z - Y plane) is given in Figure 3.4, with normalized dimensions. Major experimental components and measurement capabilities will be discussed below.

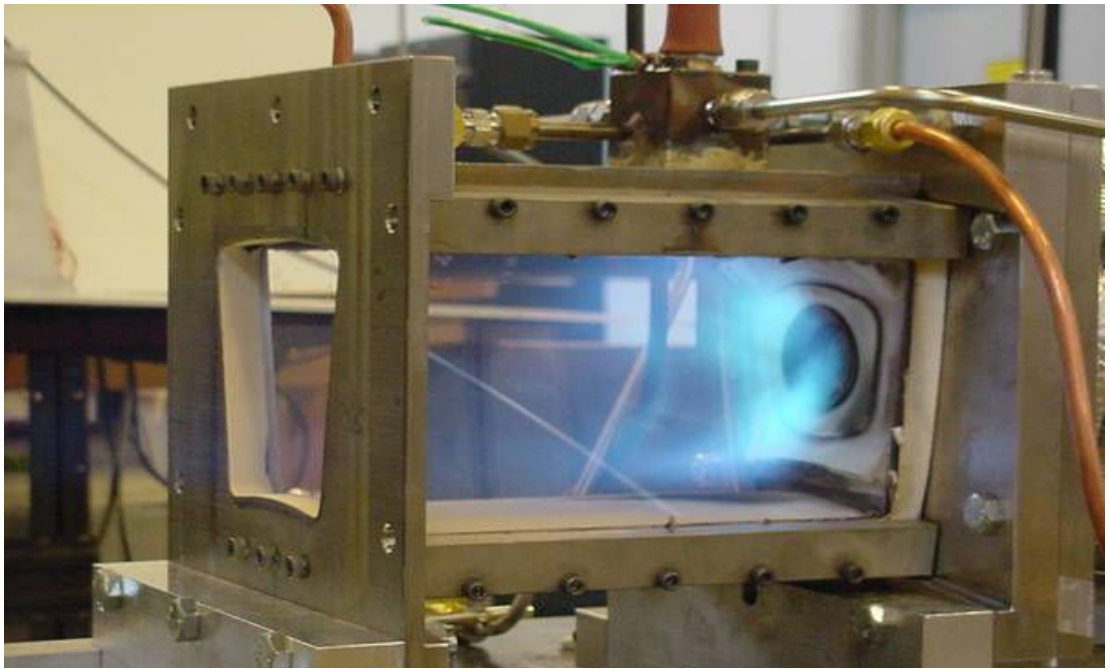


Figure 3.1 Operation of the Counter-Swirl Stabilized Liquid Combustor

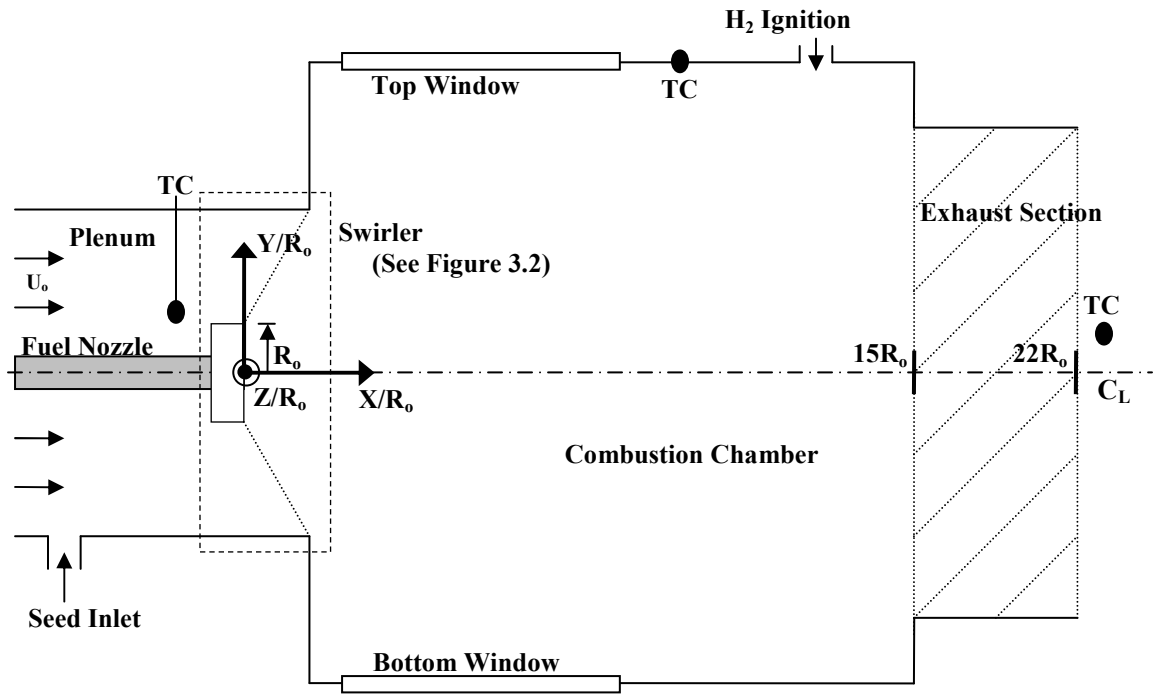


Figure 3.2 Experimental Geometry Downstream, Vertical Cross-Section

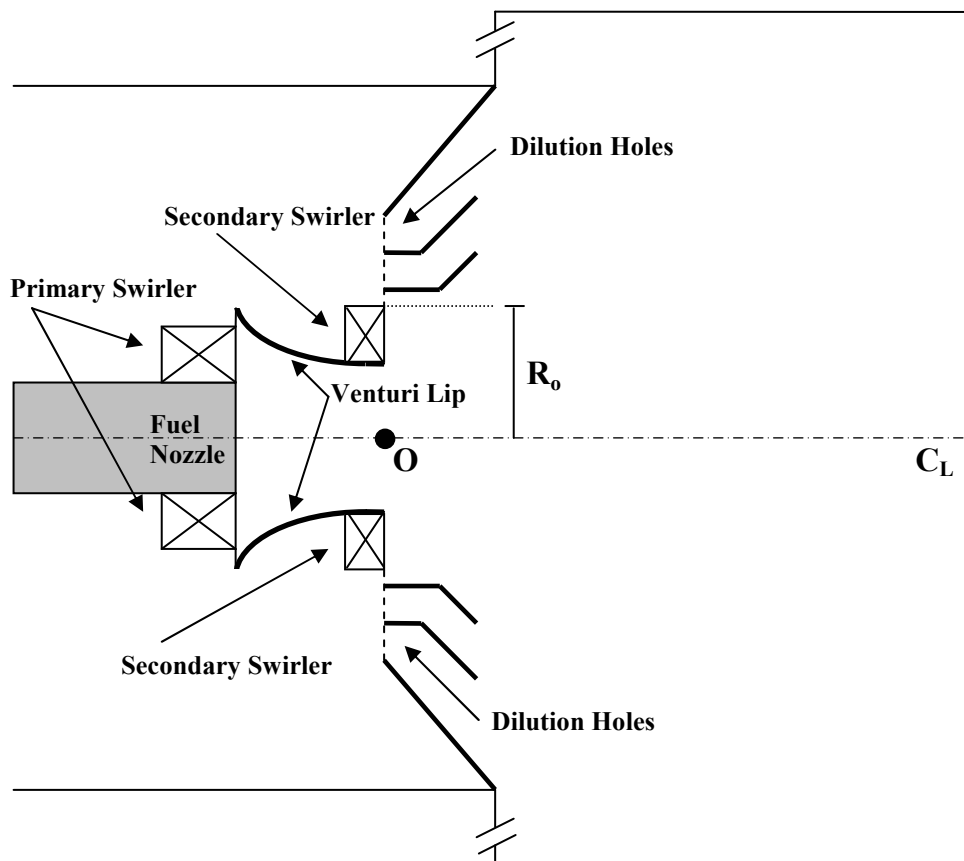


Figure 3.3 Experimental Counter-Swirl Burner, Vertical Cross-Section

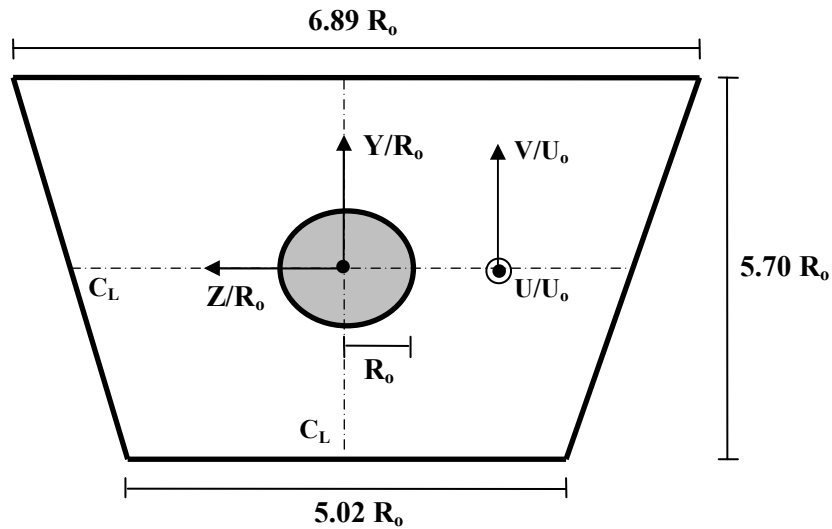


Figure 3.4 Combustion Chamber Cross-Section

Hardware

Air Supply

Compressed air is supplied from the laboratory at a nominal operating line pressure of 125 psia (0.862 MPa) at 298 K. The mass flow rate of air through the combustor is controlled by a valve far upstream of the combustion chamber, and the operating conditions are determined by the desired pressure drop across the swirl burner. For all results shown, the pressure drop across the swirler was fixed, in good agreement with typical values found in industrial applications [1]. The total mass flow of air is calculated by a calibrated rotameter fitted with a pressure gage, then preheated using a Watlow electric heater. The preheated flow is then allowed to straighten in an insulated settling chamber, or plenum, shown in Figure 3.2. Seed particles can be introduced just upstream of this section, ensuring a uniform seed distribution throughout the inlet air stream. Following the plenum, the combustor inlet temperature, T_{AIR} , is measured just before the preheated air enters the swirler, seen in Figure 3.2 and discussed below.

Fuel Supply

For all experimental results shown, pressurized liquid fuel, Jet-A, whose average properties are given by [23], was used. Regulated gaseous nitrogen was used to pressurize the liquid fuel upstream of a viscosity calibrated turbine flowmeter. The use of this digital flowmeter allowed precise measurement and control of the fuel mass flow rate, and a subsequent calculation of the thermal load, L_T , where

$$L_T = \dot{m}_{FUEL} \cdot HHV \quad (3.1)$$

It was found that particulate matter inherent to the Jet-A necessitated two levels of filtering, a large canister fuel filter followed by a fine mesh filter just upstream of the precision flowmeter. Using this two filter system minimized pressure loss associated with the clogging of the nozzle over long operating periods. Further, the precise control of the liquid fuel mass flow rate allowed for careful study of the LBO limit of this combustor, as fluctuations in fuel mass fraction influence the localized extinction events associated with LBO.

Swirler

The counter-rotating flow field is generated using a GE CFM56-5B commercial aircraft combustor burner. Swirl is introduced by two sources, a primary, axial swirler with elliptical jets, and a secondary, radial, curved vane swirler; the primary swirl is oriented anti-clockwise, while the secondary swirl is clockwise when viewed from downstream. While the pre-manufactured burner geometry is quite complex, the precise details and dimensions of this swirler are proprietary. Figure 3.3 shows a schematic drawing of the swirler geometry for reference. While a calculation of the swirl number is not presented, it is safe to assume that this swirl burner produces a high swirl number, S , flow. Specifically, the results below suggest that $S > 0.6$, and that the axial flux of angular momentum is a significant fraction of, if not larger than, the axial thrust [3].

Measurements of the primary and secondary swirler inner diameters, not presented for proprietary reasons, suggest that the primary swirler is not exactly concentric with the secondary swirler. Further, the asymmetry is such that the primary swirler is shifted towards $Z/R_o < 0$ relative to the primary-secondary swirl interface. Thus, the primary swirl is able to impede the outer, secondary air stream for $Z/R_o < 0$. Previous research clearly identified a strong dependence on machining tolerances and symmetric assembly in optimization studies of co- and counter-rotating radial inflow swirler assemblies with and without the venturi lip geometry [24]. Results presented here confirm the importance of the primary and secondary swirler dome assembly in generating a symmetric flow field downstream of the fuel injector.

Fuel Nozzle

Two industrial-type Goodrich peanut fuel nozzles with rated 90° and 70° spray angles and $40 \mu\text{m}$ SMD at 100 psig (0.69 MPa) were used to spray liquid fuel into the combustion chamber. Both nozzles produce a hollow cone spray with similar flow number, $FN = 1.1$, where the flow number is given as [1]:

$$FN = \frac{\dot{m}_{FUEL} \text{ (lb / hr)}}{\sqrt{\Delta P_{INJ}} \text{ (psi)}} \quad (3.2)$$

Based on the swirler geometry depicted in Figure 3.3, the fuel nozzle is placed well inside of the burner, coincident with the primary swirl. With this placement, the fuel droplets discharge into the anti-clockwise swirling flow, and impinge upon the venturi lip wall. The fuel is then re-atomized when leaving the venturi lip, at the interface between the two counter-rotating swirls, with a very similar characteristic SMD as the fuel nozzle.

Ignition

An automotive spark plug is used as the primary igniter. Gaseous hydrogen supplied through the top plate of the combustion chamber, shown in Figure 3.2, is ignited

downstream of the swirler by the spark. The spark plug and H₂ supply lines are flush with the combustor ceiling, so that no flow disturbances are introduced once the liquid fueled combustor is operating at a stable power setting.

Combustion Chamber

The cross-sectional geometry of the combustion chamber is shown schematically in Figure 3.4, with normalized dimensions given. The trapezoidal cross-section is used to mimic the normal application of this swirl burner in annular combustors. While the normal operation would also include burner-burner interactions, this study is limited to single burner dynamics. The walls of the combustion chamber are made of fused silica to allow full optical access of the entire combustion flow field. Both the top and bottom of the combustion chamber are fitted with smaller optical ports, as well as thermocouple and pressure measurement fittings.

Exhaust

The combustion chamber is fitted with a slight constriction, seen in Figure 3.2, which provides some direction and uniformity to the exhaust products. These products are entrainment cooled for a short distance before being drawn out by the laboratory exhaust system. The placement of the exhaust suction well downstream ensures that it does not affect the combustion exhaust flow field. Optical access is restricted by the constriction, but validation measurements are made just outside of this exhaust section.

Measurement Capabilities

For all current work, the following properties were measured: temperatures, pressures, exhaust gas composition (%O₂, [CO], [NO_x]), aerodynamic variables (U , V , u' , v' , $u'v'$), and droplet diameters. The specific measurement capabilities of the experimental set-up are addressed below, including a short note on droplet sizing and its challenges.

Temperature and Pressure Measurements

Temperature measurements were made with K-type Omega thermocouples in the inlet flow just before the swirler, on both top and bottom outer combustor walls, and outside of the exhaust region. These locations allow the characterization of the inlet air flow temperature, steady state operating wall temperature, and combustion product temperature. Analog pressure gages throughout the experimental system monitor the operating conditions and aid in trouble shooting. All temperature data acquisition was managed with a National Instruments DAQ board with LabView or MATLAB as the operating software.

Flow Field Measurements

All flow velocity and droplet measurements were made with a 2-D TSI Phase Doppler Particle Analyzer (PDPA)/Laser Doppler Velocimeter (LDV) system. An argon-ion laser was used, 4W output, with the 514.5 nm and 488 nm lines chosen for the axial and vertical measurements, respectively. The flow was seeded with aluminum oxide particles, of median nominal particle size = $5 \pm 0.9 \mu\text{m}$ [25], for all gas-phase measurements. A maximum of ten thousand (minimum two thousand) samples were collected at each spatial location throughout the combustor, with data rates determined by the local density of seed particles or droplets. Results are neglected in regions where the data rate declined below ~ 20 Hz for the non-reacting flow, and below ~ 50 Hz for the reacting flow.

LDV Measurements

The 2-D TSI LDV system, operated in coincident, back scatter mode, enabled the simultaneous measurement of both axial and vertical velocities, as well as 2-D fluctuating velocity correlations, u'^2 , v'^2 , and $u'v'$. The transmitting optics have a focal length, $f = 353$ mm, and beam separation, $b = 48$ mm for both channels. For the 514 nm and 488 nm beams, the fringe spacing is thus $3.79 \mu\text{m}$ and $3.60 \mu\text{m}$, respectively. Since the seed

particle diameter is of the order of the fringe spacing, it is unlikely that a particle will cross two-fringes at once. As such, the imposed single burst per measurement criteria is met. A standard Bragg cell provides frequency modulation at 40 MHz to a single beam on each channel, producing the relative fringe velocity necessary for the accurate measurement of both flow reversal and zero flow conditions [26]. Real time histograms are monitored using the Flowsizer software provided, and the quality of the LDV measurements is controlled by a number of parameters, most importantly the downmix frequency and band pass filter width [26]. Specifically, the downmixing process enhances LDV quality by optimizing the frequency shift applied to the source signal. Further discussion of LDV as an experimental tool is not included, as a firm knowledge of such is assumed. Alternatively, details can be found in [26].

PDPA Measurements

The detailed analysis of droplet behavior in the near injector region was performed using the 2-D TSI PDPA system at an off-axis receiving angle of 30°. While this measurement technique is a natural extension of the LDV system mentioned previously, a more thorough discussion is provided of droplet diameter measurements and the PDPA system.

While droplet velocity measurements depend strictly on the frequency of the intensity variation of scattered light due to droplet–fringe interactions, accurate droplet diameter measurements depend on the spatial frequency of the scattered light [26]. In essence, the scattered fringe spacing, or phase shift, is determined by the size of the scattering droplet, while the frequency of the scattered light is a measure of the droplet velocity. For this reason, at least two photo detectors are needed to measure droplet diameters. The TSI system used here contains three detectors, allowing two independent measurements to be made simultaneously [26].

The refractive index, n_{drop} , of the scattering droplet is an important parameter, as the angle of refraction, and thus, the scattered fringe spacing, changes with varying liquid sprays. For all cases shown here, $n_{\text{fuel}} = 1.45$, was used for liquid Jet-A [26]. To account for the known loss of laser power through liquid Jet-A, an attenuation coefficient, $\alpha = 50 \text{ mm}^{-1}$, was used for all data acquisition [26]. Similar to the LDV system described, PDPA measurement control is primarily achieved through downmixing and band pass filtering, both of which are varied throughout the combustor to optimize data collection at a given location. To further improve the reliability of diameter measurements, the TSI system allows for a laser-diode calibration to remove any inherent phase shift in the optical signals. Using a split red laser-diode with a known phase shift, the phase associated with the photo-multiplier tubes (PMT) can be calibrated to eliminate biases found in high frequency (velocity) flows. With the removal of further phase shifts associated with the electronic components, the remaining phase content of a “burst” signal is used to estimate the droplet diameter [26].

A number of relevant droplet diameters are calculated numerically by the TSI Flowsizer software, including the mass and volume mean diameters. This study, however, will focus on the mass, or arithmetic, mean diameter and the Sauter mean diameter (SMD), given as the diameter of a droplet with the same volume to surface area ratio as that of the entire spray and seen in Equation 1.1. Since the SMD is representative of the entire spray at a given location, it can be considered a global mean property, which should correlate with other spray combustors. Further, its wide usage across the fields of spray combustion and droplet theory enables the direct comparison of the experimental results shown here with other work in these fields.

Combustor Traverse

To facilitate local diagnostics, the combustion chamber is mounted to a 3-D traversing table. Motion is controlled in each dimension by an individual DC stepper

motor. The table is fitted with a method for tracking relative distance changes very accurately; millimeter scale rulers are attached in each direction to the stationary legs which track the position of pointers on the moving legs. The fine tip of the pointer allows position to be measured at 0.25 mm increments, significantly reducing errors due to uncertainties in spatial location.

Exhaust Gas Composition Measurements

All gas composition measurements were made with a HORIBA PG-250 Gas Analyzer downstream of the exhaust section, $X/R_o \sim 22$. Measurements focused on the NO_x ($\text{NO} + \text{NO}_2$) and CO concentrations across the horizontal centerline, as well as the oxygen content. The exhaust gas was sampled at ~ 0.4 mL/min through a ceramic tube inserted outside of the combustor exit, then cooled to below 40°C before entering the gas analyzer. The percent O_2 was determined using a galvanic cell to generate an electromotive force proportional to the gas concentration [27]. NO_x measurements were made using the chemiluminescence method and a photodiode, while CO concentrations were determined from an infrared analyzer [27]. Both the NO_x and CO measurements were then corrected to 15% O_2 to enable comparison.

Error Estimation

In the results presented below, errors can be separated in to two main types, those associated with the operating condition measurements and those associated with the flow field measurements, particularly the LDV/PDPA system and the portable gas analyzer. As such, a discussion of experimental condition and flow field measurement uncertainty follows, with emphasis on the errors associated with laser diagnostics.

Uncertainty in Experimental Conditions

Uncertainties in the inflow conditions are caused primarily by the random errors associated with measurements from both analog and digital device and systematic errors

associated with biases in these measurements. Table 3.1 below shows the properties measured, the measurement devices, and their associated random errors, or precision. From a basic analysis of the propagation of uncertainty, the precision uncertainty in the calculated equivalence ratio can be approximated as less than 2.5% [28].

The remaining sources of random error in the experimental set-up are the uncertainty associated with the LDV/PDPA measurement volume and gas analyzer probe position in space. To minimize the uncertainty in the measurement volume location, each direction of the combustor traverse is fitted with a millimeter scale. With these rulers, each independent direction measurement has an uncertainty of ± 0.2 mm. The fuel nozzle center is found from a reference location on the combustor geometry, with uncertainty of ± 0.2 mm.

Table 3.1 Uncertainty in Operating Condition Measurements

Measurement	Device	Precision
\dot{m}_{FUEL}	Digital Flowmeter	± 0.005 g/s
P_{AIR}	Analog Pressure Gauge	± 0.25 psi (1.7 kPa)
T_{AIR}	K-type Thermocouple	± 1 °C (1 K)
Q_{AIR}	Float type Rotameter	± 0.5 SCFM (0.014 m ³ /min)

Random error associated with the HORIBA Gas Analyzer is large due to the uncertainty in measurement probe location. The probe is not fixed to the combustion chamber or traverse, and as such, the uncertainty in each direction is ± 2.0 mm. While this uncertainty is significant, measurements were taken at larger spatial separations to reduce biasing. Additional error in the gas analyzer, especially in the NO_x measurements, can be attributed to the incomplete conversion of NO₂ to NO over short sampling times. To address this, a statistically significant number of gas samples were taken at each spatial location to reduce errors associated with non-equilibrium chemistry in the gas analyzer. The gas analyzer also provides a range of measurement scales to accurately

capture large and small concentrations, improving the overall sensitivity of the measurements. Errors in the temperature measurements are maximized in the combustion products, where heat losses due to radiation from the solid probe result in an under prediction of the gas temperature. Corrections for this effect are not included in this research.

Uncertainty in Flow Measurements

Random error associated with individual aerodynamic flow field measurements is mainly a function of the number and distribution of samples. Given the assumption of a Gaussian distribution of N samples for a random variable, x , Equation 3.3 gives the standard error of the sample mean [28], normalized by the sample standard deviation.

$$\frac{S_{\bar{x}}}{S_x} = \frac{1}{\sqrt{N}} \quad (3.3)$$

The velocity distributions are assumed Gaussian for all gas phase measurements, with $N = 10,000$ samples. Thus, the standard error in the velocity measurements is 1%. It is worth noting that in the shear layer, the sample tends toward a bimodal distribution; the measurement volume detects positive and negative velocities as the recirculation bubble changes position in time. In this region the assumption of a Gaussian distribution is not valid, and the associated error is larger than 1%. Further, in areas of reduced data rate (i.e. the central and corner recirculation regions), the number of samples is less than ten thousand, as a total sampling time cut-off is reached. However, the error associated with $N < 10,000$ is expected to be no larger than 3%.

Systematic errors associated with the acquisition of LDV data include seed biasing, density biasing, and incorrect signal validations. One effect of seed biasing is a general increase in measured velocity, a result of the measurement volume capturing a larger number of rapidly moving particles in a given time in regions of low data rate. Another type of seed bias arises from the inability of the seed particles to accurately

follow the flow. From this bias, measurements tend to incorrectly predict the velocity, as seed particles are not traveling at the gas velocity. Both of these biases are assumed small, as the velocities are relatively low, and the seed particles are mixed well upstream in the plenum, shown in Figure 3.2. However, this assumption may break down in regions with large velocity fluctuations or increased mean velocity gradient magnitude. In these regions, the seed particles are unable to accurately follow the flow and bias the measured values.

For measurements in the reacting flow field, yet another seed bias contributes to systematic errors. In the near injector region, unburned droplets can produce valid velocity measurements. These droplets are unlikely to have the gas phase velocity, introducing a bias in these two-phase regions. The increase in mean velocity with combustion suggests that seeding biases may also become important. Further, the measurement of both liquid and gas phases yield non-Gaussian velocity distributions, significantly increasing the standard error in the mean velocity measurements.

Density biases associated with the combustion process arise from the dependence of n_{gas} , the index of refraction of the gas phase, on the ambient density. As the incident beams cross regions of changing flow density, the measurement volume diameter changes slightly, altering the fringe spacing. Further, the location of the measurement volume changes as the beam angles are deflected with varying n_{gas} . With reactions, the increase in temperature and concentration gradients leads to significant variations in density across the combustor cross section, especially near the fuel nozzle. Thus, the overall error will be the most pronounced in the near injector, reacting gas phase measurements.

For PDPA measurements no seed particles are introduced to the flow. However, the systematic errors associated with droplet diameter and velocity measurements are similar to those for the gas phase. Smaller droplets tend to follow the gas phase velocity, while large droplets tend to follow the spray trajectory. This size segregating effect

introduces bias error to both the diameter and velocity measurements. Density biasing is also important in the droplet diameter measurements. Sizing from the scattered light of a droplet is based on n_{fuel} , the index of refraction of the liquid fuel. With the large increase in gas temperature the liquid density may vary slightly due to flow preheating [23]. Local changes in fuel density imply a non-uniform index of refraction for the scattering droplets, a potential source of error in the diameter measurements. Further, evaporation may alter the local index of refraction around the liquid droplet. While the changes may bias droplet measurements, little information is available on the effects of temperature on the index of refraction of Jet-A, thus these effects will be neglected.

To ensure that a measured signal corresponded to a real seed particle or droplet crossing the measurement volume, the LDV/PDPA system was operated in coincidence mode, with a minimum number of fringe crossings per burst. To improve the overall velocity measurements, the number of fringes crossings for a valid signal was raised from five to eight on both channels in a set coincidence window, $t_{\text{coinc}} = 100 \mu\text{s}$. In this way, biasing due to improper signal validation was minimized. Finally, to reduce error in the droplet diameter measurements due to the electronic components, a two-phase laser diode calibration, as described above, was conducted each time the PMT voltage was adjusted.

CHAPTER 4

RESULTS

The following time-averaged experimental measurements were obtained using the system described above, shown in Figure 3.1 to Figure 3.4. Measurements focus on the horizontal and vertical center planes downstream of the swirler assembly, with a direct comparison of aerodynamic and droplet properties between the non-reacting and reacting flow fields at two loading conditions. Data are presented along the combustor centerline, shown in Figure 3.3, as well as the horizontal ($Y/R_o = 0$) and the vertical ($Z/R_o = 0$) cross-section centerlines, shown in Figure 3.4, at locations downstream of the fuel nozzle ($X/R_o > 1.31$). Additional comparative plots and interpolated contour plots, given in Appendices A and B, provide full 2-D flow field visualizations in both the Z-X and Y-X center planes.

Operating Conditions

Steady state operating conditions for the non-reacting gas phase are given in Table 4.1, with known uncertainties. The Reynolds number, Re_o is calculated based on the bulk velocity in the plenum, U_o , the effective fuel nozzle diameter, $d_o = 27.4$ mm, and the kinematic viscosity of air, $\nu_o = 24.5 \times 10^{-6}$ m²/s ($T_{AIR} = 380$ K, $P_{AIR} = 1$ atm) [29].

Table 4.1 Non-Reacting Gas Phase Steady State Operating Conditions

Case	ΔP_{SW} (%)	P_{AIR} (MPag)	T_{AIR} (K)	\dot{m}_{AIR} (g/s)	U_o (m/s)	Re_o ($\times 10^4$)
1	4.25	0.255	380	30.5	45.9	5.14
		± 0.007	± 1	± 0.1		
2	7.50	0.197	405	38.5	61.0	6.82
		± 0.007	± 2	± 0.5		

Steady state operating conditions for the reacting flow are given in Table 4.2 below, with known uncertainties. Included in Table 4.2 are the calculated overall equivalence ratio and thermal load (HHV = 43.29 MJ/kg [23]) based on the air flow given in Table 4.1, and the experimentally determined blow out limit. Note the reduction in the LBO limit with increasing pressure drop across the swirler.

Table 4.2 Reacting Flow Steady State Operating Conditions

Case	P_{FUEL} (MPag)	\dot{m}_{FUEL} (g/s)	L_T (kW)	α_o (Deg.)	Φ	Φ_{LBO}
1	0.172	0.750	32	90	0.40	0.350
	± 0.007	± 0.005			± 0.01	± 0.005
2	0.552	1.250	54	70	0.50	0.430
	± 0.014	± 0.005			± 0.01	± 0.005

Cases 1 and 2 were chosen to highlight the influence of inlet air mass flow rate and fuel spray performance (i.e. spray angle, droplet size, et al.) on the non-reacting and the lean combusting flow field. The difference in fuel nozzle rated spray angle, seen in Table 4.2, is assumed to impact the liquid and the gas phase results, and is discussed below. It is worth noting, however, that both nozzles are operated below the rated fuel pressure. The spray angle is known to decrease with a reduction in pressure drop across the fuel nozzle [1], and thus, the difference in rated spray angle may be minimized at such low operating fuel pressures.

Non-Reacting Gas Phase

To understand the effects of droplet spray and heat addition in a counter-swirl stabilized spray combustor, the non-reacting flow field must be well characterized. At operational flow conditions, the downstream evolution of the Case 1 axial and vertical mean velocities, without spray or combustion, are presented across the horizontal and

vertical center planes. Case 2 non-reacting results are given at select locations downstream of the fuel nozzle to investigate the influence of pressure drop across the swirler, or inlet mass flow rate, on the non-reacting flow field. 2-D TKE and Reynolds shear stress measurements provide insight into the mixing characteristics of the non-reacting vortex break down bubble.

Combustor Centerline Downstream

The size, length, and intensity of the vortex break down bubble are of importance, as this recirculating region is the primary mechanism for flame stabilization [30]. Non-reacting gas phase velocity measurements are used to study the characteristics of this vortex breakdown. Shown in Figure 4.1 are the non-reacting gas phase axial mean and rms velocities along the combustor centerline for both Case 1 and Case 2 (seen in Table 4.1).

A comparison of the two downstream mean profiles, normalized by their respective bulk velocity, suggests the underlying flow field is essentially unchanged with 75% increase in pressure drop across the swirler. The core strength of the break down bubble does increase in the near nozzle region (solid squares), possibly increasing the mass of downstream gas recirculated for Case 2. The rear stagnation point at $X/R_0 \sim 11$ does not change with the $\sim 30\%$ increase in mass flow, a valuable asset of the swirler design given the size and weight restrictions in aeroengines. Attention should also be paid to the nearly constant rms distribution downstream. The absence of significant velocity fluctuations, $u/U_0 < 0.06$, confirms the stable convection of downstream gases back towards the nozzle, a pre-heating mechanism for improved combustion. To improve understanding of the vortex break down bubble, further measurements are presented in the horizontal and vertical center planes downstream of the swirler geometry.

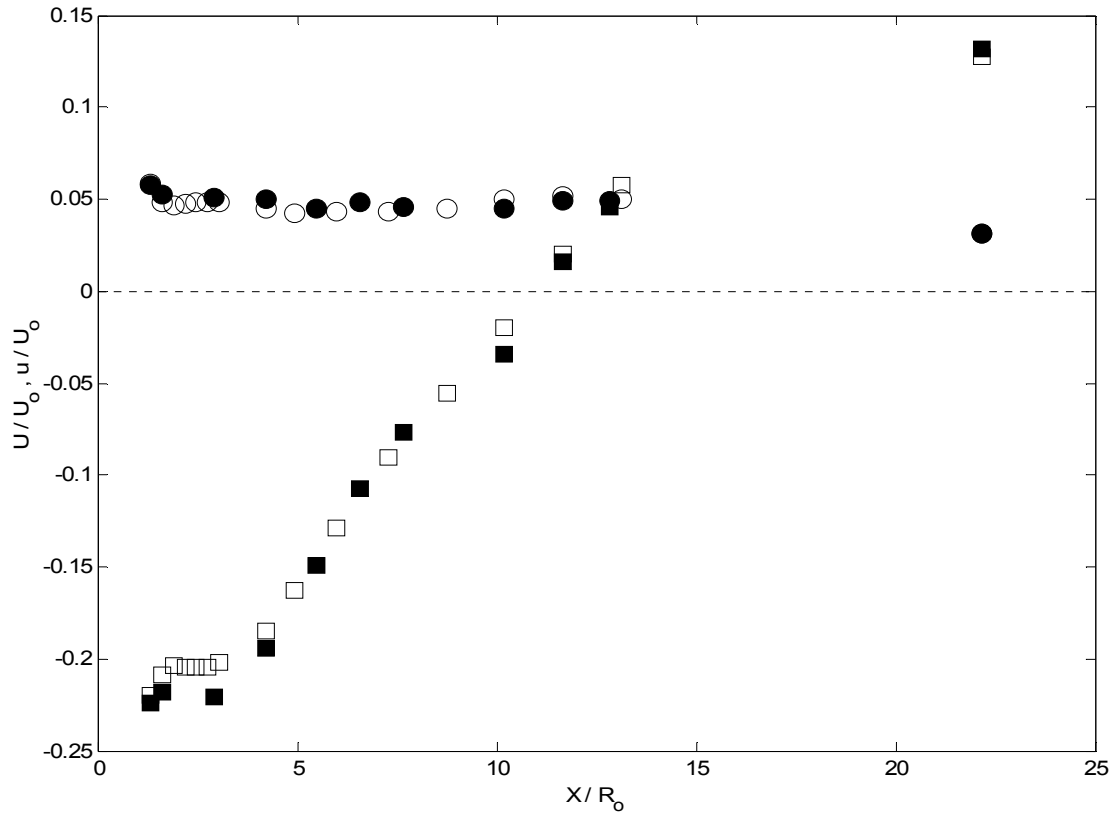


Figure 4. 1 Non-Reacting Gas Phase Downstream Centerline, Case 1 (hollow symbols), Case 2 (solid symbols): \square \blacksquare – U, \circ \bullet – u

Case 1 Flow Field

The Case 1 non-reacting gas phase, shown schematically in Figure 4.2 and seen in Figure 4.3 through Figure 4.11 (see Legend, Table 4.3), shows many of the expected properties of a high swirl number flow field. The presence of a large recirculation region, or vortex breakdown bubble, is seen clearly in Figure 4.3. In the near-injector region, $X/R_0 = 1.31$ and $X/R_0 = 1.60$, where swirl effects are the most pronounced, the flow is highly negative in the core region of the flow, while the external flow is highly positive. The static pressure drop across the swirl burner accelerates the flow, while the adverse pressure gradient associated with the large fraction of angular momentum imparted through the swirler drives the recirculating flow. As the flow expands downstream of the swirler, it is clear that the width of the breakdown bubble increases. At three and four

Table 4.3 Legend

X/R_0	Symbol
1.31	Δ
1.60	\blacklozenge
2.92	\square
4.23	\blacktriangle
10.21	\diamond
22.16	\blacksquare

nozzle radii downstream the bubble appears to extend across most of the horizontal flow field. While this result appears inconsistent with mass conservation, the three dimensional nature of the flow field and combustor geometry may allow for it. As the third velocity component is not presented, and the cross-sectional geometry is of non-constant area ratio, flow expanding into the combustion volume traveling in the Y/R_0 direction, shown in Figure 3.3, should account for the remaining mass flow. Further, results by Syred and Beer [4] show that large recirculation regions, "...occupying up to 80% of the exit area of the nozzle and recirculating more than the input mass-flow rates..." are common in high swirl flows. By $X/R_0 \sim 11$, the vortex breakdown bubble is closed, and beyond this region, the flow is entirely positive and nearly uniform. Outside of the combustion chamber, at $X/R_0 \sim 22$, the flow shows this uniformity, with the entrainment of quiescent air distorting the flow field for $Z/R_0 > 2$. It should be noted that the flow experiences a small, abrupt, acceleration through the exhaust region, partially responsible for the slight asymmetry seen in the exhaust gas profile.

The swirling nature of the flow is further verified in Figure 4.4, where the clockwise rotation, from a downstream view of the swirler face, is clear. The large vertical velocities continue to $X/R_0 \sim 4$, even increasing slightly in the outer regions. With increasing distance downstream, the swirl component decreases, with the exception of a slight increase outside of the exhaust contraction. While these results agree well with

prior swirling flow research [4, 15, 17, 20], they do not show the counter-swirling nature of the design geometry. The primary swirler, coincident with the fuel nozzle, has little effect on the non-reacting gas phase as the counter-rotating swirl decays rapidly downstream, visualized in Figure 4.2 below. However, the misalignment of the primary and secondary swirler assemblies has a sizeable effect on the vertical mean velocity, as the primary swirl is seen to influence the secondary swirl for $Z/R_0 < 0$. This asymmetric swirler influence agrees well with previous work that suggested that tight machining tolerances and strict assembly protocol were essential for improved combustor performance [24]. It is assumed that these counter-rotating features would be visible further upstream, at locations $X/R_0 < 1.31$. However, optical access is restricted below $X/R_0 = 1.31$, preventing the verification of this assumption.

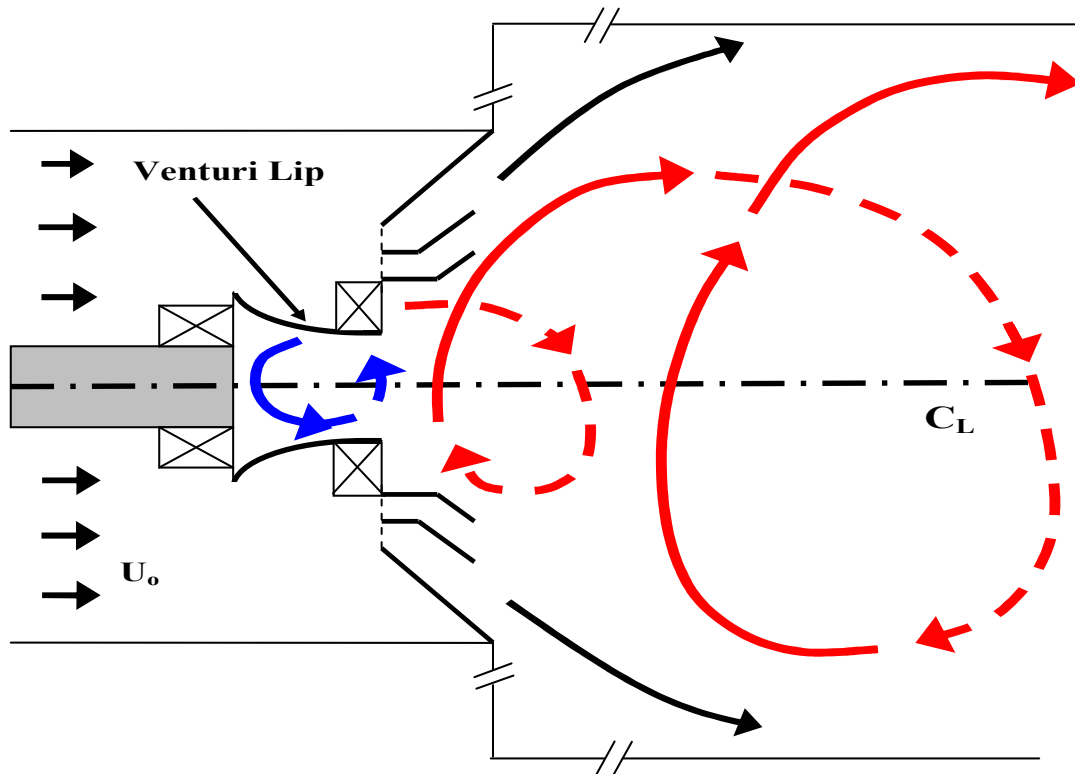


Figure 4. 2 Schematic of the Non-Reacting Gas Phase Swirling Flow Field

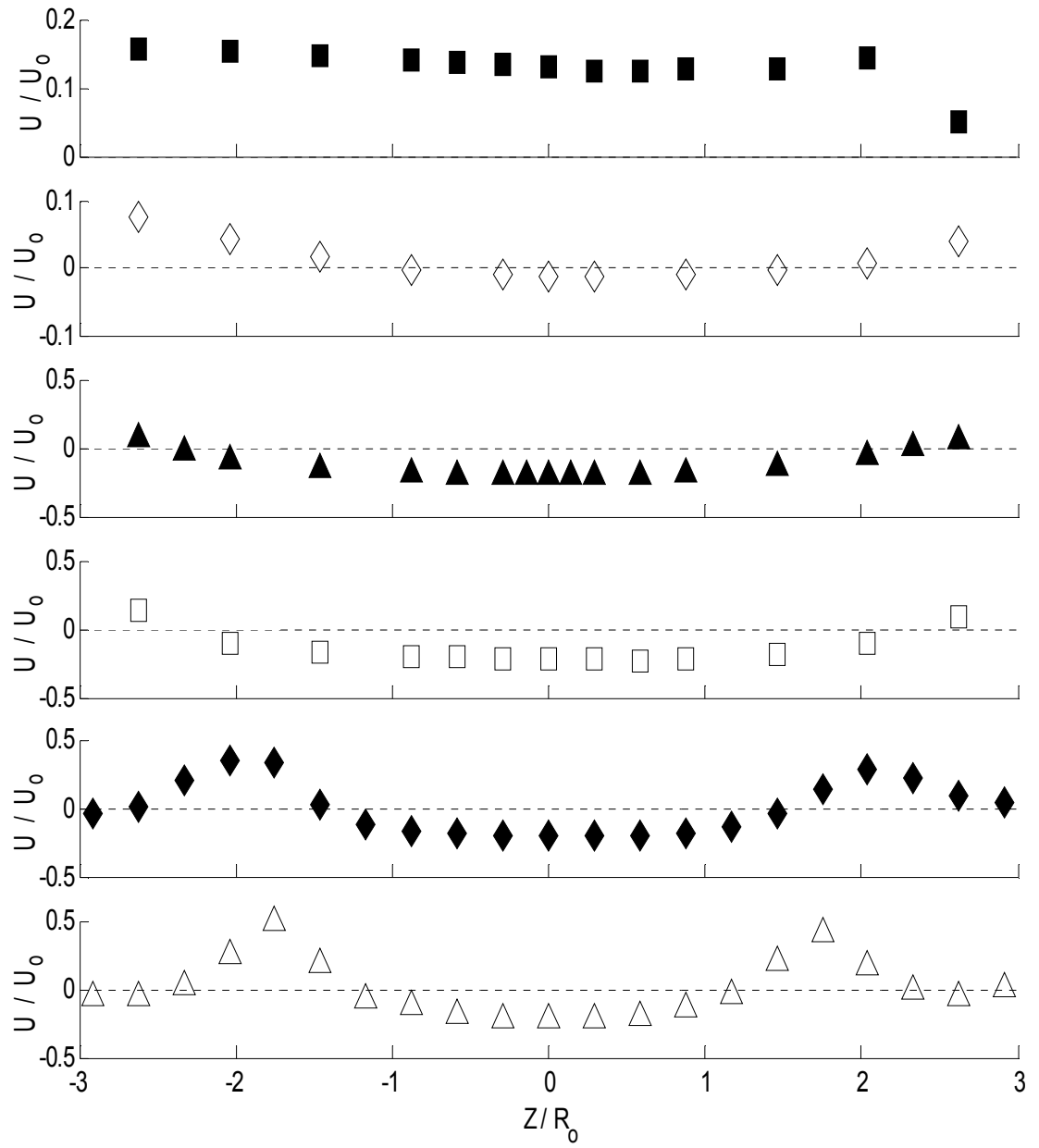


Figure 4.3 Z-Y plane ($Y/R_0 = 0$), Case 1 Non-Reacting Axial Mean Velocity, Legend see Table 4.3

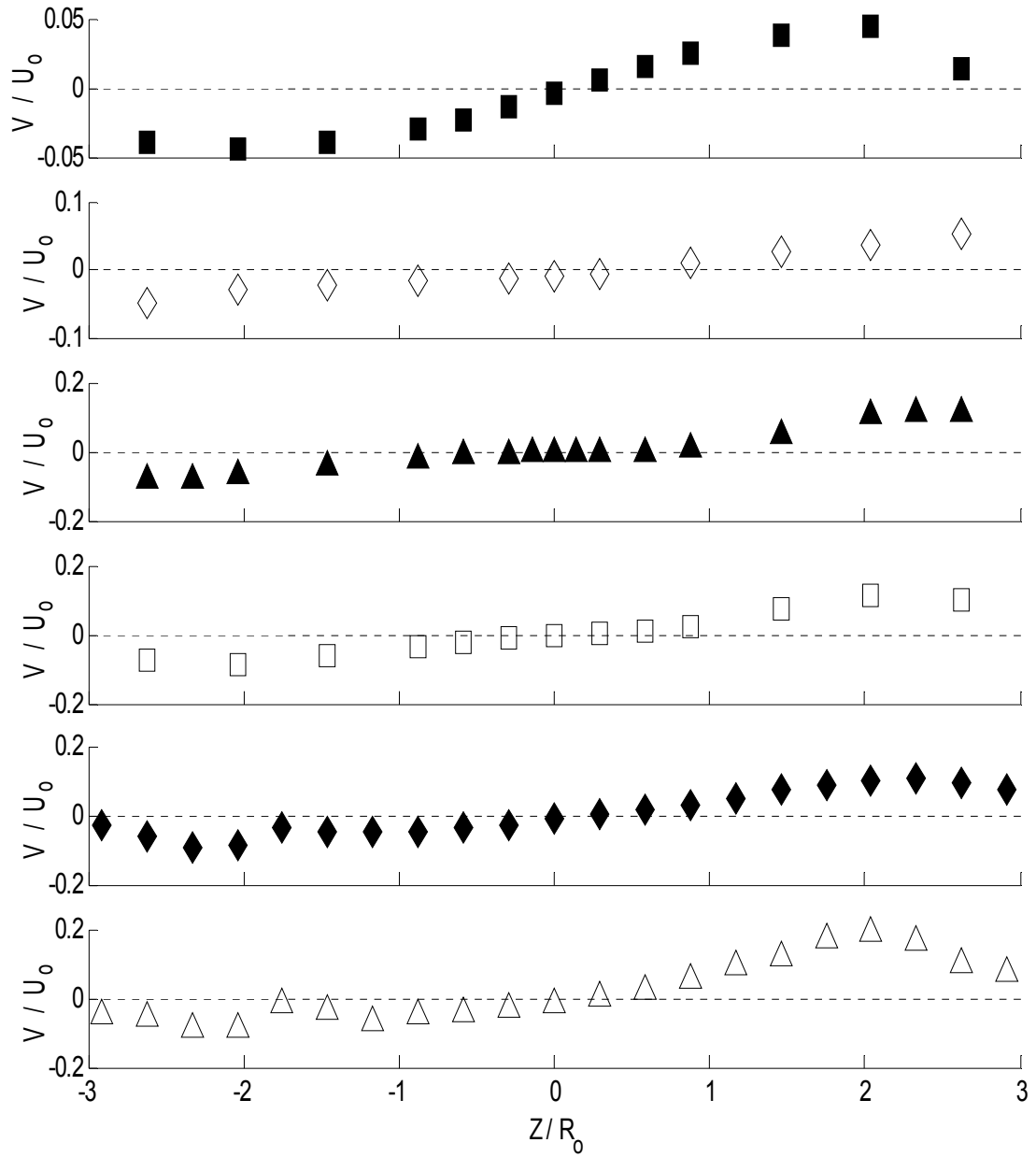


Figure 4.4 Z-Y plane ($Y/R_0 = 0$), Case 1 Non-Reacting Vertical Mean Velocity, Legend see Table 4.3

Figures 4.5 and 4.6 show the normalized 2-D TKE and Reynolds shear stress respectively, defined in Equations 4.1 and 4.2.

$$k = \langle (u')^2 \rangle + \langle (v')^2 \rangle \quad (4.1)$$

$$-uv = -\langle u'v' \rangle \quad (4.2)$$

Results presented below agree qualitatively with previous turbulence measurements in an isothermal, counter-rotating flow field [15]. The large TKE values near the injector, nearly 20% of the bulk kinetic energy, confirm the high turbulence intensity immediately downstream of the swirler geometry. These regions of maximum velocity fluctuation correspond to the shear layer present at the vortex bubble edge. The rapid decay of this turbulence downstream is shown clearly in the dramatic reduction of the total 2-D TKE, even at distances as short as 3 nozzle radii downstream. It is also important to note the lack of TKE in the combustor's central region, $|Z/R_o| < 1$, for $X/R_o < 5$. This suggests a reduction in small scale turbulent mixing, necessary for the core stability of the break down bubble [30].

The core stability is essential for the convection of downstream gas towards the fuel nozzle, an ideal flame stabilization mechanism. In addition to this convective mechanism, it was shown by Gupta et al. [9] that “high volumetric heat release rates can be achieved by matching the concentrations and directions of reactants in such a way that regions of high fuel concentration overlap regions of large shear stresses in the flow.” In the near-injector region, the large velocity fluctuations in the shear layer provide these regions of large shear stress necessary for improved heat release rates.

To improve understanding of the non-reacting gas phase mixing characteristics, the time-averaged 2-D Reynolds shear stress, $-uv$, is presented along the horizontal center plane in Figure 4.6, normalized by the bulk mean velocity squared. These results agree fairly well with similar research on the effects of counter-rotating airflow on the non-reacting turbulent mixture field in a confined combustion chamber [15, 17]. Foremost,

the assumption of a rotationally symmetric flow appears valid in the near nozzle region, $X/R_o = 1.31$ and 1.60 , and $-uv$ along the combustor centerline, ($Z/R_o = 0$), equals zero. However, the asymmetry seen in the $-uv$ results is substantially different than previous studies and results show little agreement between $Z/R_o > 0$ and $Z/R_o < 0$ in the near nozzle region. For $Z/R_o > 0$, the peak magnitude for $-uv < 0$ correlates well with the maximum mean axial and vertical gradients in the flow. Conversely, results for $Z/R_o < 0$ suggest a general smoothing out of the 2-D shear stress, with increased relative values in the flow periphery, $Z/R_o < -2$. These results suggest that non-symmetric primary-secondary swirl interactions further inhibit the diffusion of axial momentum in the radial direction [15].

Downstream, the flow behaves more symmetrically, with an apparent change in sign for $X/R_o = 10.21$. The small shear stress magnitudes downstream agree with the reduction in TKE at similar locations, Figure 4.5. Since the flow contains very little energy in the smallest scales, the transfer of turbulent momentum is minimal. At the combustor exhaust, the shear stress is nearly uniform and positive, suggesting the transport of some turbulent momentum across the entire horizontal centerline.

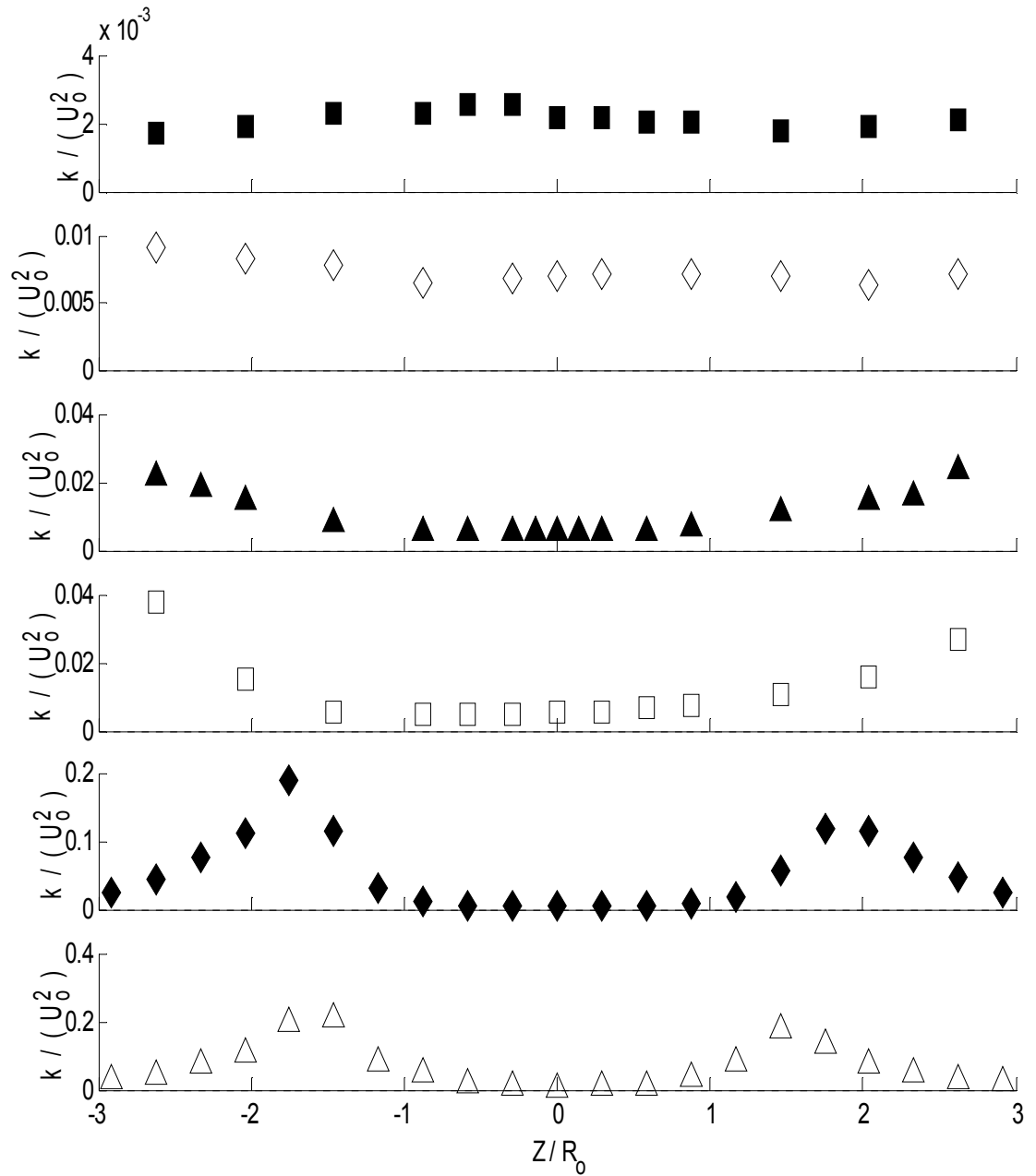


Figure 4.5 Z-Y plane ($Y/R_0 = 0$), Case 1 Non-Reacting Turbulent Kinetic Energy, Legend see Table 4.3

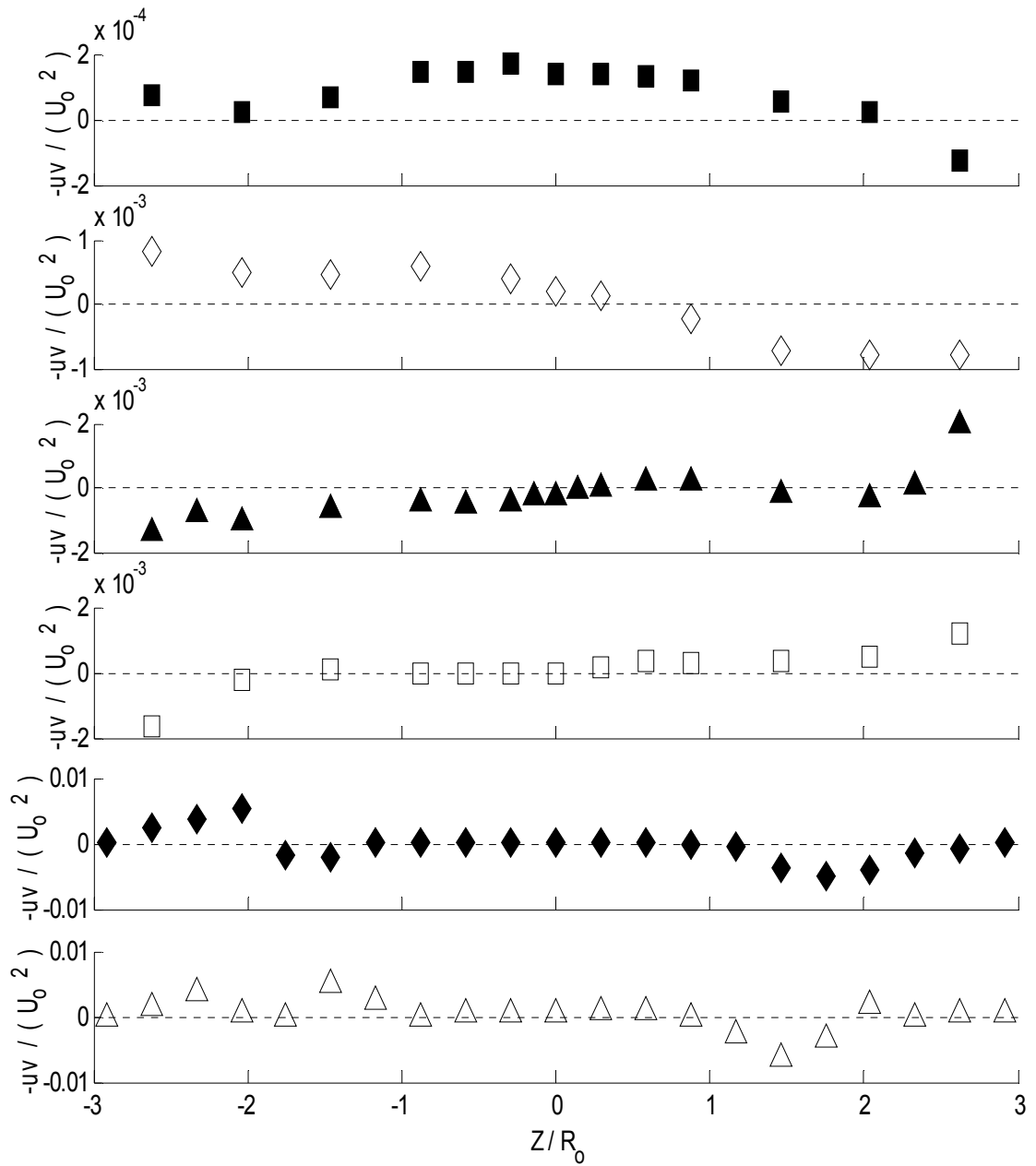


Figure 4. 6 Z-Y plane ($Y/R_0 = 0$), Case 1 Non-Reacting Reynolds Shear Stress, Legend see Table 4.3

To further quantify the Case 1 non-reacting gas phase flow, similar velocity and turbulence measurements as above were made in the vertical center plane downstream of the fuel nozzle at $X/R_0 = 1.60, 4.23,$ and 10.21 . These three locations provide insight into the near nozzle, the vortex breakdown bubble core, and the rear stagnation point respectively. The axial mean velocity, shown in Figure 4.7, confirms the presence of the large vortex breakdown bubble, extending nearly ten radii downstream. The asymmetric geometry of the vertical cross-section is apparent, as the expansion of the non-reacting flow field is restricted by the upper wall section. For $Y/R_0 < -2$, the reduction in cross-sectional area, Figure 3.4, may be responsible for the flow acceleration that extends downstream. Again, the recirculating region occupies $\sim 90\%$ of the combustor cross-section at $X/R_0 = 4.23$, in agreement with previous studies of high swirl number flow [4]. By $X/R_0 = 10.21$, the vortex bubble is almost pinched closed, and the axial mean velocity is nearly zero along the combustor centerline.

The vertical mean velocity downstream is shown in Figure 4.8. In the near nozzle region, $X/R_0 = 1.60$, the flow expansion is evident, with mean values nearly 50% of the bulk velocity. This expansion provides the large mass flow rate of air seen in the recirculation region downstream. The magnitude of the vertical velocity is greater for $Y/R_0 < 0$, as the area contraction drives the accelerated expansion. In the core of the flow, $|Y/R_0| < 1$, the vertical mean velocity is nearly zero. As such, the vast majority of the core flow is recirculated towards the fuel nozzle with velocity parallel but of opposite sign to the inflow air. By $X/R_0 = 4.23$, the vertical velocity is less than 1% of the bulk velocity. This suggests that the convection of gas from downstream towards the fuel nozzle does not include significant mass transfer normal to the swirling flow. Instead, the transfer of mass is dominated by large scale, nearly 2-D vortex structures produced by the secondary swirler. The absence of influence from the primary swirl in the vertical velocity agrees well with results from the horizontal center plane, Figure 4.4.

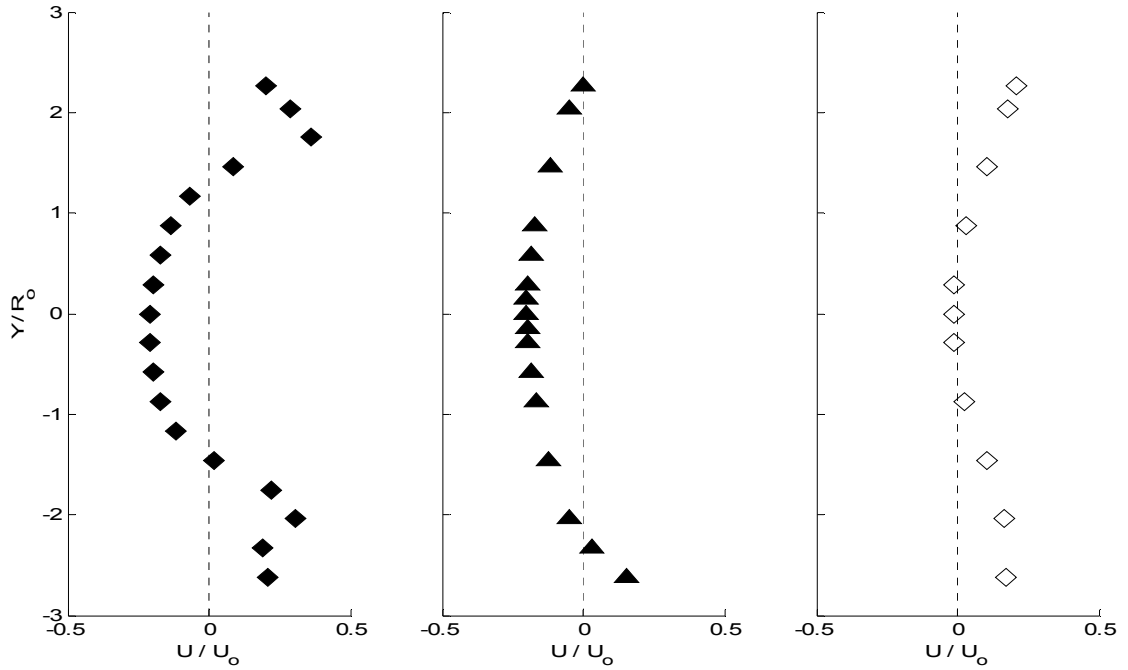


Figure 4.7 Z-Y plane ($Z/R_0 = 0$), Case 1 Non-Reacting Axial Mean Velocity, Legend see Table 4.3

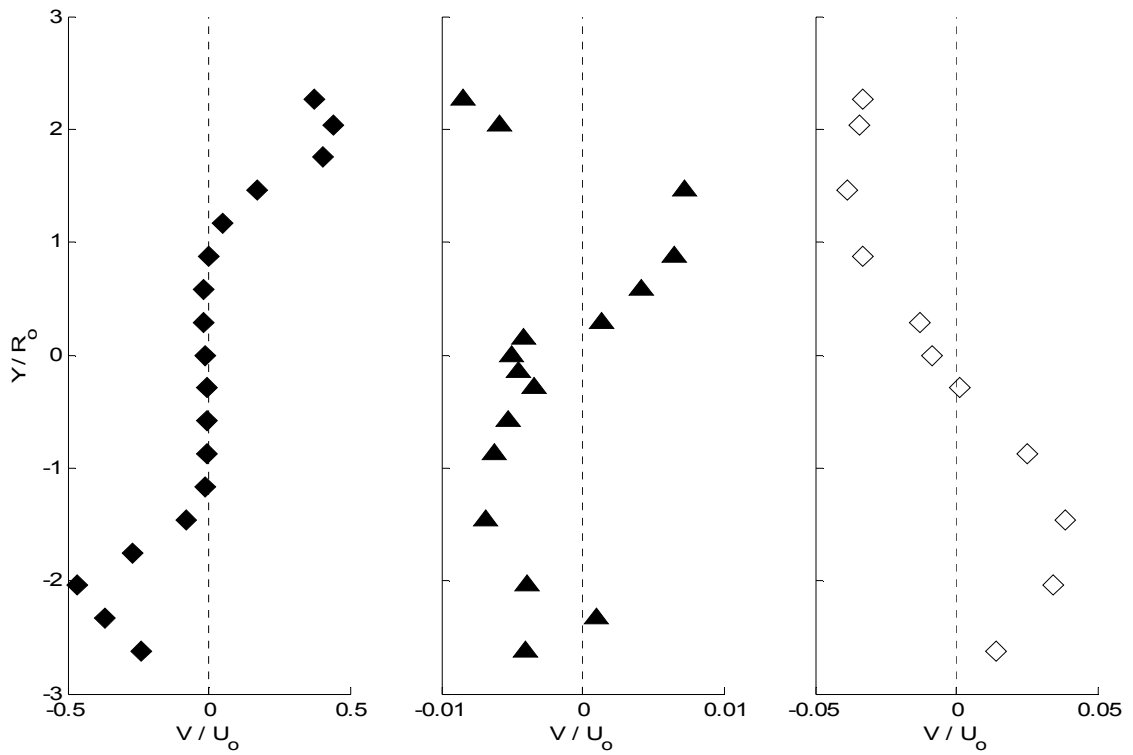


Figure 4.8 Z-Y plane ($Z/R_0 = 0$), Case 1 Non-Reacting Vertical Mean Velocity, Legend see Table 4.3

The 2-D TKE of the non-reacting gas phase along the vertical center plane, seen in Figure 4.9, agrees very well with the results presented along the horizontal center plane, Figure 4.5. The generation of TKE at the vortex bubble edge is clear at $X/R_o = 1.60$, while the absence of velocity fluctuations near $Y/R_o = 0$ confirms the uniformity of the flow in the vortex core. The peak TKE magnitude is increased as the flow accelerates for $Y/R_o < 0$, and the influence of the top wall is seen in the asymmetric distribution of TKE about the combustor centerline. Downstream, the rapid decay of the 2-D TKE suggests that turbulence is not the dominant mechanism for mixing. Instead, large scale coherent structures are responsible for the convection of gas from downstream to the near nozzle region. This convective mixing process is essential for swirl stabilized flame performance, as hot combustion products are responsible for pre-heating of the unburned fuel/air mixture in the near injector region.

To further elucidate the mixing characteristics of the non-reacting flow field, the Reynolds shear stress, $-uv$, is presented with the vertical gradient of the axial mean velocity, dU/dy , in Figure 4.10. For clarification, Figure 4.11 gives both the axial mean velocity and the vertical gradient. The Reynolds shear stress results in the vertical center plane show similar behavior to the horizontal center plane results, Figure 4.6. The assumption of rotational symmetry is satisfied downstream, and significantly better symmetry is seen across the combustor centerline. At $X/R_o = 1.60$ it is clear that in the main shear layer, $|Y/R_o| > 1.5$, the turbulent-viscosity hypothesis is correct. That is, the Reynolds stress is proportional to the mean rate of strain and the proportionality constant, the turbulent viscosity, can be modeled as a passive scalar [31]. In the core region, the nearly zero normalized shear stress and mean gradient confirm the absence of small scale fluctuations in the vortex breakdown bubble core.

Downstream, the normalized shear stress is similar in magnitude to the mean gradient, but of opposite sign. While the turbulent viscosity hypothesis appears to break

down in this region, consideration should be given to the downstream gradient of the mean vertical velocity, dV/dx , as seen in Equation 4.5 below [31].

$$\langle u'v' \rangle = -\nu_t \left(\frac{\partial U}{\partial y} + \frac{\partial V}{\partial x} \right) \quad (4.5)$$

In the vertical center plane, the downstream gradient of the vertical velocity, dV/dx , is the largest in the flow periphery, $|Y/R_0| > 1$, Figure 4.8, and should be considered in future work. Near the combustor centerline, the downstream gradient is nearly zero. As such, the influence from this term is negligible, and the gradient diffusion model does not capture the flux of turbulent momentum in the flow core. Instead, counter-gradient diffusion appears to dominate the downstream flow dynamics. Figure 4.12 below provides a schematic of the diffusion characteristics based on the correlation between $-uv$ and dU/dy . It is important to point out, however, that the typical boundary-layer type approximations are not valid in this flow; i.e., all three velocity components are of similar magnitude. As such, a simple gradient diffusion model may not capture the turbulent mixing, and the use of the full Navier-Stokes equations may be necessary in these flow fields [7]. It is worth noting that most commercial CFD codes implement the turbulent viscosity hypothesis for closure to the Reynolds Averaged Navier-Stokes equations. Given the results presented, it is unlikely that proportionality relationships between the Reynolds shear stress and the vertical gradient of the axial mean velocity will accurately capture the mixing dynamics in a confined counter-swirling flow field.

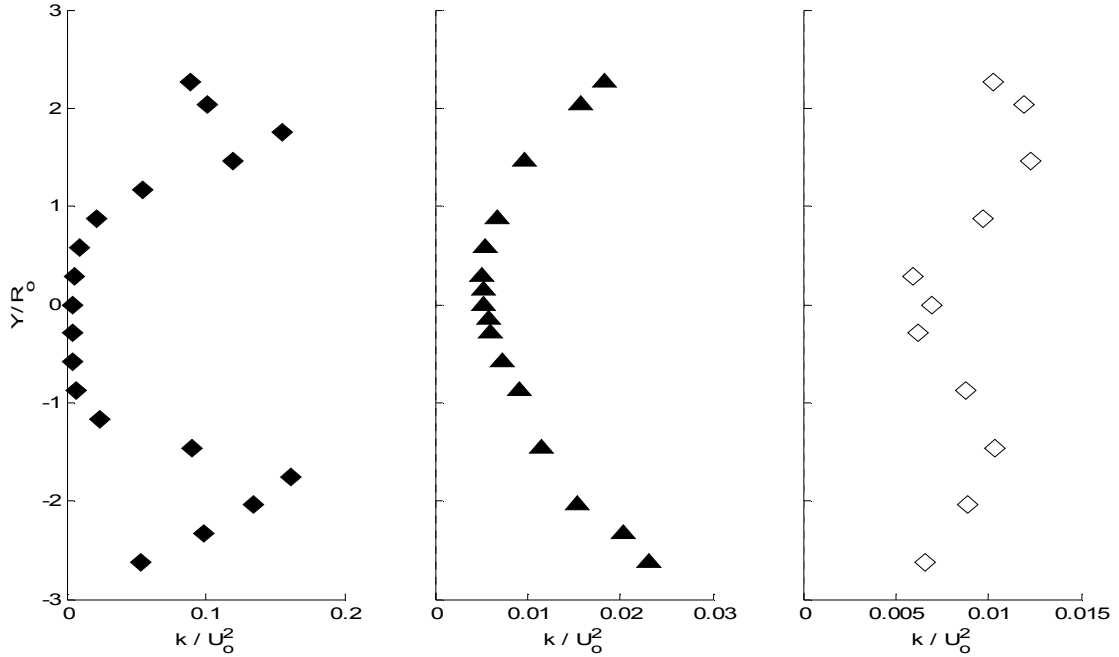


Figure 4.9 Z-Y plane ($Z/R_0 = 0$), Case 1 Non-Reacting Turbulent Kinetic Energy, Legend see Table 4.3

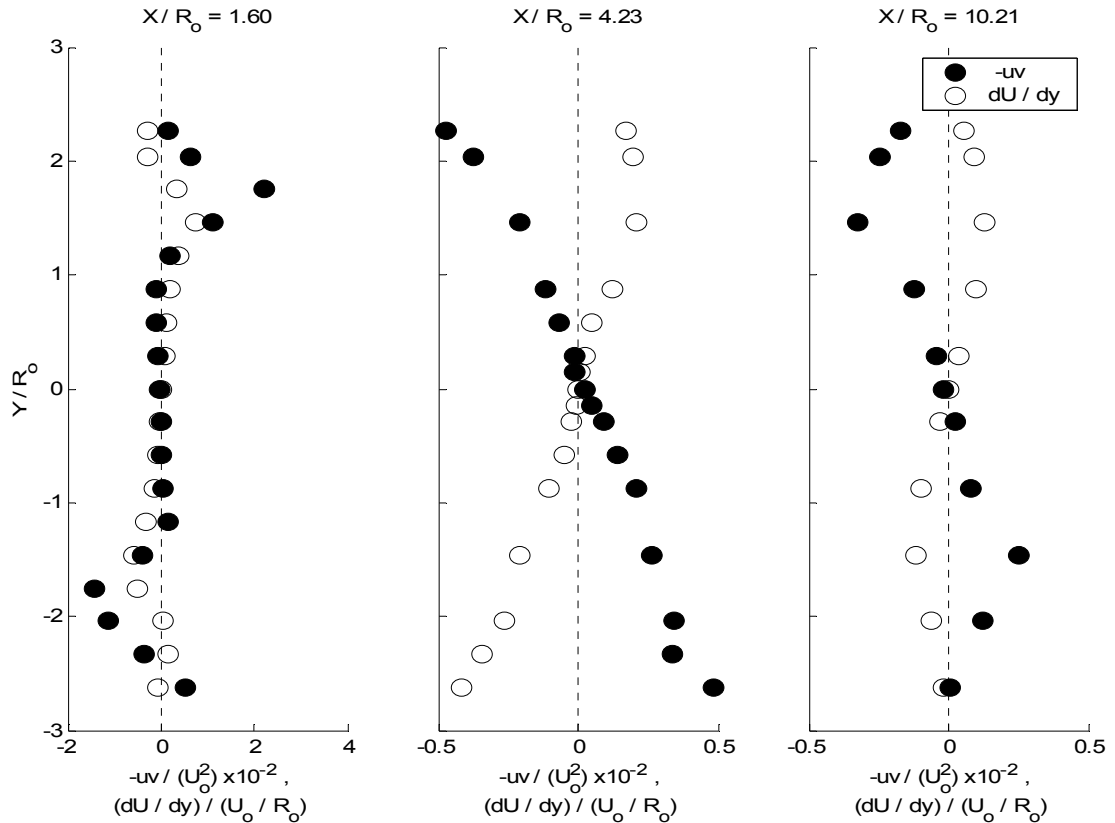


Figure 4.10 Z-Y plane ($Z/R_0 = 0$), Case 1 Non-Reacting Reynolds Shear Stress and Axial Mean Velocity Vertical Gradient

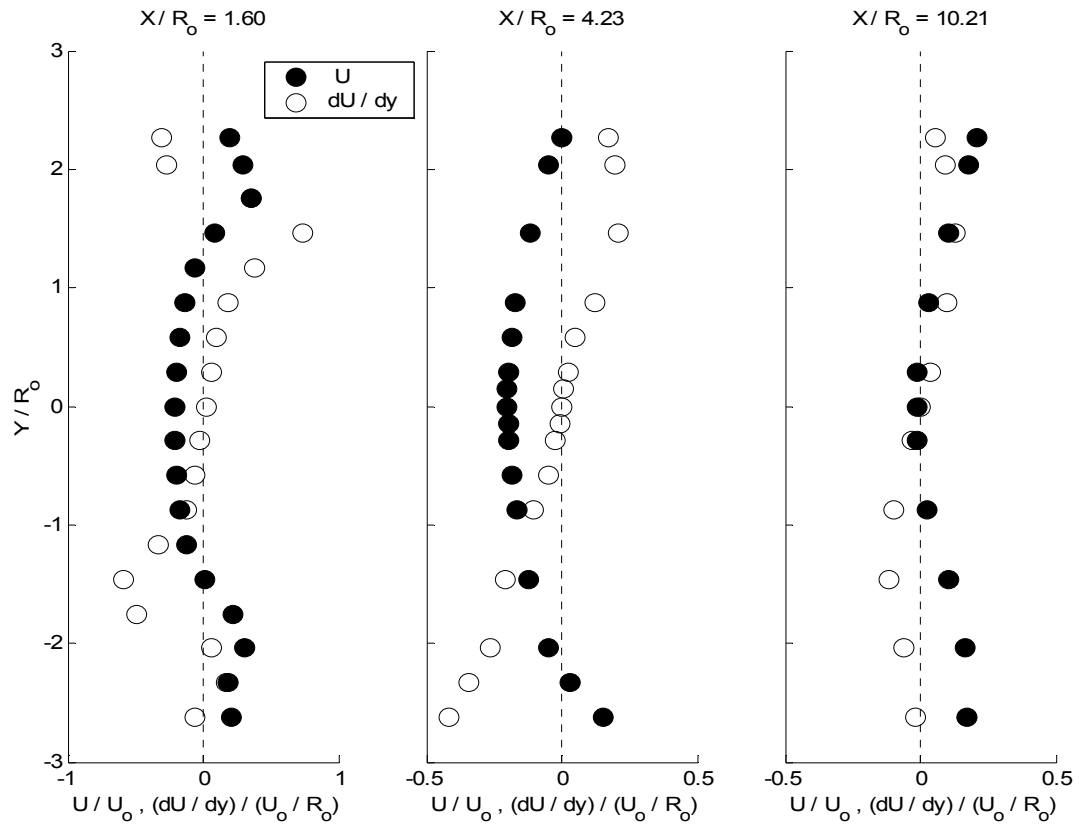


Figure 4.11 Z-Y plane ($Z/R_0 = 0$), Case 1 Non-Reacting Axial Mean Velocity and Vertical Gradient

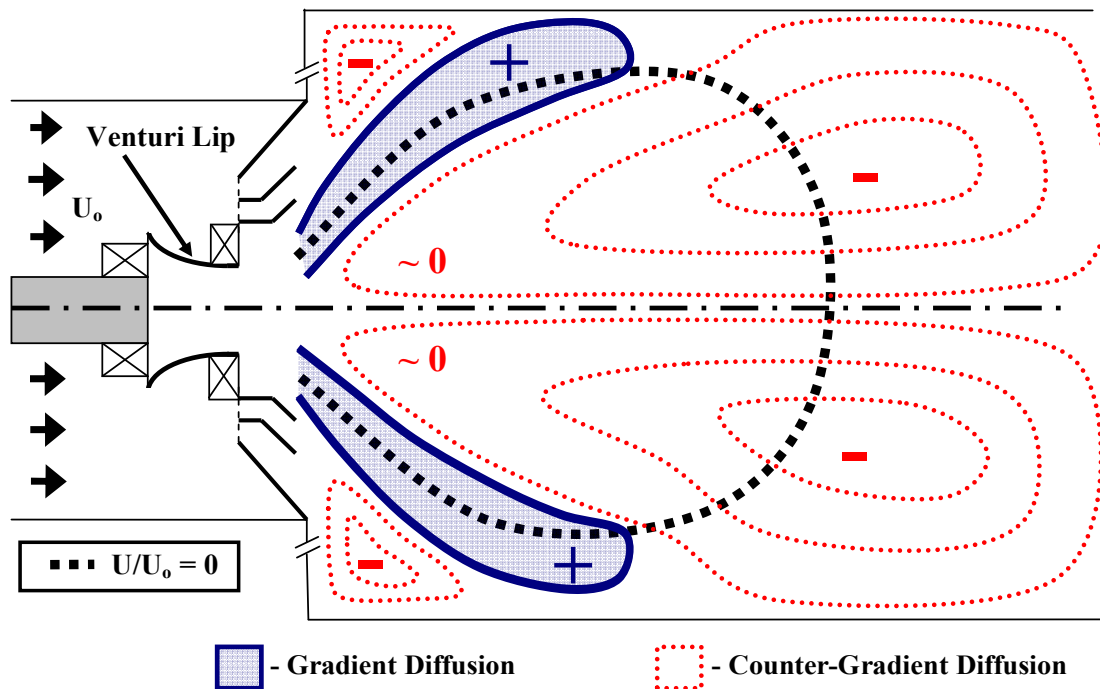


Figure 4.12 Schematic of the Non-Reacting Gas Phase Diffusion Characteristics

Case 2 Comparison

The change in pressure drop across the swirler has little effect on the non-reacting gas phase. In the near nozzle region, the peak in the axial mean velocity for Case 2 is shifted slightly to the outside of the flow for $Z/R_o > 0$, Figure 4.13 (solid circles), while the normalized magnitude is reduced slightly for $Z/R_o < 0$. However, the core strength, shape, and size of the vortex break down bubble are unchanged. This behavior is essential for lean operation near idle, as the ambient flow field must be robust to changes in power settings. Measurements outside of the exhaust contraction are almost identical, suggesting that the structure of the non-reacting gas phase is nearly unchanged with the 30% increase in mass flow rate. In fact, the swirl cup flow field appears more symmetric at an increased load. The velocity magnitude does increase with the additional mass flow rate of air, but the normalized results nearly collapse to a single flow field. This result is essential from a numerical modeling standpoint, as one flow field can be used to simulate the non-reacting gas phase dynamics over this range of loading conditions in a single burner from a gas turbine combustor.

The tangential mean velocity, or swirl component, shows less effect from the swirler misalignment at increased pressure drop for $Z/R_o < 0$. The central swirl is unchanged and remains generally asymmetric in this combustion chamber, seen in Figure 4.14. It is important to note that counter rotation from the primary swirl is not visible in the non-reacting gas phase at either pressure drop across the swirler. Without combustion, and droplets in the primary air stream, the counter-swirl is rapidly damped by the external secondary swirl, preventing measurement of the central counter-rotation. Results from a similar swirl burner confirm the absence of the primary, counter-rotating swirl in the non-reacting case [17, 20].

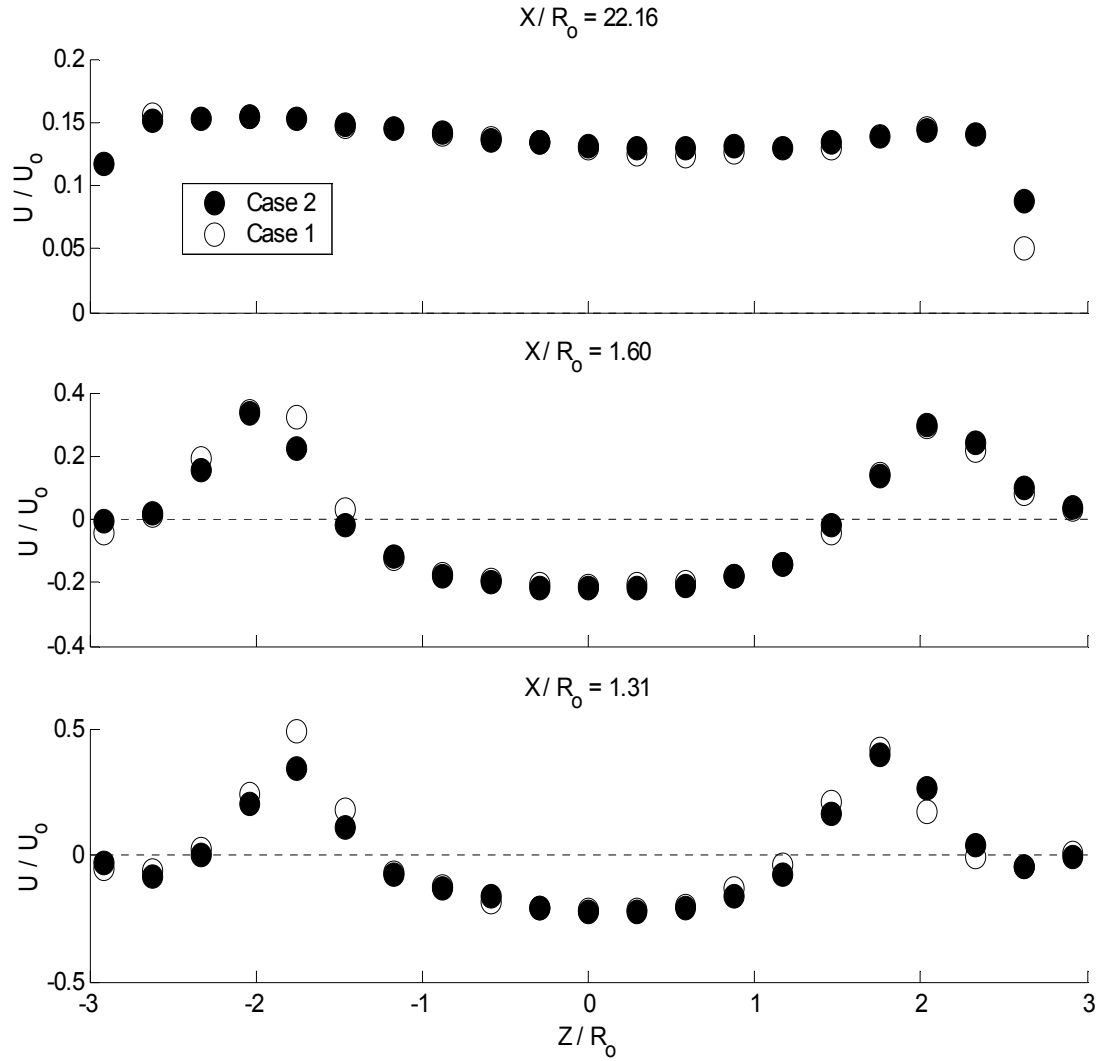


Figure 4. 13 Z-Y plane ($Y/R_0 = 0$), Case 1 and Case 2 Non-Reacting Axial Mean Velocity

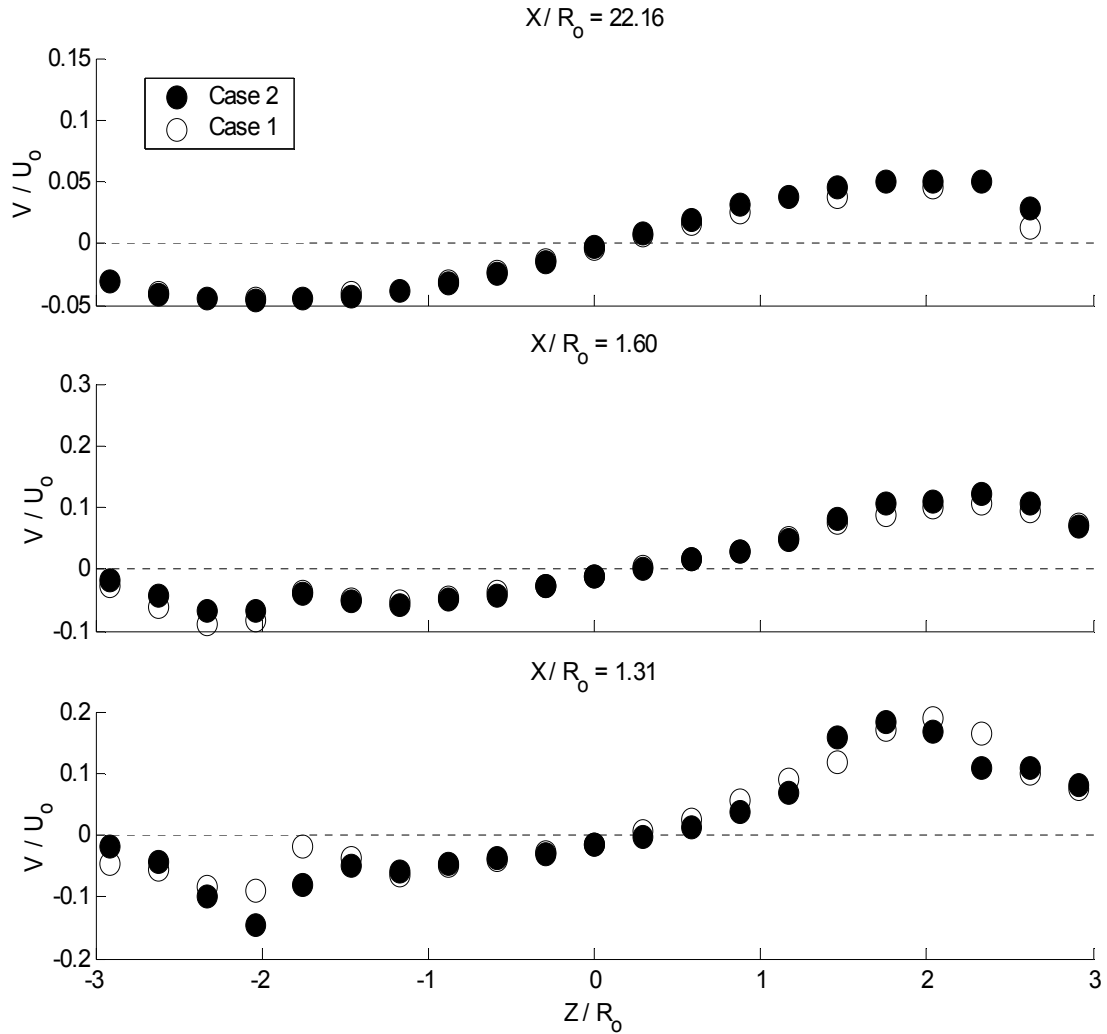


Figure 4.14 Z-Y plane ($Y/R_0 = 0$), Case 1 and Case 2 Non-Reacting Vertical Mean Velocity

Closer examination of the 2-D TKE, Figure 4.15, shows a similar improvement in the flow structure. The peak magnitude of the TKE is reduced slightly at $Z/R_0 = -2.00$ in the near nozzle region. However, the Case 2 profile shows improved symmetry, suggesting that relative mixing is enhanced at increased pressures. The stability of the recirculating core is further verified by the negligible TKE. In the core, $-1 < Z/R_0 < 1$, the fluctuating velocity field contains very little energy. As such, large scale structures are responsible for the convection of gases upstream, with negligible effects from small scale turbulence. This behavior is ideal for flame stabilization; hot products from the

post flame region preheat the core, improving evaporation and ignition delay times. Since Case 1 and Case 2 show similar isothermal flow structures, it will be assumed that the non-reacting gas phase structure is unaltered with the prescribed change in inflow pressure drop. This result suggests that the mechanism for flame stabilization in a swirl stabilized liquid combustor may be unaltered with moderate changes in the mass flow rate of inlet air.

The Reynolds stress data, shown in Figure 4.16, suggests that the active diffusion of turbulent momentum across the shear layer is generally unchanged with the increase in inlet mass flow rate. However, the increase in total air momentum improves the transport of turbulent momentum in the main shear layer, increasing the magnitude of the shear stress near $|Z/R_o| = 1.5$ at $X/R_o = 1.31$. This shift implies that the assumption of rotational symmetry may improve at increased load in the non-reacting case. The opposite trend is observed at $Z/R_o = 1.60$, where the peak shear stress magnitude is reduced slightly for $Z/R_o < 0$. Here, the swirler misalignment clearly influences the turbulence, and the flux of axial momentum is inhibited for $Z/R_o < 0$. Furthermore, these results agree well with earlier research suggesting a general reduction in the radial flux of axial momentum with counter swirl addition [15]. In general, the normalized Case 2 non-reacting flow field agrees well with the normalized Case 1 result and shows a slight improvement in symmetry at increased mass flow rates. As such, a single non-reacting flow field can be adopted for the range of loading conditions examined.

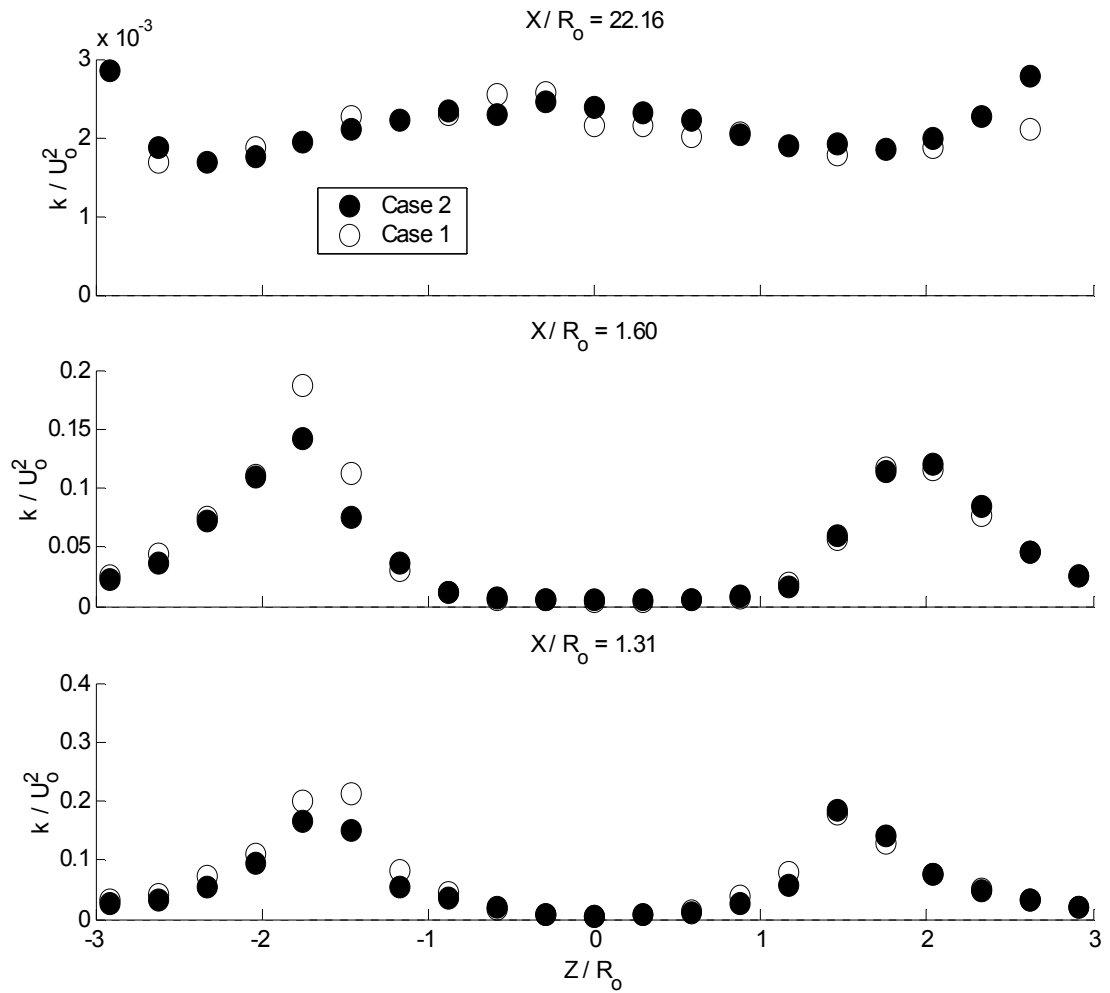


Figure 4. 15 Z-Y plane ($Y/R_0 = 0$), Case 1 and Case 2 Non-Reacting Turbulent Kinetic Energy.

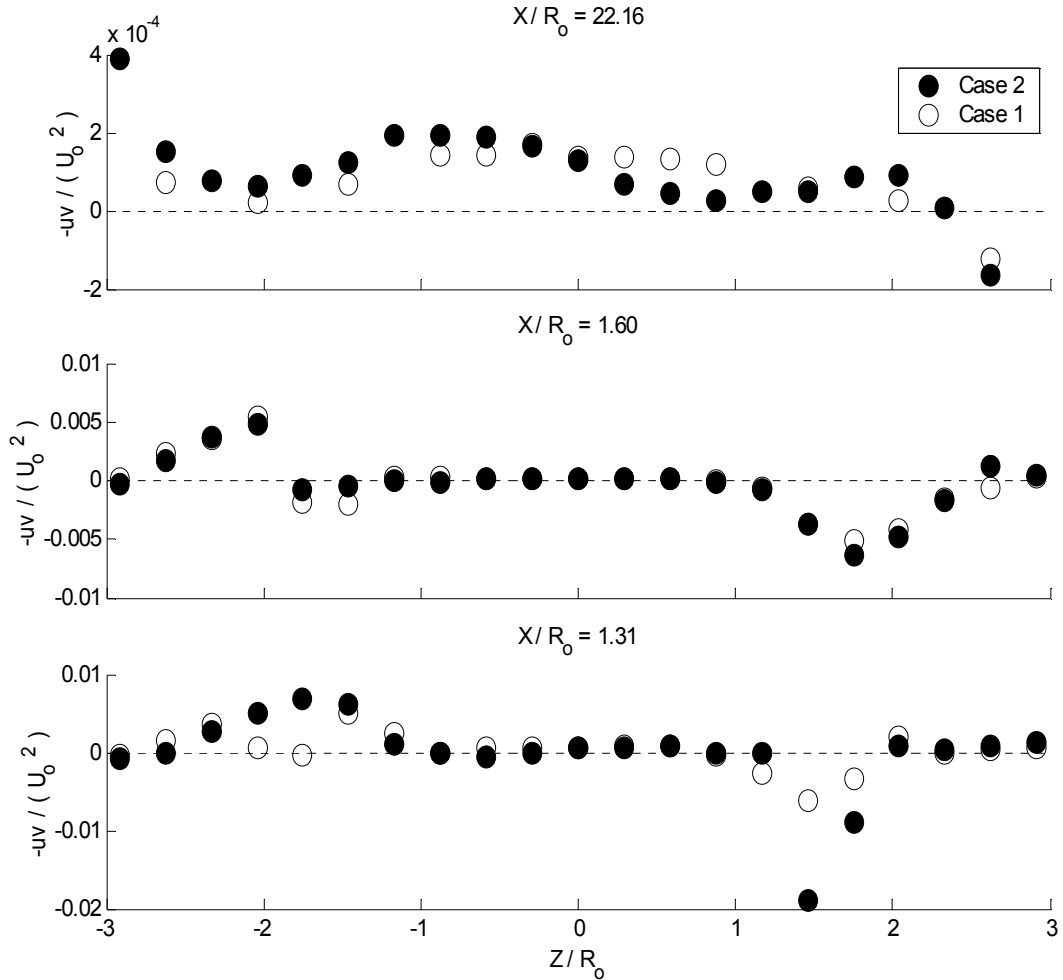


Figure 4. 16 Z-Y plane ($Y/R_0 = 0$), Case 1 and Case 2 Non-Reacting Reynolds Shear Stress

Reacting Gas Phase

Measurements of the Case 1 and Case 2 reacting flow fields are presented below. As with the non-reacting gas phase, aluminum oxide ($\sim 5 \mu\text{m}$) was used to seed the flow and results focus on the horizontal and vertical center planes downstream of the swirler. The effects of combustion, specifically heat addition, on the swirling flow field are highlighted near the LBO limit. Further, the influences of fuel pressure and fuel nozzle rated spray angle on the reacting flow field are investigated. A direct comparison between the non-reacting and the reacting gas phase results for Cases 1 and 2 are given in Appendix A, Figure A.1 through Figure A.13.

Case 1

Figures 4.17 and 4.18 illustrate the changes in the axial mean and RMS velocity profiles along the combustor centerline downstream of the fuel nozzle with the addition of combustion for Case 1. The reacting gas phase (solid symbols) is significantly different from that of the non-reacting gas phase (hollow symbols) discussed above. While the presence of the vortex bubble is still apparent, it is both shorter and stronger. The rear stagnation point is now 9 nozzle radii downstream, and the core magnitude is increased by over 50%. The effect of heat release is clear in Figure 4.17 as well, as the exhaust gas velocity rose by a factor of 3. The acceleration is due in part to the volumetric expansion associated with heat release during combustion. This expansion is also responsible for the increased recirculation strength, as hot combustion products are entrained at velocities well above the non-reacting gas phase velocity (Figure A.1).

The reacting gas phase axial RMS distribution, Figure 4.18, is also substantially different from the non-reacting results presented above. With combustion, the active mixing of hot products with non-premixed liquid fuel and air in the near nozzle region drives the large velocity fluctuations, up to 20% of the bulk velocity. This mixing is pivotal for both flame stabilization and emission levels, as the residence times in the combustor must allow for evaporation, mixing, ignition, and suitable burning time. Thus, the initial mixing of hot, radical rich combustion products with cold, unburned reactants must be efficient, reliable, and well understood. Figure 4.18 suggests that the convection of gas from downstream is not the dominant mixing mechanism in the near nozzle region with reactions. Instead the active turbulent mixing of hot products with cold reactants is seen in the rise in RMS velocity for $X/R_0 < 5$, while the absence of velocity fluctuations in the far field, $X/R_0 > 5$, suggests convection provides those hot products from downstream.

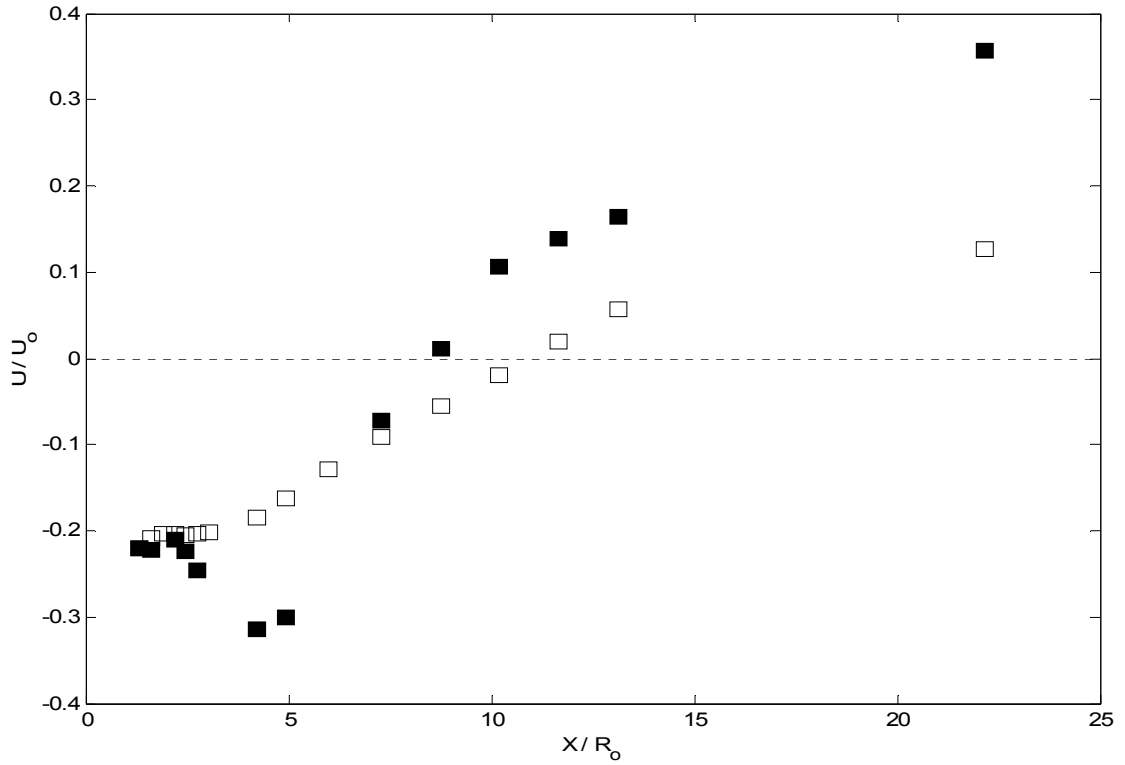


Figure 4.17 Gas Phase Axial Mean Velocity Downstream Centerline Case 1, Non-Reacting (hollow symbols), Reacting (solid symbols)

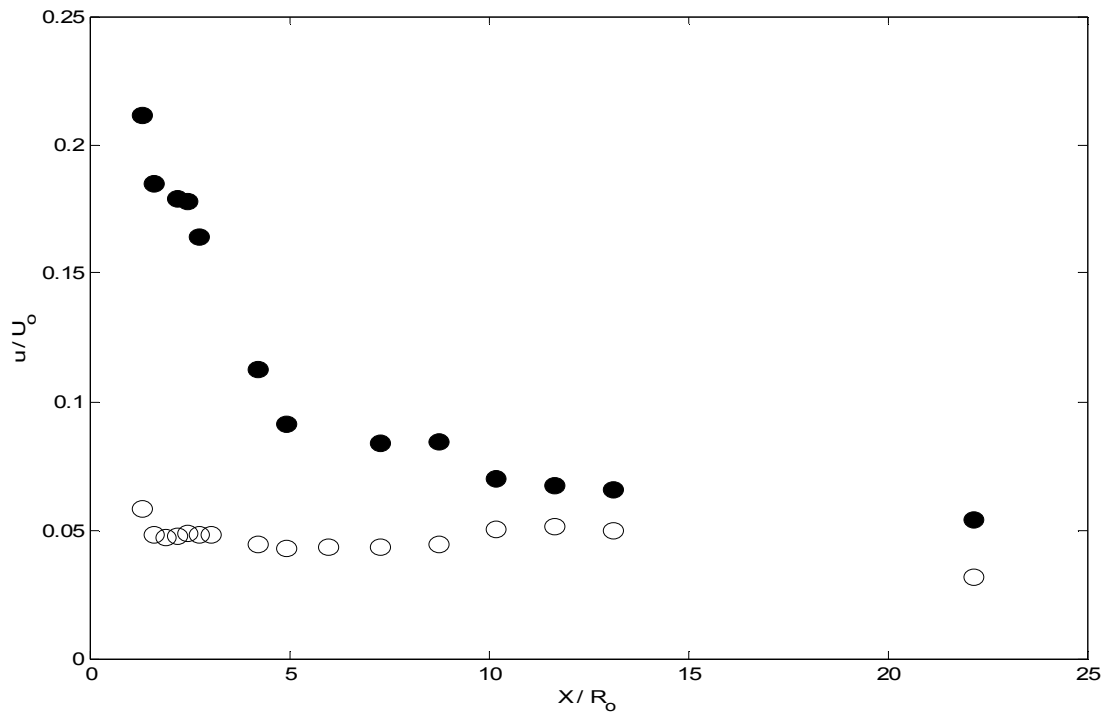


Figure 4.18 Gas Phase Axial RMS Velocity Downstream Centerline Case 1, Non-Reacting (hollow symbols), Reacting (solid symbols)

Profiles of the Case 1 reacting gas phase axial mean velocity downstream, seen in Figure 4.19, clearly show again the presence of a vortex breakdown bubble due to the swirling nature of the flow. However, the size, shape, and magnitude of this recirculating region change substantially with the addition of heat associated with combustion. In the near-injector region, $X/R_o = 1.31$ and $X/R_o = 1.60$, the flow shows the central negative velocity region surrounded by large positive values, similar to the non-reacting phase. However, there is a large reduction in the recirculating region size. In the reacting case, the negative velocities are confined to a region less than one nozzle radius across at both locations. In the non-reacting case, however, this region spans over 2 nozzle radii at $X/R_o = 1.31$ and nearly 3 nozzle radii at $X/R_o = 1.60$, seen in Figure 4.3. This pinching continues downstream, and the entire flow field is positive for $X/R_o > 10$. Further, the reacting flow shows a larger positive flow region, with mean axial velocities nearly double those seen in the non-reacting flow. These differences are highlighted in Figure A.1, where the Case 1 reacting and non-reacting flow fields are compared directly.

These two, large scale changes to the flow field can be attributed to the volumetric expansion of the local gas phase due to the large heat release rates. The axial component of the velocity is strongly influenced by this expansion, pinching the vortex bubble closed near the fuel nozzle, while significantly increasing the net flux of axial momentum. Both the bubble pinching and momentum increase are seen clearly downstream, as the recirculation region is never more than two nozzle radii wide and has completely closed well before $X/R_o = 10$. Both of these reacting results differ from the non-reacting case, where the bubble is more than 4 radii wide, with negative velocities persisting beyond $X/R_o = 10$. Reacting exhaust gas velocities are more than twice that of the non-reacting gas, additional evidence of the kinetic energy addition associated with the heat release upstream.

The influence of the combustion process in the near-injector region is further shown in Figure 4.20 by the dramatic change in the mean vertical velocity component at

$X/R_0 = 1.31$ and $X/R_0 = 1.60$. The primary, central, counter-swirl of the combustor becomes apparent with addition of the liquid phase droplets and combustion. While not symmetric, the core region of anti-clockwise rotation can be seen, centered to the right side of the combustor fuel nozzle when viewed from downstream, in good agreement with the known asymmetry in the swirler alignment. This counter-rotation quickly decays downstream, no longer evident at $X/R_0 = 2.92$. The measurement of this inner rotation suggests that the primary swirl plays an important role in the combustion process through spray-shear interactions. The axial expansion associated with the addition of heat to the flow enabled the measurement of the primary counter-swirl. Downstream, the increase in turbulence associated with the turbulent diffusion flame, discussed below, forces the rapid decay of this counter-rotating flow field to one similar to that seen in the non-reacting gas farther downstream. In fact, the reacting gas swirl strength is reduced below that of the non-reacting gas phase, seen in Figure A.2. Note, however, that the exhaust gas at $X/R_0 = 22.16$, shows significantly higher swirl in the reacting case. In addition, the larger kinetic energy associated with the post combustion products leads to a significant increase in both exhaust gas velocity components.

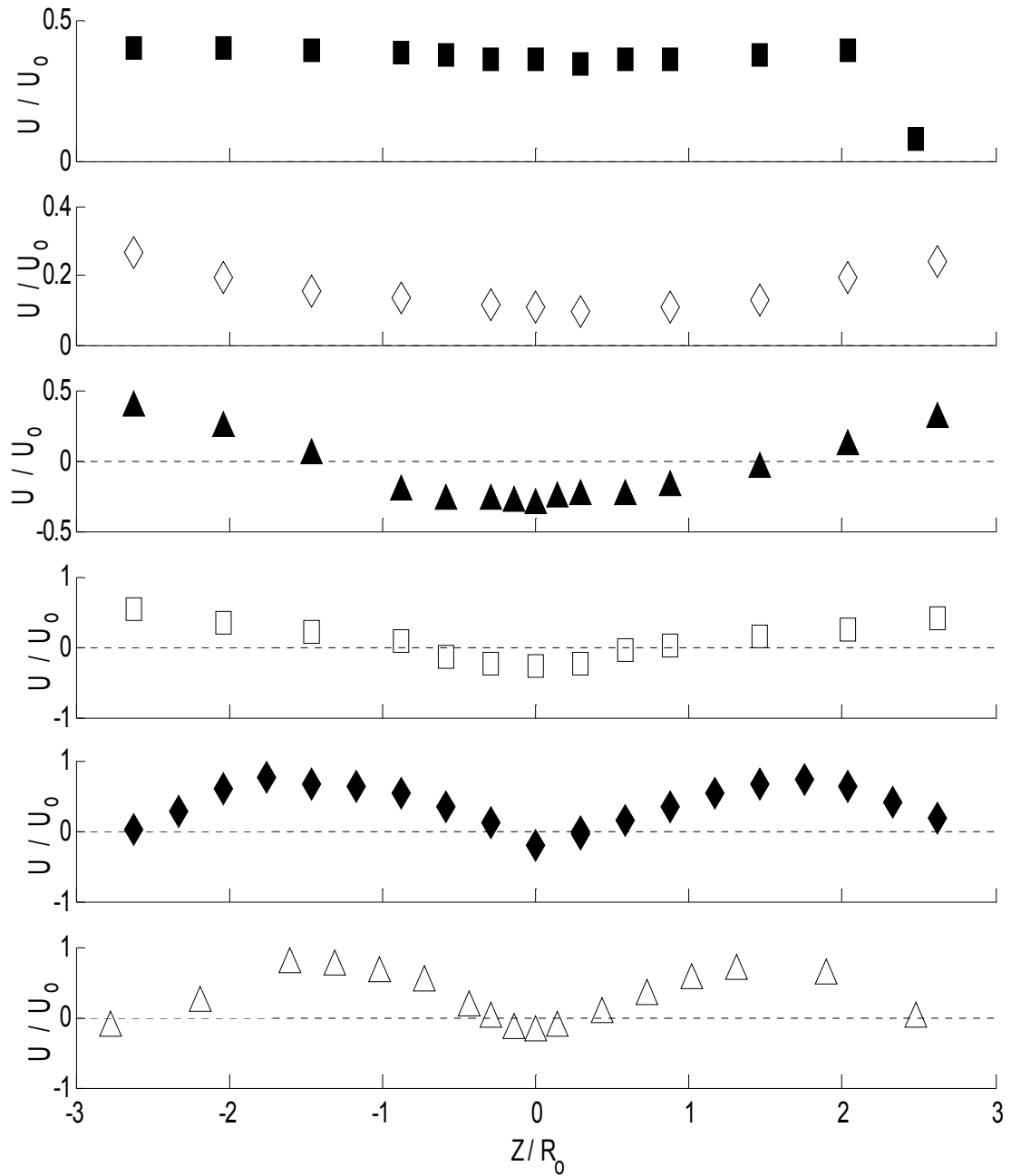


Figure 4. 19 Z-Y plane ($Y/R_0 = 0$), Case 1 Reacting Axial Mean Velocity, Legend see Table 4.3

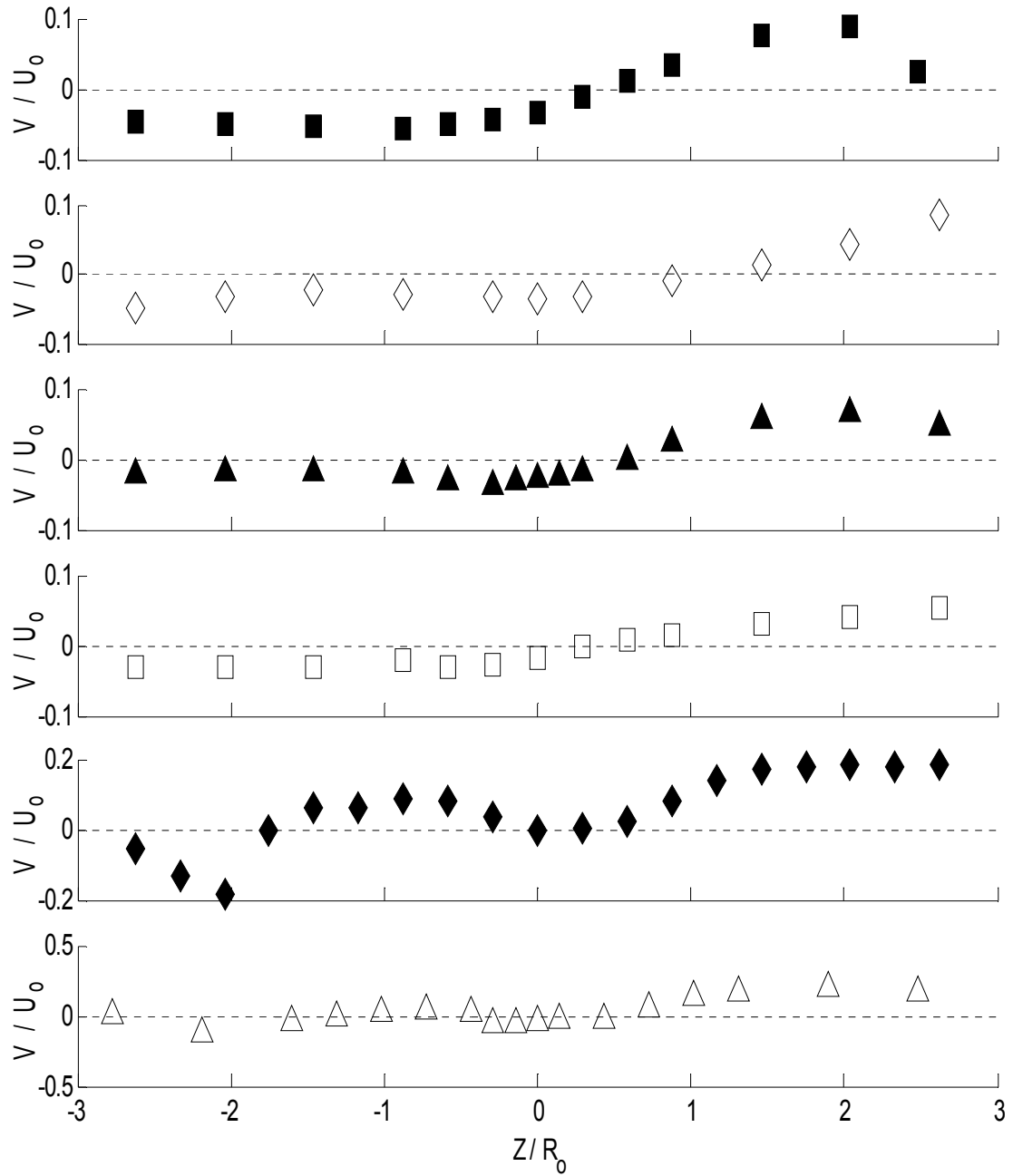


Figure 4. 20 Z-Y plane ($Y/R_0 = 0$), Case 1 Reacting Vertical Mean Velocity, Legend see Table 4.3

The 2-D turbulent kinetic energy (TKE) measurements, shown in Figure 4.21, agree well with similar results for reacting, swirling flows [17]. At $X/R_0 = 1.31$, the TKE is contained in regions on both sides of the spray nozzle. This confinement is expected, as the maxima of the rms velocity components are located in a similar region. These maxima can be attributed to the liquid-spray interactions near the nozzle, dominated by the spray angle and SMD of the droplets. As droplets enter the combustion chamber with a large amount of counter-rotation relative to the mean flow, they are generally unable to follow the existing flow. Instead, these droplets follow a trajectory through the mean flow, generating significant amounts of turbulence near the injector. Chiu [14] has also shown that in the near-injector region of spray flames, that external, or sheath type, combustion modes are common. This sheath type combustion mode is characterized by many unburned droplets surrounded by a gaseous diffusion flame. At $X/R_0 = 1.31$, unburned droplets in the core of the spray contribute significantly to the 2-D TKE, while combustion at the spray periphery may be responsible for the reduction in the turbulence intensity.

Downstream, as the evaporation and mixing processes become important, the TKE distribution is seen to broaden slightly at $X/R_0 = 1.60$, shown also in Figure A.3. As the initial droplet momentum is decreased due to drag forces on the droplets, mixing and diffusion characteristics are improved [24]. With this improved mixing, and the convection of droplets outward due to volumetric expansion, the TKE is spread across the combustor, with values increasing at the spray periphery and centerline, while decreasing in the core regions. This implies that the droplet penetration is reduced downstream, while radial diffusion is increased. Further downstream, at $X/R_0 = 2.92$, the TKE is reduced in half. This reduction is due to the partial relaminarization of the flow at high combustion temperatures [32]. At this distance downstream, evaporation and mixing have had a significant impact, and combustion occurs in both the gas/droplet and droplet phase [14]. In these phases, combustion is more complete across the chamber cross

section and a more uniform temperatures distribution is expected. Consequently, turbulence fluctuations are reduced, as is the turbulent energy at small scales [32]. This continues downstream, where the exhaust TKE is less than 1% of the total kinetic energy.

Figure 4.22 shows the 2-D Reynolds shear stress, $-uv$, for similar downstream locations as those mentioned above. From this figure, the effect of the counter-swirl addition to the liquid phase is clear. At both $X/R_0 = 1.31$ and 1.60 , the second order correlation is seen to switch signs twice on each side of the combustor. This corresponds to the associated sign changes of the axial and vertical velocity across the combustor. Due to the recirculation region, a significant shear layer is established. This shear layer is clearly visible from Figure 4.22, as the magnitude of the Reynolds stress is maximized in these regions. The increased velocity gradients with combustion across the main recirculation boundary lead to these increased stresses, seen in Figure A.4 as well. These results are similar to the findings of Merkle et al. [15], who showed similar trends in the radial flux of axial momentum for non-reacting counter-swirl flows. However, reacting shear stress results are limited in the literature, and more attention should be given to turbulent exchange of both momentum and mass in the two-phase reacting flow.

The asymmetry in this second order correlation is also visible, due in part to the increased uncertainty associated with higher order statistics, but also due to the asymmetric nature of the combustor. At $X/R_0 = 1.31$, this asymmetry is the most pronounced, with significant differences in magnitude and distribution on either side of the spray. By $X/R_0 = 2.92$, the relaminarization is seen again, as the peak magnitude of $-uv$ is reduced. Further, most asymmetries associated with the flow are significantly damped downstream. However, note that the condition that $-uv = 0$ at $Z/R_0 = 0$ is not identically satisfied at any location downstream, except $X/R_0 = 1.60$. While this may be a result of increased errors associated with low data rates in the core, it is more likely that these results show the exchange of turbulence across the combustor centerline. This

result is possible, as the geometry is non-symmetric about the centerline. This lack of symmetry agrees well with all data presented, confirming this exchange.

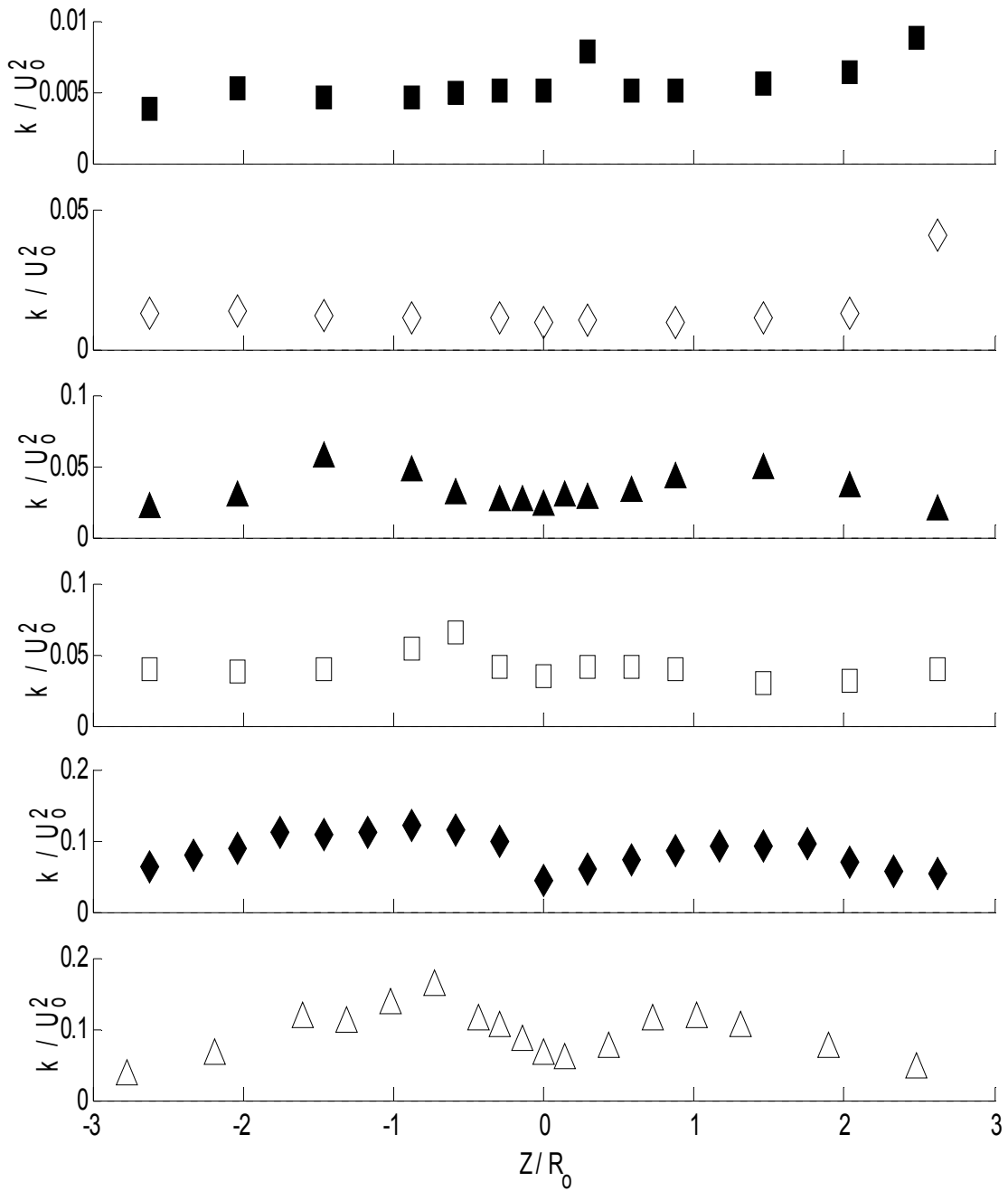


Figure 4. 21 Z-Y plane ($Y/R_0 = 0$), Case 1 Reacting Turbulent Kinetic Energy, Legend see Table 4.3

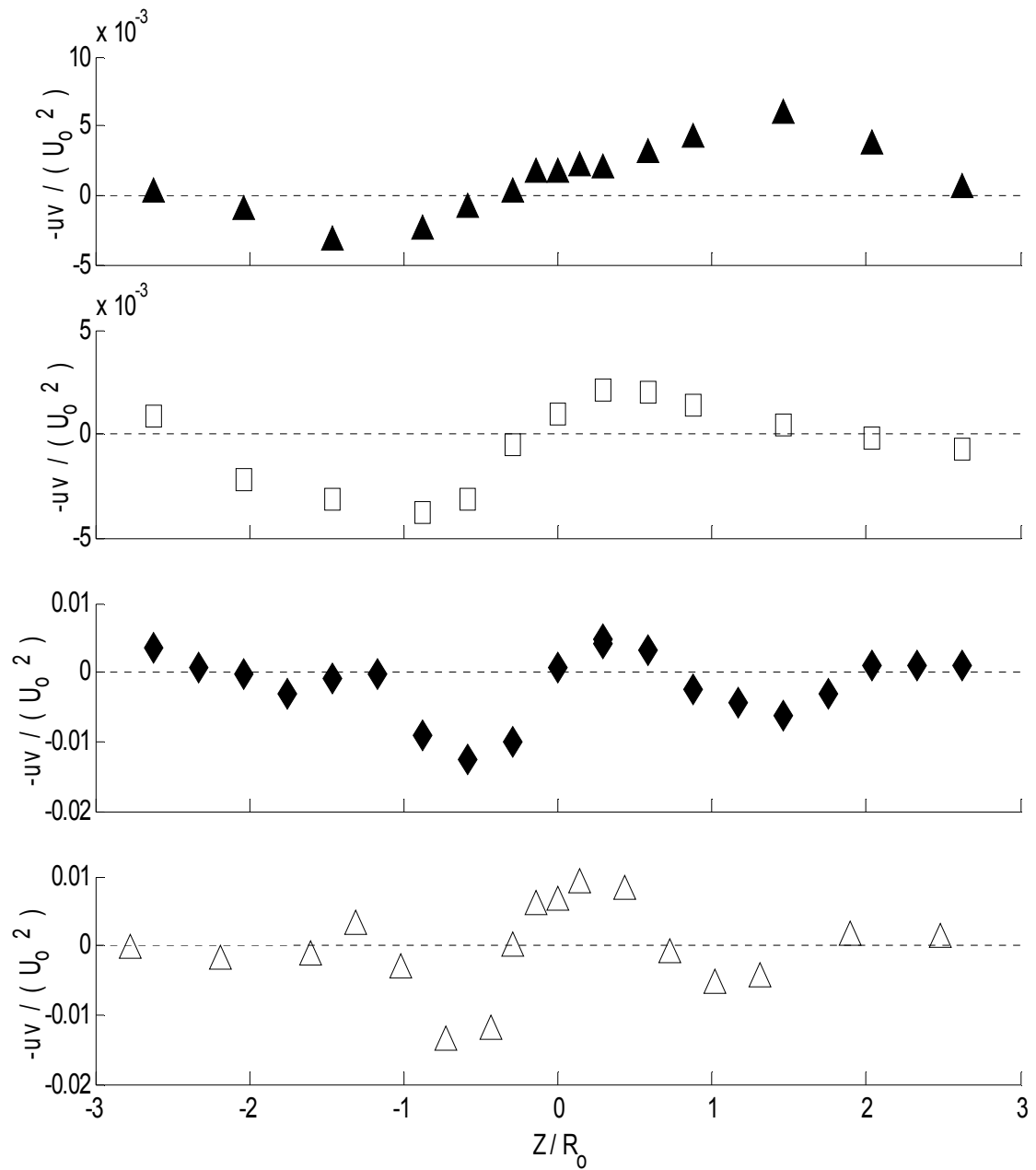


Figure 4.22 Z-Y plane ($Y/R_0 = 0$), Case 1 Reacting Reynolds Shear Stress, Legend see Table 4.3

To complete the study of the Case 1 reacting gas phase, similar aerodynamic measurements were made along the vertical center plane in the near nozzle region, the vortex bubble core, and outside of the exhaust constriction. The axial mean velocity profiles downstream, shown in Figure 4.23, show similar flow changes to the horizontal profiles shown above. The vortex bubble pinching associated with the flow expansion is evident, and further verified in Figure A.5, $X/R_o = 1.60$. Downstream, $X/R_o = 4.23$, the reacting recirculation region covers only half of the vertical center plane, compared with over 90% coverage in the non-reacting case. Similar to the horizontal center plane, the flow is nearly uniform and almost half of the bulk velocity beyond the exhaust contraction, as seen in Figure 4.23.

The Case 1 reacting vertical, or radial, mean velocity profiles along the vertical center plane are given in Figure 4.24. With reactions, the primary counter-swirl imparted at the fuel nozzle is evident, as is the significant fraction of mass expanding into the combustion chamber. At $X/R_o = 1.31$, the flow is nearly symmetric, with peak vertical velocities of order the bulk velocity. The counter-swirl imparted to the liquid phase has nearly disappeared from the reacting gas phase by $X/R_o = 1.60$, and has decayed completely by $X/R_o = 4.23$, in good agreement with Figure 4.20. Outside of the combustion chamber, $X/R_o = 22.16$, the reacting gas phase vertical velocity is less than zero across most of vertical plane, with clear evidence of the flow acceleration for $Y/R_o < 0$. The vertical mean velocity, however, is less than 5% of the bulk velocity, an order of magnitude smaller than the axial mean velocity. As such, the out flow conditions can be considered uniform and nearly two dimensional, determined by the bulk velocity and the secondary swirl characteristics.

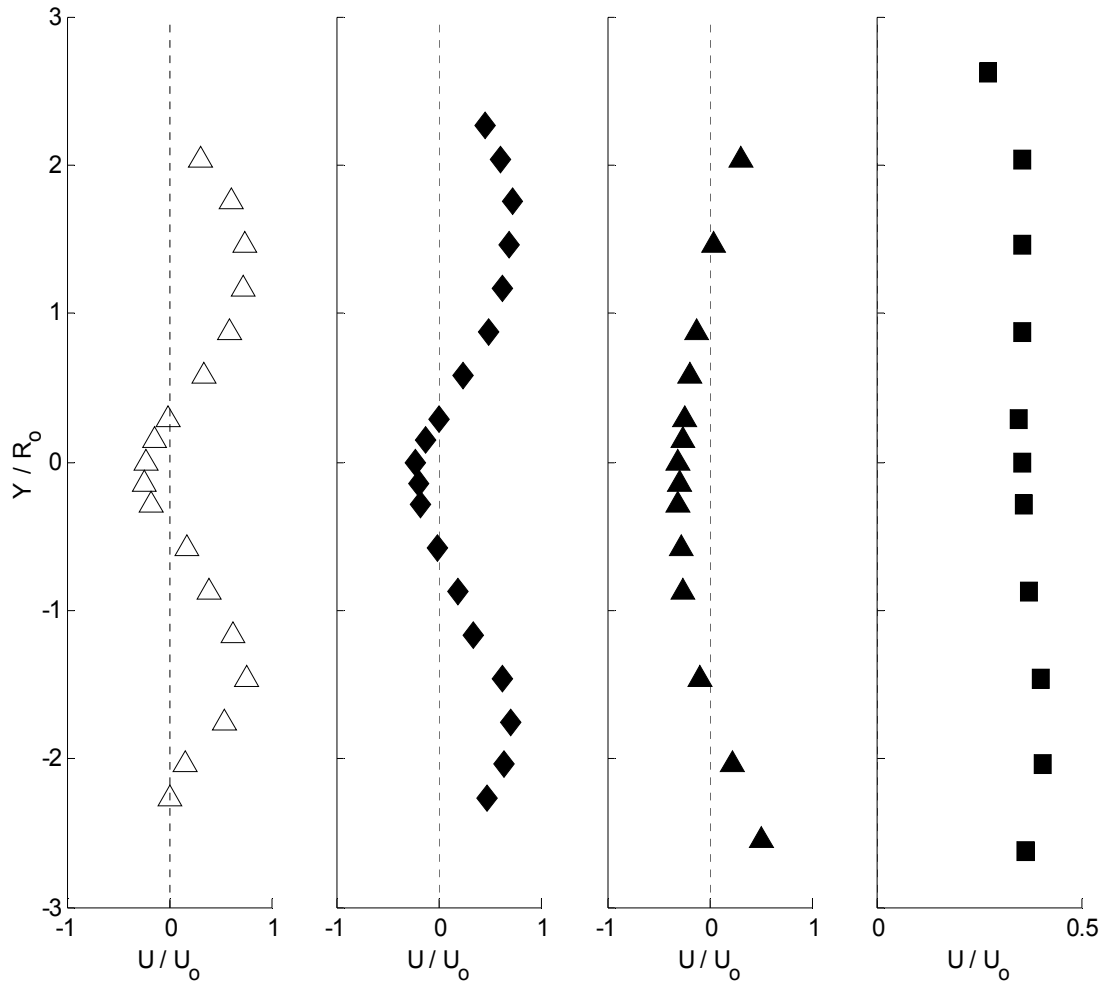


Figure 4. 23 Z-Y plane ($Z/R_0 = 0$), Case 1 Reacting Axial Mean Velocity, Legend see Table 4.3

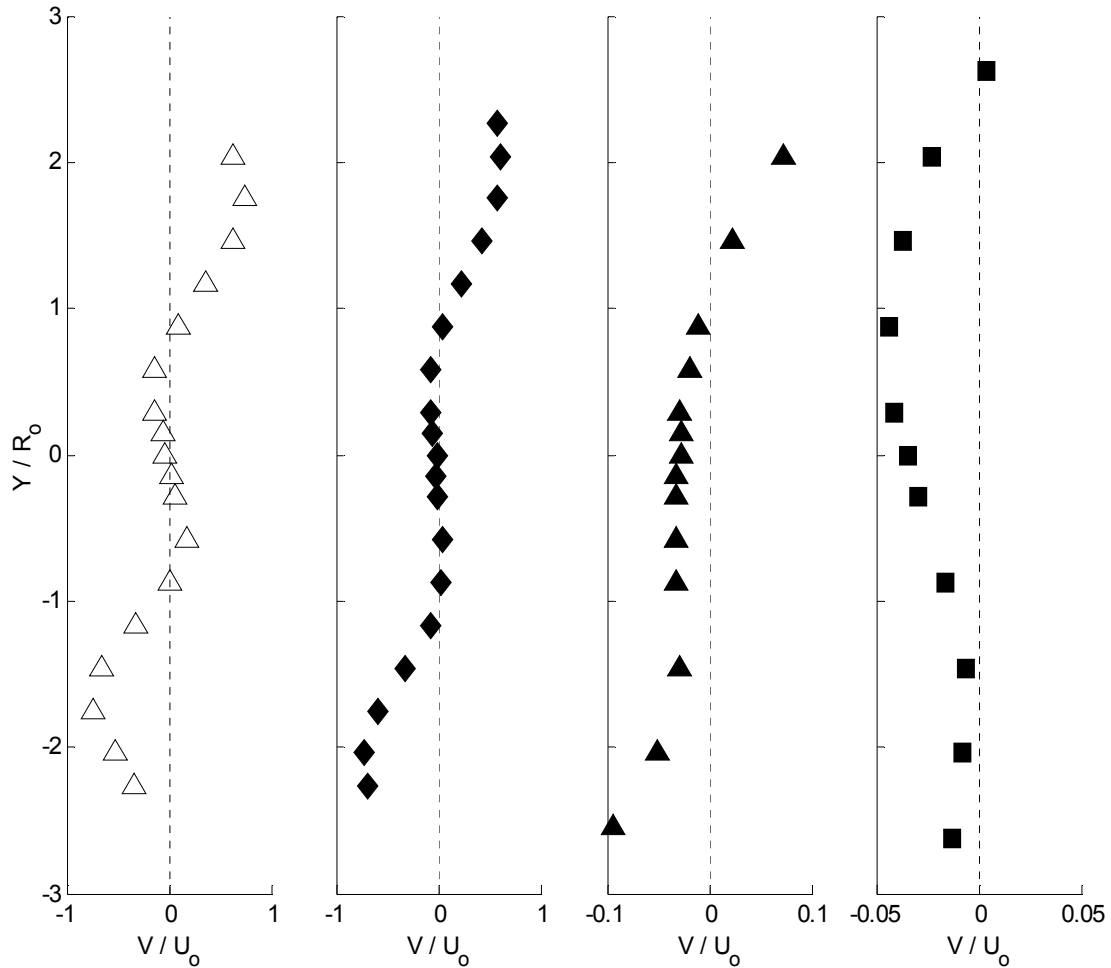


Figure 4.24 Z-Y plane ($Z/R_0 = 0$), Case 1 Reacting Vertical Mean Velocity, Legend see Table 4.3

The Case 1 reacting 2-D TKE profiles along the vertical center plane are given in Figure 4.25, which, unlike the mean profiles, show significant asymmetry in the near nozzle region before decaying downstream. At $X/R_0 = 1.31$, uniform mixing in the X-Y plane is not expected, as the peak magnitude is reduced and shifted towards the flow core for $Y/R_0 > 0$. With the addition of the liquid phase and reactions, the influence of the upper wall is more pronounced. As the reacting flow field does not have sufficient space to expand, the vortex breakdown bubble is confined towards the combustor centerline. The mixing effectiveness may be reduced as a result since the shear layer is no longer coincident with the design spray geometry, shown in Figure A.7. The asymmetry in the

vertical center plane continues to $X/R_o = 1.60$, where the active mixing of dilution air in the external recirculation zone drives the TKE generation for $Y/R_o < -1.5$. In the core of the reacting vortex breakdown bubble, $X/R_o = 4.23$, the available energy in the small scale velocity fluctuations is less than 5% of the bulk kinetic energy. As with the horizontal results, small scale mixing is no longer the dominant mechanism downstream. Instead, convection facilitates the transport of mass upstream. The exhaust gas measurements, $X/R_o = 22.16$, show very little turbulent energy in the vertical center plane, in good agreement with the previous discussion, Figure 4.21. The slight rise in TKE value for $|Y/R_o| > 2.5$ is due to the entrainment of laboratory air outside of the combustion chamber.

As with the non-reacting results above, the 2-D Reynolds shear stress, $-uv$, is presented for the Case 1 reacting gas phase with the vertical gradient of the axial mean velocity. If the turbulent viscosity hypothesis is correct, a positive scalar should correlate these two quantities. With the addition of heat, $-uv$ does not agree with the vertical mean velocity gradient, and, in fact, suggests a negative turbulent viscosity, seen in Figure 4.26. The substantial differences in behavior suggest that a gradient diffusion model may not capture the turbulent momentum transport in this combustor. Instead, the increase in the vertical gradient strength near $Y/R_o = 0$, shown in Figure A.9, and the addition of the liquid phase inhibits the diffusion of energy to the small scales in the near nozzle region. This result is consistent with Fig. 4.23; a rise in the transport of turbulent momentum coupled with a decrease in the dissipation. Figure 4.28 below provides a sketch of the reacting diffusion characteristics for improved understanding, with the non-reacting vortex breakdown bubble edge given for comparison.

To fully verify the validity of the turbulent viscosity hypothesis, the other component of the mean strain rate, dV/dx , should be examined. With the rapid decay of the primary swirl with evaporation and mixing, the gradient of the vertical velocity may be significant in the near nozzle region. Further, the magnitudes of all three velocity

components are expected to be of equal order and therefore, all three components of the shear stress, $-uv$, $-uw$, and $-vw$, will play significant roles in the exchange of turbulent momentum. As such, the correct choice of turbulence models in CFD codes is essential to accurately capture the mixing dynamics.

The Case 1 reacting flow field shows significant influence from the heat release associated with combustion. The volumetric expansion within the confined chamber increases the axial mean velocity magnitude significantly. The designed counter-swirl rotation is seen in the near nozzle reacting results, further evidence of the flow expansion with heat release, which decays rapidly into the secondary swirl downstream. Hot, radical rich combustion products are actively recirculated to the fuel nozzle where TKE and velocity gradients are maximized, enhancing the combustion process.

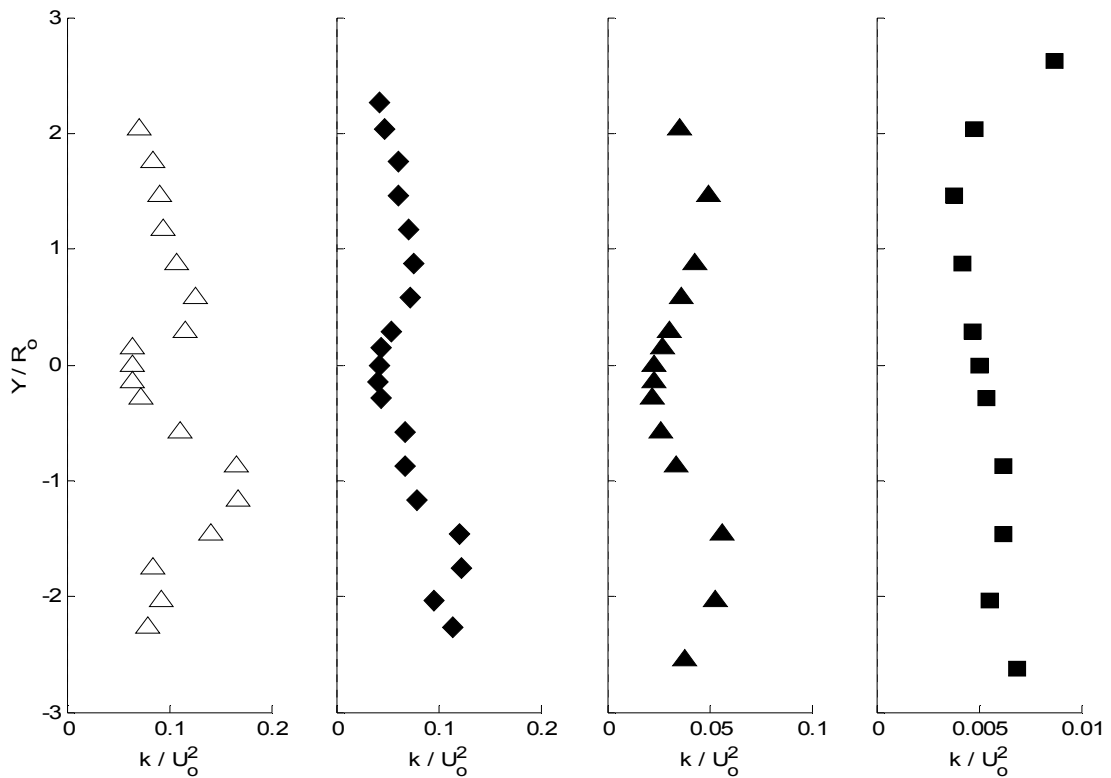


Figure 4.25 Z-Y plane ($Z/R_0 = 0$), Case 1 Reacting Turbulent Kinetic Energy, Legend see Table 4.3

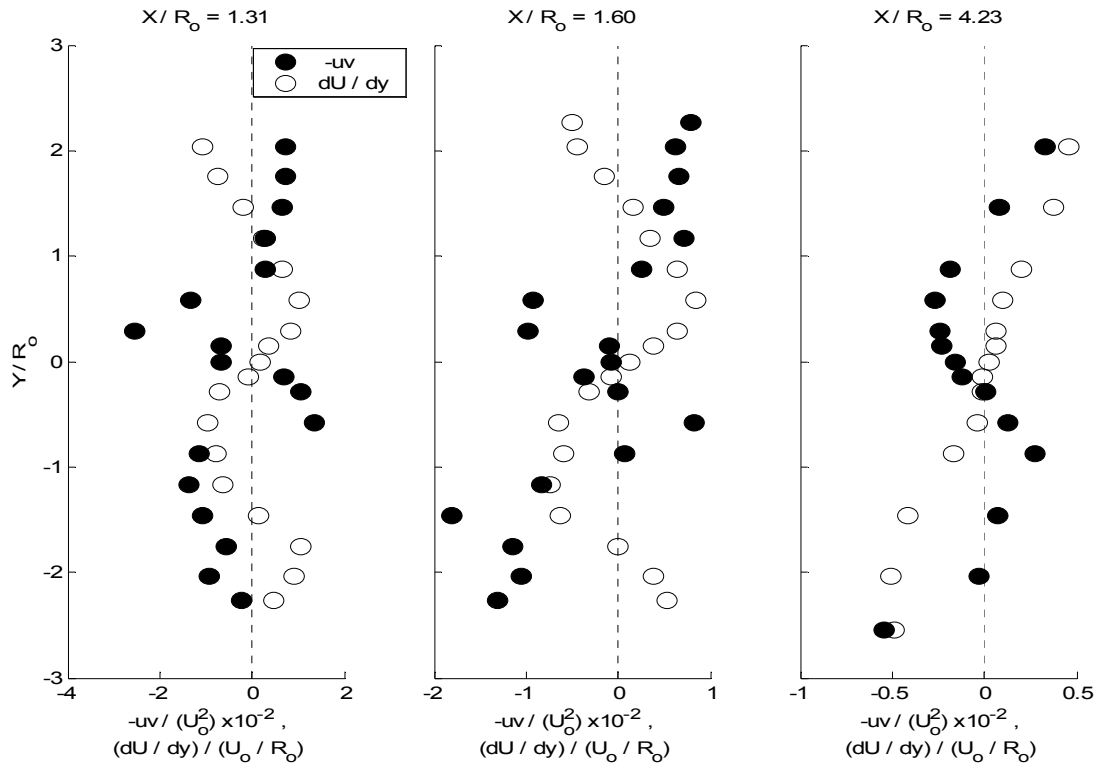


Figure 4.26 Z-Y plane ($Z/R_0 = 0$), Case 1 Reacting Reynolds Shear Stress and Axial Mean Velocity Vertical Gradient

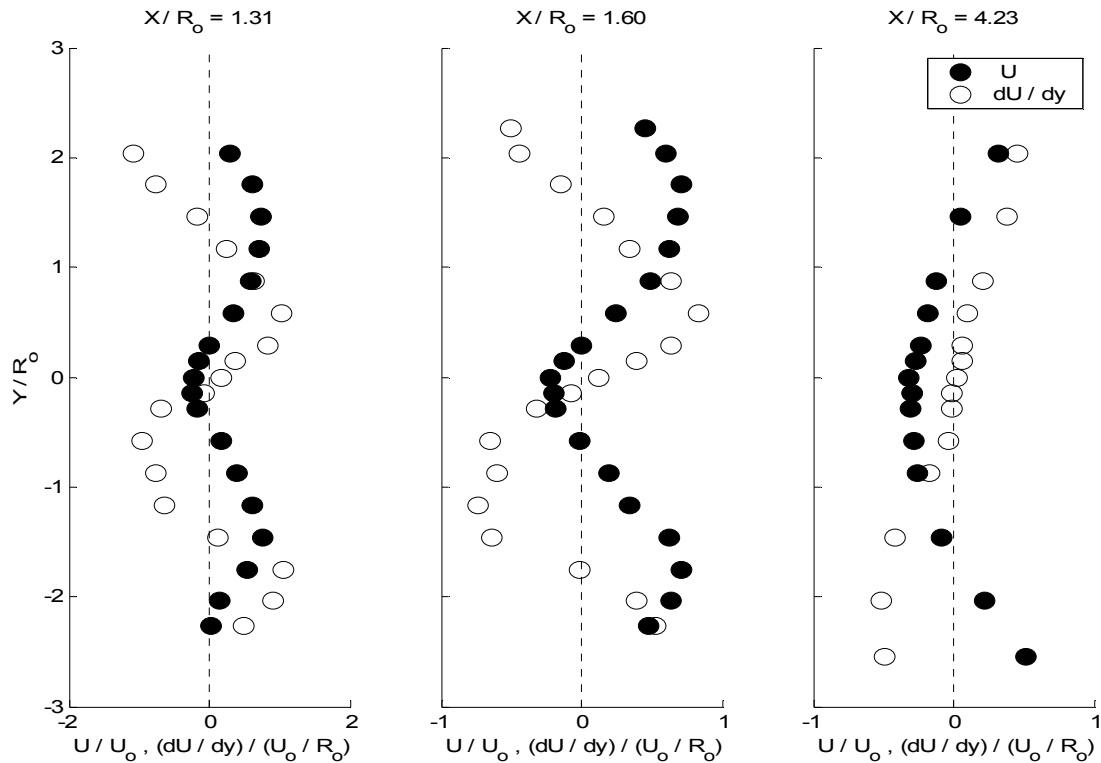


Figure 4.27 Z-Y plane ($Z/R_0 = 0$), Case 1 Reacting Axial Mean Velocity and Vertical Gradient

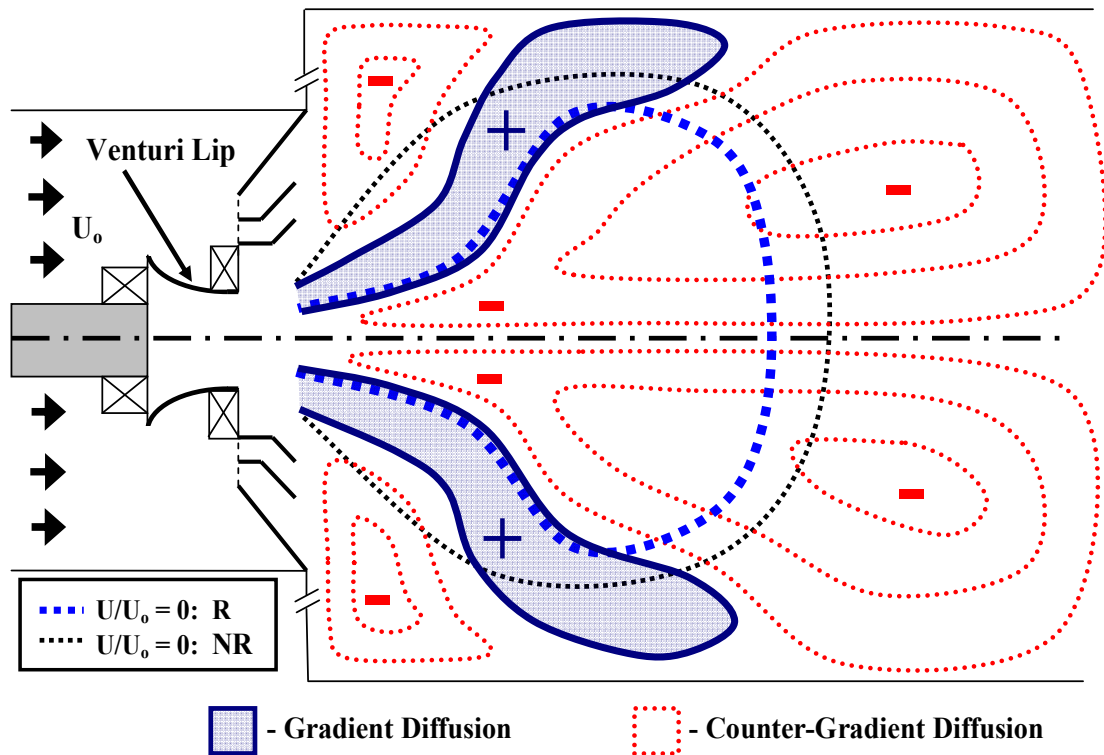


Figure 4. 28 Schematic of the Reacting Gas Phase Diffusion Characteristics

Case 2

To examine the influence of a new fuel nozzle at increased fuel pressure on the lean combusting flow field, the reacting axial mean and RMS velocity for Case 2 are presented along the combustor centerline downstream in Figures 4.29 and 4.30. As demonstrated in a previous section, the non-reacting flow field is unaffected by an increase in inlet air mass flow rate (or pressure drop across the swirler). As such, any changes seen in the Case 2 reacting flow field can be attributed to the both the increase in fuel pressure (or fuel flow rate) and the difference in fuel nozzle rated spray angles. Given the similar proximity to the measured lean blow-out, the effects of equivalence ratio variation are neglected in the following analysis.

The Case 2 reacting axial mean velocity along the combustor centerline, Figure 4.29, agrees well with the previous discussion of the Case 1 reacting axial mean velocity. The addition of heat with combustion changes the length and intensity of the vortex break

down bubble significantly, as expected. The rear stagnation point is shifted to $X/R_o \sim 7.5$, further upstream than that of Case 1, Figure 4.17. As the mass flow rate of fuel is increased, the energy available for flow expansion is increased as well, and the recirculation region is further pinched as the flux of axial momentum is increased with combustion [12]. The core strength of the recirculating region is increased in Case 2 as well, with recirculating velocities nearly 50% of the bulk velocity. While the core recirculation strength did increase slightly with increased air loading, Figure 4.1, this does not account for the large velocity increase seen between Case 1, Figure 4.17, and Case 2, Figure 4.29. Instead, the rise in fuel mass flow rate at increased thermal load is responsible for the increased recirculation strength. Thus, as more fuel is available for combustion, the volumetric expansion from heat release constricts the central vortex break down bubble, necessarily increasing the core recirculation strength.

The axial RMS distribution along the combustor centerline shows similar trends in Case 2, Figure 4.30, as those presented for Case 1, Figure 4.18. Most importantly, the active mixing of hot products with unburned fuel/air, and the resulting heat release, is seen in the rise of RMS velocity for $X/R_o < 5$. The characteristics of this mixing, however, are different at elevated fuel pressure. For Case 2, the peak RMS is located at $X/R_o = 1.31$, followed by a rapid drop in the RMS value and the subsequent decay downstream. This behavior does not agree with Case 1, Figure 4.18, where the peak RMS at $X/R_o = 1.31$ is seen to decay less rapidly in the near nozzle region. By $X/R_o = 5$, the two cases agree quite well and decay with similar roll-off characteristics. The flow field for $X/R_o < 5$ gives significant insight into the spray behavior for both cases. At low fuel pressure, Case 1, poor spray performance allows droplets to convect through the primary swirl and mix in the near nozzle region. With an increase in fuel pressure, Case 2, the improved hollow cone spray is confined by the primary swirl and droplets are unable to penetrate the core recirculation region. As a result, the Case 2 flow field shows less total RMS velocity along the combustor centerline and increased recirculation

strengths in the near nozzle region. Thus, the dynamics of the two phase interactions in the near nozzle region are of extreme importance.

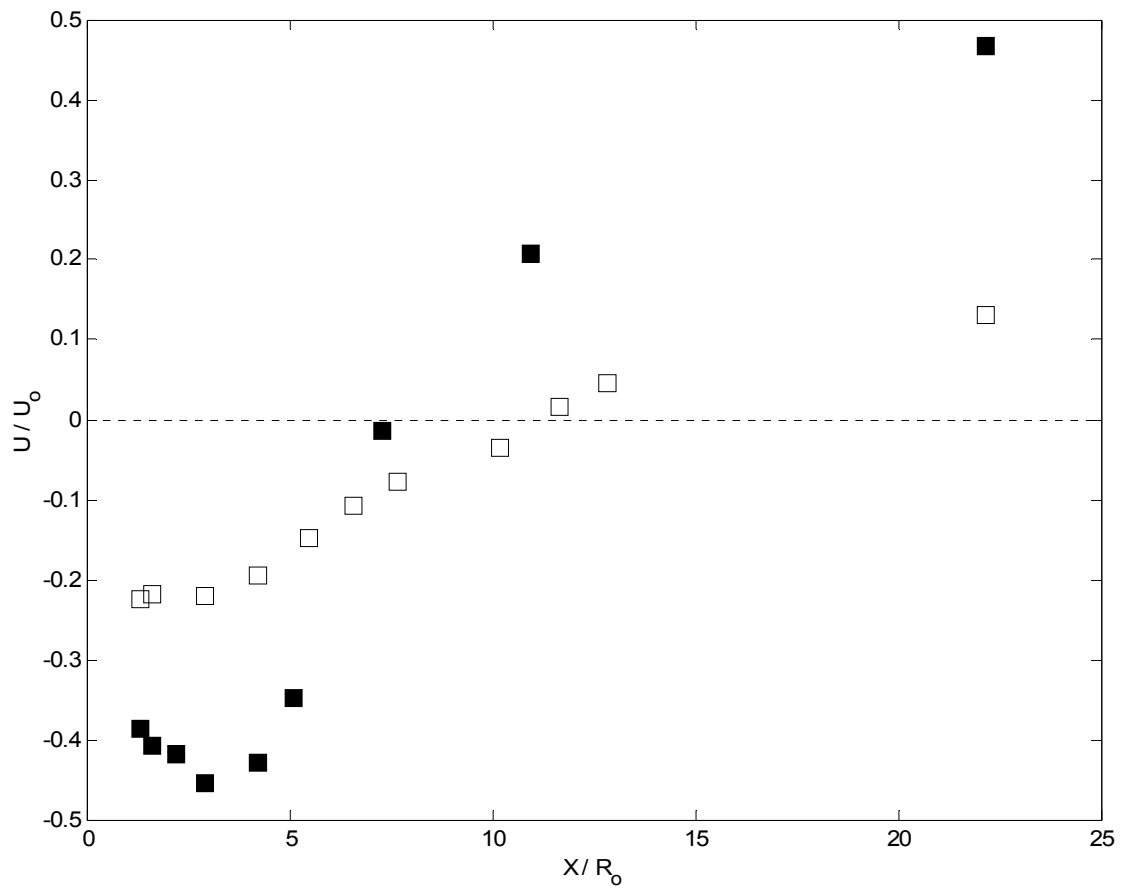


Figure 4. 29 Gas Phase Axial Mean Velocity Downstream Centerline Case 2, Non-Reacting (hollow symbols), Reacting (solid symbols)

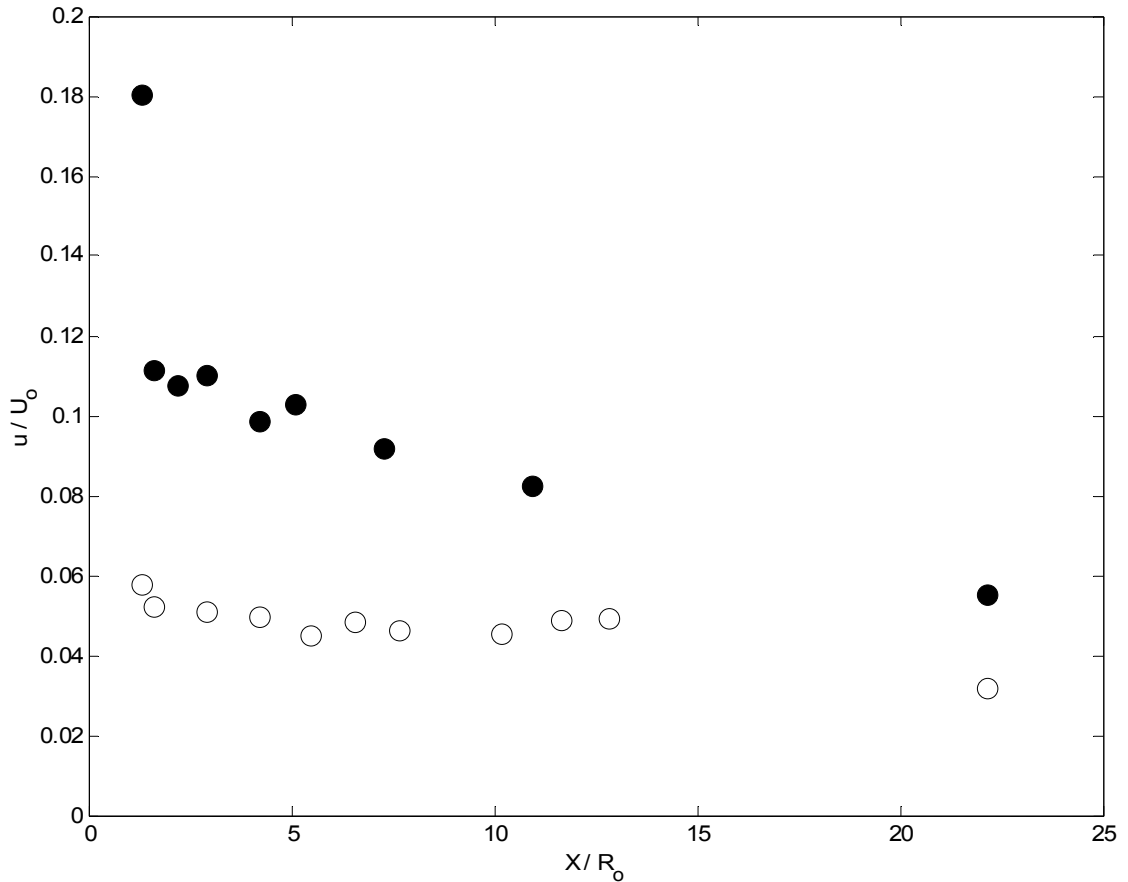


Figure 4.30 Gas Phase Axial RMS Velocity Downstream Centerline Case 2, Non-Reacting (hollow symbols), Reacting (solid symbols)

To further quantify the effects of fuel pressure and nozzle performance on the reacting flow field, the Case 2 axial and vertical mean velocity profiles along the horizontal center plane are given in Figures 4.31 and 4.32. These measurements were made at similar locations downstream, Table 4.3, but a direct comparison with Case 1 results is not given. Figures A.10 and A.11 present the reacting gas phase mean velocity with the non-reacting gas phase for comparison, with a focus on the near nozzle region.

At elevated fuel pressures, Case 2, the improvement in spray characteristics plays an important role in the reacting flow field. It is possible that the fuel droplets do not convect through the main recirculation region because the width of this region is significantly larger than that of Case 1, Figure 4.19, especially downstream of $X/R_0 = 1.61$. Instead, droplets in the hollow cone may be confined to the flow periphery with

increased momentum and swirl. Without droplets in the vortex bubble core, the flame stabilization mechanism is improved. Without drag from the axially injected droplets, the recirculation strength is improved in the near nozzle region, seen in Figure 4.29 as well. With the containment of droplets likely to be outside of the vortex break down bubble, a more controlled flame front is achieved. As such, the residence times are similar for droplets across the combustor, and more symmetric burning can be expected. While this is expected to improve emission levels significantly, the improvement in burning also leads to an increase in expansion downstream. As a result, the core strength and width of the vortex bubble are increased relative to Case 1. At $X/R_o = 4.23$, Figure 4.31, the recirculating velocity extends nearly four nozzle radii across the combustor and shows significant asymmetry.

The vertical mean velocity profiles downstream, Figure 4.32, show similar trends as seen in Case 1. However, with the reduction in droplets convecting through the spray core, the increase in the reacting radial momentum is substantial. At $X/R_o = 1.31$, the primary counter-swirl design is clearly visible for $Z/R_o < 0$, Figure 4.32, while the asymmetry seen in the Case 1 reacting gas phase results, Figure 4.20, is still present. Beyond $X/R_o = 1.60$, the two reacting flow fields are almost identical. The primary swirl imparted to the droplets is damped rapidly downstream as the liquid phase evaporates; as a result, the downstream flow field is dominated by the secondary swirl imparted to the gas phase in the flow periphery.

A comparison of the vertical mean velocity magnitudes between Figure 4.32, Case 2, and Figure 4.20, Case 1, reveals the improvement in spray performance at elevated fuel pressures. Throughout the combustor, the normalized Case 2 vertical mean velocities are larger, possibly a result of the increased heat release at a slightly higher equivalence ratio. This also implies, however, that a smaller fraction of the initial droplet momentum was in the axial direction, as more momentum is present in the swirl component. Thus, the primary atomization and swirl may have been successful in

confining the liquid phase to the venturi lip, where the secondary atomization ensured proper confinement in the external flow. This improvement in spray behavior would in turn improve the recirculating capacity, which would improve the flame holding characteristics through more efficient preheating. Thus, the confinement of the droplet phase outside of the vortex break down bubble is a key factor in efficient mixing, burning, and stabilization.

It is worth noting the lack of data in the near nozzle region for $|Z/R_o| > 2$, Case 2; seen in both Figures 4.31 and 4.32. While some seed particles were present in these regions, the rapid expansion aforementioned prevented seed particles from tracking the flow. As such, few particles were able to reach the corner recirculation regions as the flow accelerated, instead convecting downstream with the main expansion of hot combustion products.

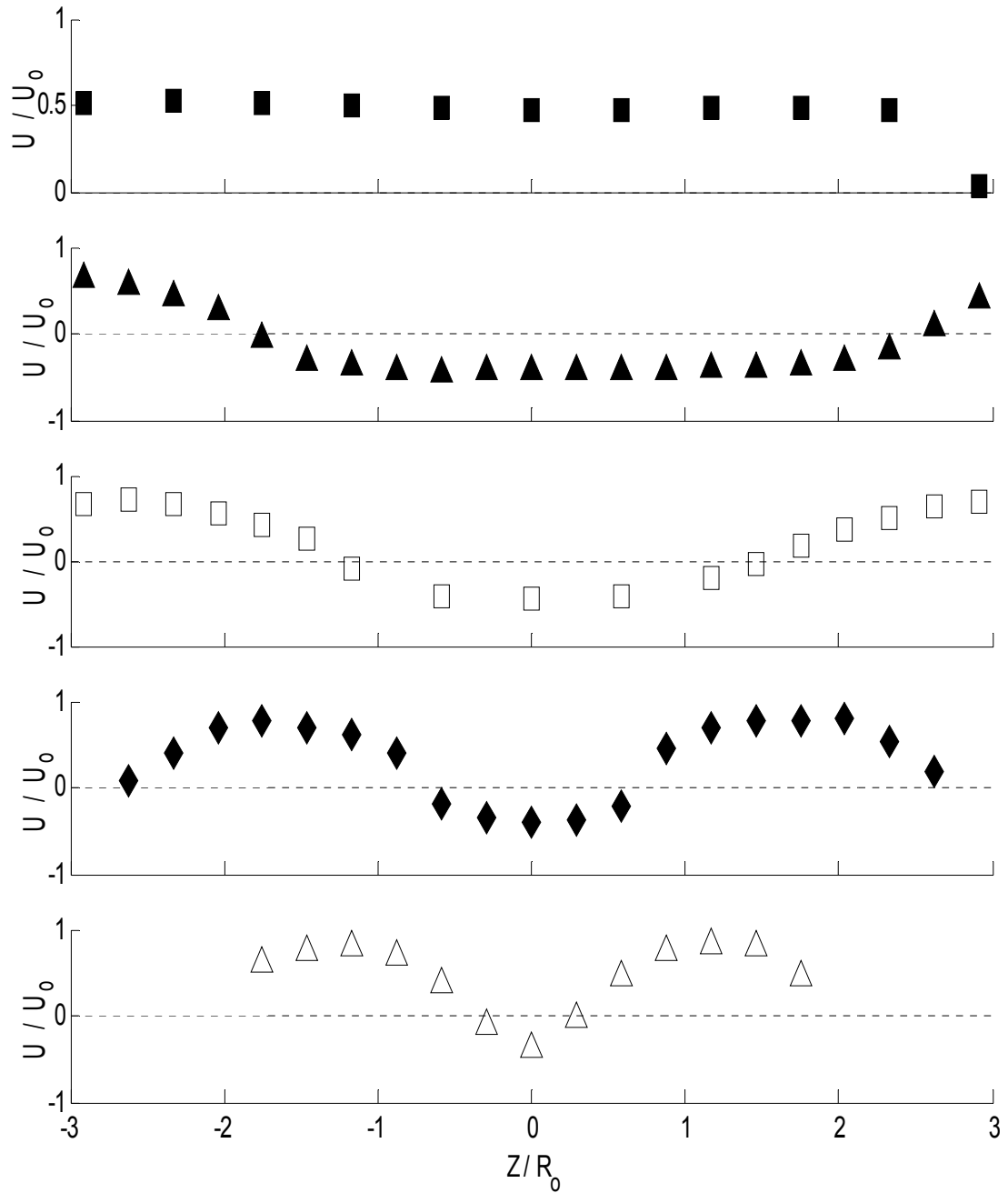


Figure 4. 31 Z-Y plane ($Y/R_0 = 0$), Case 2 Reacting Axial Mean Velocity, Legend see Table 4.3

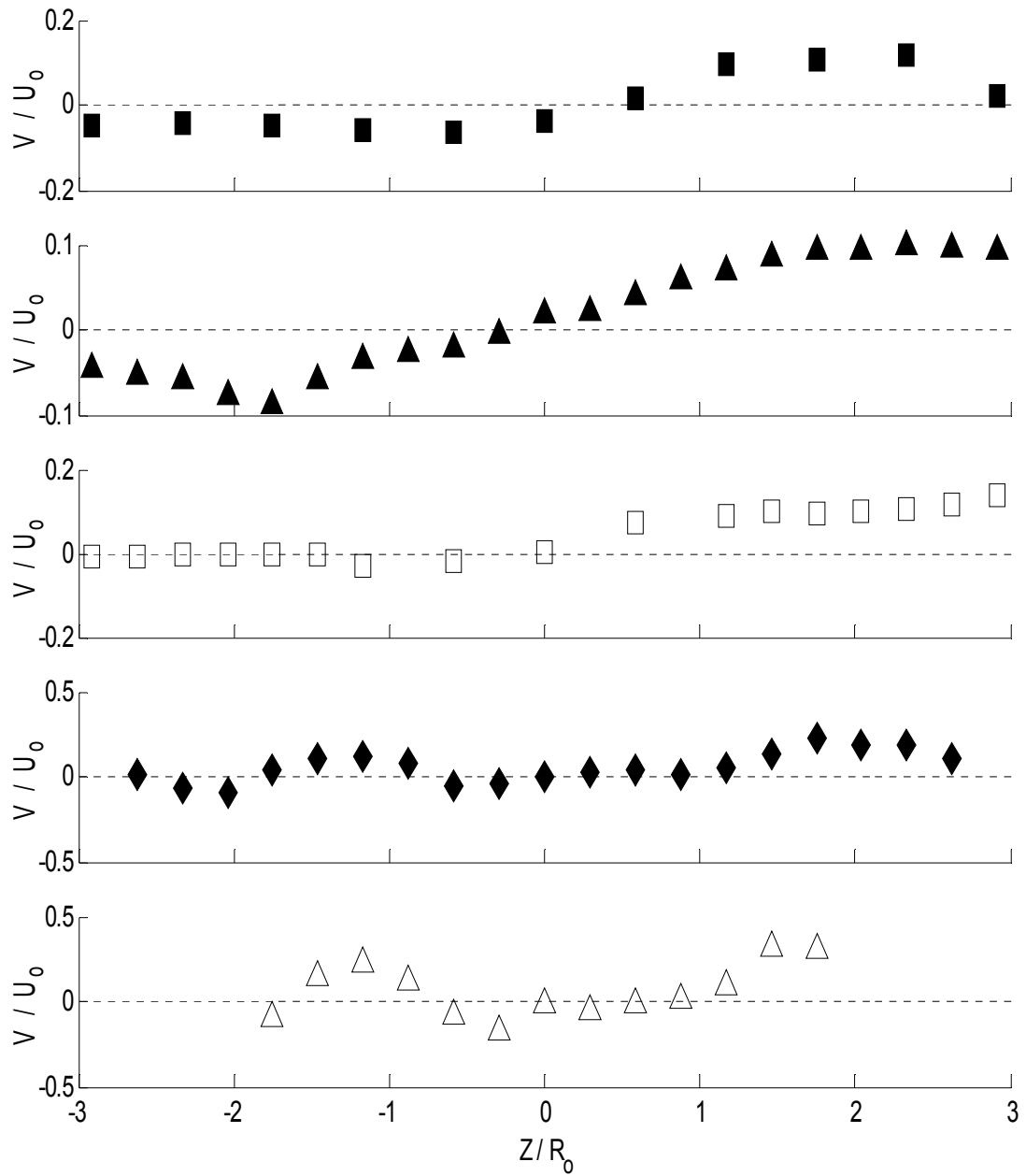


Figure 4.32 Z-Y plane ($Y/R_0 = 0$), Case 2 Reacting Vertical Mean Velocity, Legend see Table 4.3

The Case 2 reacting 2-D TKE and Reynolds shear stress, given in Equations 4.1 and 4.2, are presented in Figures 4.33 and 4.34. These turbulent quantities differ significantly from the Case 1 reacting results. Most importantly, the TKE does not show any of the spreading associated with the active mixing of droplets across the combustor. Instead, the TKE is distributed in two peaks which spread downstream non-

symmetrically. These peaks correspond to the edge of the vortex break down bubble, which is pinched closed with combustion, as mentioned above and seen clearly in Figures A.10 and A.12. Another important distinction in the Case 2 TKE results is that the core stability of the vortex break down bubble remains intact with the addition of reactions. As such, the convection of hot gases from downstream is improved, and the main stabilization mechanism is enhanced. Without droplets in the vortex core, large scale advective mixing continues to supply radicals and hot products to the incoming non-premixed fuel/air mixture. These hot products serve to reduce the evaporation and ignition delay times, as well as to initiate simple branching steps in the chemical conversion of the long chain hydro-carbon towards the more familiar combustion products. Beyond $X/R_0 \sim 4$, the TKE is seen to decay rapidly as expected [6], finally reaching nearly uniform exhaust values of less than 1% of the bulk kinetic energy. Thus, the Case 2 reacting mixture field is dominated by the secondary/primary swirl interface.

The reacting gas phase 2-D Reynolds shear stress, $-uv$, is presented along the horizontal center plane downstream of the fuel nozzle in Figure 4.34 for Case 2. It is important to note the change in shear stress distribution downstream with increasing fuel flow in the combustor. As in Case 1, the counter-swirling nature of the flow is apparent at $X/R_0 = 1.31$ and 1.60 . The normalized shear stress changes sign twice on each side of the combustor, in good agreement with the axial and vertical mean velocities. Downstream, $X/R_0 = 2.92$ and 4.23 , the Case 2 shear stress distribution do not agree well with the results shown in Figure 4.22. With the increase in combustor loading, the increased axial gas phase momentum is evident. The shear stress distribution does not decay as rapidly; the peak magnitudes of the normalized shear stress are larger across the horizontal center plane downstream. The reacting shear stress measurements at $X/R_0 = 22.16$, not presented for the Case 1 results, suggest that the far field mixing dynamics are different with and without reactions, Figure A.13.

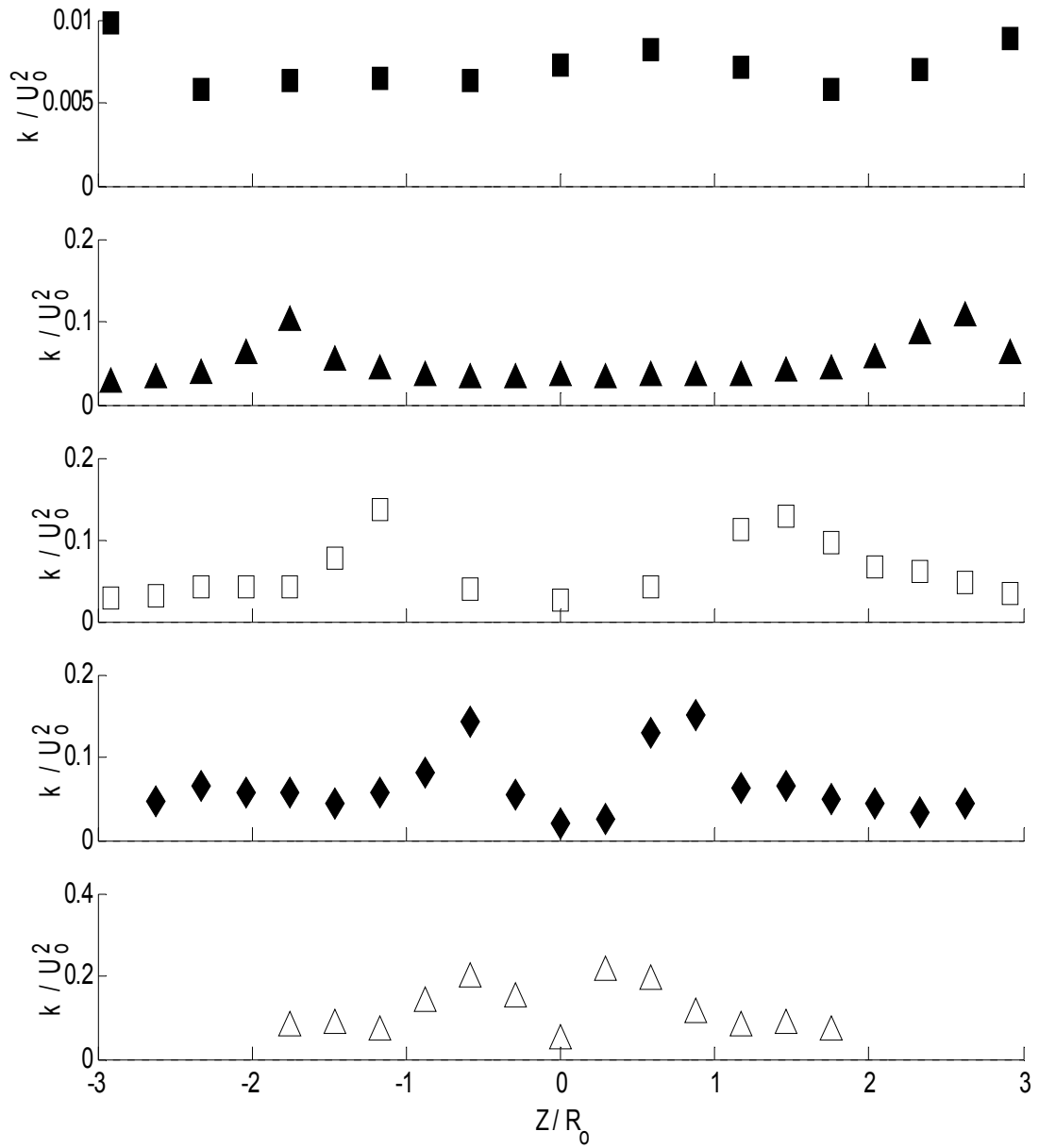


Figure 4. 33 Z-Y plane ($Y/R_0 = 0$), Case 2 Reacting Turbulent Kinetic Energy, Legend see Table 4.3

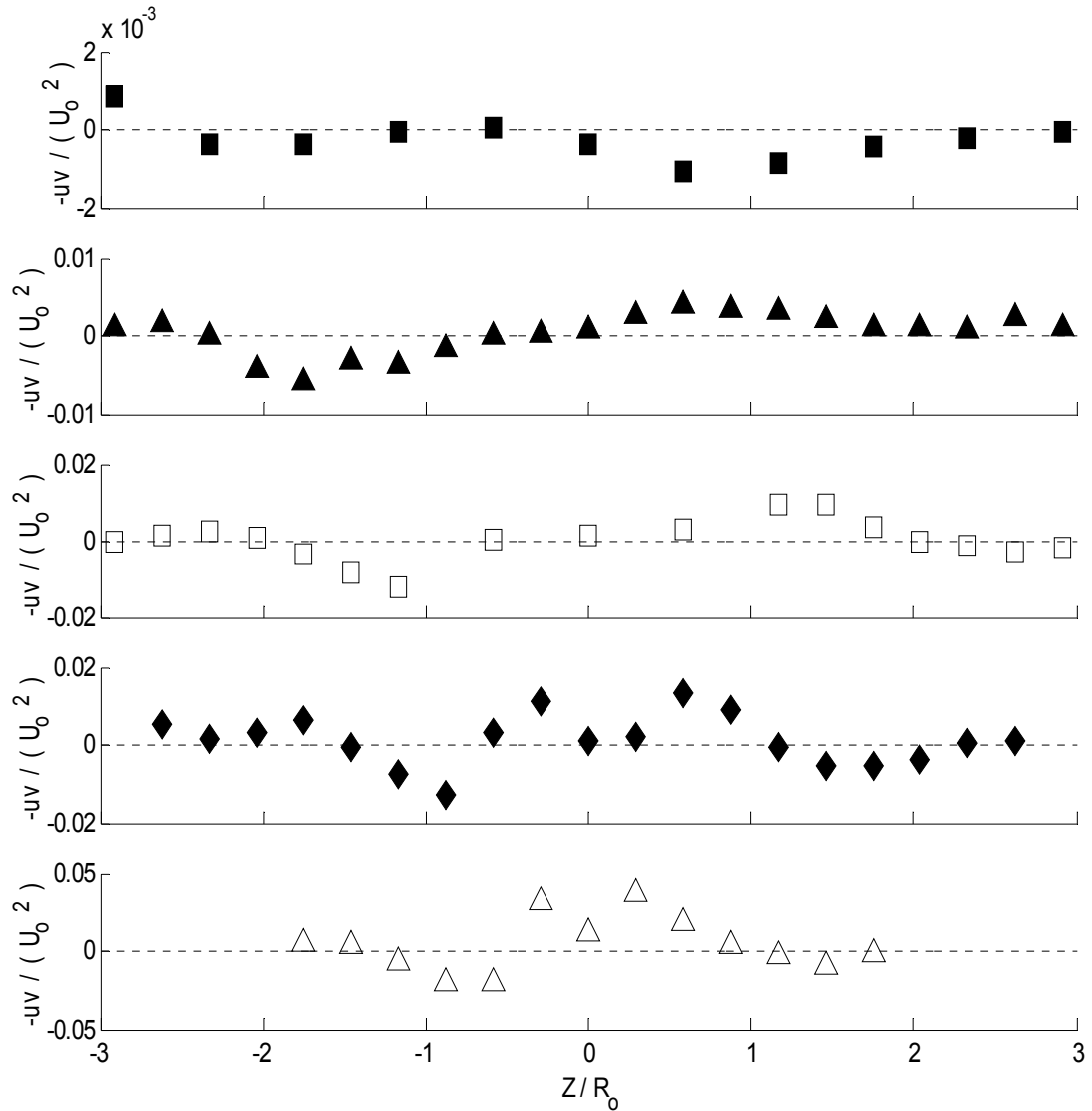


Figure 4.34 Z-Y plane ($Y/R_0 = 0$), Case 2 Reacting Reynolds Shear Stress, Legend see Table 4.3

To complete the analysis of the Case 2 reacting flow field, the 2-D mean and turbulent properties in the vertical center plane are presented at two locations downstream, $X/R_0 = 1.60$ and 4.23 . The vertical gradient of the axial mean velocity is presented for comparison with the Reynolds shear stress to further address the validity of the gradient diffusion model.

The impact of the upper wall on the axial mean velocity is clear at $X/R_0 = 1.60$, Figure 4.35. The vortex bubble is pinched significantly for $Y/R_0 > 0$ as the location of

the peak velocity magnitude is shifted toward the combustor centerline. Further, the total recirculation is reduced as the expansion is limited by the combustion chamber. Analysis of the vertical mean velocity, Figure 4.36, confirms the shift of the vortex break down bubble relative to the combustor centerline at $X/R_o = 1.60$. While the primary counter-swirl is clear, the axis of rotation is displaced $\sim 25\%$ of the effective fuel nozzle radius, in good agreement with the center of recirculation in Figure 4.35. Downstream, the reacting vertical mean velocity is entirely positive, however, the vertical component is less than 4% of the bulk velocity and may be a result of the displacement of the vortex core about the centerline.

These results suggest that with increased fuel pressure and combustor load, interactions between the reacting gas phase and the combustor liner may become increasingly important. As more fuel is available to drive the flow expansion, the liner, and even adjacent flames, may constrict the flow in a similar manner. Such constrictions would lead to the non-symmetric vortex pinching and recirculation reduction seen below, and may have a large impact on the decrease in lean blow-out limit at elevated fuel pressures, seen in Table 4.2. These complex interactions may also lead to significant temperature and emission asymmetries.

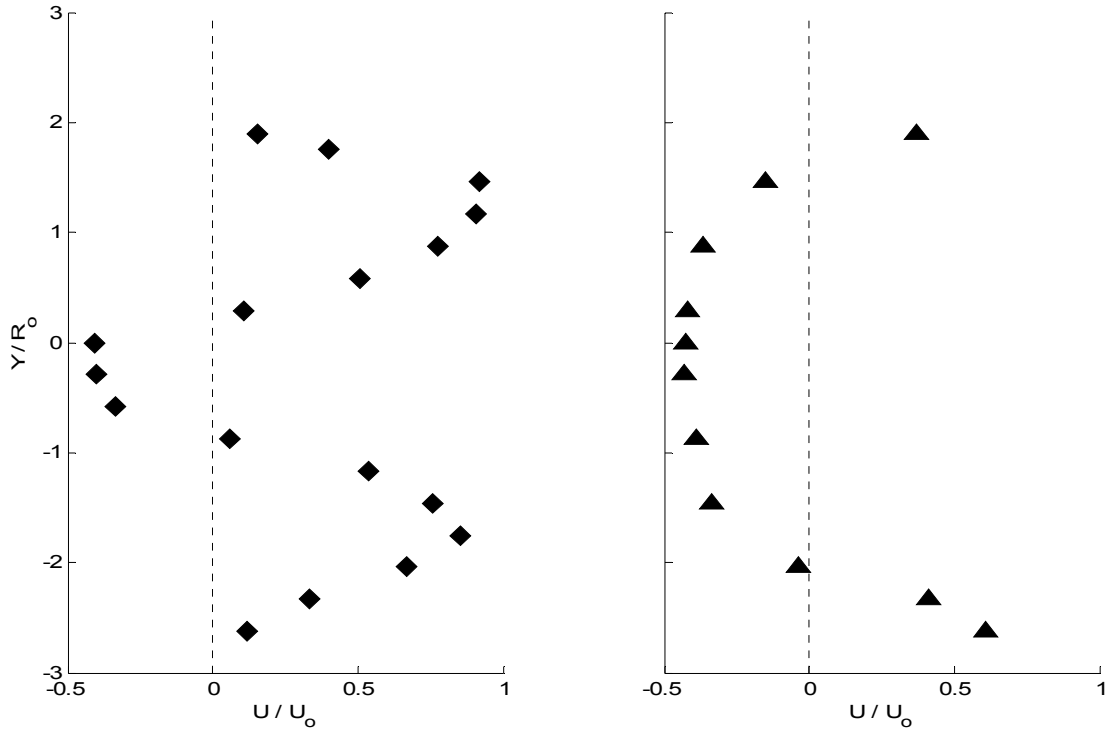


Figure 4.35 Z-Y plane ($Z/R_0 = 0$), Case 2 Reacting Axial Mean Velocity, Legend see Table 4.3

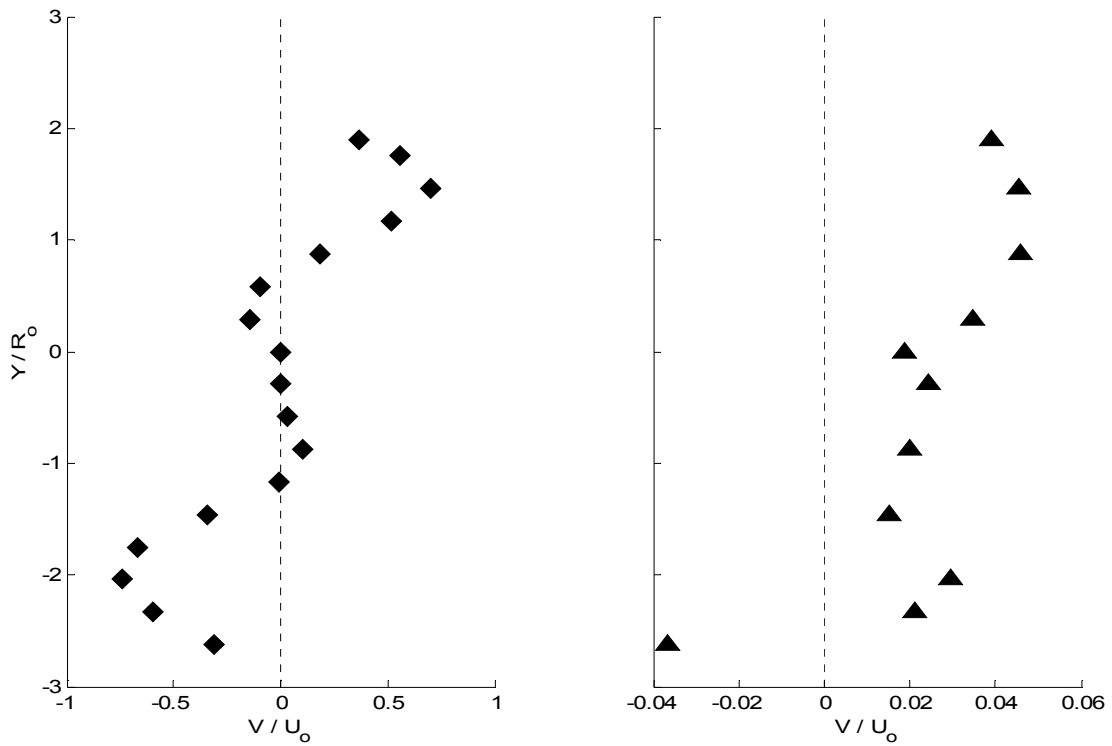


Figure 4.36 Z-Y plane ($Z/R_0 = 0$), Case 2 Reacting Vertical Mean Velocity, Legend see Table 4.3

The 2-D reacting TKE measurements, Figure 4.37, highlight the impact of the upper wall on the turbulence generation in the vertical center plane. The peak in the TKE is shifted towards $Y/R_0 = 0.25$ at $X/R_0 = 1.60$, while the second peak is seen at $Y/R_0 = -1$. These results do not agree with the horizontal center plane, where the peaks are centered at $Y/R_0 = 0.75$ and -0.5 , Figure 4.33. Thus, the asymmetric cross-section of the combustor plays a significant role in the near nozzle reacting flow field. As with Case 1, the effect of the dilution cooling is seen in the increased TKE for $Y/R_0 < -2$. Further downstream, $X/R_0 = 4.23$, the flow shows improved core stability and more uniform mixing. Better agreement is also seen between the horizontal and vertical center planes, evidence of the mixing quality well downstream of the nozzle.

To further understand the reacting mixture field for Case 2, the 2-D Reynolds shear stress, $-uv$, is presented along the vertical center plane in Figure 4.38, with the vertical gradient of the axial mean velocity for comparison. As in Case 1, the counter-swirling nature of the flow is apparent at $X/R_0 = 1.60$. The normalized shear stress changes sign twice on each side of the combustor, in good agreement with the axial and vertical mean velocities. At these locations, the axial mean velocity gradients are maximized, Figure 4.39, and the shear stress magnitudes are maximized as well, Figure 4.38. Downstream, $X/R_0 = 4.23$, the Case 2 shear stress distribution agrees well with the results shown in Figure 4.26 and the diffusion characteristics shown in Figure 4.28. These results confirm that a simple turbulent viscosity hypothesis may not be applicable for the swirling, reacting flow field presented. While the axial gradient of the vertical mean velocity should first be included, it is evident that a single, passive scalar may not correlate the Reynolds shear stress and the mean strain rate adequately.

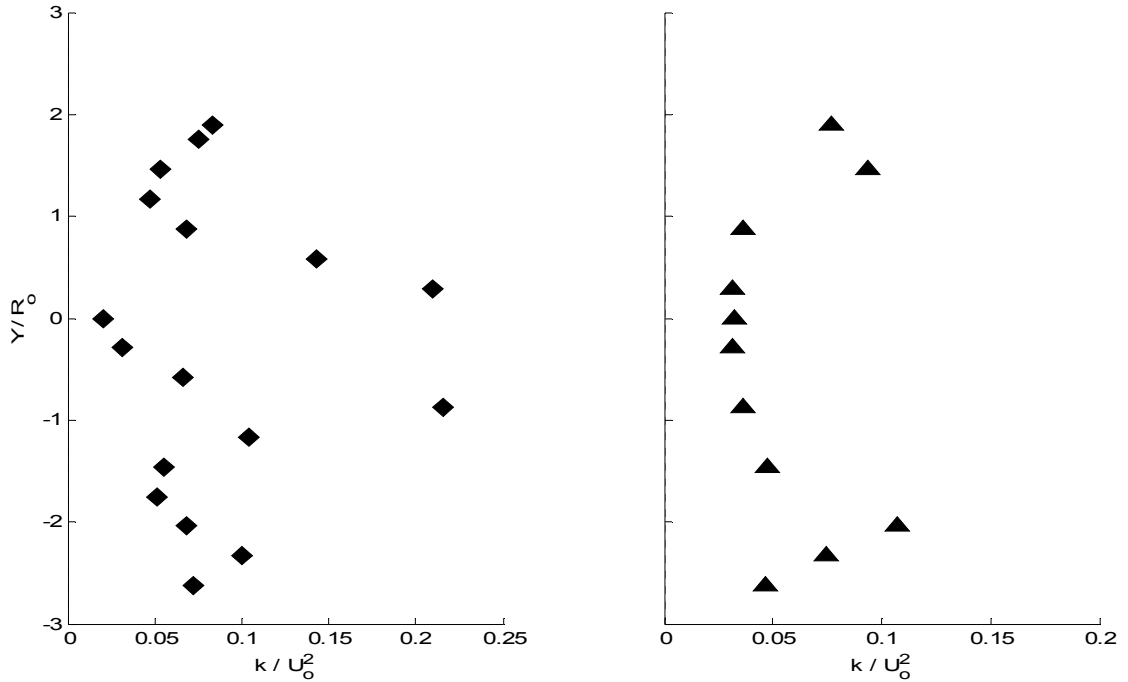


Figure 4.37 Z-Y plane ($Z/R_0 = 0$), Case 2 Reacting Turbulent Kinetic Energy, Legend see Table 4.3

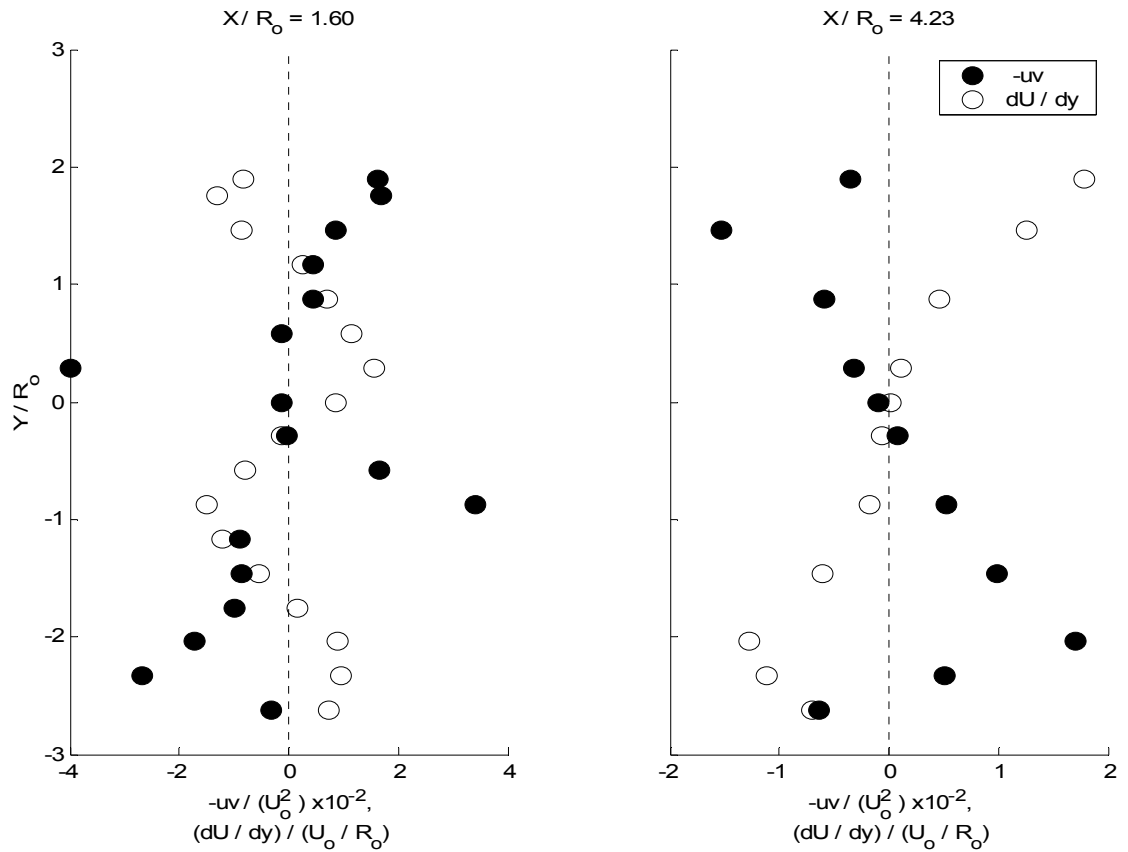


Figure 4.38 Z-Y plane ($Z/R_0 = 0$), Case 2 Reacting Reynolds Shear Stress and Axial Mean Velocity Vertical Gradient

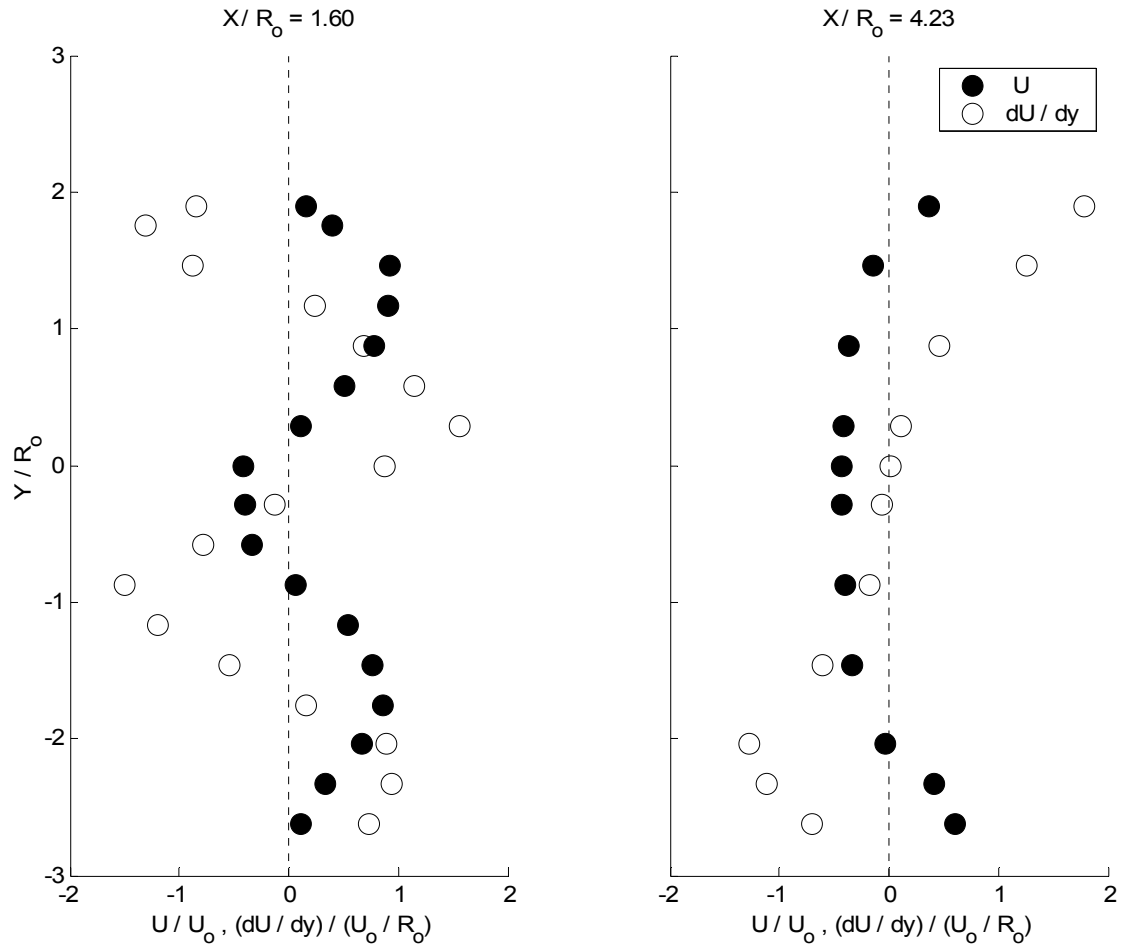


Figure 4.39 Z-Y plane ($Z/R_0 = 0$), Case 2 Reacting Axial Mean Velocity and Vertical Gradient

Liquid Phase

Both the non-reacting and the reacting droplet dynamics were examined using the TSI PDPA system described above. For all liquid phase results shown, the flow was not seeded and measurements were made throughout the near-injector region where the data rate exceeded 50 Hz. To identify the changes in droplet statistics with the addition of heat in the combustion chamber, the Case 1 non-reacting and reacting droplet distributions are given at various locations across the horizontal combustor centerline at $X/R_0 = 1.60$. The calculated mass mean diameter and Sauter mean diameter are presented for the non-reacting and the reacting droplet distributions, as well as the associated

droplet aerodynamic measurements. Contour plots of the Case 1 reacting droplet diameters in the horizontal center plane downstream of the nozzle highlight the liquid phase distribution in the combustion chamber. To identify the changes in droplet statistics with the second nozzle at increased fuel pressure, the Case 2 reacting droplet distributions are presented at $X/R_0 = 1.60$. The calculated mass mean diameter and SMD are also included. In all of the droplet measurement contour plots presented, the large white portion downstream is a region where few to no droplets are found, due mainly to the hollow cone nature of the spray and the large residence times associated with recirculation. Most, if not all, droplets have evaporated and burned before being recirculated, thus ensuring the stabilization mechanism of hot combustion products convecting upstream.

Case 1

The normalized droplet distributions at six locations across the combustion chamber horizontal centerline, $X/R_0 = 1.60$, are presented in Figure 4.40 for both the non-reacting and reacting liquid phase. For all droplet diameter distributions, a bin width of $2.5 \mu\text{m}$ was chosen with results presented for the center of each bin. With combustion, the peak value in the droplet distribution is seen to shift towards smaller droplet diameters across the combustor, except at $Z/R_0 = -1.75$. This is accompanied by a significant increase in droplet population for the smallest diameter bins. These trends are a direct result of the increase in evaporation rates at elevated combustor temperatures. Of concern, however, are the small population of large droplets, $D/D_0 \sim 3$, in the reacting case, especially for $|Z/R_0| = 2.33$. Droplets of this size may not be physical, as no similar droplets were seen in the non-reacting case. Further, the maximum diameter the PDPA system could measure with the given focal length and beam separation was slightly less than $3D_0$. Thus, some of the droplets measured, $D > 3D_0$, were larger than the maximum cut-off diameter in the Flowsizer software [26].

While droplet coalescence and ligament formation are possible [14], it is more likely that these large measured values are incorrect. Instead, laser reflections from the side windows may contribute to the erroneous measurements by artificially increasing the light intensity near the measuring volume. As such, the size of the scattering droplet would be over predicted. The reduction in droplets larger than $2D_0$ towards the combustor centerline, $Z/R_0 = 0$, suggests that the influence of reflections is significant near the combustor walls. Given the periodic nature of the phase shift from diameter measurements, these errors may also result from incorrect sizing of droplets in the smallest size class, $D < 1 \mu\text{m}$. These droplets are below the software precision and may be incorrectly labeled as large droplets. Figure 4.40 may confirm this behavior, as distributions with the largest number of unphysical droplets, $D \sim 3D_0$, also have the largest number of droplets with $D < 0.1D_0$. That is, droplet distributions with an increasing number of droplets in the smallest diameter class also have an increasing number of droplets in the largest droplet class, mainly due to the inability of the measurement system to accurately capture these smallest droplets. Further, these smallest droplets should have the lowest signal intensity, and therefore, should represent a small fraction of the entire droplet population. This assumption is consistent with the discussion of Figure 4.40; a number of small droplets, less than 5% of the total droplet number, are incorrectly labeled as large droplets.

Given the non-physical nature of these large droplets, a filter was applied to remove all droplets with $D/D_0 > 2$. The aerodynamic measurements of these large droplets were also removed, and the filtered velocity statistics recalculated. To examine the influence of droplets larger than twice the rated nozzle SMD, both the mass mean diameter and SMD were first calculated for the filtered data. A comparison of the non-reacting droplet diameters is presented in Figure 4.41 while a comparison of the reacting droplet diameters is given in Figure 4.42. From the comparison of the filtered and unfiltered non-reacting mass mean diameters across the combustor, Figure 4.41, it is clear

that very few large droplets are present in the non-reacting case, in good agreement with the distributions seen in Figure 4.40. In fact, the unfiltered and filtered mass mean diameter values are almost identical across the combustor. However, a few erroneous droplets do effect the SMD, with an over prediction of up to 15% in the unfiltered data. Given the definition of the SMD, Equation 1.1, the influence of a few large droplets is significant. The cubic dependence in the numerator dominates at large diameter values, and subsequently skews the SMD to large values.

The substantial influence of large droplets on the Case 1 reacting droplet diameters is clear in Figure 4.42. In the flow periphery, $|Z/R_o| > 2$, the population of droplets with $D/D_o > 2$ (<2%, Figure 4.40), is responsible for up to an apparent 400% increase in the SMD. The corresponding mass mean diameters are over predicted by less than 75%, further evidence of the D^3 dominance at large values of D . In the flow core, $|Z/R_o| < 2$, the small population of large droplets, Figure 4.40, is verified by the similarity between the filtered and unfiltered mass mean diameters. The SMD values are within $\sim 25\%$ of each other, except for $-1 < Z/R_o < 0$. The differences in droplet behavior across the combustor centerline, $Z/R_o = 0$, are discussed below. A previous publication of these results did not include this filtering process [30], which may explain the unusually large SMD magnitudes presented.

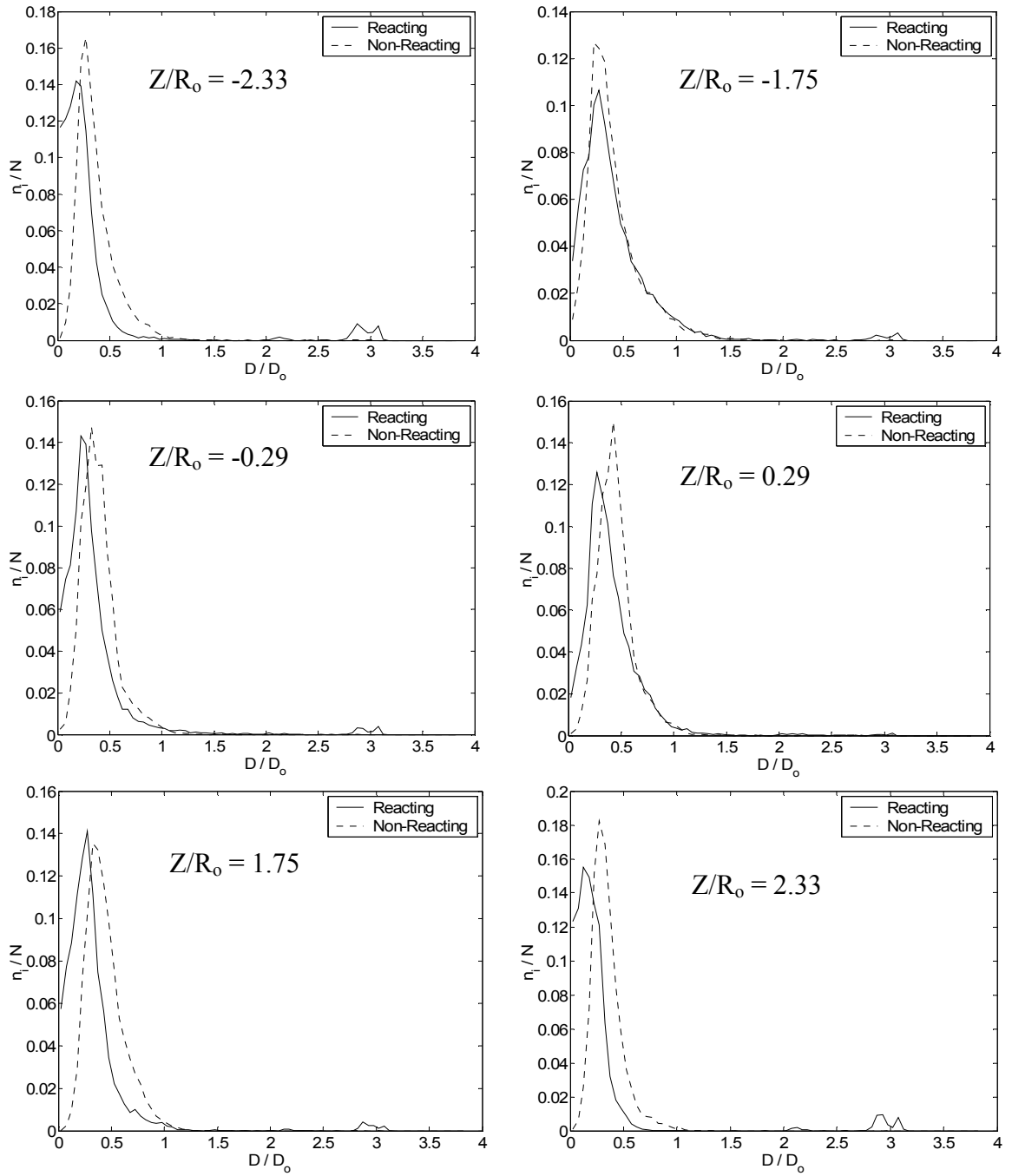


Figure 4.40 Z-Y Plane at $X/R_0 = 1.60$ ($Y/R_0 = 0$), Case 1 Reacting and Non-Reacting Droplet Distributions

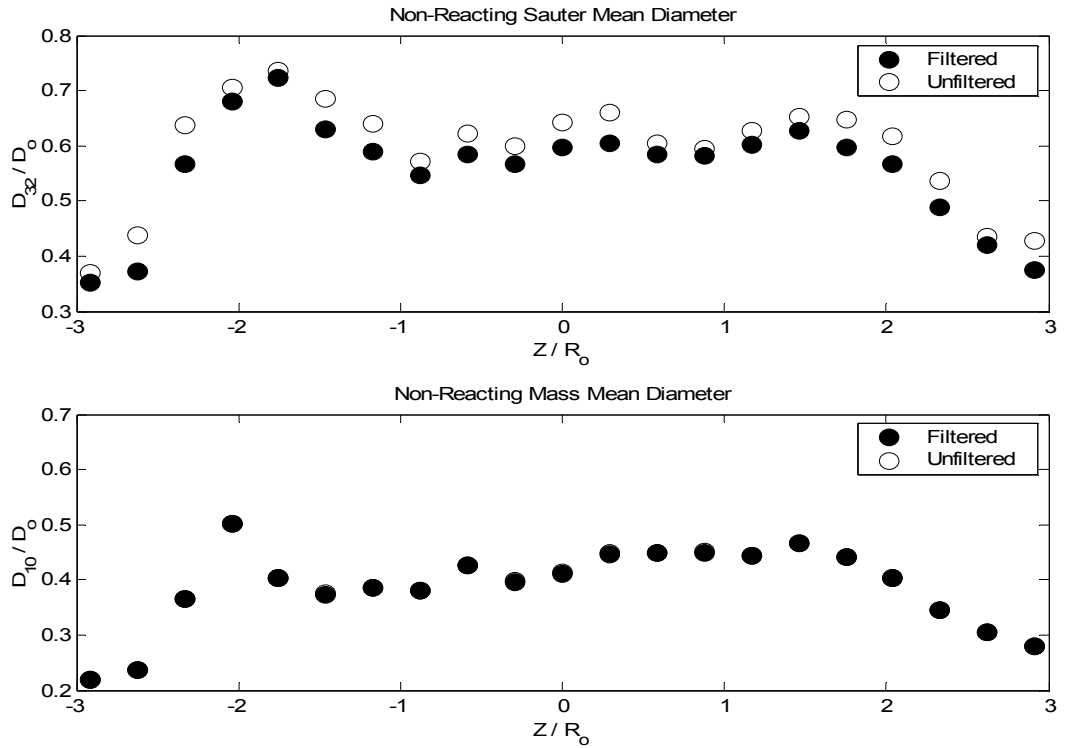


Figure 4.41 Z-Y Plane at $X/R_0 = 1.60$ ($Y/R_0 = 0$), Case 1 Filtered and Unfiltered Non-Reacting Mass Mean Diameter and Sauter Mean Diameter

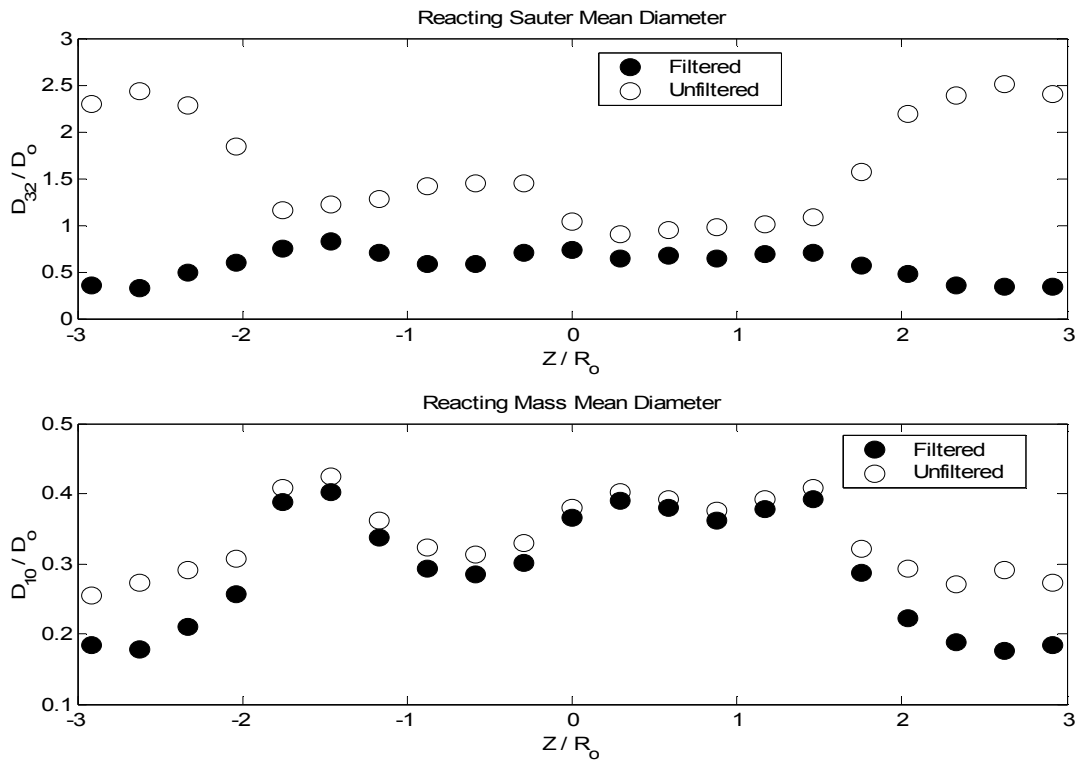


Figure 4.42 Z-Y Plane at $X/R_0 = 1.60$ ($Y/R_0 = 0$), Case 1 Filtered and Unfiltered Reacting Mass Mean Diameter and Sauter Mean Diameter

To further examine the influence of heat release on the droplet diameter statistics, the filtered Case 1 reacting and non-reacting droplet diameters are compared in Figure 4.43. The filtered and unfiltered aerodynamic properties of both the reacting and non-reacting droplets are shown in Figure 4.44 to identify the flow field changes due to combustion and the influence of filtering on the mean velocity field. For all filtered droplet results presented below, no droplet with diameter $D > 2D_0$ was considered.

Examination of the filtered non-reacting and reacting mass mean diameters suggests that the increase in gas temperature with reactions plays a significant role in shortening evaporation times near the injector. The reduction in mass mean diameter with combustion at all locations except $Z/R_0 = -1.5$ is consistent with the droplet distributions presented above, Figure 4.40. The peaks in droplet diameter are shifted towards smaller droplet sizes; larger droplets shift downward in size due to evaporation. These effects are most pronounced in the flow periphery, $|Z/R_0| > 2$, where the mass mean diameter is reduced by over 100% in some places. Evidence for the replacement of large droplets with small droplets is seen in the corresponding SMD results, which decrease with reactions as well in the periphery. In the flow core, $|Z/R_0| < 1.75$, slightly different behavior is observed. While the peaks in the diameter distributions are generally shifted towards smaller values, larger droplets are absent in the tails, seen in Figure 4.40. As a result, the arithmetic mean diameter decreases, however, the SMD increases. This result is due directly to the volumetric dependence of the SMD, and is highlighted well by the distributions seen at $Z/R_0 = 0.25$, Figure 4.40. The peak diameter is shifted to a smaller value, but the number of large droplets, $D > 0.75D_0$ is unchanged. Thus, the mean diameter decreased due to an increase in the smallest droplets in the population while the SMD rose due to the increase in the relative volume of the largest droplets.

To further quantify the differences between the non-reacting and reacting droplets, Figure 4.44 shows the unfiltered and filtered axial and vertical mean velocity

and the TKE for both the Case 1 non-reacting and reacting liquid phase at $X/R_o = 1.60$. The filtering has no effect on the velocity measurements, as the two data sets are nearly indistinguishable. This result suggests that the smallest droplets may have been mislabeled as large droplets; the smallest droplets act as tracers and travel with velocities near the mean velocity while the largest droplets travel with velocity determined by the fuel nozzle. Since the removal of the largest droplets has little impact on the mean velocity, Figure 4.44, (i.e. the largest droplets appear to act as tracers), it is unlikely the largest droplets are physical. Instead, the large droplets may be small droplets whose diameter was incorrectly measured.

It is clear that the impact of heat release, and the associated volumetric expansion, has a major effect on droplet velocities. In the reacting case, mean axial droplet velocities exceed the non-reacting droplet velocities across the entire combustor, except near the combustor walls. This behavior is as expected, as droplets are accelerated throughout the flow due to the gas phase expansion. The flow acceleration associated with combustion has a significant impact on the droplet vertical mean velocity as well. For the non-reacting liquid phase, the impact of the counter-swirl is negligible by $X/R_o = 1.60$. However, the reacting droplets show substantial counter-swirl at the same location, Figure 4.44. This seeming inconsistency is explained with consideration of the aforementioned flow acceleration. With the addition of heat, and the subsequent flow expansion, the region of intense counter-swirl is extended downstream. For the non-reacting case, the counter-swirl behavior expected is likely upstream of $X/R_o = 1.60$. However, since optical access is blocked for $X/R_o < 1.31$, this can not be experimentally verified. With combustion, however, the region of counter-swirl is clearly visible at $X/R_o = 1.60$. Thus, the extension of the main counter-swirl region is attributed to the volumetric expansion of the flow. It is also clear that this counter-swirl is not symmetric, in agreement with the previous results concerning the asymmetric flow field.

At $X/R_0 = 1.60$, as the evaporation and the mixing processes become important, the droplet TKE distribution is seen to broaden. Given the initial droplet momentum is decreased due to drag forces on the droplets, and evaporation times are shortened with combustion, mixing and diffusion characteristics are improved with heat release. With this improved mixing, and the convection of droplets outward due to volumetric expansion, the TKE is spread across the combustor, with values increasing at the spray periphery and centerline. This implies that the droplet penetration is reduced downstream in the reacting case, while radial diffusion is increased with the addition of heat due to combustion.

Figure 4.44 also clarifies the physical nature of the largest droplets ($D/D_0 > 2$). Given that the filtered and unfiltered data sets are nearly identical, the “questionable” droplets have no influence on the measured velocity field. This confirms that the droplet measurements are not physical in nature, as the largest droplets should carry the largest momentum, and thus convect through the ambient gas phase with the largest velocities. If so, the overall aerodynamic properties of the droplet measurements should depend heavily on these largest droplets. Since the total droplet velocity is unchanged with removal of these droplets, it is safe to assume the largest droplets measured are not found in the combustion chamber. Instead, internal reflections may lead to the measurement of phantom droplets with unphysical diameter. Since droplet sizing depends on the intensity of the refracted light while velocity measurements depend only on the frequency of scattered light, window and wall reflections would produce biased droplet diameter sizes without biasing the aerodynamic variables.

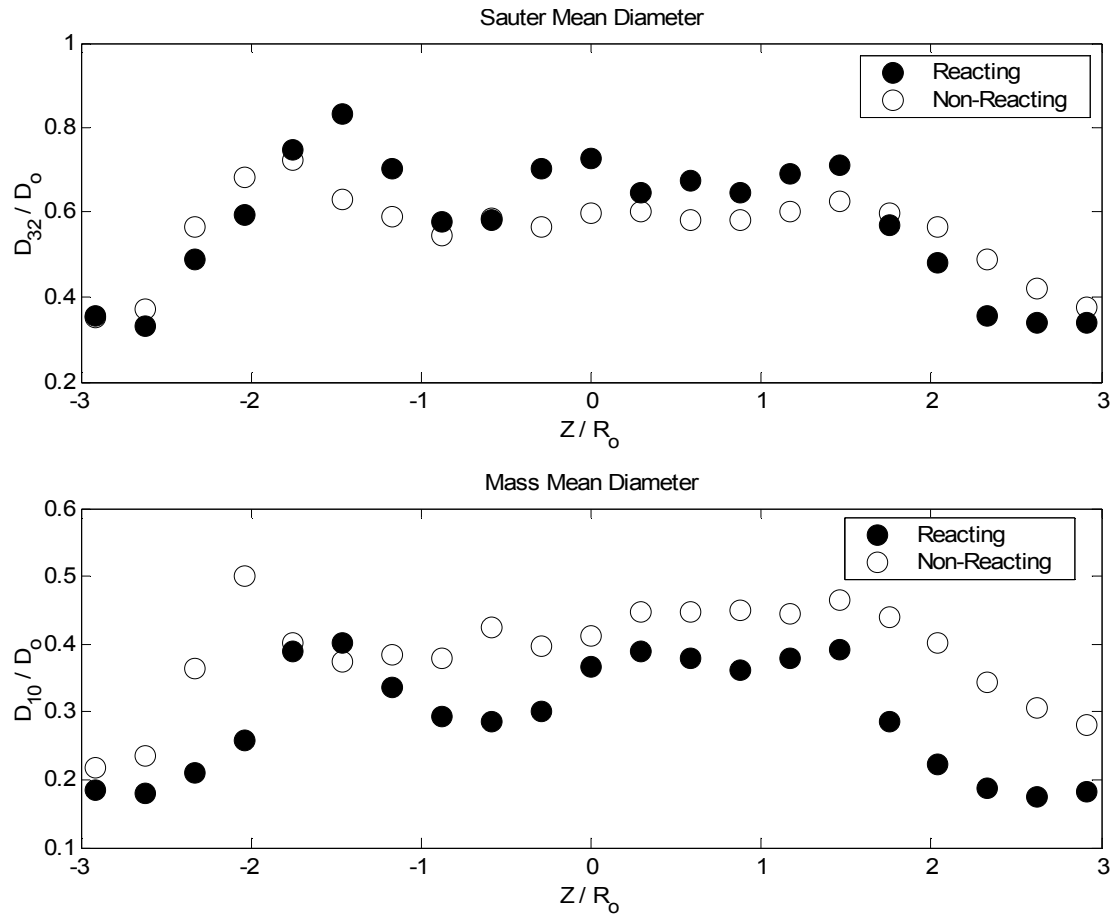


Figure 4. 43 Z-Y Plane at $X/R_0 = 1.60$ ($Y/R_0 = 0$), Case 1 Filtered Reacting and Non-Reacting Mass Mean Diameter and Sauter Mean Diameter

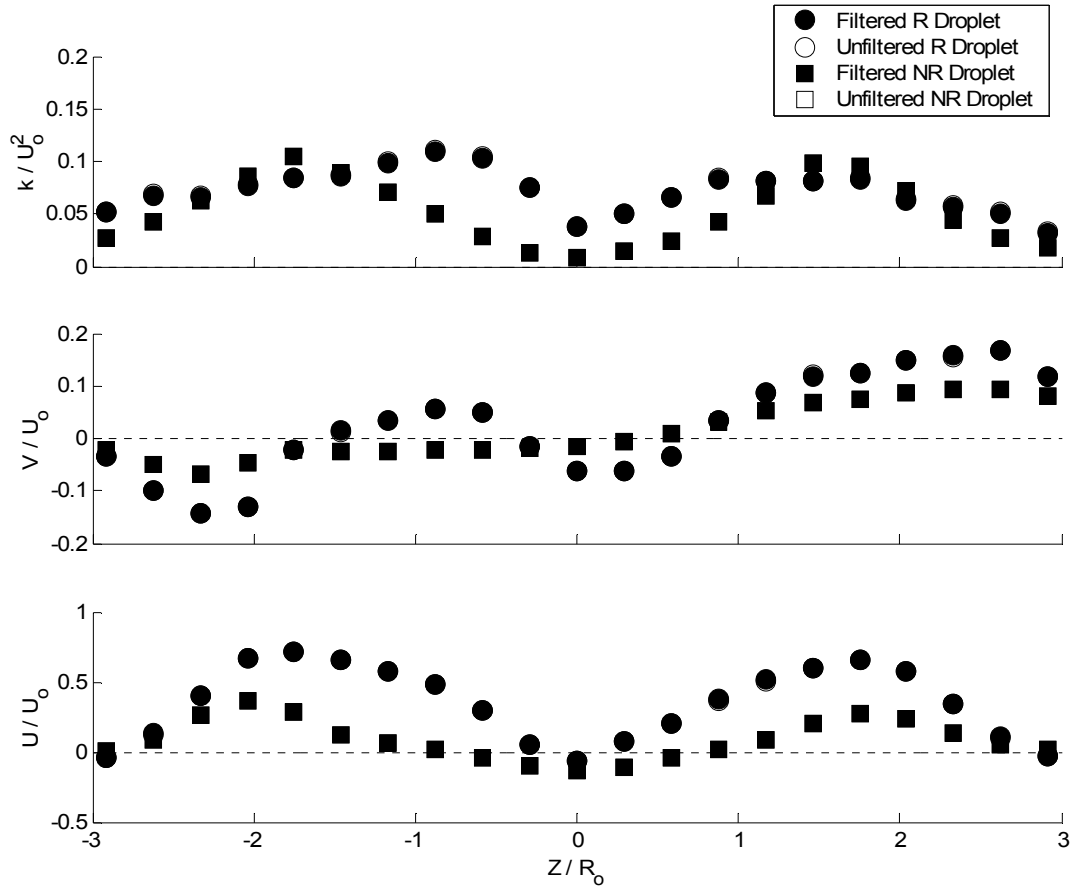


Figure 4.44 Z-Y plane at $X/R_0 = 1.60$ ($Y/R_0 = 0$), Case 1, Filtered and Unfiltered, Reacting and Non-Reacting Droplet Axial, Vertical Mean Velocity, Turbulent Kinetic Energy

Contour plots of the Case 1 reacting SMD and mass mean diameter are given in Figures 4.45 and 4.46. Figure 4.47 presents the droplet number density, determined by the total number of droplets in a sampling time (mean data rate), the total droplet velocity $(U^2 + V^2)^{1/2}$, and the measurement volume cross-sectional area ($\sim 80 \mu\text{m} \times 160 \mu\text{m}$). These interpolated plots present the liquid phase average diameters and concentration along the horizontal center plane, and allow visualization of the spray distribution and nozzle performance. The contour plots clearly show the effects of poor atomization and evaporation on the mass and Sauter mean diameters. Large droplets from the primary atomization are seen across a wide region of the combustor for $Z/R_0 > 0$, Figure 4.45, while large droplets, $D_{10} > .4D_0$, appear confined to a smaller region of the flow for Z/R_0

< 0 , confirming the swirler misalignment. The non-uniform atomization across the combustion chamber is clear in Figure 4.47 as well, where a significantly larger droplet density is seen over a larger region of the combustor for $Z/R_0 < 0$. This result may be due to an asymmetric spray distribution at low fuel pressure and/or the previously discussed swirler misalignment.

Figure 4.46 provides further insight into the asymmetric spray distribution. For $Z/R_0 < 0$, re-atomization from the venturi lip at the primary/secondary swirl interface is the dominant break up mechanism and the droplet confinement is clear. The measured values, $D_{32}/D_0 \sim 0.8$ agree well with the design specifications for secondary re-atomization from the venturi lip of this swirl burner. The liquid phase distribution for $Z/R_0 > 0$, however, shows different behavior. Larger droplet SMD values are seen across the combustor, evidence that droplets from the primary atomization do not impinge on the venturi lip, instead convecting through the primary swirl region and into the recirculation zone. This behavior agrees well with Figure 4.44, where the primary swirl is damped significantly for $Z/R_0 > 0$. Downstream, both the mass mean diameter and SMD increase due to evaporation and burning, in good agreement with previous research [13].

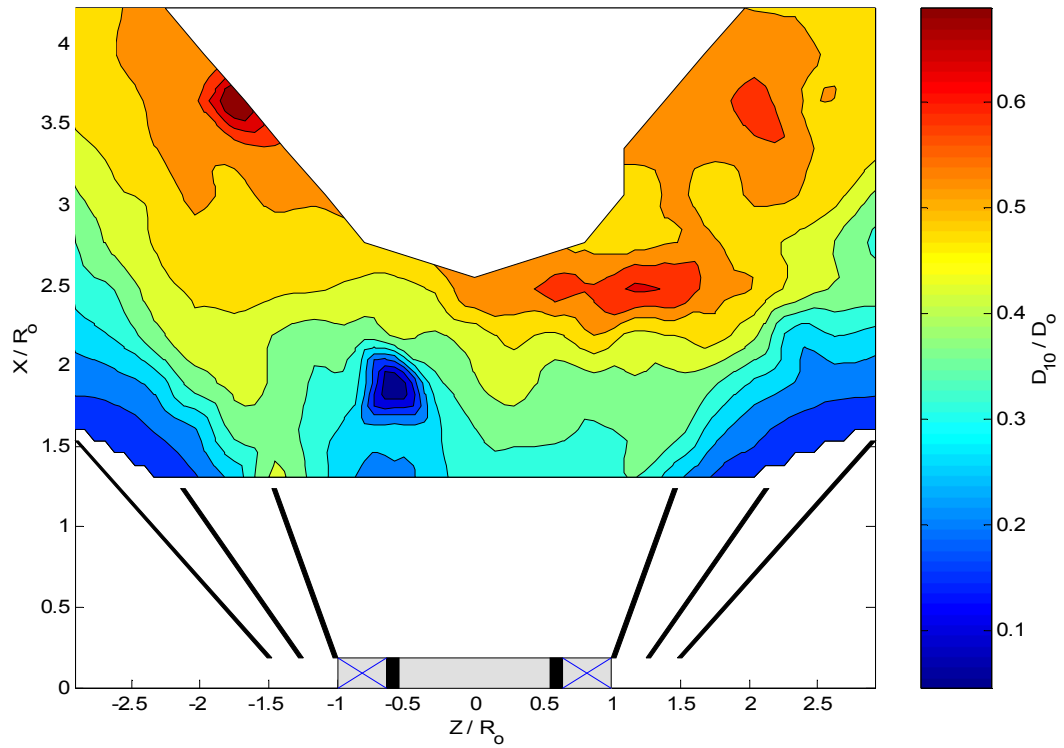


Figure 4. 45 Z-X plane ($Y/R_0 = 0$), Case 1 Reacting Droplet Arithmetic Mean Diameter Contours

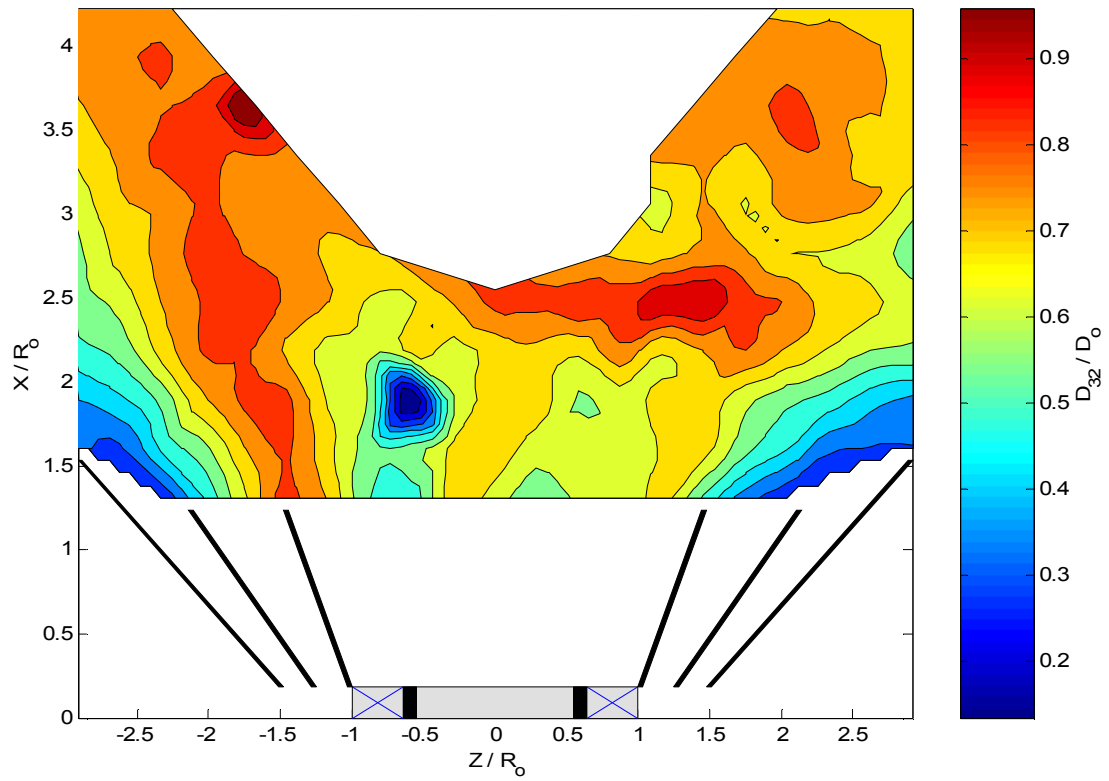


Figure 4. 46 Z-X plane ($Y/R_0 = 0$), Case 1 Reacting Droplet Sauter Mean Diameter Contours

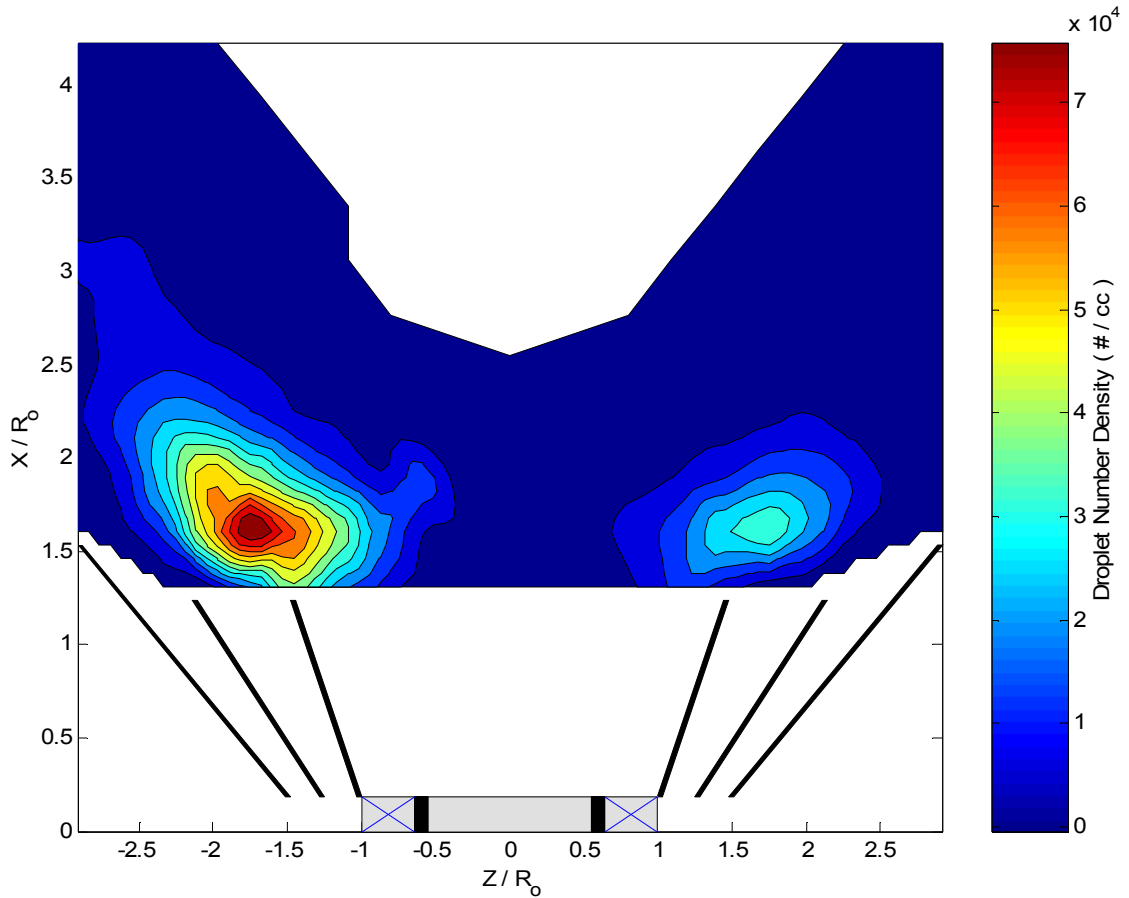


Figure 4.47 Z-X plane ($Y/R_0 = 0$), Case 1 Reacting Droplet Number Density Contours

Case 2

The Case 2 reacting droplet diameter distributions are presented in Figure 4.47 across the combustion chamber horizontal centerline downstream of the fuel nozzle, $X/R_0 = 1.60$. Case 2 non-reacting droplet statistics were not measured in an effort to save time and fuel. Locations to match the Case 1 results were chosen to enable some comparison; however, these comparisons will be limited given the changes to a number of relevant parameters, most importantly the fuel nozzle. While a substantially smaller population of large droplets, $D/D_0 > 2$, is seen, a similar filtering technique was used for calculation of the mass mean diameter and SMD, seen in Figure 4.48.

Unlike the Case 1 reacting droplet results, Figure 4.41, the droplet size filtering has little effect on the mass mean diameter, Figure 4.48. Given the negligible population of droplets with diameter greater than the rated fuel nozzle diameter, Figure 4.47, it is little surprise that the filtered mass mean diameter values are nearly identical to the unfiltered values. However, the Case 2 reacting droplet SMD values do show the influence of the few unnaturally large droplets. As discussed previously, the cubic diameter dependence in the SMD, Equation 1.1, is significant. The droplet distributions for the Case 2 reacting liquid phase are narrower than the Case 1 distributions, suggesting a relatively larger population of smaller droplets. As such, a relatively smaller population of larger droplets is able to skew the calculated SMD value, with predictions up to 20% above the filtered value.

The results for the Case 2 reacting droplet diameters confirm the improvement in spray performance with a new fuel nozzle operating at increased fuel pressure. At no location across combustion chamber at $X/R_0 = 1.60$ is the droplet SMD larger than half of the rated fuel nozzle SMD, a significant improvement from the Case 1 results presented. This reduction in droplet diameter is expected to improve the combustion efficiency significantly, as evaporation times are reduced substantially [33]. With this improvement in evaporation, the subsequent mixing and ignition downstream improve as well. The lack of droplets across a region of the Case 2 flow field, $|Z/R_0| < 1$, evidences these trends. Droplets from the initial atomization are well confined in the secondary flow field and evaporation is complete, as are mixing and combustion, before the downstream recirculation.

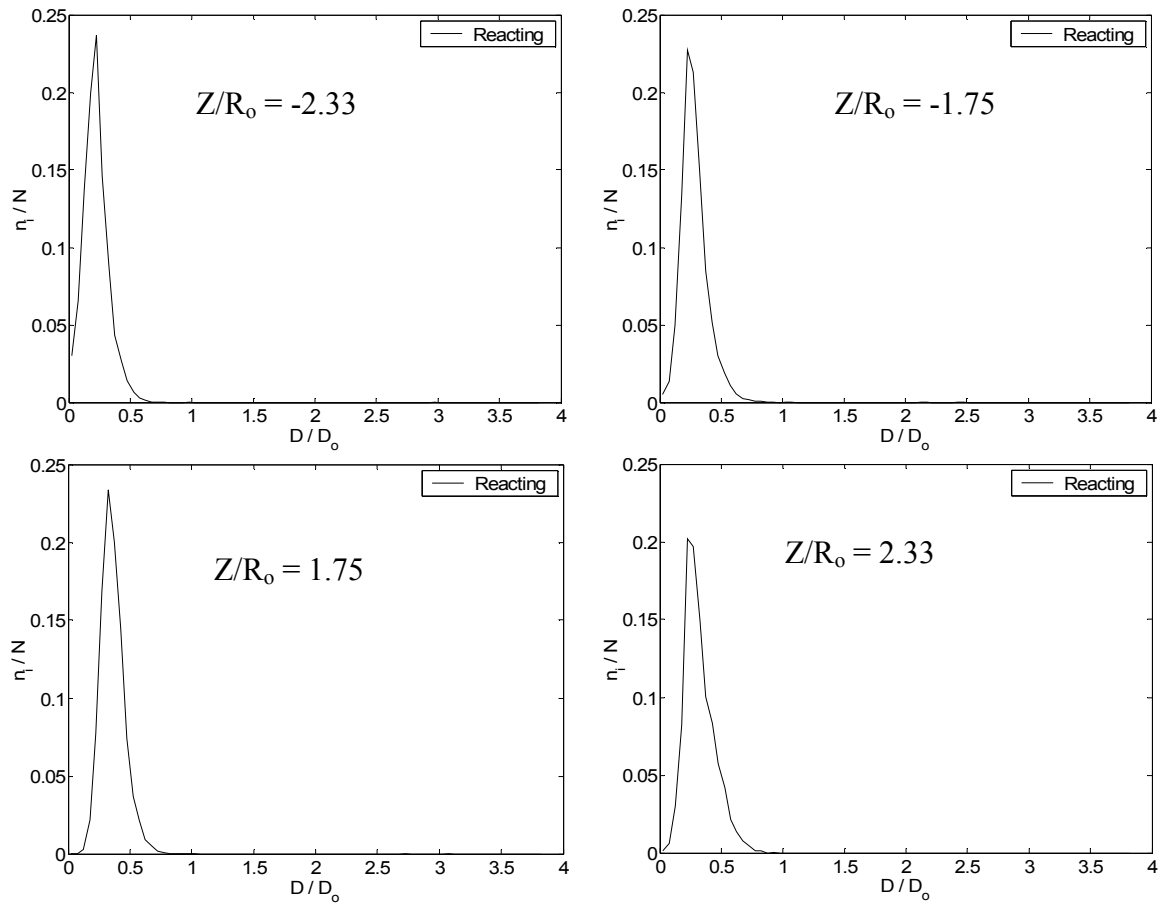


Figure 4. 48 Z-Y Plane at $X/R_0 = 1.60$ ($Y/R_0 = 0$), Case 2 Reacting Droplet Distributions

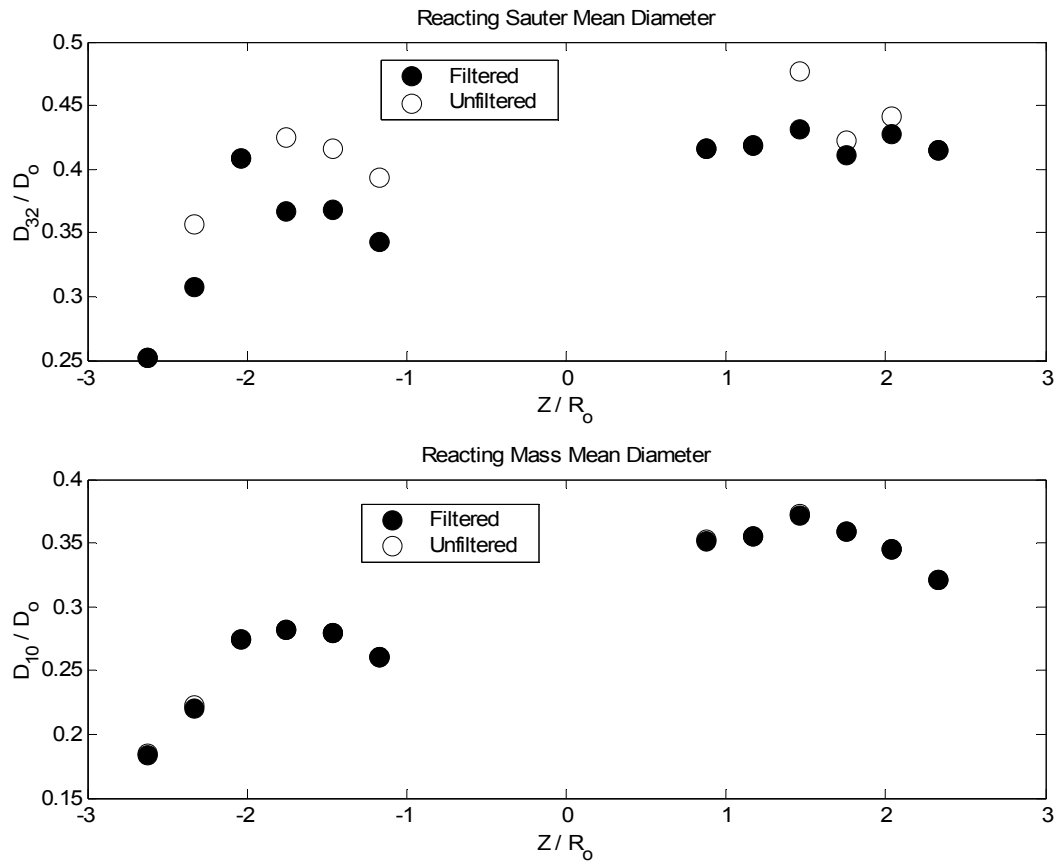


Figure 4.49 Z-Y Plane at $X/R_0 = 1.60$ ($Y/R_0 = 0$), Case2 Filtered Reacting Mass Mean Diameter and Sauter Mean Diameter

To visualize the Case 2 reacting liquid phase downstream of the fuel nozzle, contour plots of the mass mean diameter and SMD in the horizontal center plane are given in Figure 4.50 and 4.51, and a contour plot of the droplet number density is given in Figure 4.52. Significant flow asymmetry is seen well downstream of the fuel nozzle. The increase in SMD downstream agrees well with the previous results [13], but suggests that larger droplets are present for $Z/R_0 < 0$ than $Z/R_0 > 0$. The asymmetric rise in mass mean diameter downstream, Figure 4.50, confirms the larger population of droplets with increased diameter. In the near nozzle region of the flow, the asymmetric confinement is again clear. For $Z/R_0 < 0$, it is evident that the secondary atomization process is dominant from the confinement of larger droplets in a narrow region downstream. The more uniform presence of larger diameter droplets across a wider region of the combustor

is clear for $Z/R_0 > 0$, evidence of droplets from the primary atomization spreading through the primary air stream. A close examination of the droplet distributions, Figure 4.47, confirms this behavior. By comparing the droplet distributions across the horizontal centerline at $X/R_0 = 1.60$, with specific attention to $Z/R_0 = 2.33$ and $Z/R_0 = -2.33$, it is clear that the number of droplets with diameters $D > 0.5D_0$ is significantly larger for $Z/R_0 > 0$ than for $Z/R_0 < 0$. As such, the mass mean diameter and SMD are larger at this location. These larger droplets may be the result of poor secondary atomization at the venturi lip. Further downstream, both the mass mean diameter and SMD values remain asymmetric, with significantly smaller droplets seen for $Z/R_0 > 0$ beyond $X/R_0 = 3$. While these droplets are relatively smaller, it is interesting to note that the mean diameter values did not change significantly downstream. These results suggest that evaporation favors $Z/R_0 < 0$ as smaller initial droplets evaporate and burn more rapidly. For $Z/R_0 > 0$, larger droplets from the primary atomization are slow to break up, while the reduced supply of small droplets lengthens the evaporation times downstream.

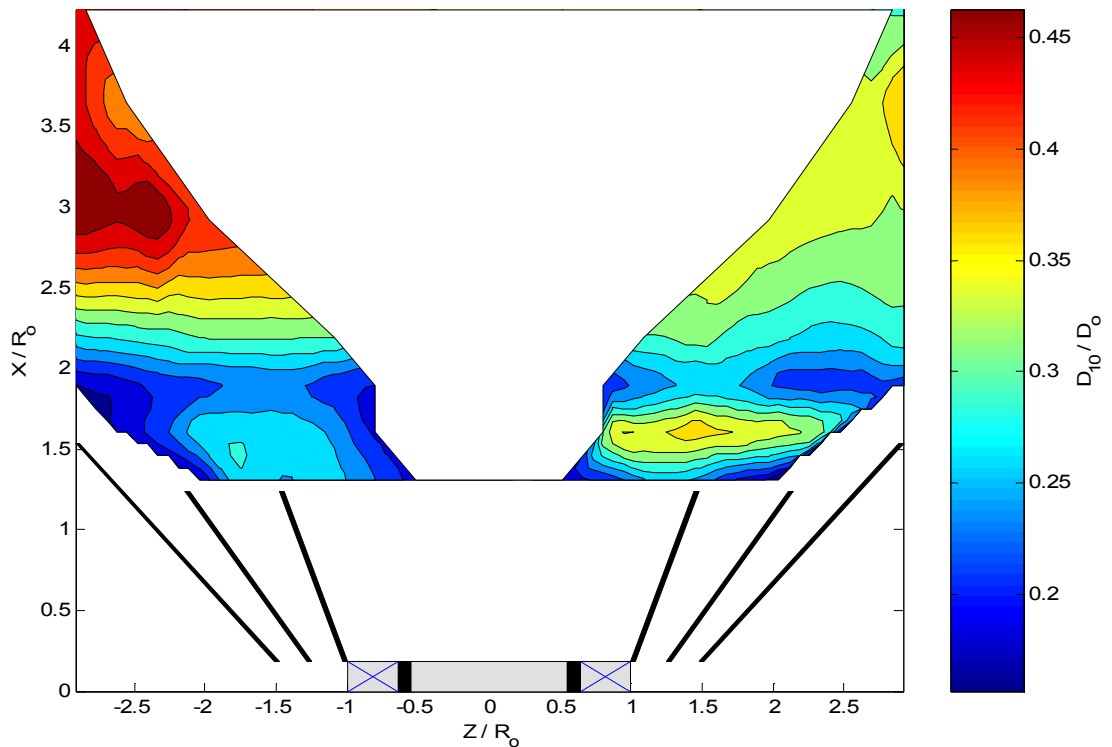


Figure 4.50 Z-X plane ($Y/R_0 = 0$), Case 2 Reacting Droplet Arithmetic Mean Diameter Contours

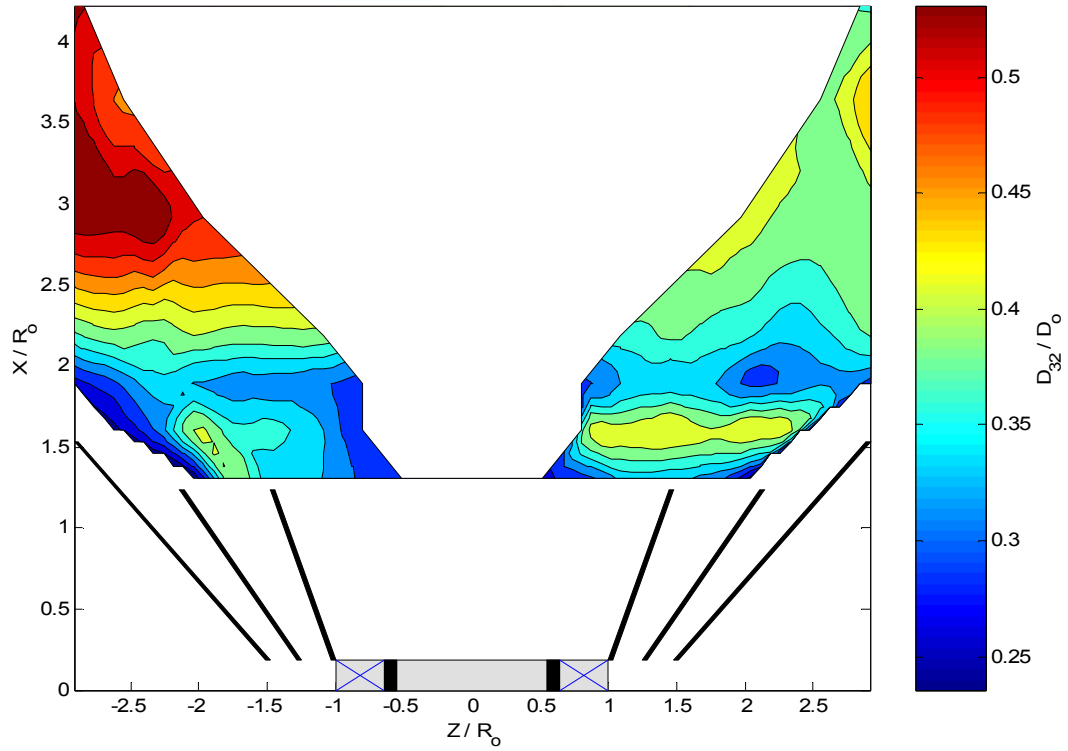


Figure 4. 51 Z-X plane ($Y/R_0 = 0$), Case 2 Reacting Droplet Sauter Mean Diameter Contours

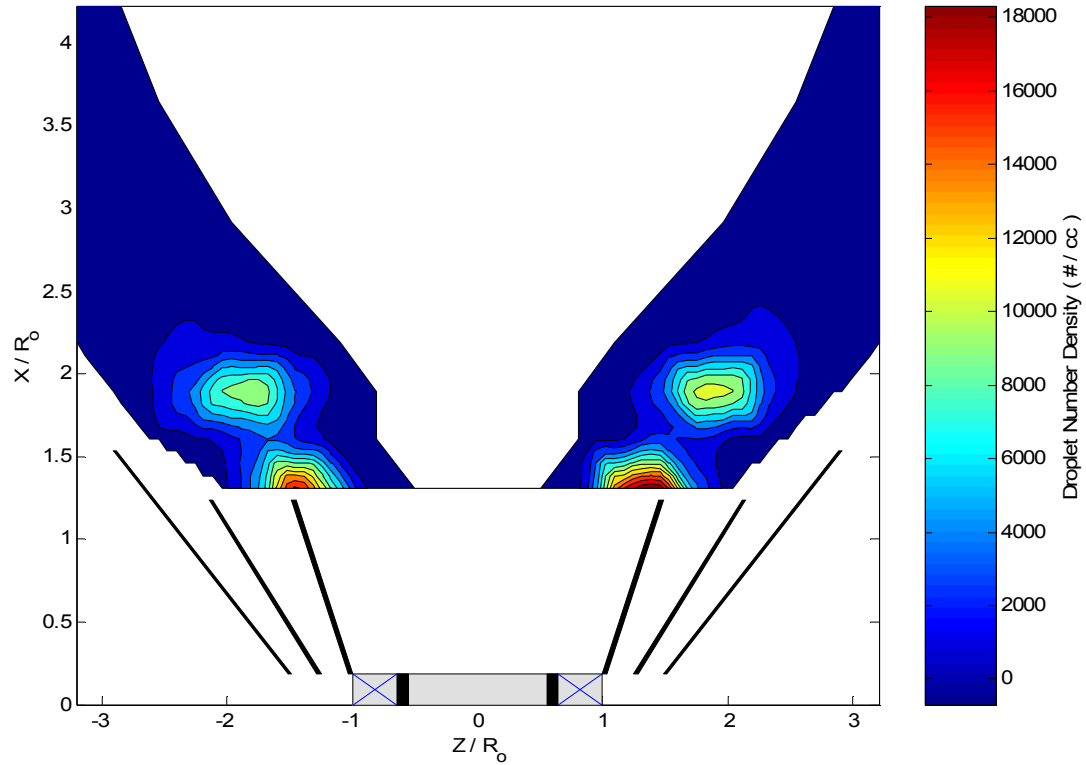


Figure 4. 52 Z-X plane ($Y/R_0 = 0$), Case 2 Reacting Droplet Number Density Contours

Exhaust Gas Properties

A careful examination of the temperature distribution and the composition measurements downstream of the exhaust section, Figure 3.1, provides insight into the combustor performance with lean operation. Specific attention is given to the NO_x ($\text{NO} + \text{NO}_2$) and CO concentrations, each corrected to 15% O_2 . The percent volume O_2 is also presented with the combustion product temperature to examine the relative uniformity of combustion upstream. To improve understanding of the combustor performance, the equilibrium product temperature and percent volume O_2 for both Case 1 and Case 2 were calculated using Gaseq [34]. 1-Butene, C_4H_8 , was used as the fuel for these calculations because the carbon to hydrogen ratio and heating value were more similar to Jet-A than the other available fuels. While equilibrium conditions for this combustor are not expected given the reduced time scales of the gas phase dynamics, the temperature and percent O_2 calculations give a reference point to verify if combustion upstream was complete and/or uniform.

Case 1

The combustion exhaust temperature and percent O_2 measured downstream of the exhaust section, $X/R_0 = 22.16$, are shown in Figure 4.53. The effect of the asymmetric combustion described above is clear, as the exhaust temperature changes dramatically across the exhaust section. For $Z/R_0 > 0$, the gas temperatures (solid circles) are below 1000K. For $Z/R_0 < 0$, however, exhaust gas temperatures approach 1200 K, still well below the equilibrium product temperature, Figure 4.53. The percent O_2 measurements (solid triangles) also show significant asymmetry, with over 15% O_2 available for $Z/R_0 > 0$ compared with less than 13% for $Z/R_0 < 0$. These results may suggest that combustion is more complete downstream for $Z/R_0 < 0$. As a result, the overall temperature is high and the oxygen content drops slightly below the dry percent O_2 equilibrium value. For $Z/R_0 > 0$, however, the excess percent O_2 and reduced temperatures suggest either the

incomplete combustion of liquid fuel upstream or an increase in air entrainment downstream. Figures 4.3 and 4.19 do show the influence of some laboratory entrainment for $Z/R_o > 2$, however, this is unlikely to account for the large percent O_2 measurements seen close to the combustor centerline, $0 < Z/R_o < 2$.

To further quantify the exhaust gas composition, Figure 4.54 presents the CO and NO_x concentrations in ppm, corrected to 15% O_2 . The low NO_x , ~ 5 ppm, and high CO, $\sim 4,000$ ppm, seen in Figure 4.54, $Z/R_o > 0$, agree well with the low product temperatures and large amount of excess O_2 available from incomplete combustion. Results for $Z/R_o < 0$, Figure 4.54, show significantly different emission levels, with corrected NO_x concentrations above 10ppm and corrected CO concentrations below 1000 ppm. These results correlate well with the temperature and O_2 measurements seen in Figure 4.53; more complete combustion increases local gas temperatures downstream, thereby increasing thermal NO_x production and reducing the formation of CO from inadequate burning in the primary zone [1].

The fuel spray dynamics in the near nozzle region, Figures 4.45 and 4.46, may provide some insight into the asymmetric exhaust gas properties. A direct comparison, however, may not be appropriate given the large degree of swirl in this combustor. In the region of maximum exhaust temperature, $Z/R_o < 0$, the reacting droplet SMD values are largest in the downstream part of the combustor. The increase in diameter values near $X/R_o = 3.5$, Figures 4.45 and 4.46, suggest a population of relatively larger droplets for $Z/R_o < 0$, which may extend the reaction region. The droplet number density results, Figure 4.47, suggest that a larger number of droplets are also present for $Z/R_o < 0$, further extending the combustion zone. The confinement of the largest droplets into a ligament like structure, Figure 4.46, may also extend the combustion zone downstream, increasing evaporation times while reducing the total time for heat loss. In this region of larger, confined droplets, sheath type combustion may occur at equivalence ratios closer to stoichiometric, further elevating the local flame temperature and the NO_x formation [1].

For $Z/R_o > 0$, where exhaust temperatures are significantly lower, the liquid phase exhibits different behavior. Instead of confinement, the diameter measurements suggest that droplet spreading is significant. The narrow region of droplets with large mass mean diameter ($D_{10} > 0.35D_o$) seen for $Z/R_o < 0$ is replaced by a wide region of droplets with mass mean diameters $\sim 0.35D_{10}$, Figure 4.45. Further, except for the peak value near $Z/R_o = -2$, larger droplets are seen for $Z/R_o > 0$ than $Z/R_o < 0$. As such, individual droplet spreading from ineffective re-atomization may retard the stable recirculation of combustion products, possibly explaining the incomplete combustion seen in the exhaust gas measurements for $Z/R_o > 0$. These individual droplets are more likely to evaporate and partially premix before combustion, reducing the reaction zone length and the local flame temperature. The largest of the individual droplets may also convect through the primary reaction zone with residence times less than the total time necessary for combustion and fail to react completely. Any unburned or partially oxidized fuel would lead to the increase in O_2 and CO seen above; however, unburned hydro-carbons were not measured in these experiments.

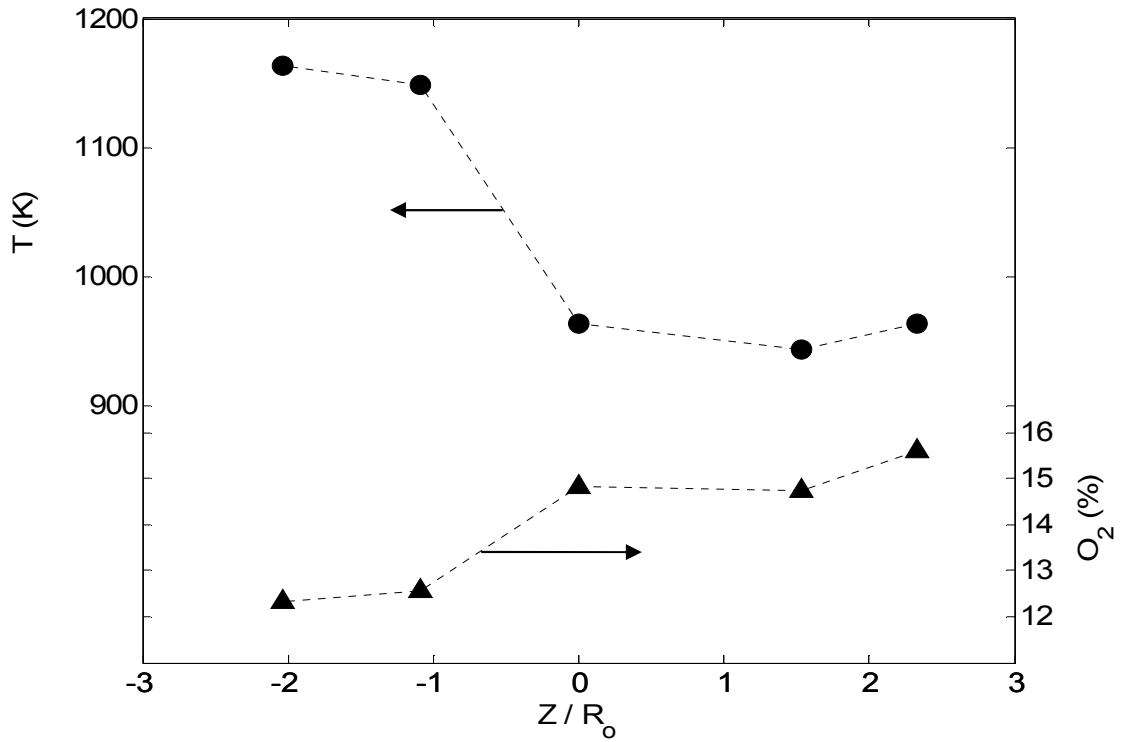


Figure 4.53 Z-Y plane ($Y/R_0 = 0$) Case 1 Exhaust Gas Temperature and Oxygen Content ($T_{eq} = 1405$ K, $(O_2)_{eq} = 12.9$ % [34])

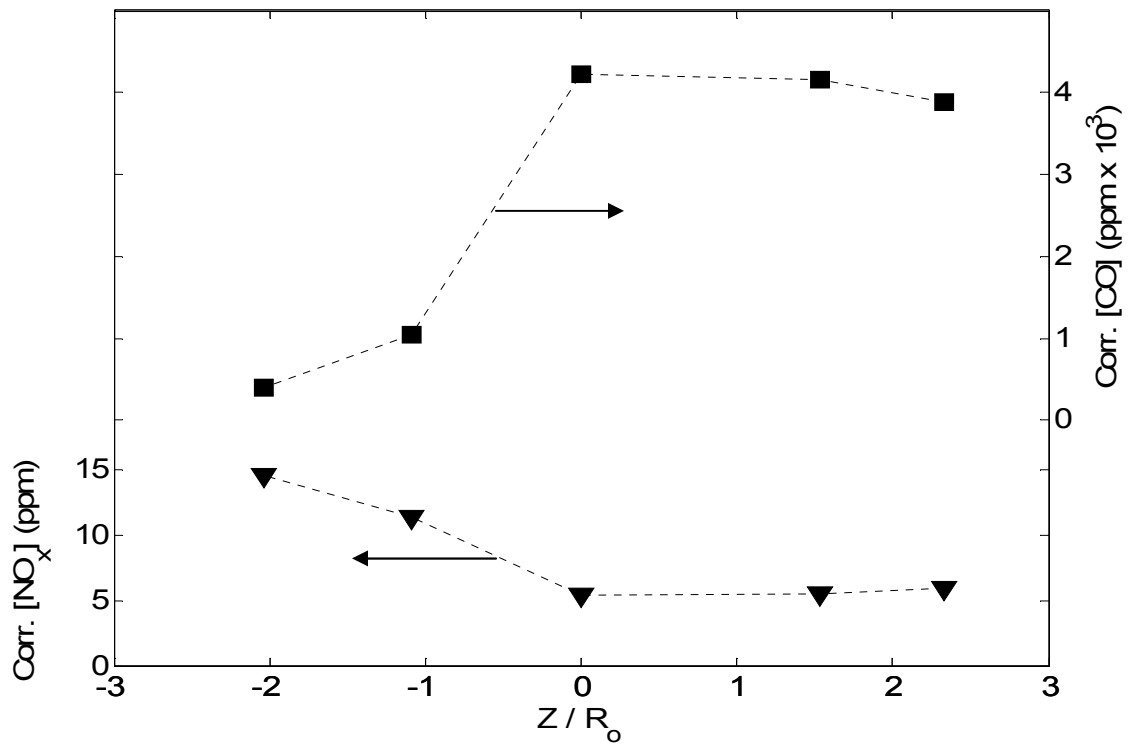


Figure 4.54 Z-Y plane ($Y/R_0 = 0$) Case 1 Exhaust Gas Corrected Emission Concentrations

Case 2

The Case 2 reacting gas phase exhaust temperature, Figure 4.55 (solid circles), further verifies the non-uniform spray distribution upstream. However, a significant improvement in the flow symmetry is seen with the new fuel nozzle operating at elevated pressure. For $Z/R_0 < 0$, the maximum temperature increases to just over 1200 K, in agreement with the increase in overall equivalence ratio. A minimum exhaust temperature just below 1100 K is seen at $Z/R_0 = 0$, with a slight increase in temperature for $Z/R_0 > 0$. These exhaust temperatures are significantly lower than the equilibrium value, Figure 4.55, and confirm the large heat losses downstream of the combustion zone. Percent O_2 measurements (solid triangles) agree well with the exhaust temperatures presented and again suggest more complete combustion for $Z/R_0 < 0$. The increase in global equivalence ratio for Case 2 is also seen in the reduction of corrected O_2 across the entire exhaust section relative to Case 1, Figure 4.53. These results, however, show more available O_2 than the equilibrium calculation, with near equilibrium conditions in the flow periphery for $Z/R_0 < 0$. As with Case 1, some entrainment, seen in Figure 4.31, may be responsible for the slight rise in O_2 near $Z/R_0 = 2$.

The Case 2 corrected concentrations of both CO (solid squares) and NO_x (solid, inverted triangles) are shown in Figure 4.56. As with the previous Case 2 measurements, a significant improvement in the flow symmetry is seen, as is the influence of an increase in global equivalence ratio. Corrected NO_x concentrations are higher across the entire exhaust for Case 2, with a maximum value near 25 ppm. This increase in NO_x with increasing equivalence ratio (below stoichiometric, $\Phi = 1$) agrees well with the increase in flame temperature, Figure 4.55, and standard gas turbine operation [1]. The general decrease in corrected CO concentrations further confirm the improvement in combustion quality and the increase in overall equivalence ratio (below $\Phi \sim 0.5$) [1]. The maximum value near 1200 ppm is 2-3 times below the Case 1 maximum, and very low concentrations are seen in the flow periphery, $|Z/R_0| > 1$. The increase in fuel pressure

and equivalence ratio reduces the reacting droplet SMD while both the liquid phase velocity and flame temperature increase. The increase in flame temperature accelerates the production of thermal NO_x while the reduction in droplet diameter encourages more complete combustion and the overall reduction in CO formed from partially oxidized fuel.

Consideration of the reacting liquid phase diameter measurements in the horizontal center plane, Figures 4.50 and 4.51, provides some insight into the improved exhaust symmetry. Similar to the Case 1 results discussed above, the larger SMD values downstream for $Z/R_o < 0$ correspond to the region of maximum exhaust temperature. However, these Case 2 droplets have SMD values roughly half the SMD values seen in Case 1. This reduction in droplet size throughout the combustor for Case 2, both mass mean diameter and SMD, may be responsible for the improvement in exhaust gas symmetry. The relatively smaller droplets should evaporate more quickly, allowing more time for partial mixing before ignition. With the reduction in mean evaporation time and improved mixing, more uniform combustion is expected across the horizontal center plane. The improved symmetry in the droplet number density, Figure 4.52, also suggests more uniform combustion is likely for Case 2.

The absence of droplets along the combustor centerline, $Z/R_o = 0$, agrees well with the rise in CO emissions and drop in NO_x emissions downstream. Without droplet penetration into the main vortex breakdown bubble, reactions are confined to the flow periphery and post combustion products are efficiently recirculated back to the incoming cold reactants. As such, the centerline temperature is reduced and the NO_x emissions are minimized while the CO emissions are maximized.

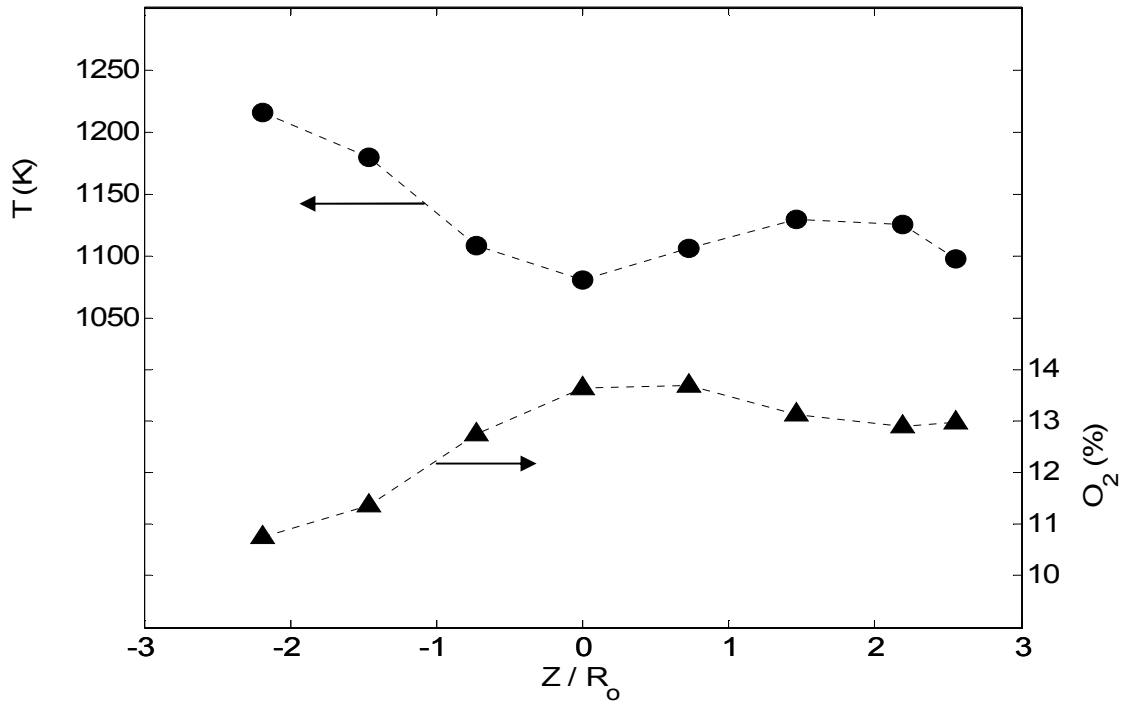


Figure 4. 55 Z-Y plane ($Y/R_0 = 0$) Case 2 Exhaust Gas Temperature and Oxygen Content ($T_{eq} = 1636$ K, $(O_2)_{eq} = 10.8$ % [34])

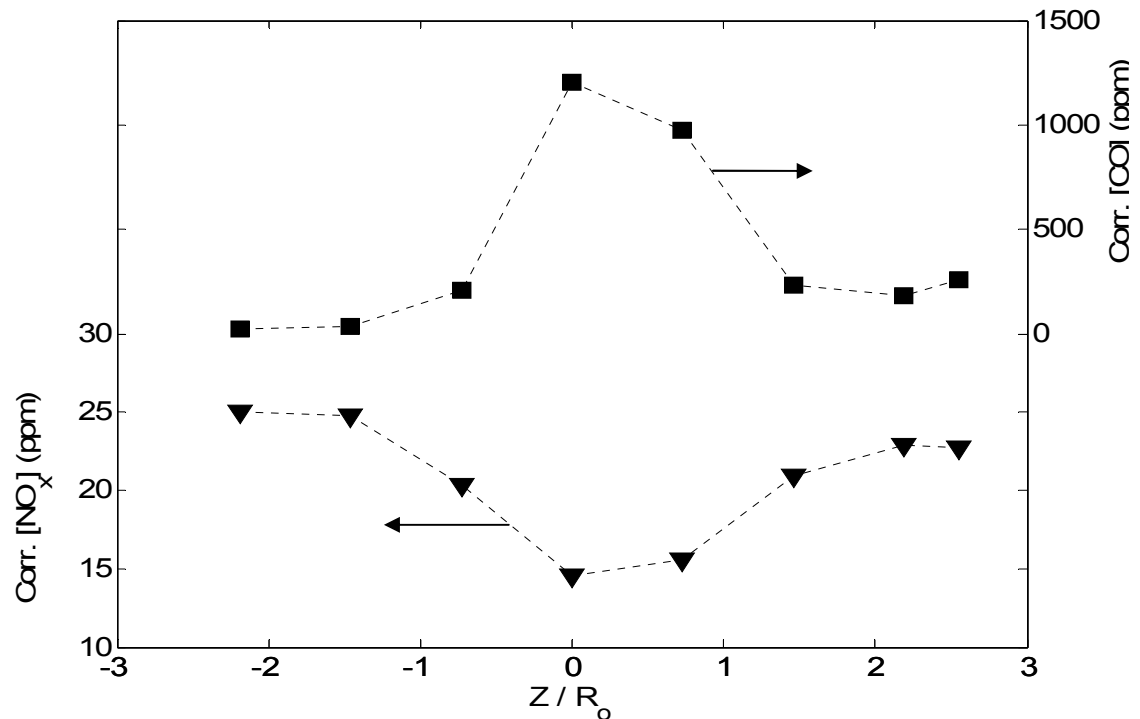


Figure 4. 56 Z-Y plane ($Y/R_0 = 0$) Case 2 Exhaust Gas Corrected Emission Concentrations

CHAPTER 5

CONCLUSIONS

The existence of a large vortex breakdown bubble, typical of high swirl flows, is clear in the non-reacting and reacting gas phase flow. This breakdown bubble is characterized by a large area of recirculating flow, responsible for the convection of gas from downstream back to the near-injector region. Along with enhanced mixing in the resulting shear layer, this mechanism plays a key role in both flame stabilization and combustion efficiency by returning hot, radical rich, combustion products to the unmixed, unburned reactants near the fuel nozzle.

The normalized non-reacting gas phase flow structure is unaffected by modest changes in inlet air mass flow rates. The size and shape of the vortex breakdown bubble are unchanged by the increase in pressure drop across the swirler, while the core recirculation strength is increased. These results confirm the value of counter-swirl stabilization in aeroengines.

The volumetric expansion associated with the addition of heat due to combustion constricts the vortex bubble, reducing the length and width while increasing the core velocity magnitude. Similarly, the mean axial velocity is increased significantly, as are the near nozzle turbulence properties.

Droplet diameter measurements suggest that the non-reacting droplets do not follow the primary counter-swirl, but instead follow the secondary swirl imparted at the venturi lip. With combustion, however, the reacting droplets do show counter-rotation as the volumetric expansion extends these structures downstream.

Poor spray performance at low fuel pressure and an asymmetric combustion chamber produce regions of droplets with larger SMD values. Atomization quality in the near nozzle region plays an important role in emission levels. If the designed re-atomization from the venturi lip is effective, smaller droplets in the secondary flow

evaporate and burn more rapidly along the shear layer at the recirculation zone edge, acting to stabilize the non-premixed flame. Without effective re-atomization from the venturi lip, larger droplets with primary swirl convect through the vortex break down bubble, reducing combustor performance.

In the near injector region, the influence of the liquid phase and subsequent heat release tends to increase and redistribute the 2-D TKE across the combustor cross section. The fuel-shear layer interaction contributes directly to the maximization of heat release in the near nozzle region, essential for stable lean combustion. Reynolds shear stress measurements suggest that a gradient diffusion model may not capture the transport of turbulent momentum in a counter-swirling flow field.

Results presented on the effects of inlet air mass flow rate and fuel pressure on the non-reacting and reacting flow field in a counter-swirl stabilized combustor provide a quality data set for LES model validation. With correct turbulence closure models and inflow velocity conditions, the future design of gas turbine engine combustors will be aided significantly by numerical simulations.

CHAPTER 6

RECOMMENDATIONS

To continue this research, methods for improved atomization should be examined with an emphasis on low fuel pressure spray characteristics. Work should focus on ensuring the designed re-atomization from the venturi lip, even at fuel pressures lower than those currently used as design criteria for aero-gas turbine engines. With better spray characteristics at low fuel flow rates, the stability of lean operation could be ensured. To improve understanding of this process, high speed imaging could be done in the near nozzle region to capture instantaneous droplet distributions across the combustor.

The measurement of the remaining velocity component, as well as the final two shear stress terms is essential. The validity of both the turbulent viscosity hypothesis and gradient diffusion model should be determined beyond this initial examination. As the three mean velocity components are of similar order, the full 3-D stress tensor should be used for closure in a robust numerical simulation. The accurate measurement of this tensor experimentally is essential to validate or generate any such simulation.

A calculation of the relative velocity between the reacting droplets and the reacting gas phase would provide insight into the momentum transfer between the two phases. The relative velocity could help identify regions where the liquid phase biased the reacting gas phase aerodynamic measurements, i.e. small droplets acted as solid particles. The relative velocity could also quantify the ability of droplets to penetrate the core recirculation region, an important factor in evaporation, mixing, and combustion performance.

Finally, improvements in the emission measurements should be made. Specifically, the unburned hydrocarbon concentration should be measured at the combustor exit to quantify the overall combustion efficiency. In addition, an optical

analysis of the radical field would improve understanding of the physical location of the main reaction regions in the combustion chamber. Finally, to improve uncertainty in the exhaust gas measurements, the exhaust section should be fitted with a collar to house the gas analyzer probe. If the location of the probe were fixed in space, significant improvements could be made in the statistical certainty of the composition measurements.

APPENDIX A
GAS PHASE COMPARISONS

Reacting Gas Phase vs. Non-Reacting Gas Phase Flow Field

Case 1

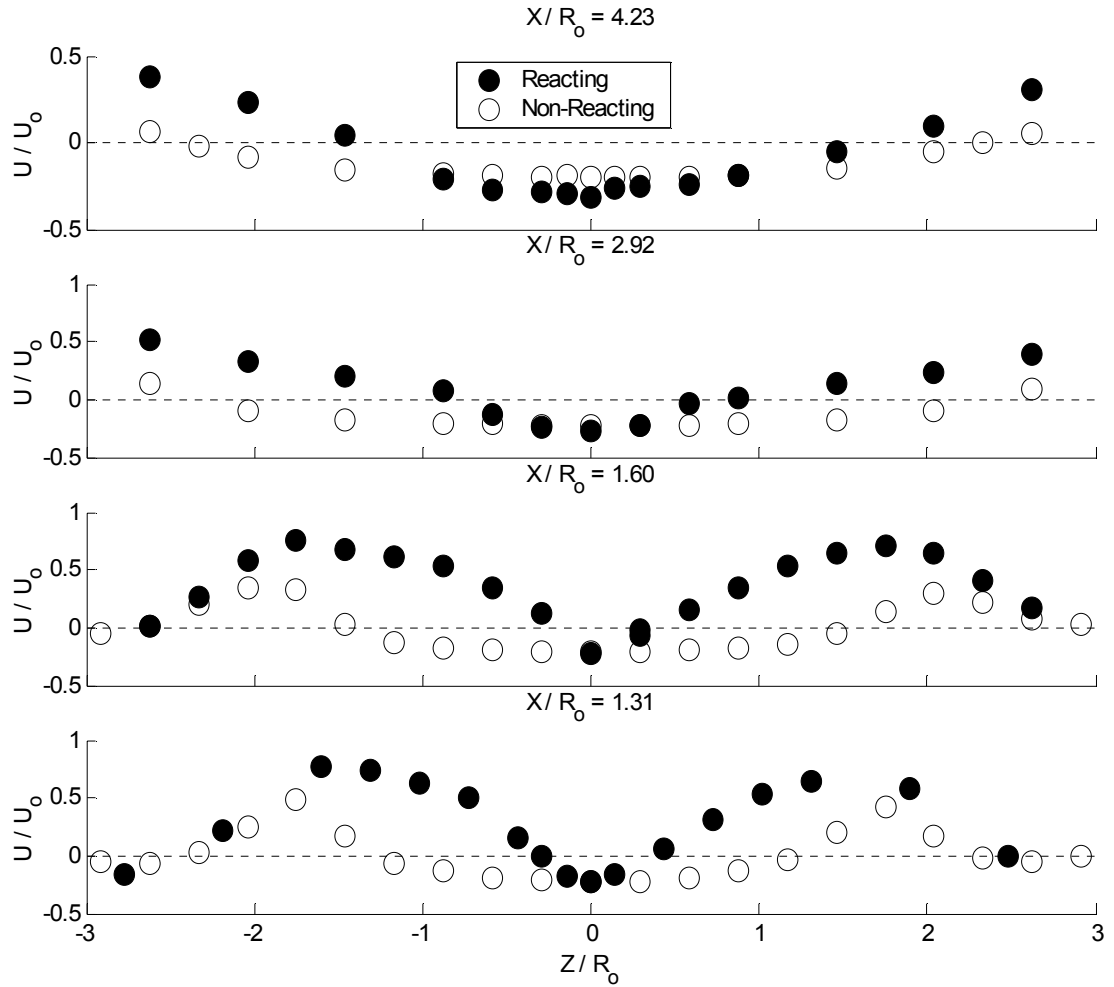


Figure A. 1 Z-Y plane ($Y/R_0 = 0$), Case 1 Reacting and Non-Reacting Axial Mean Velocity

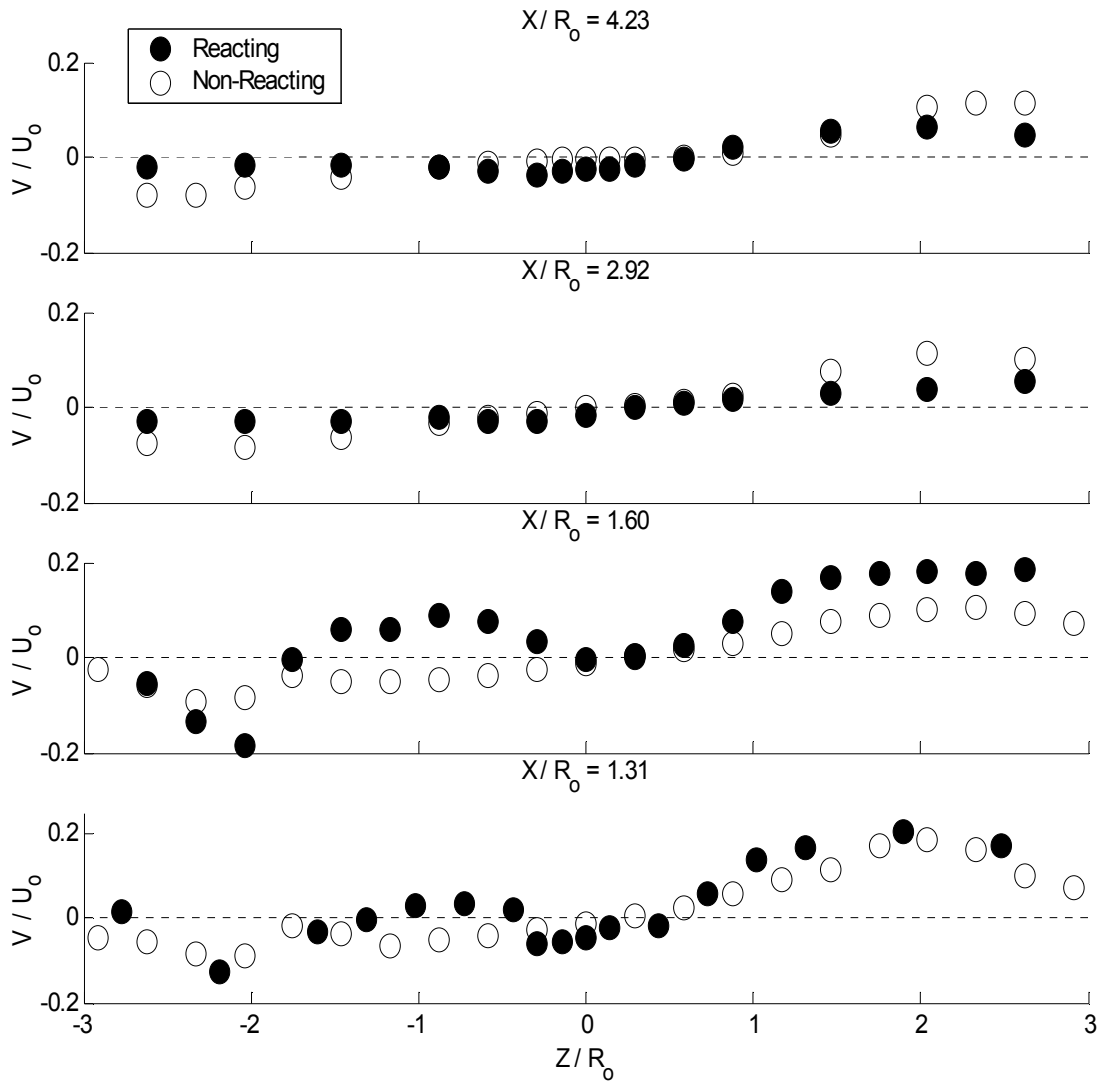


Figure A. 2 Z-Y plane ($Y/R_0 = 0$), Case 1 Reacting and Non-Reacting Vertical Mean Velocity

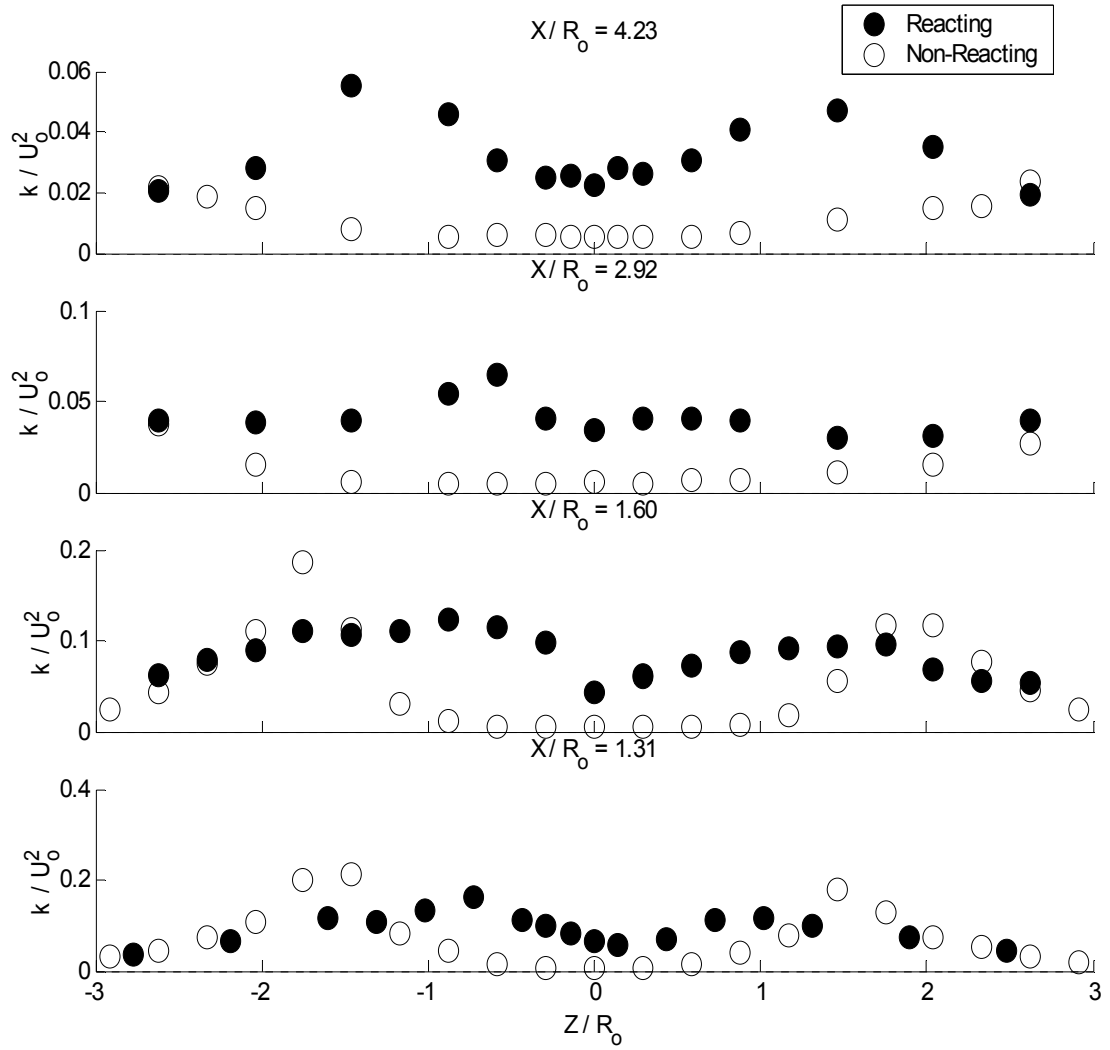


Figure A. 3 Z-Y plane ($Y/R_0 = 0$), Case 1 Reacting and Non-Reacting Turbulent Kinetic Energy

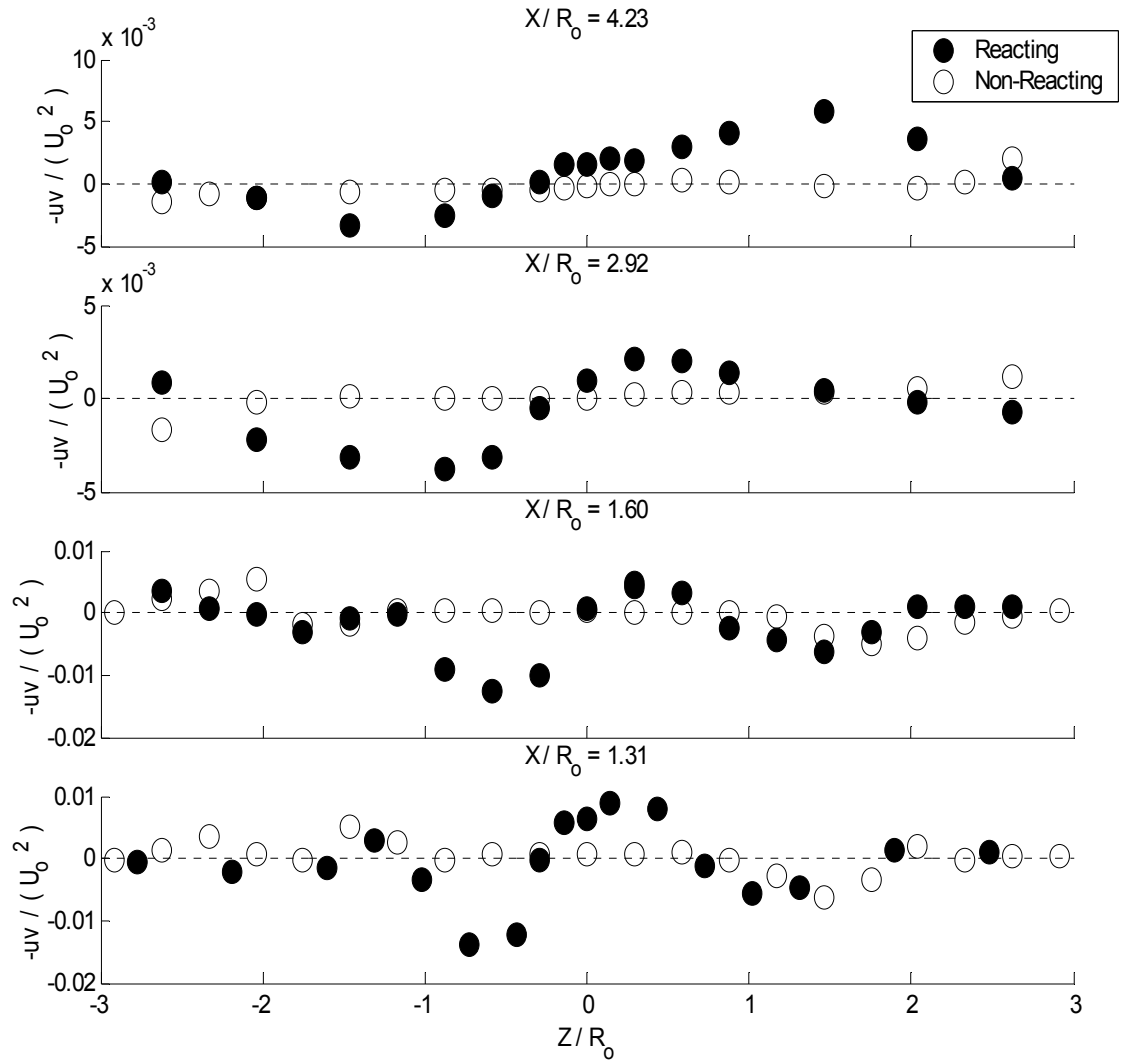


Figure A. 4 Z-Y plane ($Y/R_0 = 0$), Case 1 Reacting and Non-Reacting Reynolds Shear Stress

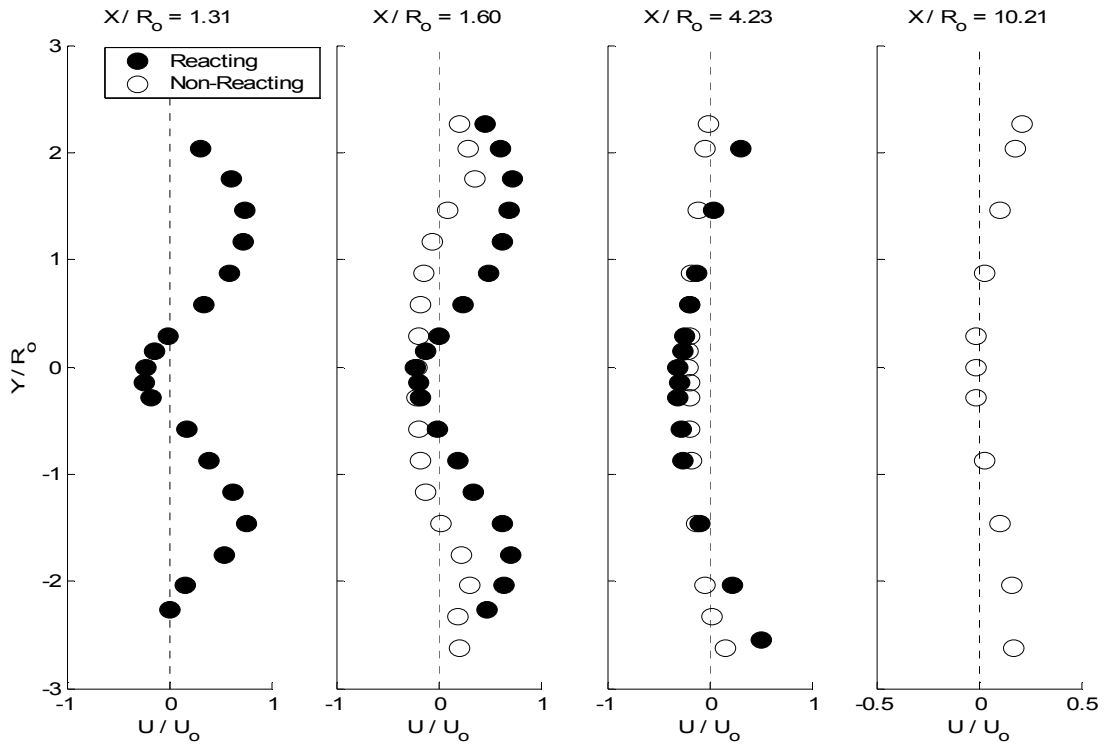


Figure A. 5 Z-Y plane ($Z/R_0 = 0$), Case 1 Reacting and Non-Reacting Axial Mean Velocity

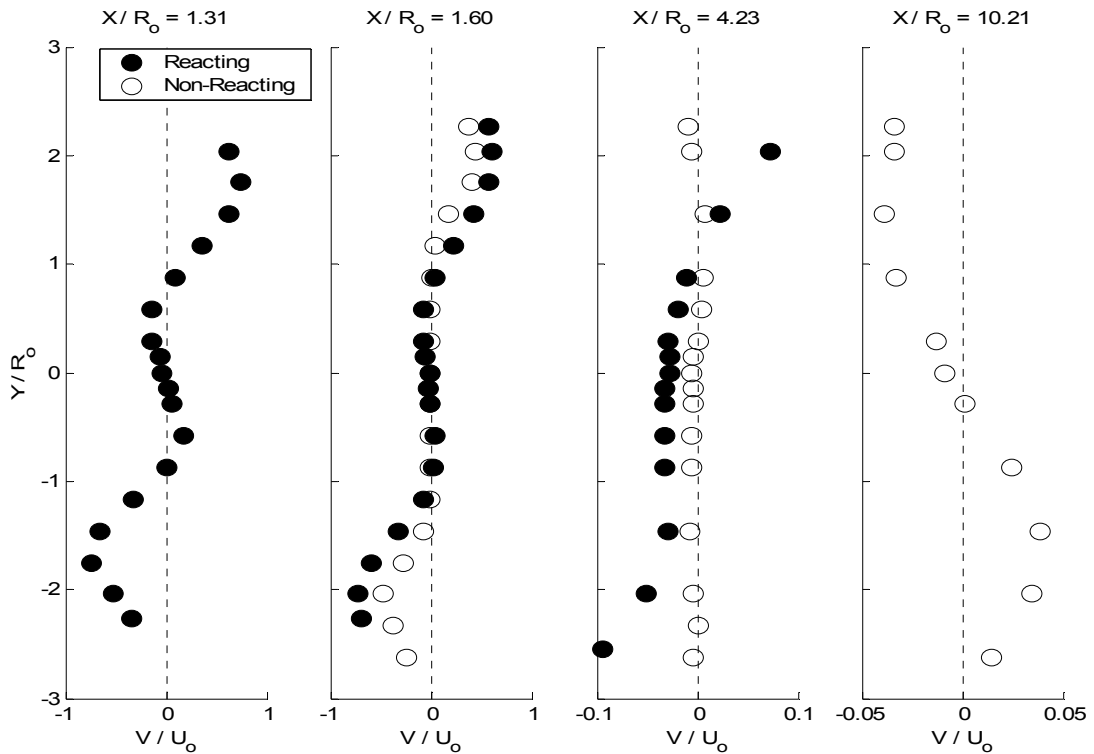


Figure A. 6 Z-Y plane ($Z/R_0 = 0$), Case 1 Reacting and Non-Reacting Vertical Mean Velocity

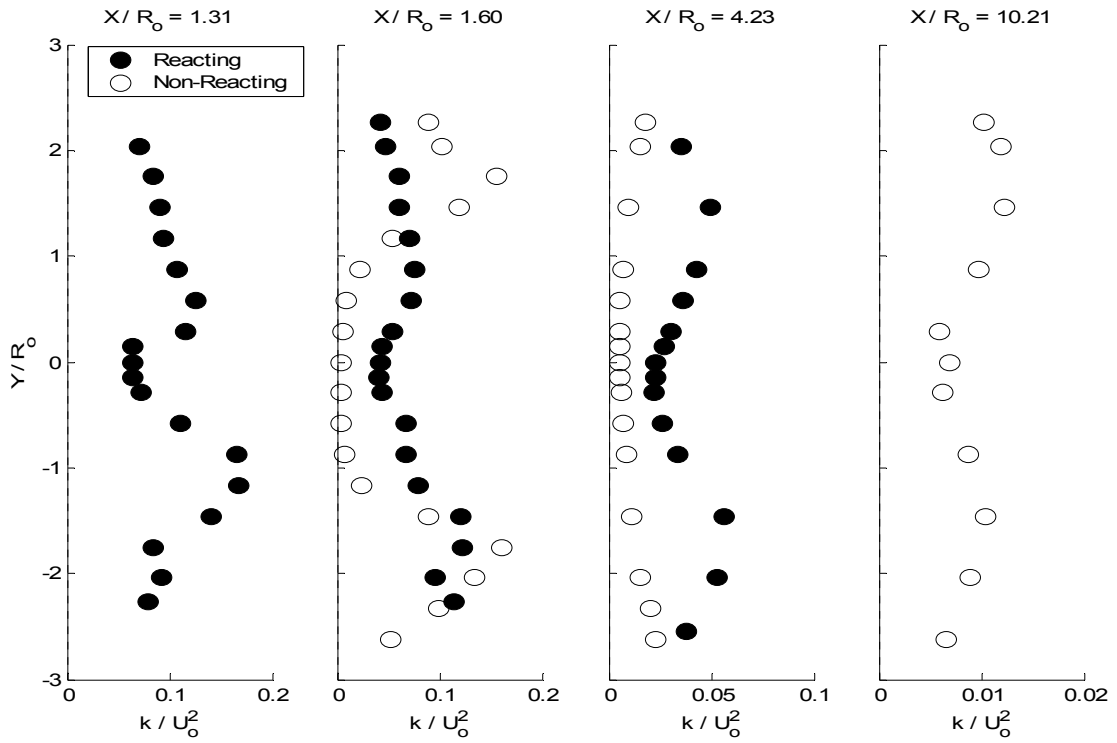


Figure A. 7 Z-Y plane ($Z/R_0 = 0$), Case 1 Reacting and Non-Reacting Turbulent Kinetic Energy

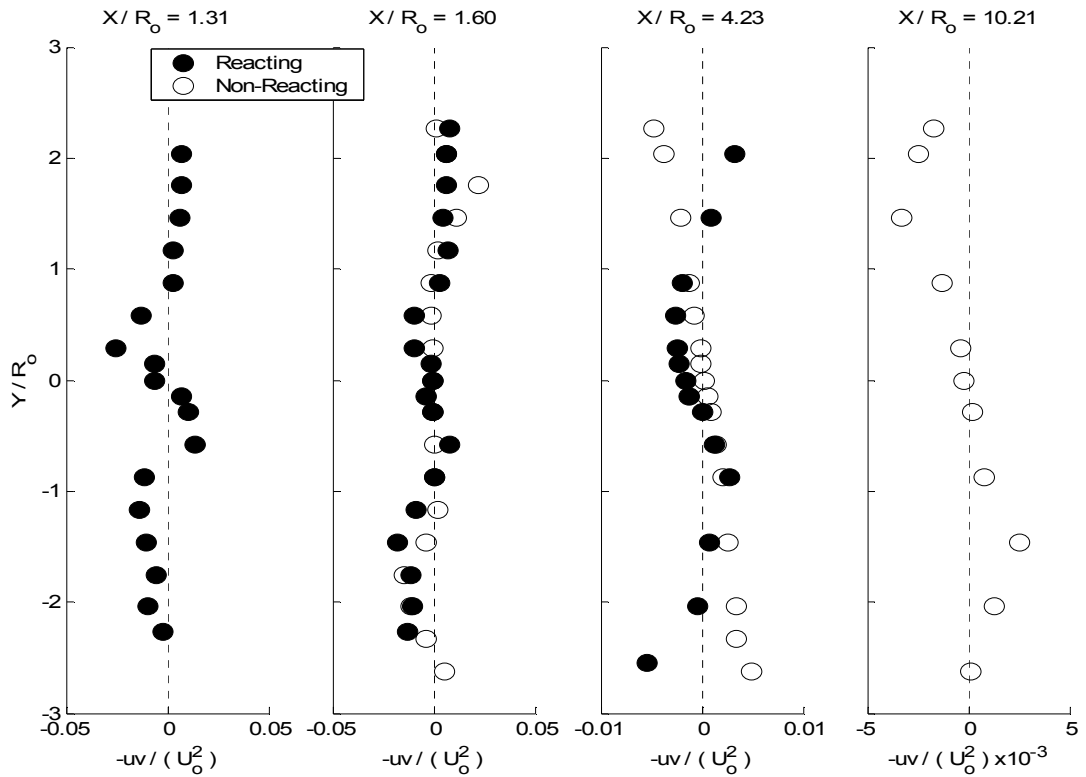


Figure A. 8 Z-Y plane ($Z/R_0 = 0$), Case 1 Reacting and Non-Reacting Reynolds Shear Stress

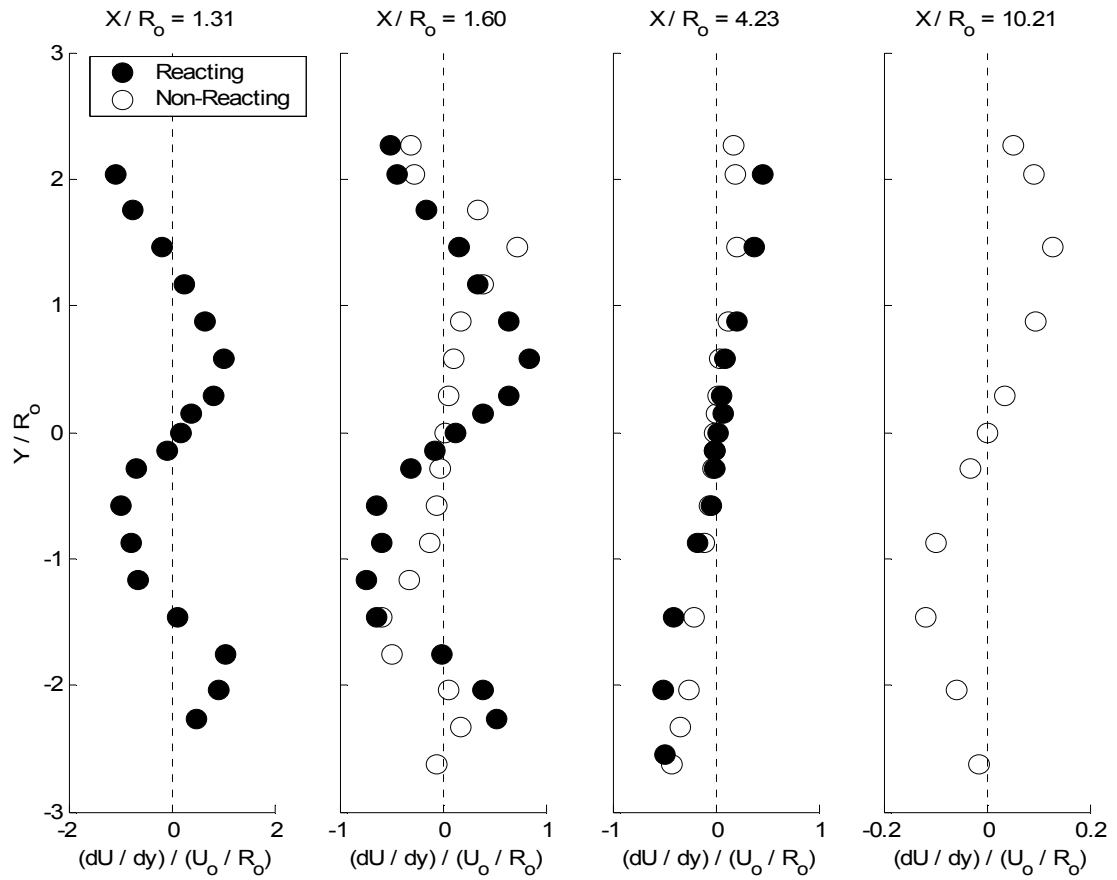


Figure A. 9 Z-Y plane ($Z/R_0 = 0$), Case 1 Reacting and Non-Reacting Axial Mean Velocity Vertical Gradient

Case 2

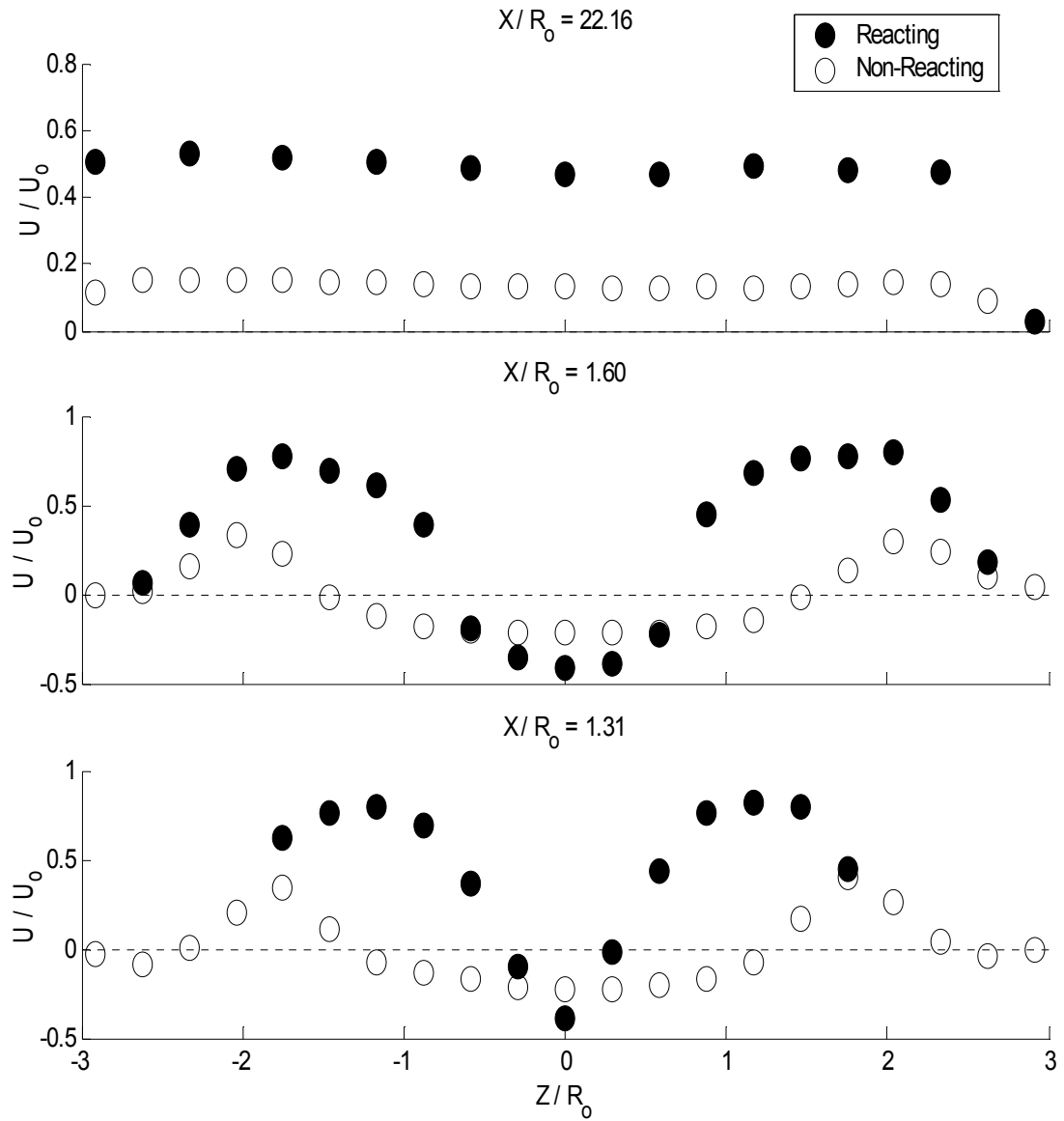


Figure A. 10 Z-Y plane ($Y/R_0 = 0$), Case 2 Reacting and Non-Reacting Axial Mean Velocity

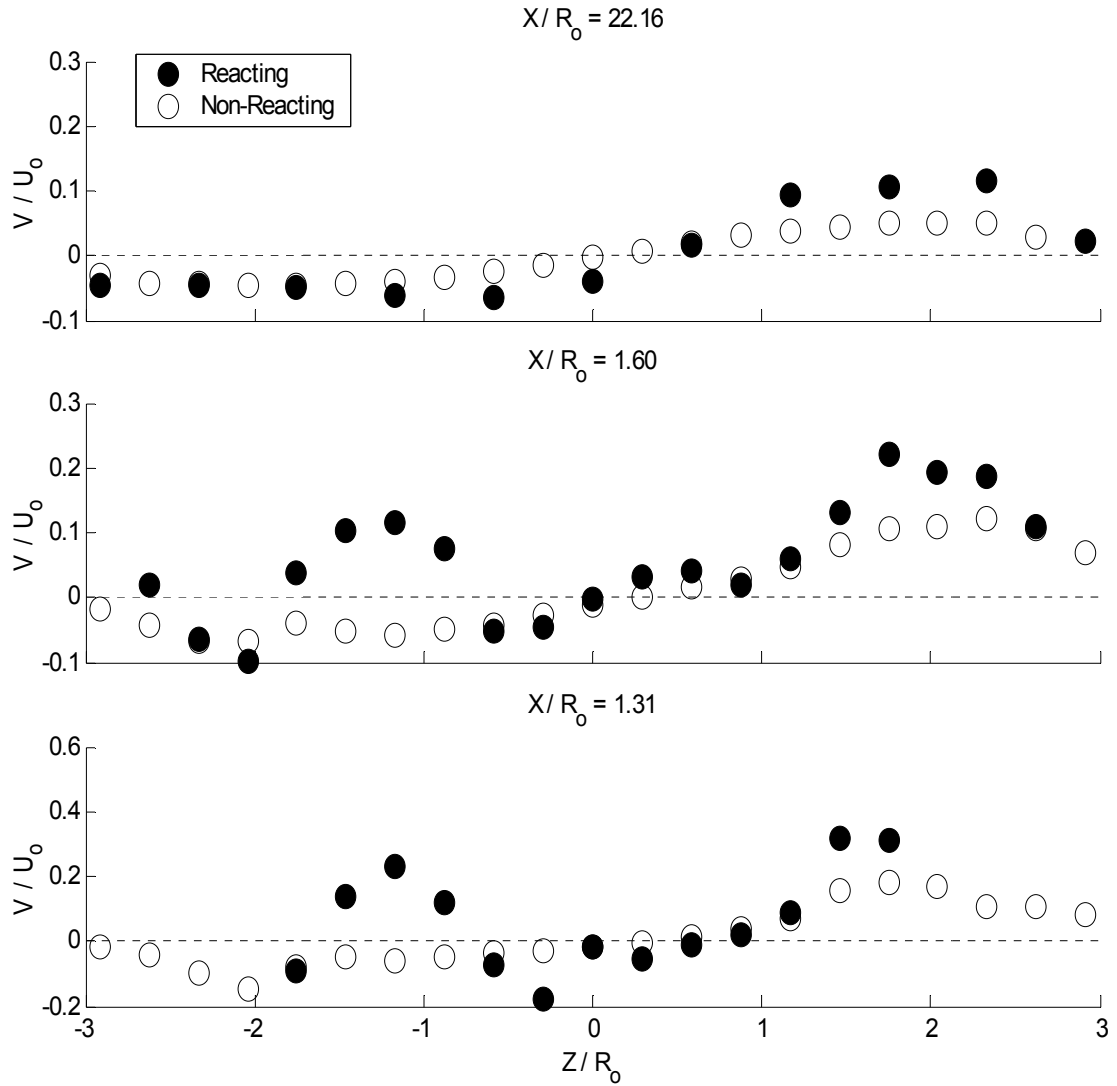


Figure A. 11 Z-Y plane ($Z/R_0 = 0$), Case 2 Reacting and Non-Reacting Vertical Mean Velocity

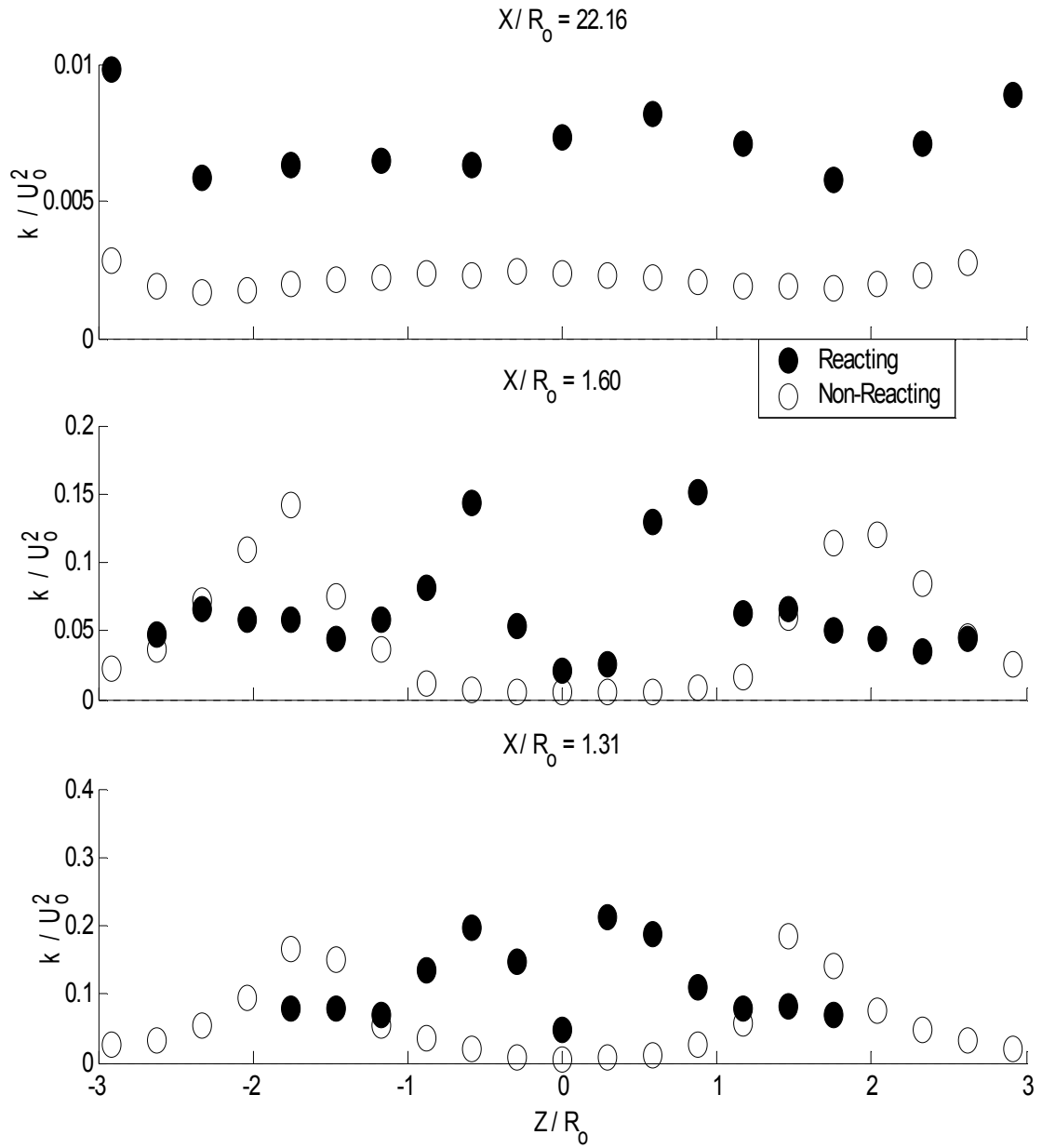


Figure A. 12 Z-Y plane ($Z/R_0 = 0$), Case 2 Reacting and Non-Reacting Turbulent Kinetic Energy

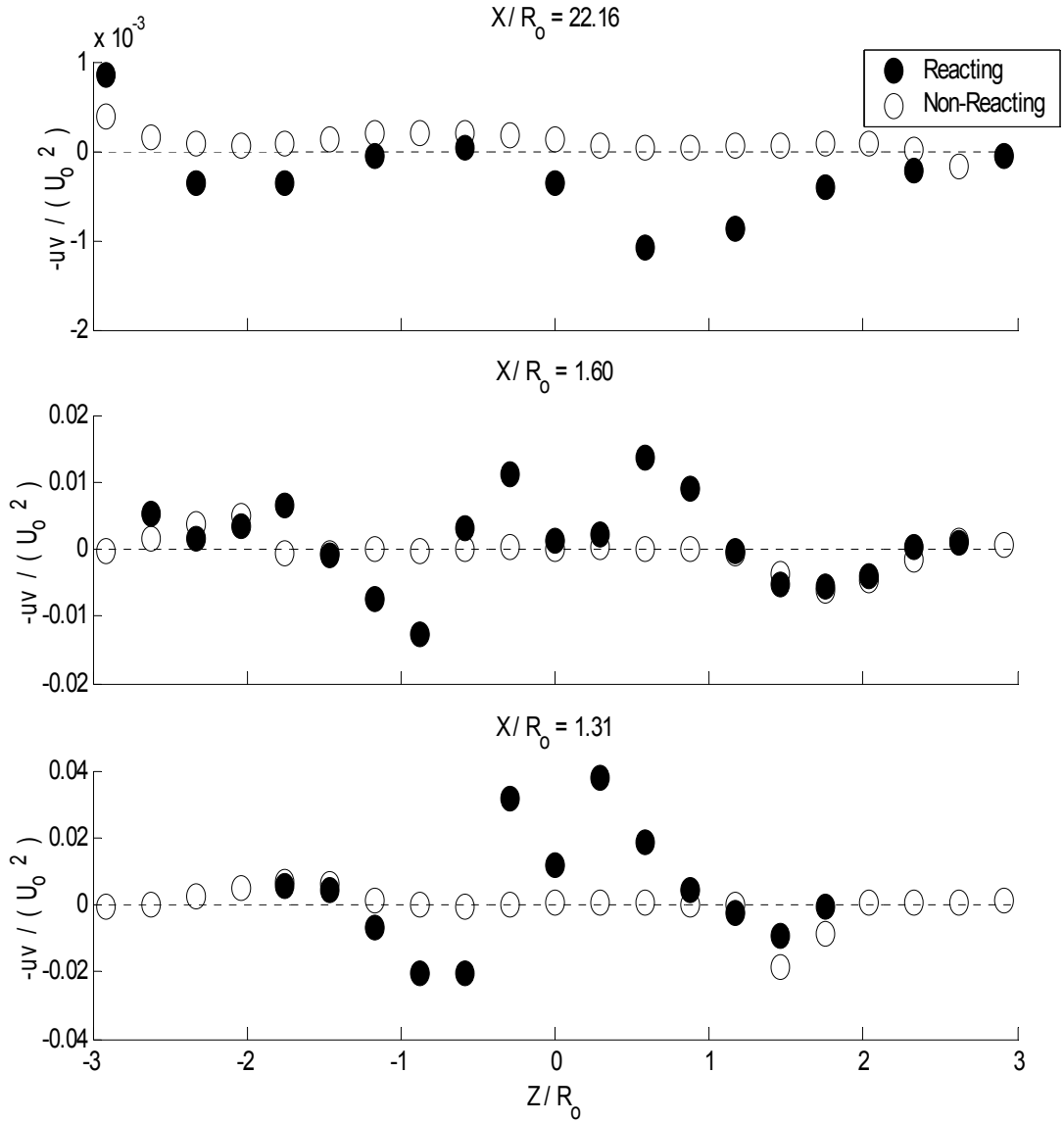


Figure A. 13 Z-Y plane ($Y/R_0 = 0$), Case 2 Reacting and Non-Reacting Reynolds Shear Stress

Non-Reacting Droplet vs. Non-Reacting Gas Phase $X/R_0 = 1.60$

Case 1

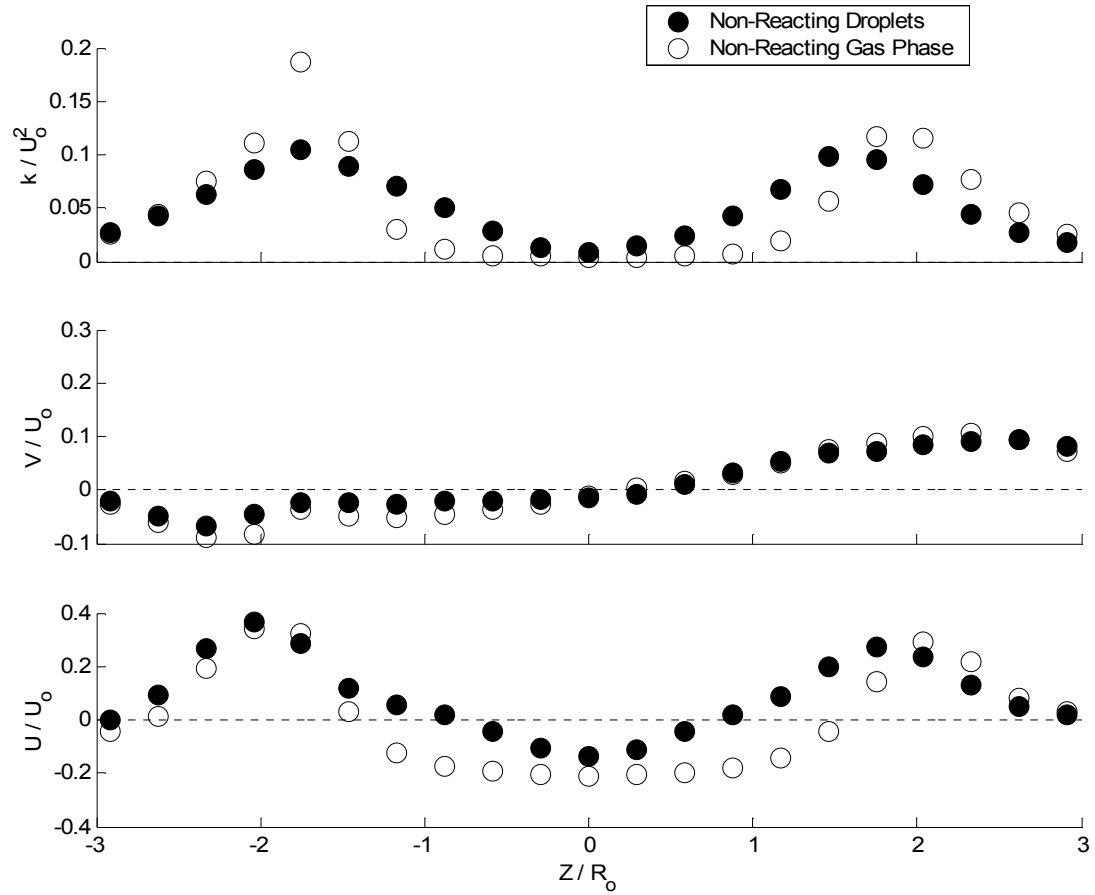


Figure A. 14 Z-Y plane at $X/R_0 = 1.60$ ($Y/R_0 = 0$), Case 1 Non-Reacting Droplet and Gas Phase Axial, Vertical Mean Velocity, Turbulent Kinetic Energy

Reacting Droplet vs. Reacting Gas Phase Flow Field

Case 1

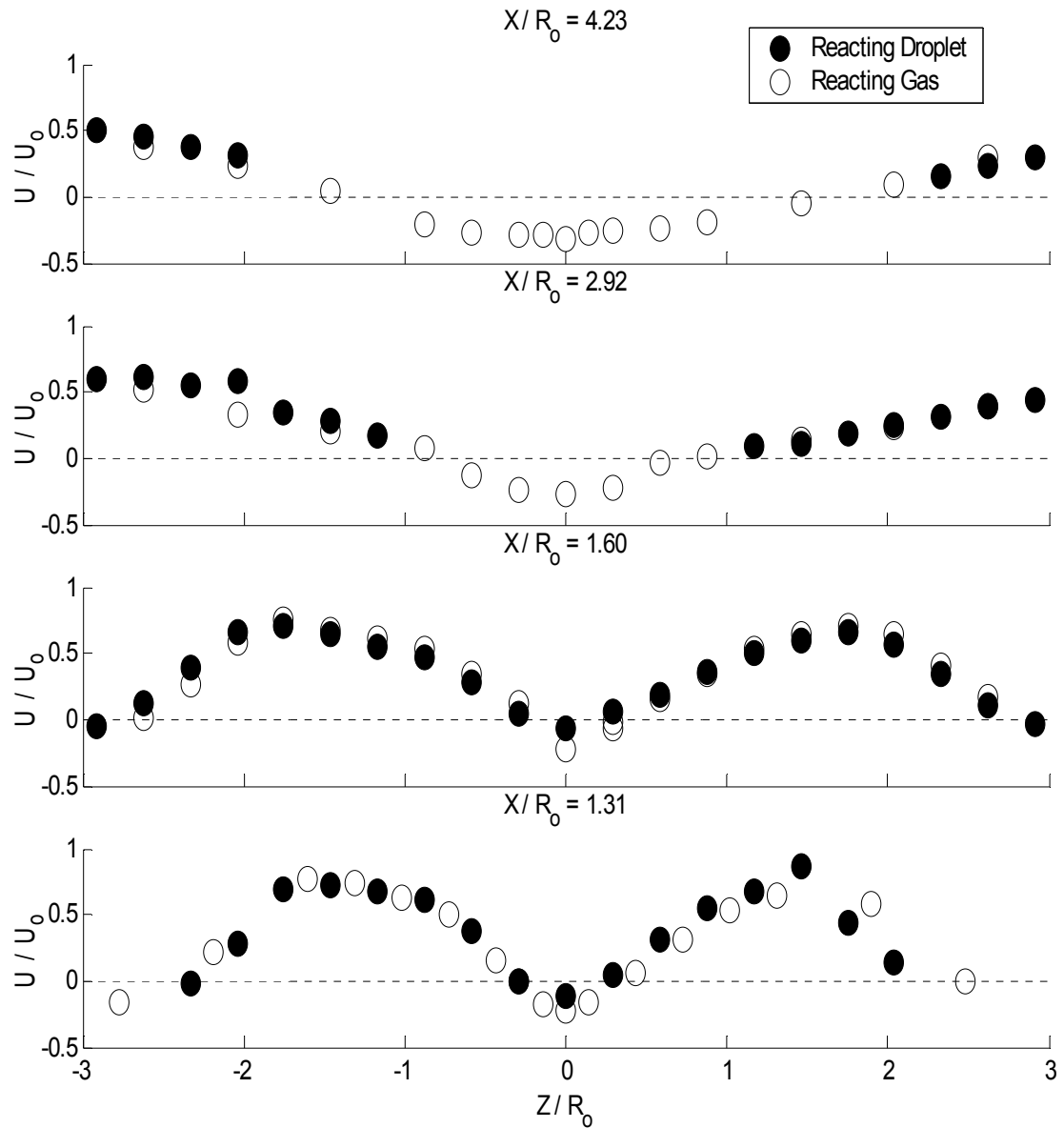


Figure A. 15 Z-Y plane ($Y/R_0 = 0$), Case 1 Reacting Droplet and Gas Phase Axial Mean Velocity

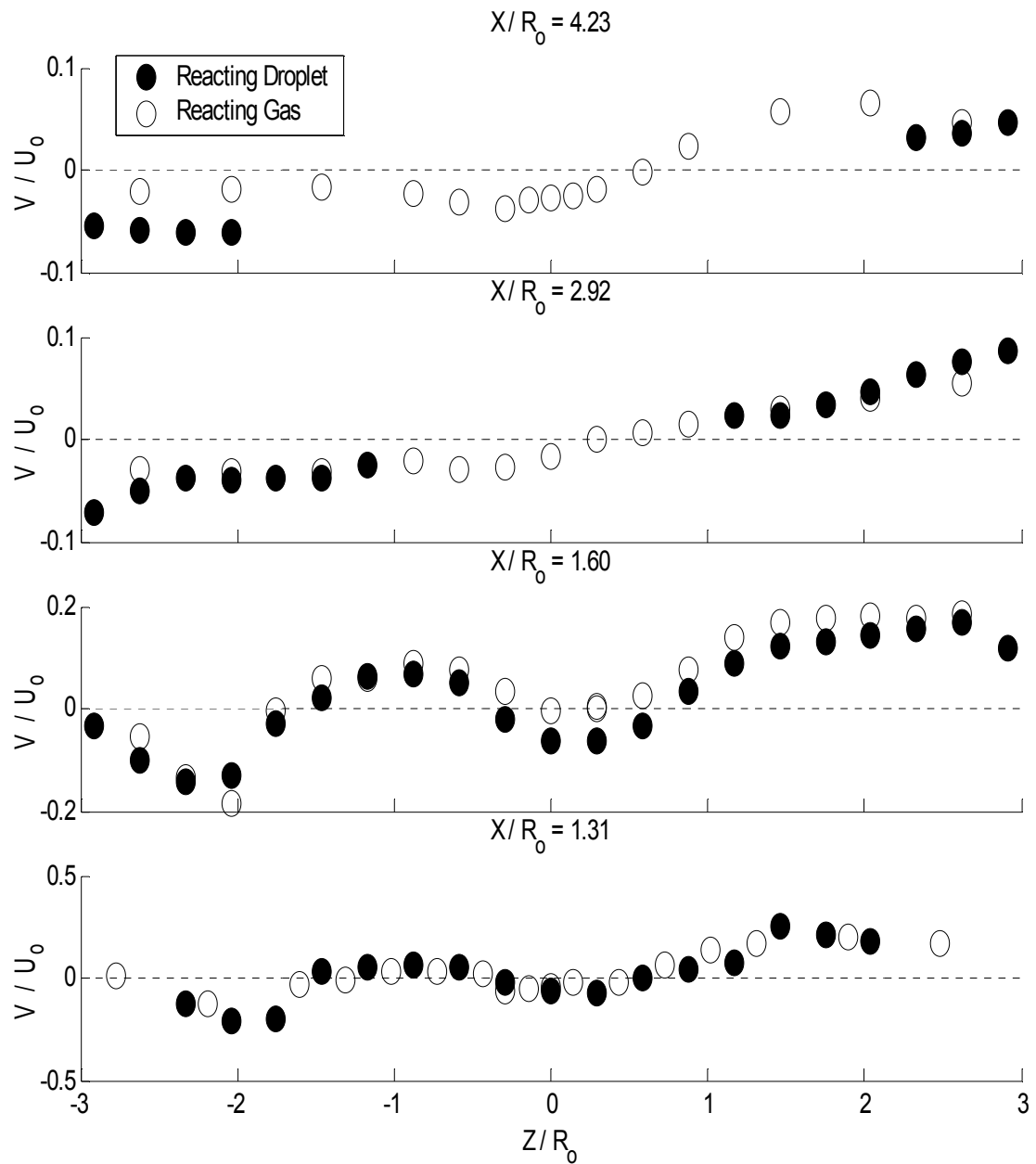


Figure A. 16 Z-Y plane ($Z/R_0 = 0$), Case 1 Reacting Droplet and Gas Phase Vertical Mean Velocity

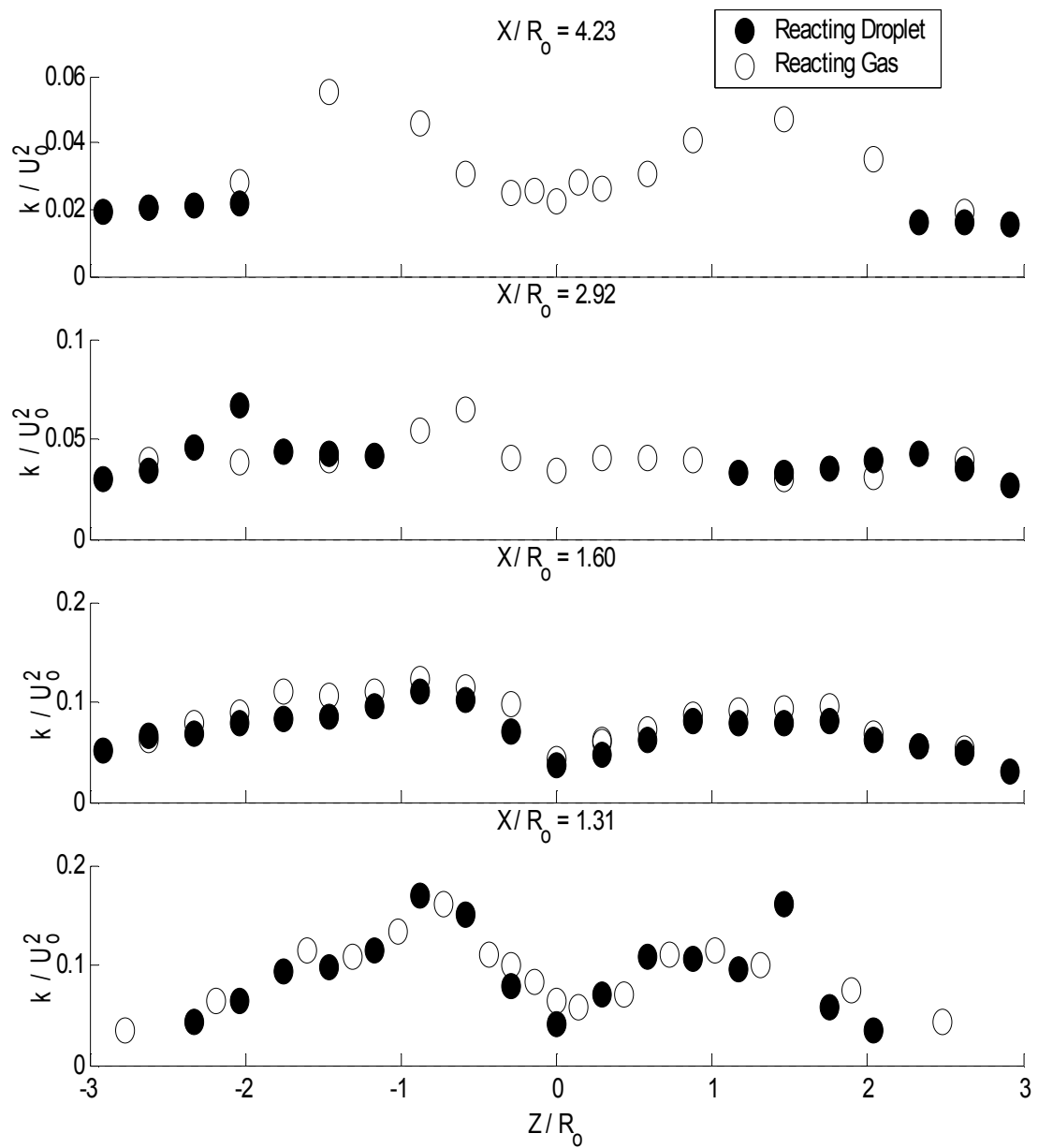


Figure A.17 Z-Y plane ($Z/R_0 = 0$), Case 1 Reacting Droplet and Gas Phase Turbulent Kinetic Energy

Case 2

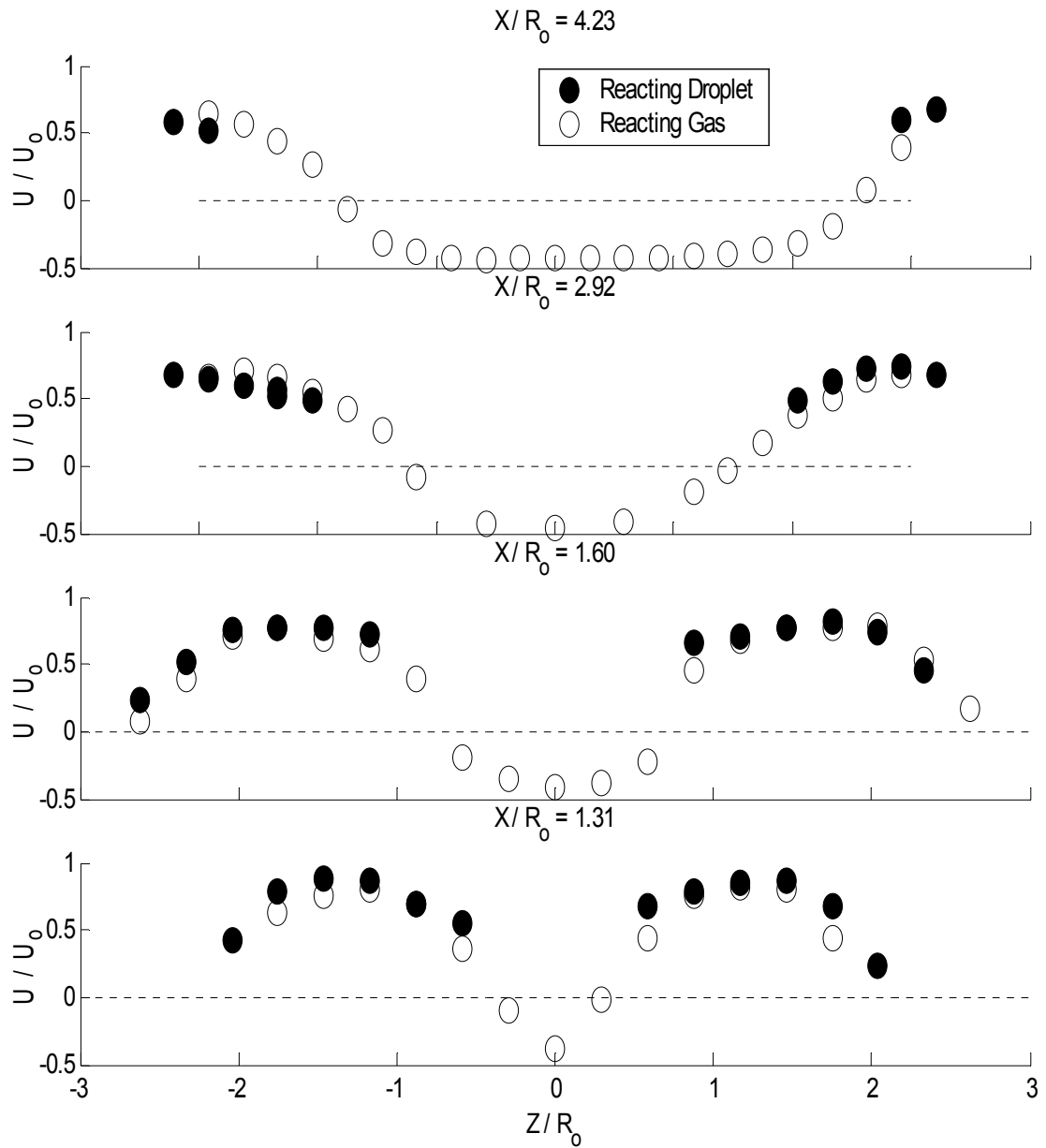


Figure A. 18 Z-Y plane ($Y/R_0 = 0$), Case 2 Reacting Droplet and Gas Phase Axial Mean Velocity

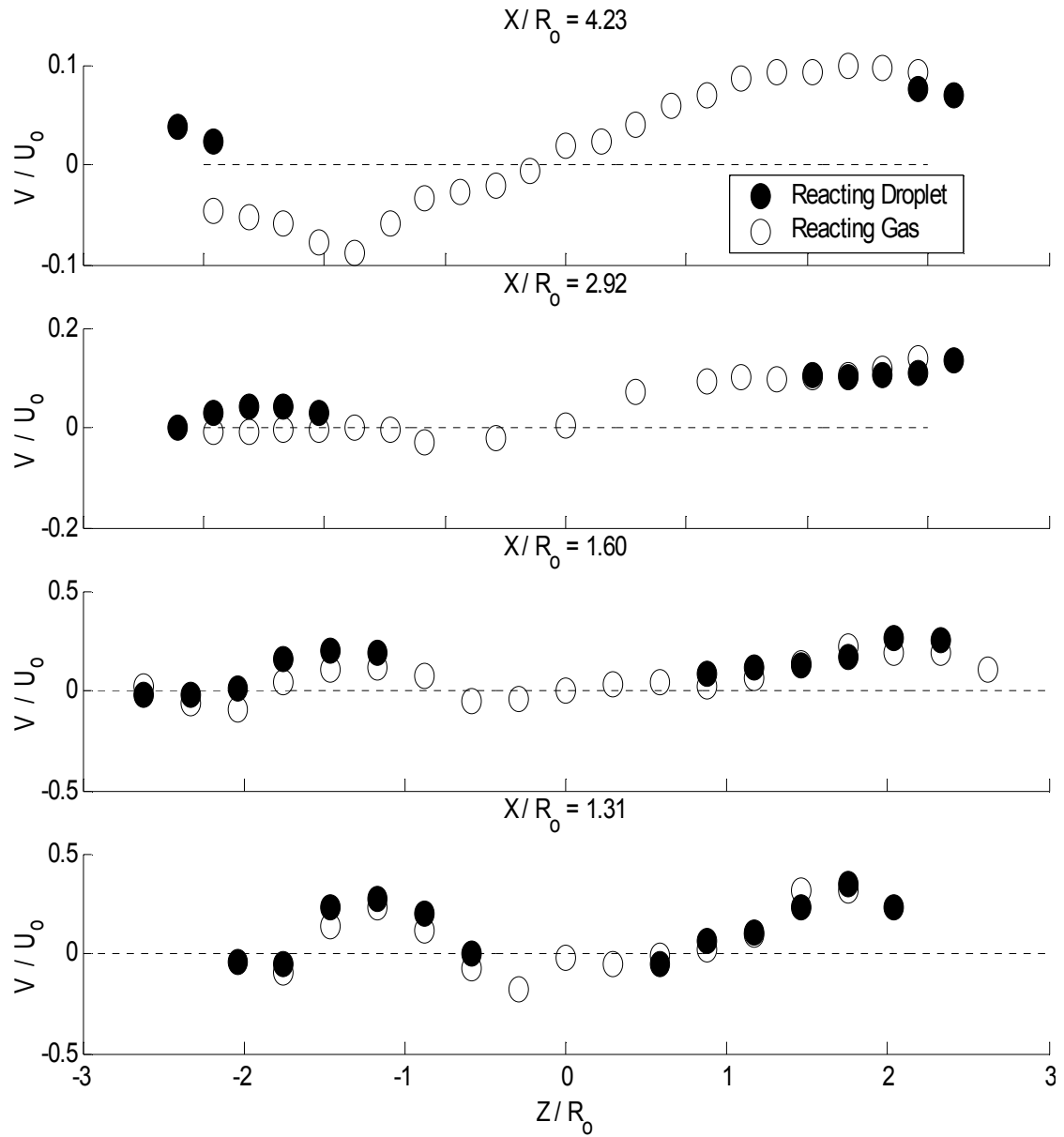


Figure A. 19 Z-Y plane ($Y/R_0 = 0$), Case 2 Reacting Droplet and Gas Phase Vertical Mean Velocity

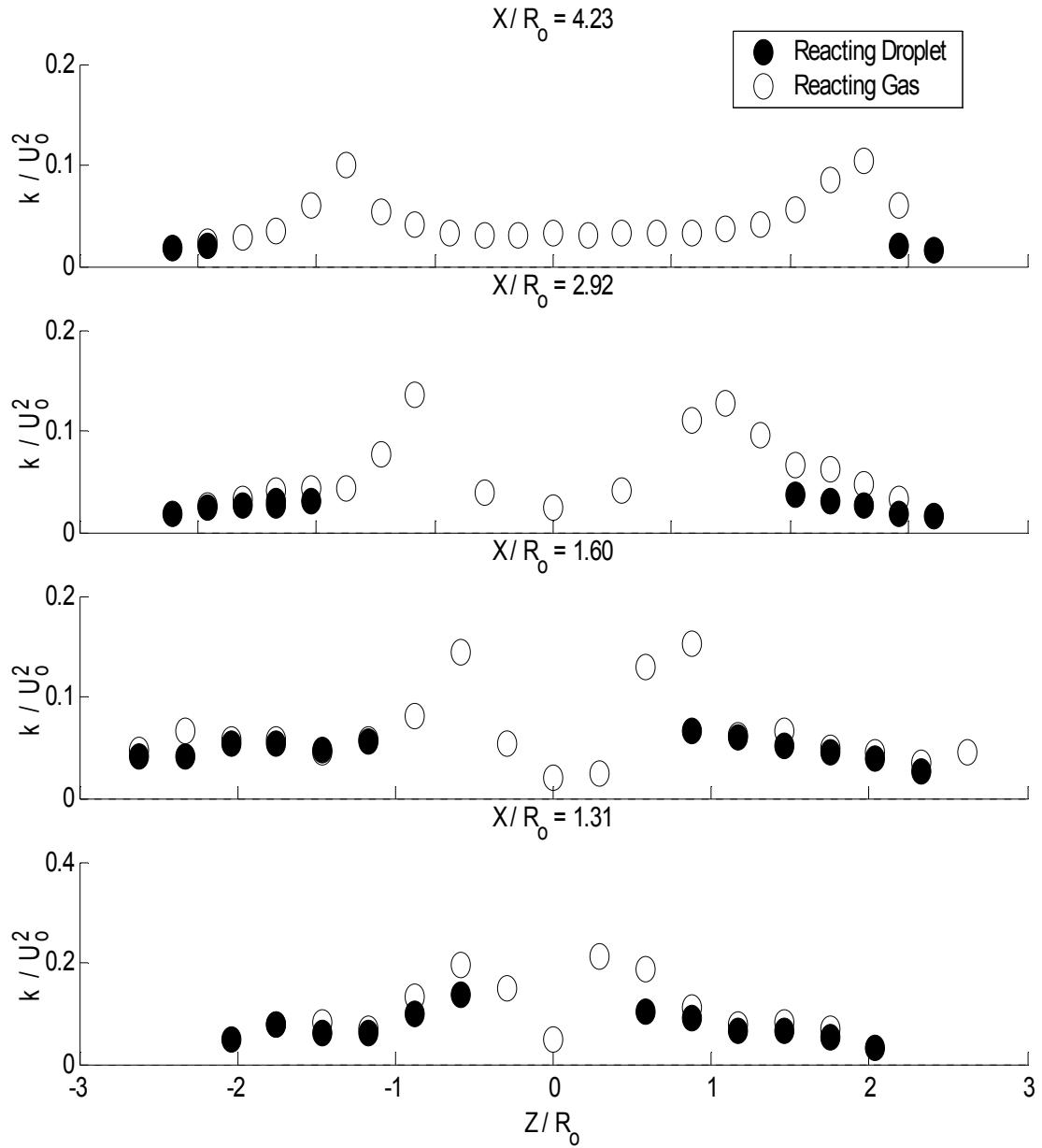


Figure A. 20 Z-Y plane ($Y/R_0 = 0$), Case 2 Reacting Droplet and Gas Phase Turbulent Kinetic Energy

APPENDIX B
CONTOUR PLOT COMPARISONS

Case 1

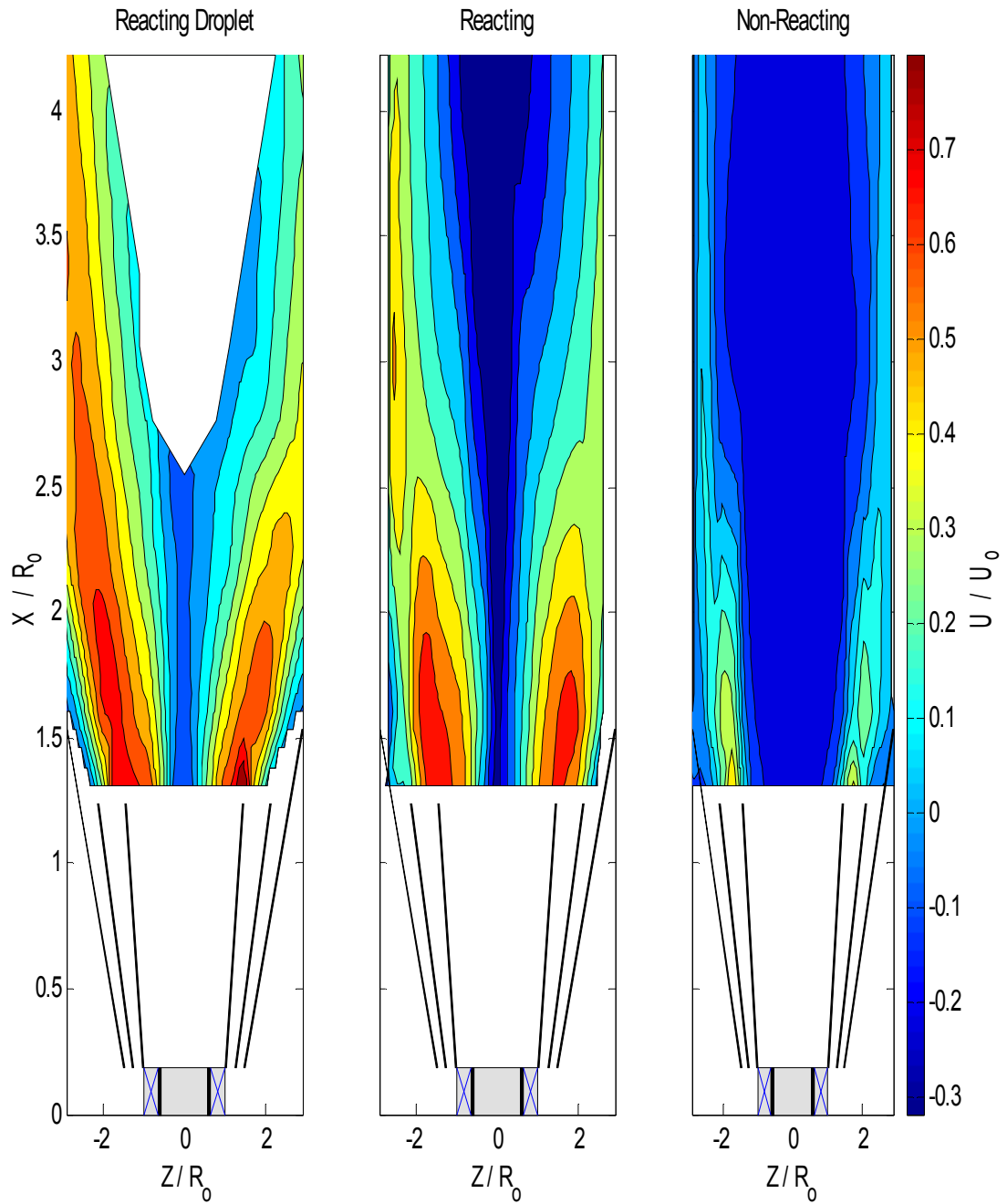


Figure B. 1 Z-X plane ($Y/R_0 = 0$), Case 1 Axial Mean Velocity Comparison

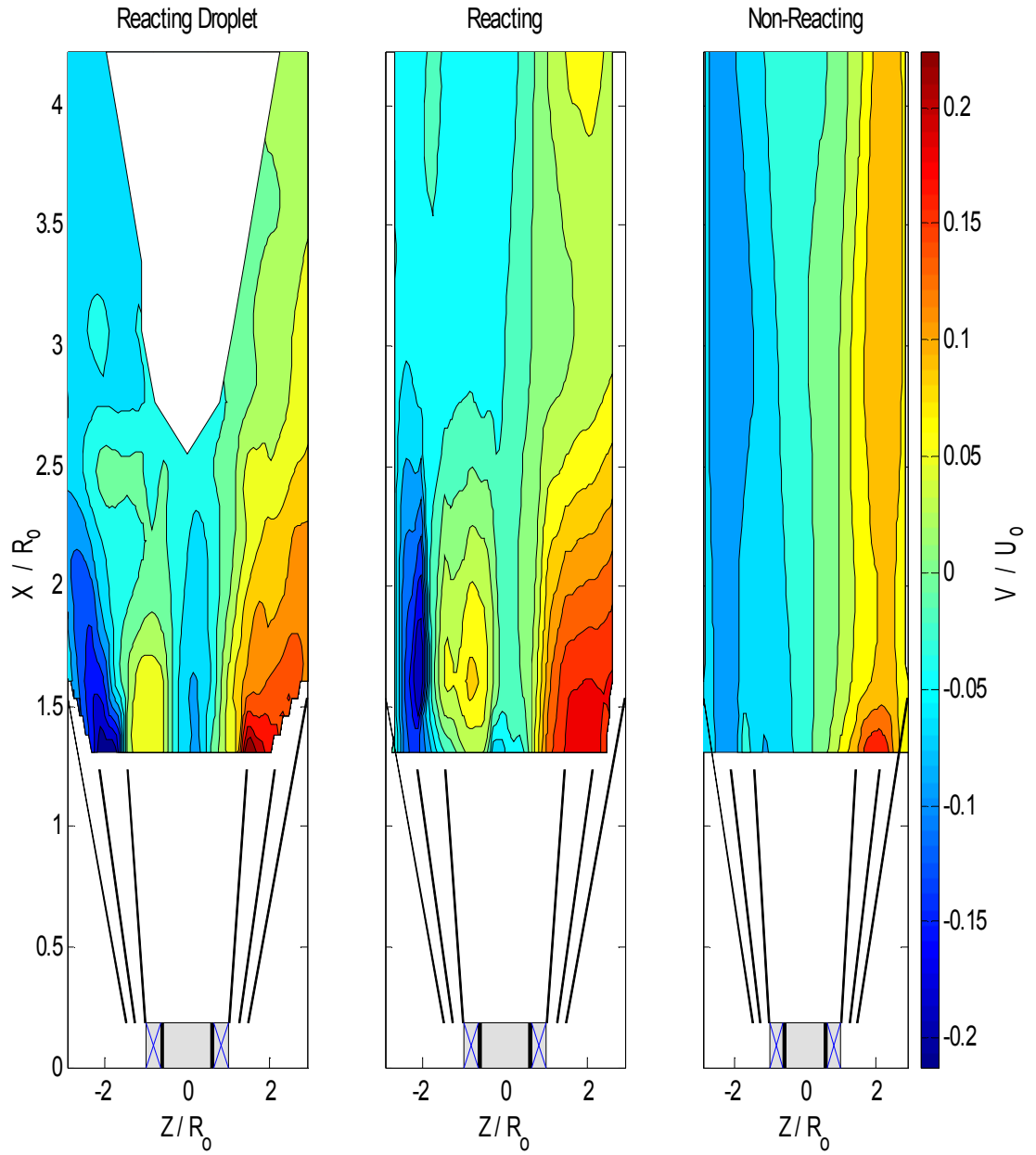


Figure B. 2 Z-X plane ($Y/R_0 = 0$), Case 1 Vertical Mean Velocity Comparison

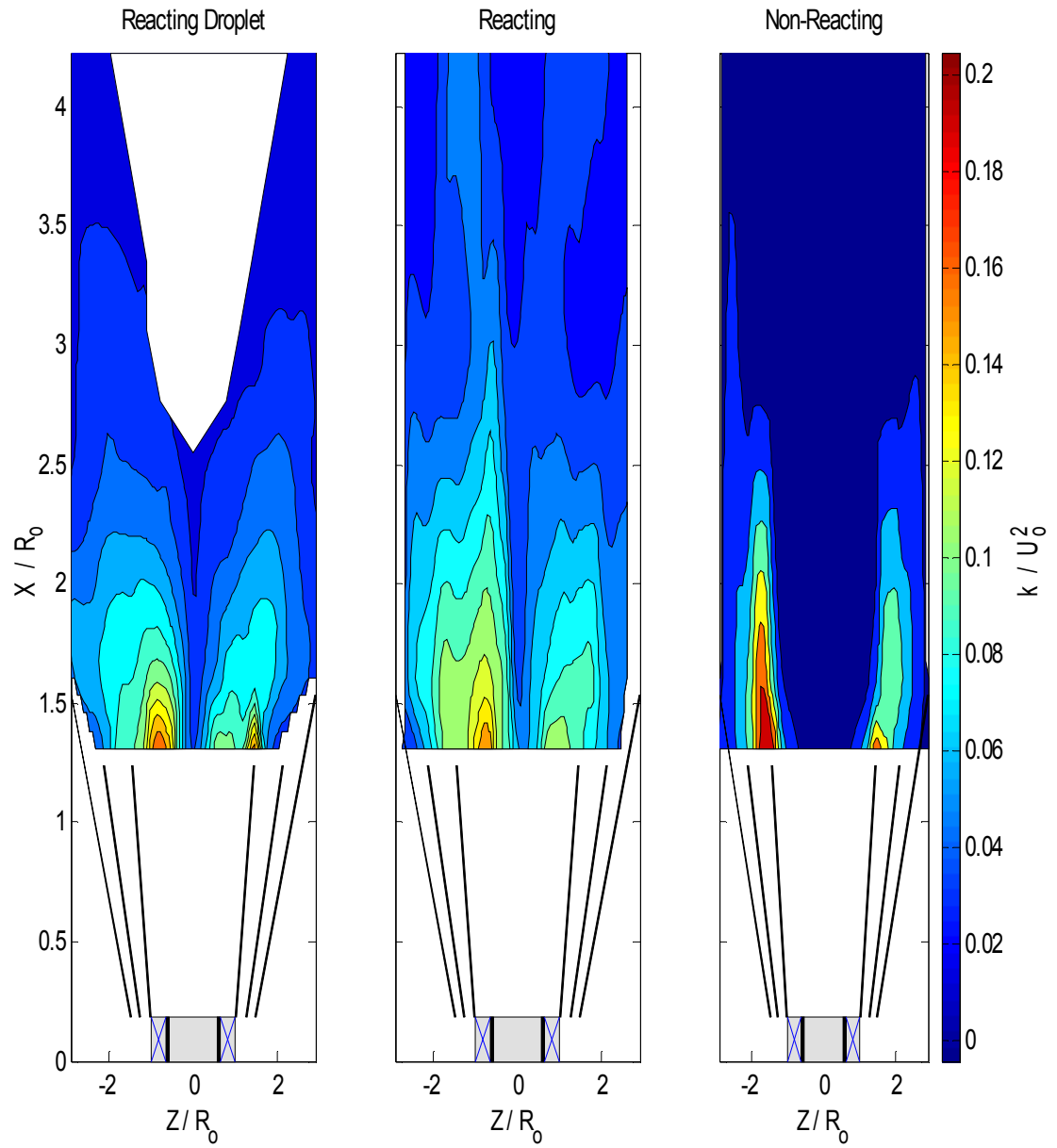


Figure B. 3 Z-X plane ($Y/R_0 = 0$), Case 1 Turbulent Kinetic Energy Comparison

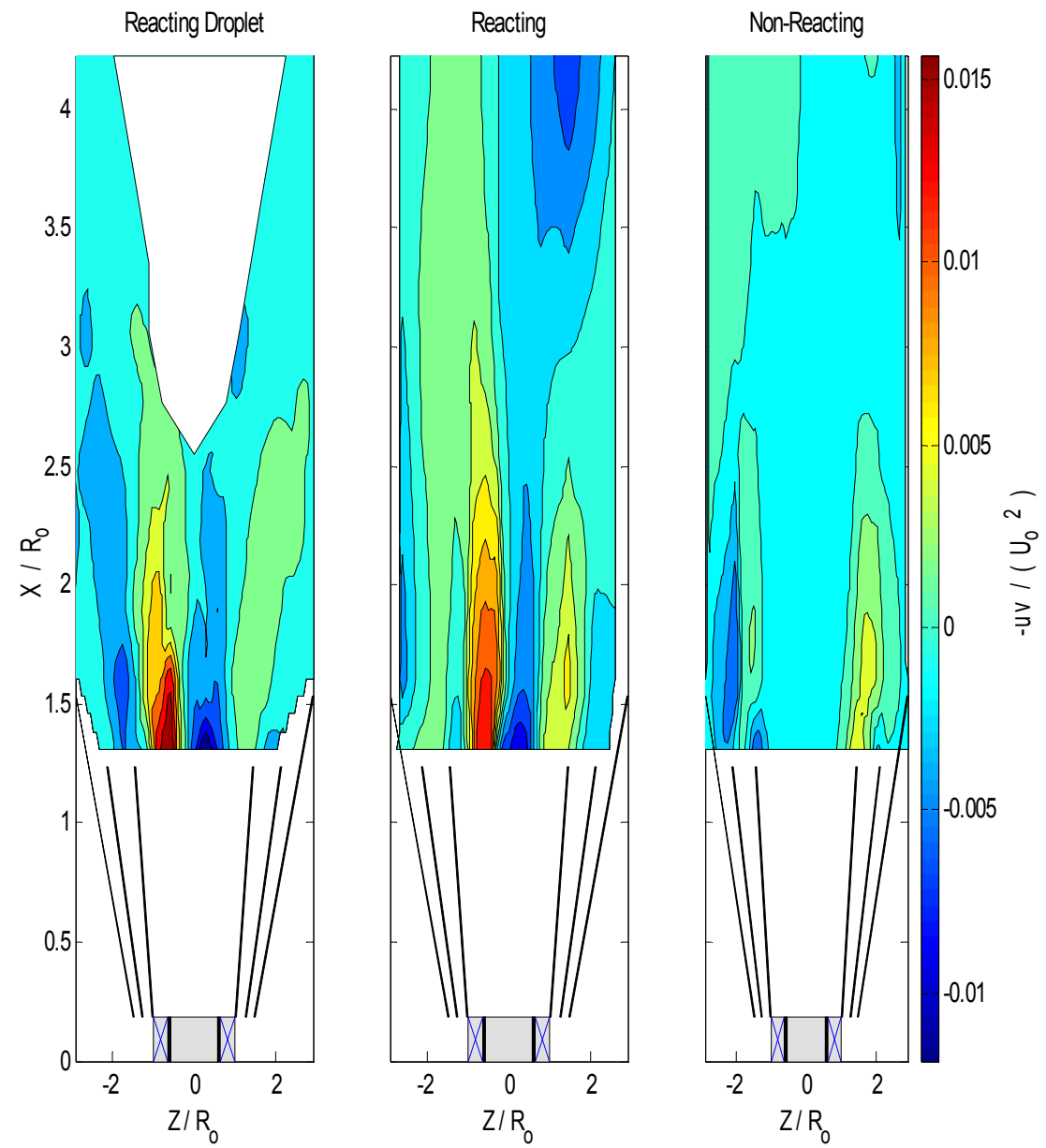


Figure B. 4 Z-X plane ($Y/R_0 = 0$), Case 1 Reynolds Shear Stress Comparison

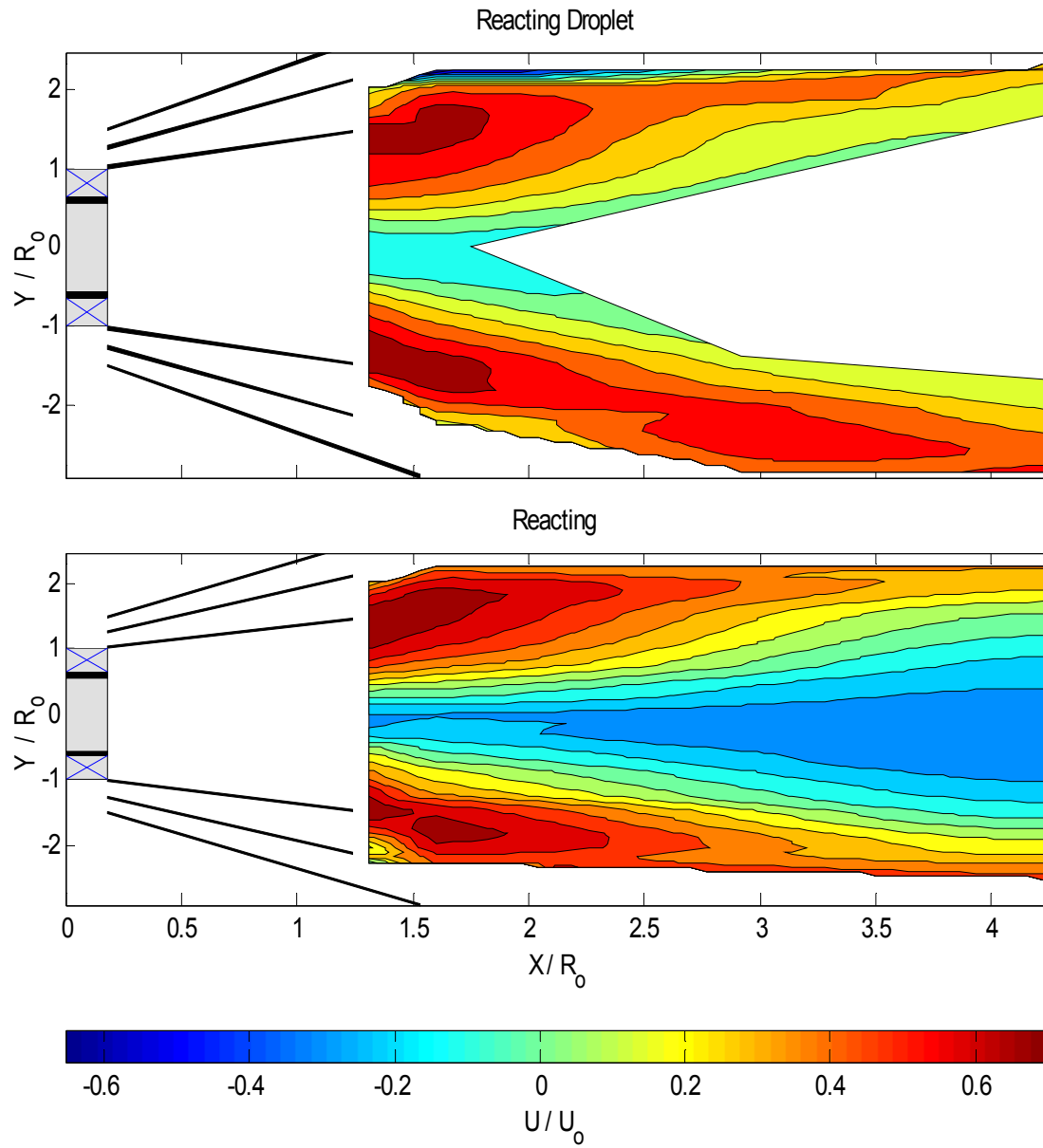


Figure B. 5 X-Y plane ($Z/R_0 = 0$), Case 1 Axial Mean Velocity Comparison

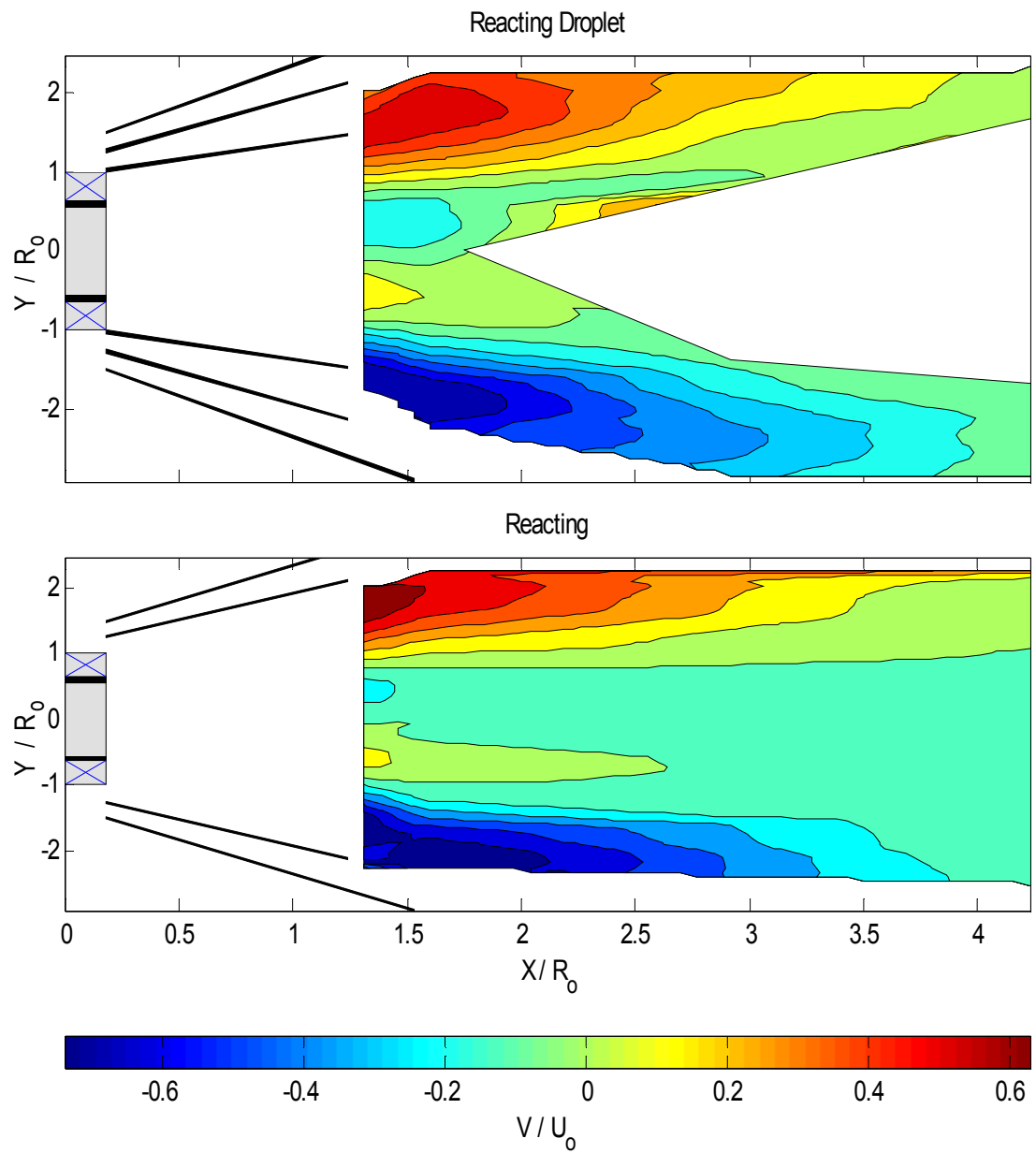


Figure B. 6 X-Y plane ($Z/R_0 = 0$), Case 1 Vertical Mean Velocity Comparison

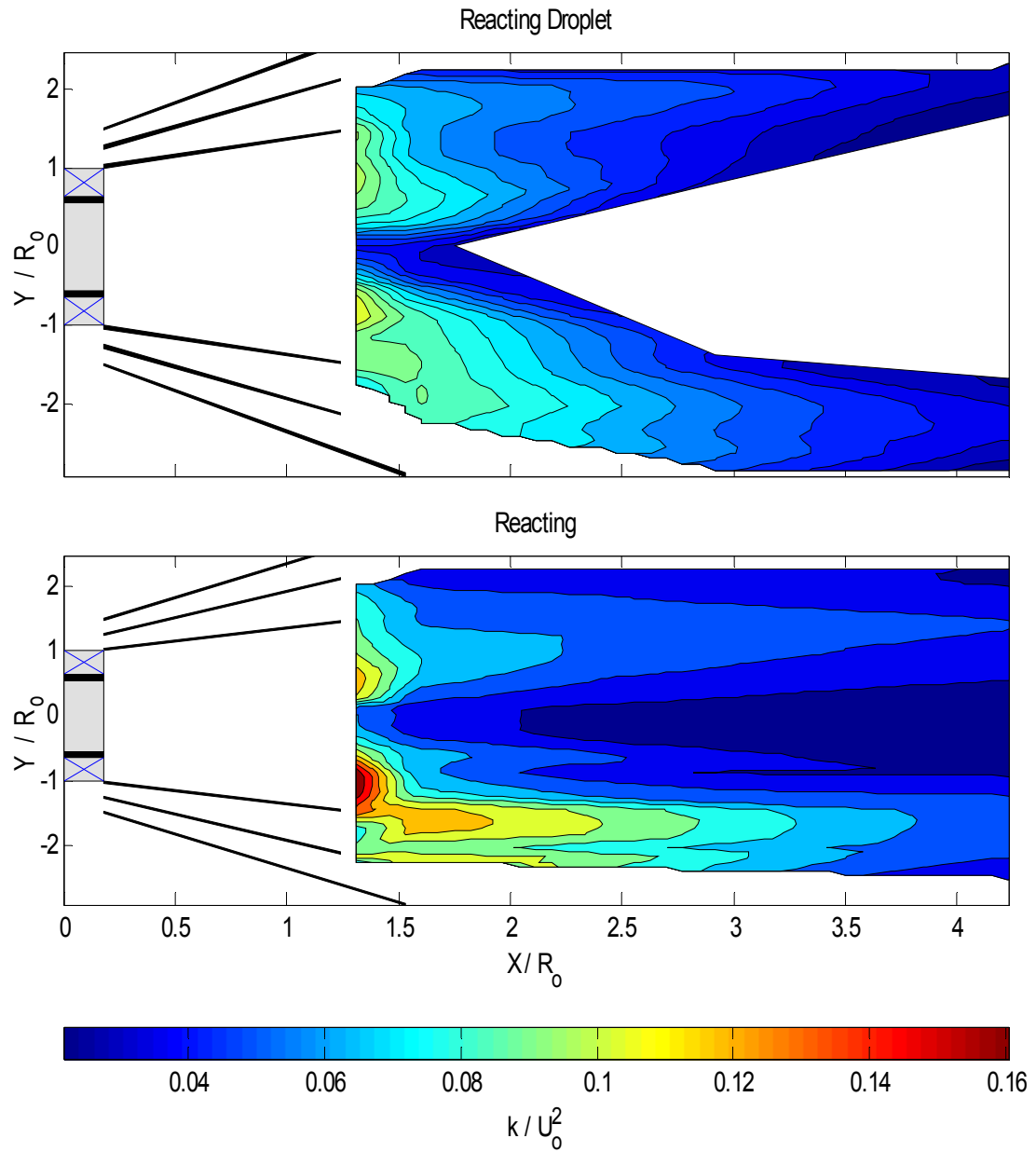


Figure B. 7 X-Y plane ($Z/R_0 = 0$), Case 1 Turbulent Kinetic Energy Comparison

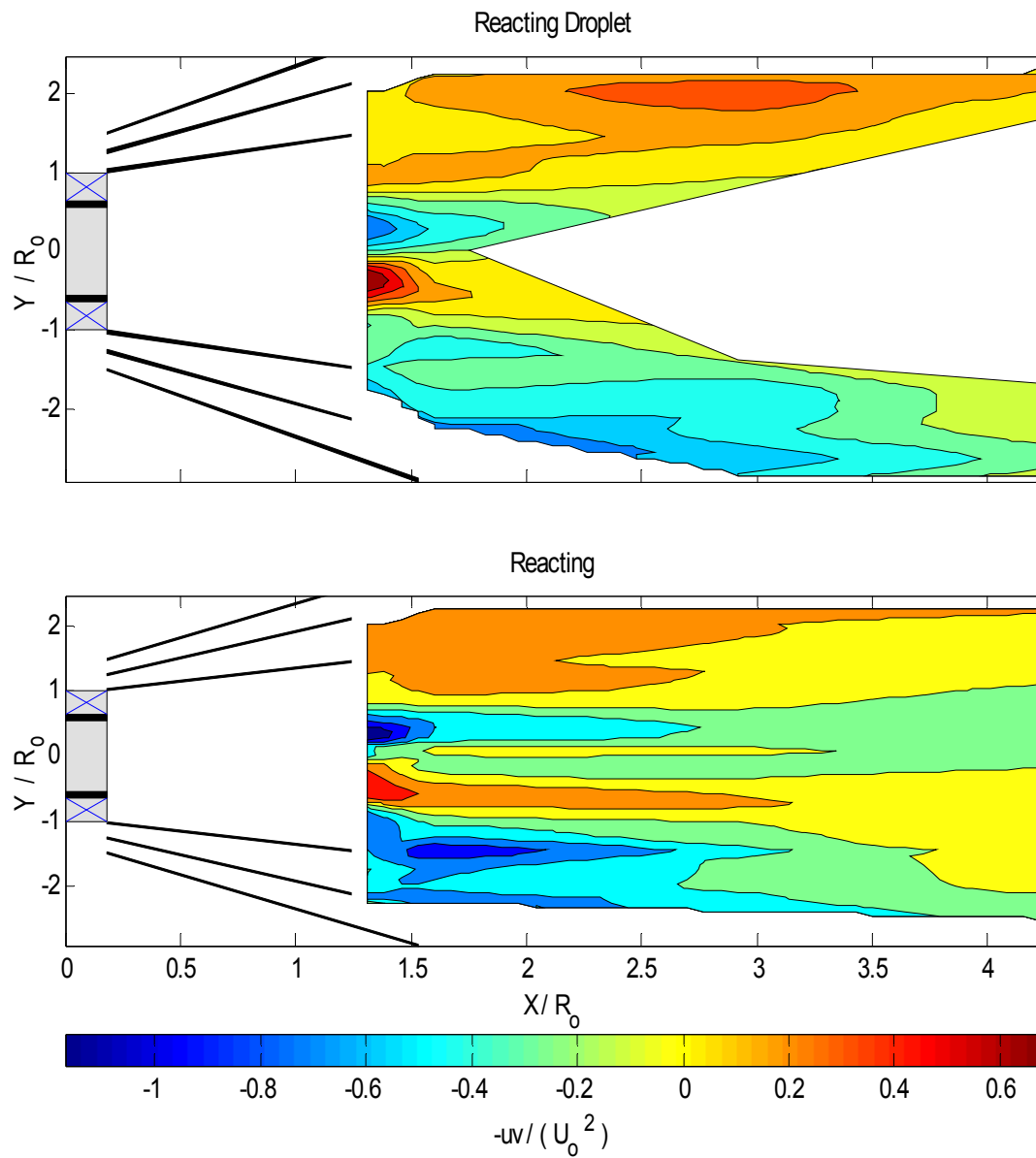


Figure B. 8 X-Y plane ($Z/R_0 = 0$), Case 1 Reynolds Shear Stress Comparison

Case 2

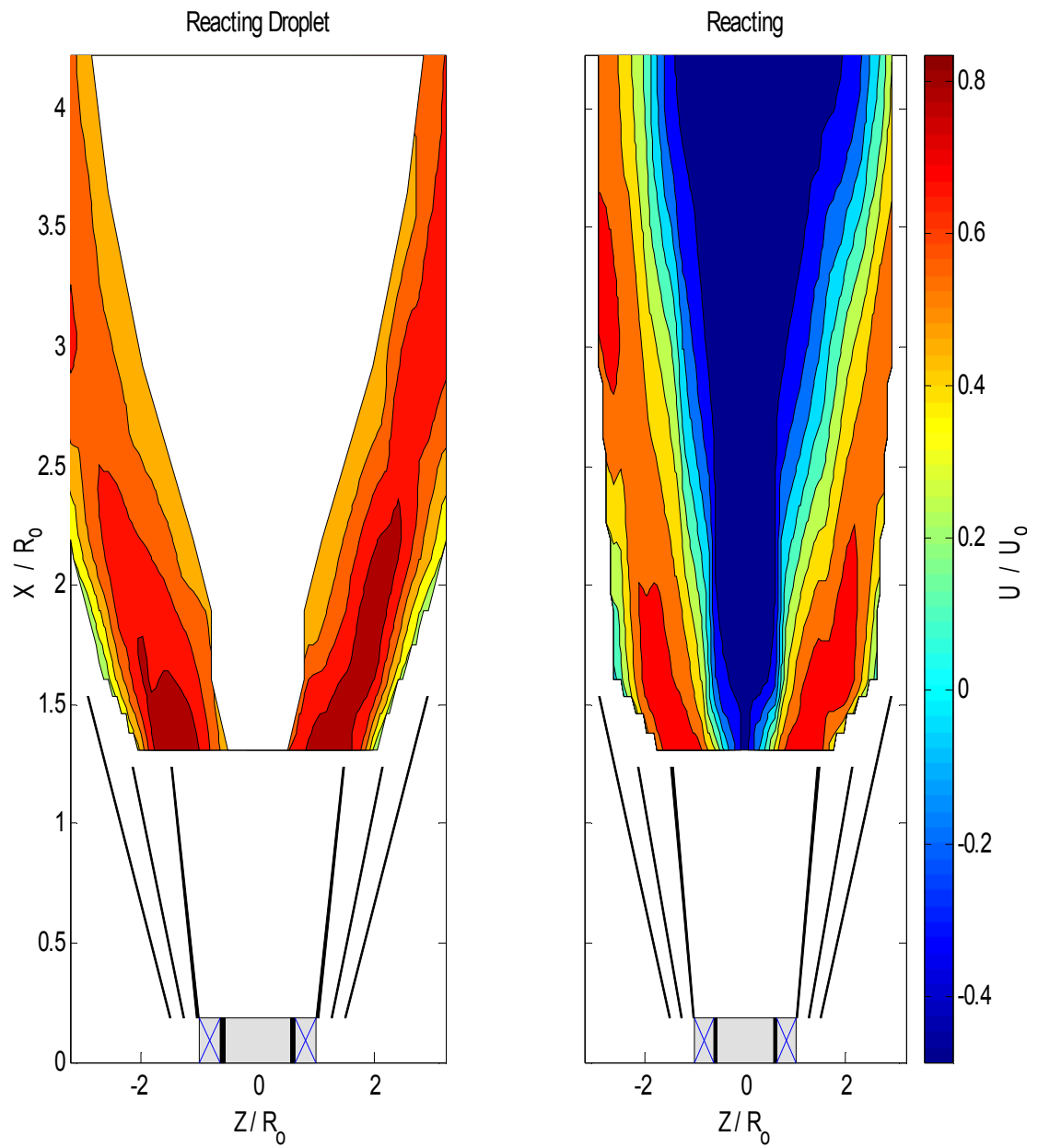


Figure B. 9 Z-X plane ($Y/R_0 = 0$), Case 2 Axial Mean Velocity Comparison

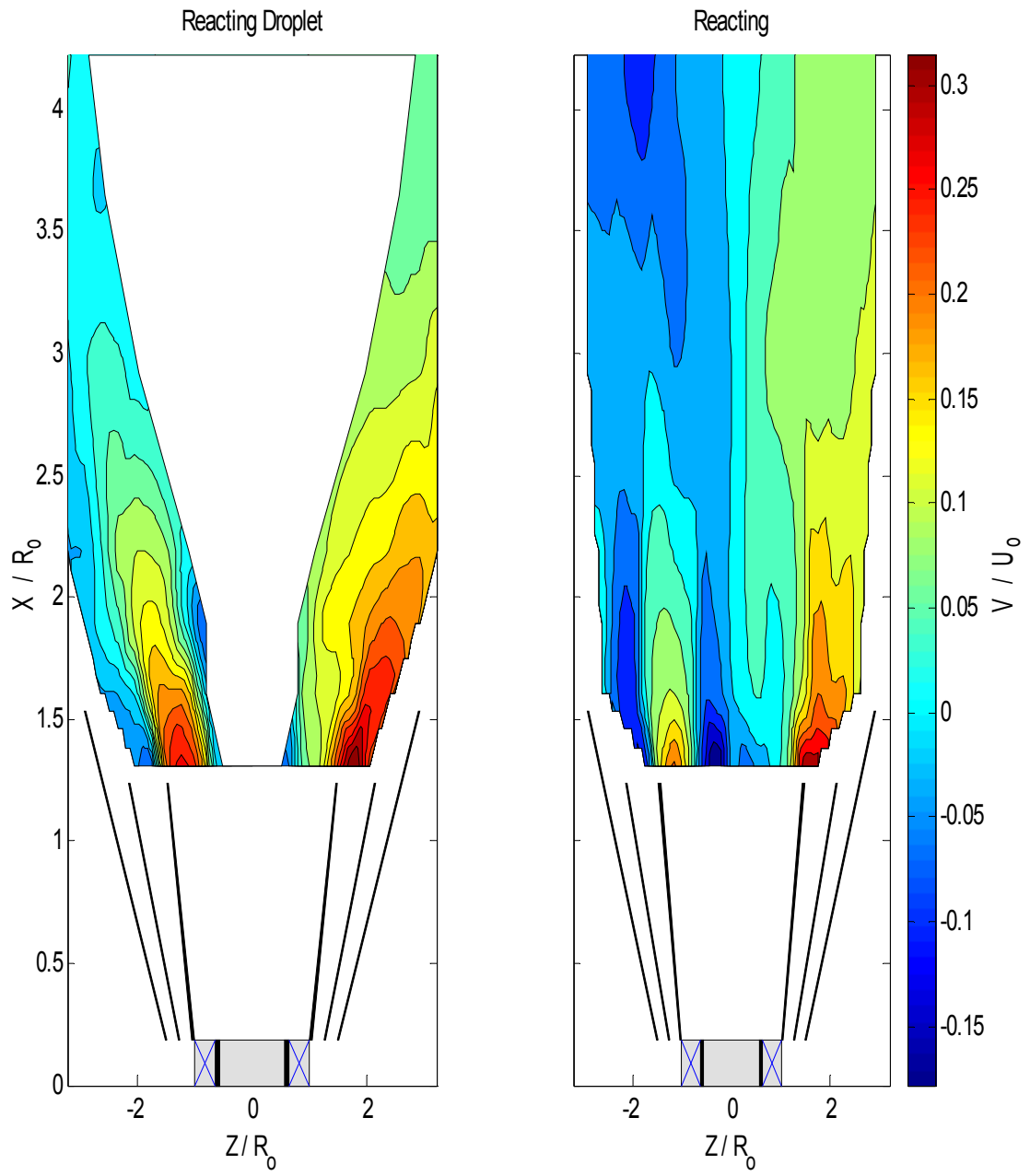


Figure B. 10 Z-X plane ($Y/R_0 = 0$), Case 2 Vertical Mean Velocity Comparison

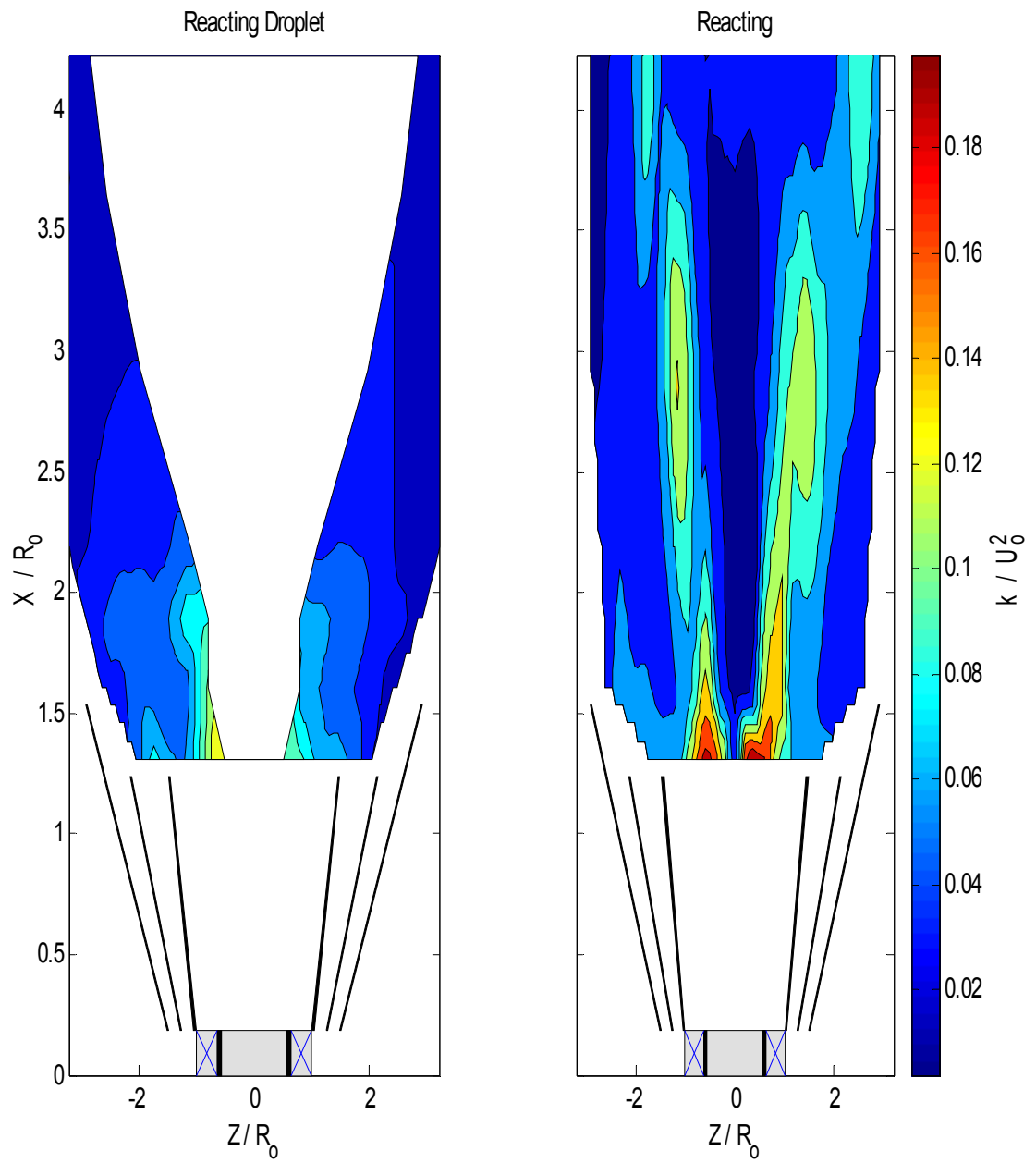


Figure B. 11 Z-X plane ($Y/R_0 = 0$), Case 2 Turbulent Kinetic Energy Comparison

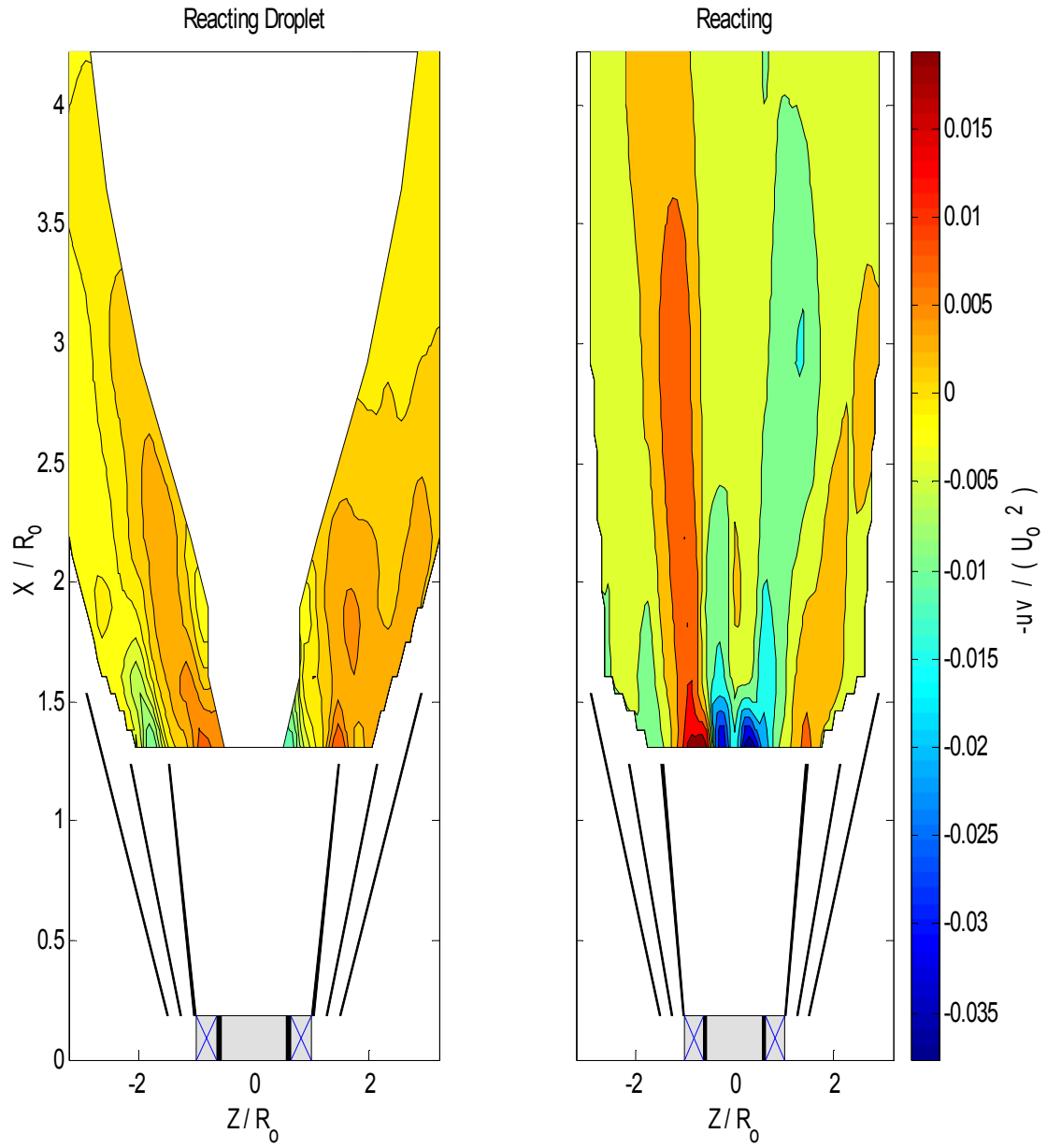


Figure B. 12 Z-X plane ($Y/R_0 = 0$), Case 2 Reynolds Shear Stress Comparison

REFERENCES

- [1] LEFEBVRE, A.H., Gas Turbine Combustion, Taylor and Francis, Philadelphia, PA, 1999.
- [2] NAIR, S. et al., "Lean blowout detection in a single nozzle swirl cup combustor," AIAA Paper 2004-0138, Presented at the 42nd Aerospace Sciences Meeting and Exhibit, Reno, NV, 2004.
- [3] CHIGIER, N.A. and BEER, J.M., Combustion Aerodynamics, John Wiley and Sons, Inc., New York, NY, 1972.
- [4] SYRED, N. and BEER, J.M., "Effect of combustion upon precessing vortex cores generated by swirl combustors," *Fourteenth Symposium (International) on Combustion*, The Combustion Institute, Pittsburgh, p. 537-550, 1973.
- [5] SYRED, N., GUPTA, A.K., and BEER, J.M., "Temperature and density gradient changes arising with the precessing vortex core and vortex breakdown in swirl burners," *Fifteenth Symposium (International) on Combustion*, The Combustion Institute, Pittsburgh, p. 587-597, 1974.
- [6] CHIGIER, N.A. and DVORAK, K., "Laser anemometer measurements in flames with swirl," *Fifteenth Symposium (International) on Combustion*, The Combustion Institute, Pittsburgh, pp. 573-585, 1974.
- [7] OWEN, F.K., "Measurements and observations of turbulent recirculating jet flows," AIAA J., vol. 14, no. 11, pp. 1556-1562, 1976.
- [8] OWEN, F.K., et al., "Effects of inlet swirl and fuel volatility on the structure of confined spray flames," *Symposium (International) on Combustion*, The Combustion Institute, Pittsburgh, pp. 467-473, 1979.
- [9] GUPTA, A.K., BEER, J.M., AND SWITHEENBANK, J., "Concentric multi-annular swirl burner: stability limits and emission characteristics," Combustion Institute, Pittsburgh, pp. 79-91, 1977.
- [10] MCDONELL, V.G and SAMUELSEN, G.S., "Application of two-component phase doppler interferometry to the measurement of particle size, mass flux, and velocities

in two-phase flows,” *Twenty-Second Symposium (International) on Combustion*, The Combustion Institute, Pittsburgh, pp. 1961-1971, 1988.

- [11] EDWARDS, C.F. AND RUDOFF, R.C., ”Structure of a swirl-stabilized flame by imaging, laser doppler velocimetry, and phase doppler anemometry,” *Twenty-Third Symposium (International) on Combustion*, The Combustion Institute, Pittsburgh, pp. 1353-1359, 1990.
- [12] BULZAN, D.L., “Velocity and drop size measurements in a swirl-stabilized, combusting spray,” *Laser applications in combustion and combustion diagnostics*, SPIE vol.1862, pp.113-122, 1993.
- [13] BOSSARD, J.A. AND PECK, R.E., “Droplet size distribution effects in spray combustion,” *Twenty-Sixth Symposium (International) on Combustion*, The Combustion Institute, Pittsburgh, pp. 1671-1677, 1996.
- [14] CHIU, H.H., “Progress and challenges in droplet and spray combustion,” ASME Paper 97-AA-71, Presented at the ASME Asia '97 Congress & Exhibition, Singapore, 1997.
- [15] MERKLE, K. et al., “Effect of co- and counter-swirl on the isothermal flow- and mixture-field of an airblast atomizer nozzle,” *Int. J. of Heat and Fluid Flow*, vol. 24, pp. 529-537, 2003.
- [16] DATTA, A., “Influence of inlet flow conditions on the performance of a swirl-stabilized combustor burning liquid fuel spray,” *Int. J. of Energy Research*, vol. 24, pp. 373-390, 2000.
- [17] MONGIA, H. C., et al., “Swirl cup modeling part 1,” AIAA Paper 2001-3576, Presented at the 37th AIAA/ASME/SAE/ASEE Joint Propulsion Conference and Exhibit, Salt Lake City, UT, 2001.
- [18] HSIAO, G. and MONGIA, H., “Swirl cup modeling part II: inlet boundary conditions,” AIAA Paper 2003-1350, Presented at the 41st Aerospace Sciences Meeting and Exhibit, Reno, NV, 2003.
- [19] HSIAO, G. and MONGIA, H., “Swirl cup modeling part III: Grid independent solution with different turbulence models,” AIAA Paper 2003-1349, Presented at the 41st Aerospace Sciences Meeting and Exhibit, Reno, NV, 2003.

- [20] GIRIDHARAN, M. G., MONGIA, H. C., and JENG S.-M., "Swirl cup modeling - part VIII: spray combustion in cfm-56 single cup flame tube," AIAA Paper 2003-0319, Presented at the 41st Aerospace Sciences Meeting and Exhibit, Reno, NV, 2003.
- [21] EGGENSPIELER, G. and MENON, S., "Finite-rate kinetics modeling for predicting pollutant emission near lean blowout," AIAA Paper 2003-4941, Presented at the 39th AIAA/ASME/SAE/ASEE Joint Propulsion Conference and Exhibit, Huntsville, AL, 2003.
- [22] MENON, S., STONE, C., PATEL, N., "Multi-scale modeling for LES of engineering designs of large-scale combustors," AIAA Paper 2004-0157, Presented at the 41st Aerospace Sciences Meeting and Exhibit, Reno, NV, 2004.
- [23] Handbook of aviation fuel properties: prepared by the Coordinating Research Council, Inc., The Council, Atlanta, GA, 1983.
- [24] ATESHKADI, A., MCDONELL, V. G., SAMUELSEN, G. S., "Effect of hardware geometry on gas and drop behavior in a radial mixer spray," *27th Symposium (International) on Combustion*, The Combustion Institute, Pittsburgh, pp. 1985-1992, 1998.
- [25] Personal communication with Fisher-Scientific, lot # 028003, 10/12/2004.
- [26] Phase Doppler Particle Analyzer (PDPA)/Laser Doppler Velocimeter (LDV) Operations Manual, TSI Inc., St. Paul, MN, 2001.
- [27] Instruction Manual for PG-250 Portable Gas Analyzer, Horiba Instruments Inc., Irvine, CA, 1997.
- [28] BECKWITH, T.G., MARANGONI, R.D., LIENHARD, J.H., Mechanical Measurements, Addison-Wesley Publishing Company, New York, NY, 1995.
- [29] KUETHE, A. M., CHOW, C.-Y., Foundations of Aerodynamics, John Wiley and Sons, Inc., New York, NY, 1998.
- [30] COLBY, J., MENON, S., JAGODA, J., "Flow field measurements in a counter-swirling spray combustor," AIAA Paper 2005-4143, Presented at the 41st AIAA/ASME/SAE/ASEE Joint Propulsion Conference and Exhibit, Tucson, AZ, 2005.

- [31] POPE, S. B., Turbulent Flows, Cambridge University Press, Cambridge, UK, 2000.
- [32] KARPETIS, A. N., GOMEZ, A., “An experimental study of well-defined turbulent Nonpremixed spray flames,” *Combustion and Flame*, vol. 121, pp. 1-23, 2000.
- [33] ANDERSON, R. W., et al., “The effect of drop size on emissions from the primary zone of a gas turbine type combustor,” *16th Symposium (International) on Combustion*, The Combustion Institute, Pittsburgh, pp. 265-275, 1976.
- [34] MORLEY, C., *Gaseq*, Version 0.79.
- [35] TURNS, S. R., An Introduction to Combustion, McGraw-Hill, New York, 2000.